2011-04-27

Small-Signal Modeling and Analysis of Parallel-Connected Power Converter Systems for Distributed Energy Resources

Yu Zhang
University of Miami, angela77777@gmail.com

UNIVERSITY OF MIAMI

SMALL-SIGNAL MODELING AND ANALYSIS OF PARALLEL-CONNECTED POWER CONVERTER SYSTEMS FOR DISTRIBUTED ENERGY RESOURCES

By

Yu Zhang

A DISSERTATION

Submitted to the Faculty
of the University of Miami
in partial fulfillment of the requirements for
the degree of Doctor of Philosophy

Coral Gables, Florida

May 2011

UNIVERSITY OF MIAMI

A dissertation submitted in partial fulfillment of
the requirements for the degree of
Doctor of Philosophy

SMALL-SIGNAL MODELING AND ANALYSIS OF PARALLEL-CONNECTED POWER CONVERTER SYSTEMS FOR DISTRIBUTED ENERGY RESOURCES

Yu Zhang

Approved:

_____ Kamal Premaratne, Ph.D. Professor of Electrical and Computer Engineering	_____ Terri A. Scandura, Ph.D. Dean of the Graduate School
_____ Mohamed Abdel-Mottaleb, Ph.D. Professor of Electrical and Computer Engineering	_____ Michael Wang, Ph.D. Professor of Electrical and Computer Engineering
_____ Hongtan Liu, Ph.D. Professor of Mechanical and Aerospace Engineering	_____ Sung Jin Kim, Ph.D. Assistant Professor of Electrical and Computer Engineering

ZHANG, YU (Ph.D., Electrical and Computer Engineering)

Small-Signal Modeling and Analysis of Parallel-Connected Power Converter Systems for Distributed Energy Resources (May 2011)

Abstract of a dissertation at the University of Miami.

Dissertation supervised by Professor Kamal Premaratne.
No. of pages in text. (197)

Alternative energy resources (such as photovoltaics, fuel cells, wind turbines, micro-turbines, and internal combustion engines) and energy storage systems (such as batteries, supercapacitors, and flywheels) are increasingly being connected to the utility grid, creating distributed energy resources which require the implementation of an effective distributed power management strategy. Parallel-connected power converters form a critical component in such a distributed energy resources system. This dissertation addresses small-signal modeling and analysis of parallel-connected power converter systems operating in distributed energy environments. This work focuses on DC-DC and DC-AC power converters.

First, this work addresses the small-signal modeling and analysis of parallel-connected power converters in a battery/supercapacitor hybrid energy storage system. The small-signal model considers variations in the current of individual energy storage devices and the DC bus voltage as state variables, variations in the power converter duty cycles as control variables, and variations in the battery and the supercapacitor voltages and the load current as external disturbances. This dissertation proposes several different control strategies and studies the effects of variations in controller and filter parameters on system performance. Simulation studies were carried out using the Virtual Test Bed

(VTB) platform under various load conditions to verify the proposed control strategies and their effect on the final states of the energy storage devices.

Control strategies for single DC-AC three-phase power converters are also identified and investigated. These include a novel PV (active power and voltage) control with frequency droop control loop, PQ (active power and reactive power) control, voltage control, PQ control with frequency droop control, and PQ control with voltage and frequency droop control. Small-signal models of a three-phase power converter system with these control strategies were developed, and the impact of parameter variations on the stability of a PV controlled converter were studied. Moreover, a small-signal model of parallel-connected three-phase DC-AC power converters with individual DC power supplies and network is proposed. The simulations carried out in stand-alone and grid-connected modes verify the combined control strategies that were developed. In addition, a detailed small-signal mathematical model that can represent the zero-sequence current dynamics in parallel-connected three-phase DC-AC power converters that share a single DC power source is presented. The effects of a variety of factors on the zero-sequence current are investigated, and a control strategy to minimize the zero-sequence current is proposed. Time-domain simulation studies verify the results.

Simulations of a parallel-connected DC-AC power converter system with nonlinear load were carried out. The active power filter implemented in this system provides sharing of harmonic load between each power converter, and reduces harmonic distortion at the nonlinear load by harmonic compensation.

Key words: Small-signal modeling, parallel, converter, inverter, power sharing, power management, distributed energy resources, distributed generation, control strategy, battery, supercapacitor, hybrid energy storage system, zero-sequence current, active power and voltage control, nonlinear load.

To my beloved mother and father, Yajun and Zhiwei,
for their endless love, understanding, support and encouragement

Acknowledgement

The research documented in this work was carried out at the Department of Electrical and Computer Engineering, University of Miami, during 2007-2011. I gratefully acknowledge and thank all of those who assisted, inspired and encouraged me in my graduate program at the University.

I want to express my sincerest gratitude to my advisor, Dr. Kamal Premaratne. His guidance, technical advice, patience and personal time throughout my years as a graduate student have been truly appreciated. I deeply thank him for technical discussions and assistance in my research paper and for his enthusiasm and kindness. I would like to give my sincere thanks to Dr. M. A. Pai for his invaluable comments that helped to improve this dissertation greatly.

Let me take this opportunity to give special thanks to Dr. Hongtan Liu, Dr. Michael Wang, Dr. Mohamed Abdel-Mottaleb, and Dr. Sung Jin Kim. I would like to thank Dr. Liu for his encouragement, support and advice. Special thanks go to Dr. Wang, for his consideration and valuable suggestions. I am grateful to Dr. Abdel-Mottaleb for his

concern, help and support in my studies. I also would like to thank Dr. Kim for always being thoughtful and willing to help. I would like to give my thanks to Dr. Zhenhua Jiang for his assistance when he was affiliated with the University of Miami.

I also wish to mention my friends and laboratory colleagues, especially Reuven Lask, Yona Munro, Ji Wen, Xunwei Yu, Zhouyi Xu, Lin Lin, Wei Jiang, Dian Fan, Michelle Perez, Rosamund Coutts, and all my other friends for their concern and collaboration during my Ph.D. studies.

Abbreviations and Symbols

APF	Active power filter
DER	Distributed energy resources
DG	Distributed generation
I	Current
IC	Internal combustion
LHP	Left half plane
MAS	Multi agent systems
PHEV	Plug-in hybrid electric vehicle
P	Active power or real power
PI	Proportional and integral
PV	Photovoltaics
PWM	Pulse width modulation
Q	Reactive power
RES	Renewable energy sources

RHP	Right half plane
S	Complex power
SVPWM	Space vector pulse with modulation
V	Voltage
V2G	Vehicle to grid
VSI	Voltage-source inverters
VTB	Virtual Test Bed
WWEA	World Wind Energy Association
ω	Angular frequency

TABLE OF CONTENTS

List of Tables

List of Figures

Chapter 1. Introduction

1.1 Motivation

Distributed energy resources (DER) have been available for many years and DER development is increasing. Photovoltaic (PV), wind, microturbine, fuel cells, internal combustion engines, and so on are included in the energy systems [1-8]. In addition, energy storage systems, such as batteries, supercapacitors, and flywheels, are necessary to harness excess electricity produced by the most efficient generators during low loading [9]. This harvested energy can be released onto the grid to cover high demand when needed. In the future, using hybrid electric vehicles along with the utility grid in the form of plug-in hybrid electric vehicles (PHEV) and vehicle-to-grid systems (V2G) will be a very promising option to be included in the distributed energy systems classification. All of these technologies require specific power electronics capabilities to convert the generated power into useful power that can be directly interconnected with the utility grid or that can be used for other energy related applications.

New opportunities for distributed energy resources at the distribution level have been brought about by recent technological advances in small generators, power electronics,

and energy storage devices. Government incentives to utilize renewable energy have especially encouraged a more decentralized approach to power delivery.

Due to their energy dispatching features, parallel-connected power converters will be needed extensively in energy distributed systems, shown in Fig. 1-1. These systems enable the load current to be shared among the constituent converters and thus reduce the stress on each unit. The parallel operation structure has various advantages in its cost and the effectiveness of its maintenance compared with the single unit structure, and may bring about desirable outcomes, such as higher output power, lower harmonic currents, and lower switching frequency.

Due to the existence of a large number of power converters, the stability problem in distributed energy systems becomes increasingly important. This importance will cause small-signal modeling of power systems to become more significant and widespread. The main emphasis of this dissertation is on small-signal modeling and analysis for parallel-connected DC-DC power converters in a hybrid energy storage system and also for parallel-connected DC-AC inverter systems. It appears that small-signal modeling and analysis can help to design the system and controller parameters and will lead to improvements in the stability, performance, and design of distributed energy systems.

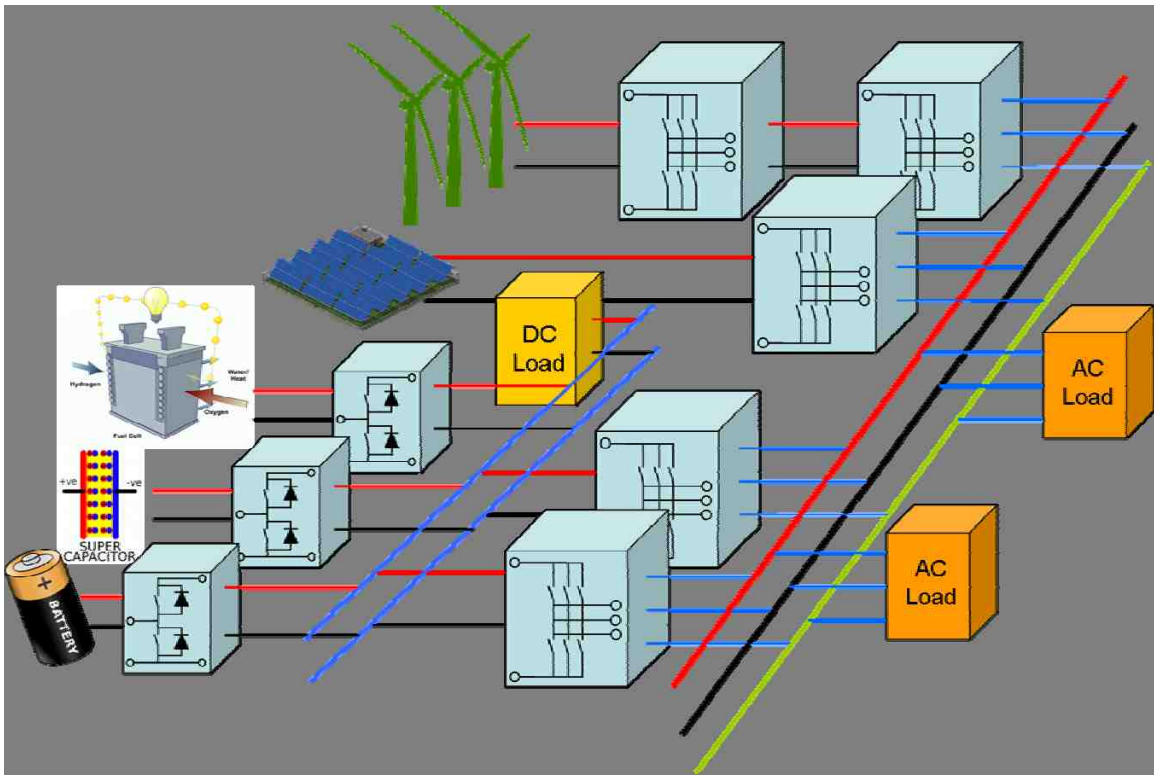

Fig. 1-1. Architecture of parallel-connected power converters in distributed energy resources.

This dissertation attempts to address some of these concerns, to propose solutions, and to use small-signal modeling and a systematic analysis of the parallel-connected structure power converters, including DC-DC and DC-AC power converters, in the distributed energy systems. The result would be better modeling, analysis, and control techniques. The specific objectives of the dissertation are the following:

- Small-signal modeling and stability analysis of parallel connected DC-DC power converter systems, and applying it to a hybrid energy storage system.

- Small-signal modeling and stability analysis of parallel connected DC-AC power inverter systems with different individual power sources, in both stand-alone mode and grid-connected mode.
- Small-signal modeling and stability analysis of parallel connected DC-AC power inverter systems sharing a single DC power source, with zero-sequence current control using Space Vector Pulse Width Modulation (SVPWM).
- Harmonic reduction when parallel connected DC-AC power inverters share with nonlinear load.

1.2 **Background**

This section reviews distributed energy resources; hybrid energy storage systems; and modeling, analysis and control of both parallel DC-DC and parallel DC-AC power converters.

1.2.1 Distributed Energy Resources (DER)

Distributed generation (DG) is the term used to describe small-scale power generation. It usually ranges in size from a few kW to a few MW, and is located at a distribution system close to the loads. In recent years, DG based on renewable energy sources (RES) and micro-sources such as internal combustion (IC) engines, gas turbines, micro-turbines, photovoltaic, fuel cells, and wind turbines have been experiencing rapid development due

to their promising advantages in reducing air pollution, improving power system efficiency, and relieving the stress on power transmission and delivery systems [10]. Smart grids, including DER, transform an energy production and power distribution system into a more intelligent, reliable, self-balancing, and interactive network. This enables enhanced environmental stewardship, operational efficiencies, and energy security. These DG systems are often used to deliver electrical power into the utility grid or are used in remote areas as stand-alone power supplies.

The microsources of special interest for micro generation have small (lower than 100 kW) units, with power electronic interfaces. These sources, including wind turbines, PV panels, micro-turbines, and fuel cells, are placed at customers' sites. They are low cost, low voltage, highly reliable and environmentally friendly.

Wind-turbine technology has undergone a dramatic transformation during the last 20 years. The first wind-electric systems were built in the United States in the late 1890s. The technology developed from a fringe science in the 1970s to the sophisticated wind turbines of the 2000s, which use the latest in power electronics, aerodynamics, and mechanical drive train designs [11]. The global installed capacity of wind turbines has been growing at over 30% per year since 2000. In 2010, the wind capacity reached worldwide 196630 MW. Based on a report of the World Wind Energy Association

(WWEA), the forecast in 2015 for worldwide wind installations is 600,000 MW. This represents growth for the wind energy market despite the general economic crisis [12].

Photovoltaic technology involves converting solar energy directly into electrical energy. A solar cell, typically made of semiconductor materials such as crystalline silicon, produces electricity from light through a process called the photovoltaic effect. The efficiency of a solar cell is determined by its ability to convert available sunlight into usable electrical energy. Therefore, to produce a significant amount of electrical energy, solar cells must have large surface areas. Solar cells usually are packaged in PV modules, often electrically connected in multiples as solar PV strings and arrays. The first practical applications of PV power were for portable electronics, and orbiting satellites and other spacecraft, but today PV modules are widely used for grid-connected power generation. PV production has been doubling every two years, increasing by an average of 48% each year since 2002. It is one of the fastest-growing energy technologies in the world.

A fuel cell is an electrochemical energy conversion device. It produces electrical power directly from the chemical energy contained in fuel (such as hydrogen, natural gas, and methanol). The fuel-to-electric-power efficiency for a fuel cell can be as high as 65%. This high efficiency gives fuel cells the potential to be roughly twice as efficient as the average central power station operating today [13].

Despite the many advantages of RES-based DG systems, DG presents a quite different and challenging picture in terms of grid connection. For example, the voltage generated by variable speed wind-power generators (with variable output frequency), PV systems (DC voltage) and fuel cell systems (DC voltage) cannot be directly connected to a grid. Thus, power electronics are essential components for converting generated power into useful power which can be directly interconnected to the utility grid.

1.2.2 Energy Storage Systems

Energy storage is increasingly important in solving the global energy shortage and climate change problems [14]. Renewable energy sources are promising, but they are typically intermittent, so energy storage is necessary to smooth out the power generation. While plug-in hybrid electric vehicles have potential to solve the energy problems in the transportation sector by exposing the automotive industry to renewable energy [15-18], energy storage is vital. Additionally, the load on the grid typically experiences significant fluctuations, especially when plug-in hybrid electric vehicles are moving or are connected to the grid at unpredictable times and locations. Therefore, reversible energy storage devices are needed, to save excess energy temporarily for meeting a later emergent load requirement. This will increase the response rate and power capacity of the power supply, and will improve stability, power quality, and reliability of supply.

Batteries are usually used as mid-term energy storage devices due to their relatively high energy density and low power density [19-22]. Supercapacitors, with extremely high cycling capability, mechanical robustness, and relatively high power density but low energy density, are an interesting option for short-term high-power applications. They can cover large power fluctuations, especially for intermittent power supplies and instantaneous high load requirements, and can find their place as a complement to batteries [23-27]. It is then advantageous to combine these two energy storage devices to accomplish better power and energy performance.

Some hybrid power sources have been studied, such as the fuel cell/supercapacitor, and fuel cell/battery [28-31]. Generally, active hybrids are more flexible than passive hybrids, which connect the power sources directly to the terminal voltage bus. There are two main types of active structure for the battery/supercapacitor hybrid energy storage system. In the first type, a DC-DC power converter is placed between the two power sources [32, 33]. Pay and Baghzouz consider a case where the supercapacitor bank is connected in parallel with the battery through a DC-DC converter that is necessary to achieve optimal performance [32]. In another case, the battery is isolated from the load through a DC-DC converter, and the load voltage and the battery current are controlled by the converter [33]. In the second type, a parallel system is designed to balance the

stresses among the parallel DC-DC converters. Each energy device connects to the output terminal so that power sharing among all energy storage devices can be actively regulated by controlling each corresponding power converter [34-36]. Supercapacitors can be used to regulate DC-link voltage, and batteries can also be used as the DC-link voltage regulator to assist with the power supply [35].

Parallel DC-DC converters have been widely used in many applications in distributed power supply systems since the first paper on basic parallel DC-DC converters was published in 1980 by Hebel [37]. They have many desirable features: increased reliability, expandability, and hot plug-in capability. However, the analysis, design, and control of such converters are not simple [38-53]. Actually, the modules of parallel converters in general are not identical, due to component tolerances, component differences, and varying physical conditions. In addition, loads are not ideally balanced in practice, which increases the stress on one or more units, thereby reducing the reliability of the system [43].

A master-slave control strategy, which is often used to regulate the slave output current to track the master output current, can be applied in hybrid energy storage technology. Energy management is achieved by regulating the supercapacitor current according to the battery current. Moreover, small-signal modeling and analysis around a

certain operating point may be used to study the effects of variations in control and system parameters on the response of the hybrid energy storage systems. This relates to dynamic stability, which is widely used in power systems [54, 55].

1.2.3 Microgrid and Control of Parallel-Connected Three-Phase Power Converter Systems

Technological development and environmental pressures encourage the interconnection of renewable energy sources to the distribution network. The interconnection of large amounts of alternative energy generation, however, causes problems in a network designed for conventional operation. The use of power electronics interfaces and the bundling of micro-generation and loads into so-called microgrids offers a potential solution [56, 57]. In reference [58], the microgrid concept assumes a cluster of loads and microsources working as a single system that supplies both power and heat to its local area. This concept provides a new paradigm for defining the operation of distributed generation. To the utility, the microgrid can be thought of as a controlled cell of the power system [58]. Marnay Chris et al [59] introduced the features and benefits of microgrid , such as enhanced local reliability, reduced feeder losses, which supports local voltage, providing increased efficiency through using waste heat, combined heat and power, voltage sag correction, and providing uninterruptible power supply functions.

Driesen, J. and F. Katiraei presented the major differences between conventional methods of distribution system planning and the emerging planning approaches [60]. The conventional planning method designs are based on electricity production in centralized power generation stations and on delivery through passive distribution networks to end users. They proposed a general classification of possible microgrid architecture and their characteristics based on applications, ownership structure, and type of loads served by the microgrid, a single or multi-facility industrial/commercial microgrid, and a remote microgrid.

One classification of microgrid control is centralized control vs decentralized control, based on where the response decision is made. Centralized control of a microgrid, based on a communication infrastructure, is studied [61]. The operation of a central controller for microgrids is described [62]. The controller aims to optimize the operation of the microgrid during interconnected operations, i.e., to maximize its value by optimizing the production of the local DGs and power exchanges with the main distribution grid. Funabashi, T., et al [63] discussed a centralized architecture of multi agent systems (MAS) to control the microgrid. However, for microgrids in remote areas, with long connection distance between inverters, it is impractical and costly to distribute the dynamic sharing signals. Furthermore, centralized architecture is usually very sensitive to the system's

failure. This is because once the central agent fails to work, the whole system is under risk of collapse. To overcome the reliability limitations of a centralized control approach, decentralized controllers emerge. Aris L. Dimeas et al. [64] presented the operation of a multiagent system for the control of a microgrid. They compare the proposed fully decentralized approach with a more centralized one. In other applications, several levels of decentralization may be applied, ranging from centralized control to a fully decentralized approach.

A microgrid can be operated either in grid connected mode or in stand-alone (islanded or autonomous) mode. In grid connected mode, most of the system-level dynamics are dictated by the main grid due to the relatively small size of micro sources. In stand-alone mode, the system dynamics are dictated by the microsources themselves, their power regulation control and the network.

The basic control objective in a microgrid is to accomplish accurate power sharing, and voltage magnitude and frequency regulation of the microgrid. Control loops with different control objectives are investigated and proposed [65-68]. Droop controllers, used to emulate the droop characteristics of synchronous generators, were proposed as power sharing controllers of microgrid generators [68-71]. Chandorkar et al. and Katiraei, F. and M.R. Iravani [68, 69] used a static droop compensator for power sharing. Josep M.

Guerrero et al. utilized an enhanced droop control featuring a transient droop performance [71].

In a microgrid, most DERs that can be installed in a microgrid are not connected to the power grid directly because of the characteristics of the produced energy. This dispatching feature of DERs in a microgrid requires the power converters to have a parallel operation structure. There are several possible structures of three-phase power converter parallel connections. One possibility, which is suitable for DERs in the microgrid, is to connect the AC sides of power converters together and have different DC side inputs. This is similar to using separate power supplies. In this structure, multiple DERs such as fuel cells and photovoltaic arrays are operated in parallel through power converters.

Another possible structure of three-phase power converter parallel connections is to connect both sides of the power converters together. This approach enables higher power to be shared by a set of power converters and can also achieve further goals such as voltage and power regulation. With this approach, the open-circuit zero-sequence channel of both three-phase power converters are connected together, and a path for the circulating (or zero-sequence) current is then created [72-74]. Therefore there are potential zero-sequence currents circulating among the parallel converters. In the past,

many approaches and strategies have been developed to solve this problem, such as isolation, high impedance and synchronized control [75-77]. Lee [75] proposed a novel instantaneous current sharing control scheme in parallel connected UPS (inverters) with separate DC power supplies. An approach was presented by Hashii, M. et al. [77] that can minimize the zero-sequence current by controlling redundant switching vectors. A parallel technique for current-controlled Pulse Width Modulation (PWM) inverters was described by Ogasawara, S., et al. [78] to reduce the switching frequency and harmonic current content, attain high speed current response and regulate the zero-sequence current to zero. Two voltage source inverters are connected in parallel through current balancers. Inter-phase reactors are used to provide high zero-sequence impedance. In a non-isolated paralleling scheme, a zero-sequence path is formed, so it is necessary to regulate zero-sequence current. There are many electric loads on the grid with nonlinear characteristics such as diodes, rectifiers, power transistors, other electronic switches, variable speed drives, and even common office equipment such as computers and printers [79-81]. They can draw harmonic and reactive power components of current from AC mains. The injected harmonics and reactive power burden could also cause unbalance currents, low system efficiency, poor power factor, and even cause disturbances to the nearby communication network [82-84].

Active power filter (APF) is a very useful tool for eliminating harmonic pollution in the power grid [85-90]. APF injects a current equal in magnitude but in opposite in phase to harmonic current. Compared with traditional passive filters, APF has significant advantages such as good controllability, fast response and high control accuracy.

There are other approaches to handle the nonlinear load situation. Borup, U. et al. [84] presented a load sharing technique that shares harmonic currents among converters equipped with active compensation for harmonic distortion without mutual communication. To avoid the use of band-trap filters for decomposing the positive and negative-sequence *d-q* components of current and voltage, a new control scheme with multi frequency proportional-resonant controller in the stationary $\alpha\beta$ frame is employed [91] to improve the steady state and dynamic response under generalized unbalanced operation conditions. The DC-link current spectrum drawn by a three-phase inverter supplying a balanced load can be used to monitor the state of the inverter or load. A method for calculating the DC link current harmonics in a three-phase inverter was described and validated by comparison with measured values for unbalanced and nonlinear loads [92].

1.2.4 Small-Signal Modeling

Due to the existence of a large number of power converters, the dynamic stability problem in distributed energy systems becomes increasingly important. Dynamic stability of power electronics systems has been studied for many years. The significance of knowing the system transient stability for an assortment of variations leads to the widespread use of small-signal modeling. Small-signal analysis and synthesis around certain operating points (steady state points) are often used to investigate both the interactions among several power electronic modules and the stability issues of the whole system. It is a common analysis technique in electrical engineering, which is used to approximate the behavior of nonlinear devices through linear equations. It has been used for several decades in electronics [93-95] after the Lindholm-Hamilton theory [96] for systematic modeling of solid-state devices. It remains a very useful systematic method for power electronics [40, 42, 44, 49, 54, 66, 97-99] .

To describe power system dynamic performance, differential equations can be expressed as a set of n first order, nonlinear, ordinary differential equations. These can be represented in the state-variable form as the vector equations:

$$\dot{x} = f(x,u) \tag{1-1}$$

where:

$$x=\begin{bmatrix} x_1 \\ x_2 \\ \vdots \\ x_n \end{bmatrix} \quad f=\begin{bmatrix} f_1 \\ f_2 \\ \vdots \\ f_n \end{bmatrix} \quad u=\begin{bmatrix} u_1 \\ u_2 \\ \vdots \\ u_r \end{bmatrix} \tag{1-2}$$

The column vector x is referred to as the state vector, x_i as the state variables. The column vector u is the vector of inputs to the system.

$$y=g(x,\ u) \tag{1-3}$$

where:

$$y=\begin{bmatrix} y_1 \\ y_2 \\ \vdots \\ y_n \end{bmatrix} \qquad g=\begin{bmatrix} g_1 \\ g_2 \\ \vdots \\ g_r \end{bmatrix} \tag{1-4}$$

The column vector y is the vector of inputs, and g is the vector of nonlinear functions relating state and input variables to output variables.

The equilibrium point or singular point is the point whose trajectory speed is zero. From the mathematical view, it must satisfy the following equation:

$$f(x_0, u_0)=0 \tag{1-5}$$

The stability of any hyperbolic equilibrium point x_0 of Eq. (1-1) is determined by the signs of the real parts of the eigenvalues of the matrix $Df(x_0)$.

A method, originated by Lyapunov, is very useful for determining the stability of nonhyperbolic equilibrium points.

Based on Lyapunov theory, if a small-signal linear model is valid near an equilibrium state and it is stable, then there is a region containing the equilibrium state in which the nonlinear system is stable. From this concept, the system model can be linearized within the neighborhood of the equilibrium point.

Here is an expansion of the nonlinear equation in terms of perturbations from these equilibrium values:

$$x = x_0 + \tilde{x}\ ;\ \ u = u_0 + \tilde{u} \tag{1-6}$$

The nonlinear function can be expressed in terms of Taylor's series expansion. Neglecting the second and higher order powers, the equations become:

$$\dot{\tilde{x}} = A\tilde{x} + B\tilde{u} \tag{1-7}$$

$$\tilde{y} = C\tilde{x} + D\tilde{u} \tag{1-8}$$

where $A=Df(x_0)$.

Then the equilibrium point x0 has been translated to the origin of the linear system.

We can use the eigenvalues to study the small-signal stability of the operating point. It is apparent that the system is locally stable if all of the eigenvalues are on the left-hand side of the imaginary axis of the complex plane. Otherwise, if at least one of the eigenvalues appears on the right of this axis, the corresponding modes are said to be unstable. This is confirmed by looking at the time dependent characteristic of the

oscillatory modes corresponding to each eigenvalue λ_i, given by $e^{\lambda i}$. The latter part shows that a real eigenvalue corresponds to a non-oscillatory mode. If the real part of the eigenvalue is negative, the mode decays over time. If the real part of the eigenvalue is positive, the mode is said to have aperiodic instability.

On the other hand, conjugate complex eigenvalues correspond to oscillatory modes. A pair with a positive real part represents an unstable oscillatory mode since eigenvalues yield an unstable time response of the system.

Therefore, small-signal modeling and analysis for parallel connected converters is used to explore the characteristics of their system, and to select system and controller parameters, and thus become indispensable and unavoidable tasks for system designers.

1.3 **Outline and Contributions of This Dissertation**

This dissertation addresses the small-signal modeling and stability analysis of parallel-connected power converter systems operating in distributed energy environments. The work focuses on DC-DC and DC-AC power converters.

First, this work addresses the small-signal modeling and analysis of parallel-connected power converters system and applies it in a battery/supercapacitor hybrid energy storage system. The small-signal model considers the variations in the currents of individual DC power supplies and the DC bus voltage as state variables, the variations in

the power converter duty cycles as control variables, and the variations in the voltages of the DC power supplies and in the load current as external disturbances. This dissertation proposes a novel energy management method using three control strategies and in three different conditions. The method is realized in a hybrid energy storage system comprising a battery and a supercapacitor as well as appropriate bidirectional DC-DC power converters. The proposed method is more flexible than previous methods. Under certain load situations, the proposed strategies can determine the current sharing ratio of the supercapacitor and the battery. Moreover, in a specific control strategy, the power sharing ratios are dependent on the load. In addition, frequency-domain analysis of the small-signal model is verified by the simulation results based on the average model. Simulation results indicate that an increase in proportional gains k_{p1}, a large change in integral gain k_{i1} of the voltage controller, an increase in inductance, or a decrease in capacitance may deteriorate the stability of the system. The effects of the controller and system parameter variations are studied in order to help designers to define control parameters, filter inductance and capacitance for improved performance of the system. And last, simulation studies were carried out using the Virtual Test Bed (VTB) platform under various load conditions to verify the proposed control strategies and their effect on the final states of the energy storage devices.

Control strategies for single DC-AC three-phase power converters are also identified and investigated. These include a novel PV (active power and voltage) control with frequency droop control loop, PQ (active power and reactive power) control, voltage control, PQ control with frequency droop control, and PQ control with voltage and frequency droop control. Small-signal modeling in *d-q* rotating reference frame of a three-phase power converter system with these control strategies was developed. The impact of parameter variations on the stability of a PV controlled converter was studied. Moreover, small-signal modeling of parallel-connected three-phase converters with individual DC power supplies and network is proposed. The proposed model considers the variations in the output voltages and currents, line currents, local load currents and shared load currents, duty cycles of individual inverters, and the variations in the voltages of their DC power supplies. The loci of the eigenvalues shows an increase in droop control parameter K will decrease damping ratio and eventually cause the system instability. Several simulations carried out in stand-alone and grid-connected modes verify small-signal analysis results and the combined control strategies. Furthermore, a detailed small-signal mathematical model is presented that can represent the zero-sequence current dynamics in parallel-connected three-phase voltage source converters that share a single DC power source. Also the effects of a variety of factors on the zero-

sequence current are investigated, and a control strategy to minimize the zero-sequence current is proposed. Time-domain simulation studies verify the results.

A simulation of a parallel-connected DC-AC power converter system with a nonlinear load is carried out. The active power filter implemented in the parallel-connected DC-AC three-phase power converter system provides sharing of harmonic load for each power converter, and reduces harmonic distortion at the nonlinear load by harmonic compensation.

Chapter 2. Small-Signal Modeling and Analysis of Parallel-Connected DC-DC Power Converter System

Small-signal modeling and analysis are frequently used as a tool to design the control loops and study the effects of system and controller parameter variations on system performance.

In order to investigate the stability of a parallel-connected DC-DC power converters system and design parallel system, a small-signal model based on a time average model of a parallel-connected converters system is addressed, which includes two boost converters and two DC power sources. The small-signal model considers the variations in the currents of individual DC power supplies and the DC bus voltage as state variables, the variations in the power converter duty cycles as control variables, and the variations in the output voltages of the DC power supplies and the load current as external disturbances. Moreover, this model is applied to a battery/supercapacitor hybrid energy storage system. Several active control strategies are proposed to maintain the DC bus voltage and regulate discharging and charging currents of the battery and supercapacitor.

Based on the proposed small-signal model and analysis, the impacts of variations in the system are studied and controller parameters on the system performance.

2.1 Small-Signal Modeling of Parallel-Connected Converters System

A basic circuit diagram of the two parallel-connected converters system including two boost converters and two DC power sources is shown in Fig. 2-1. The current source i_{Load} represents the load current, i_x represents the current of the xth power converter, v_{gx} represents the output voltage of the xth power converter, v_{out} represents the bus voltage and d_x represent the duty cycle of the xth power converter. An equivalent circuit of the time-average model of a two parallel-connected converters system is shown in Fig. 2-2. Neglecting the switching transients and using the volt-second principle, the time-average model of the two parallel-connected converters system can be obtained as follows.

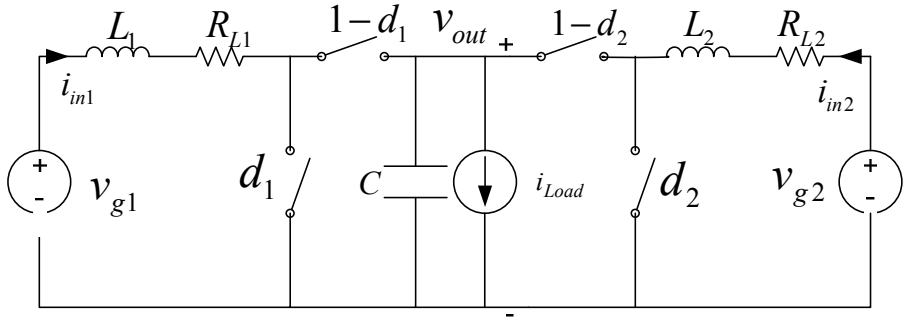

Fig. 2-1. Circuit diagram of a two parallel-connected converters system.

$$L_1 \frac{di_{in1}}{dt} = v_{g1} - (1-d_1)v_{out} - i_{in1}R_{L1} \tag{2-1}$$

$$L_2 \frac{di_{in2}}{dt} = v_{g2} - (1-d_2)v_{out} - i_{in2}R_{L2} \tag{2-2}$$

$$C \frac{dv_{out}}{dt} = (1-d_1)i_{in1} + (1-d_2)i_{in2} - i_{Load} \tag{2-3}$$

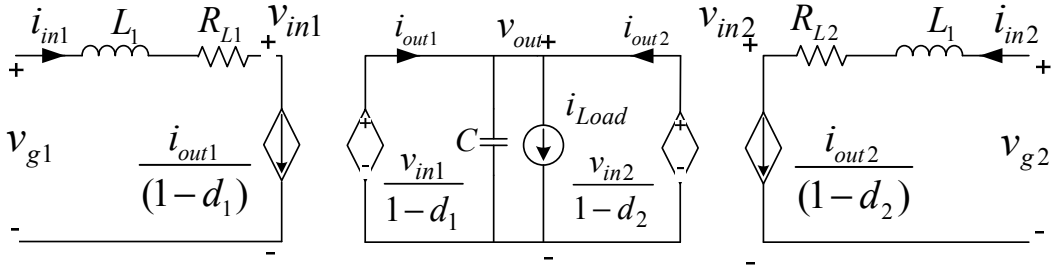

Fig. 2-2. Equivalent circuit of the time-average model of a two parallel-connected converters system.

In order to design the control loops and study the effect of system and controller parameter variations on system performance, small-signal modeling is used as a tool for analysis. Suppose the two parallel-connected converters system is operating at the steady-state point. By perturbing and linearizing the time-average model Eqs. (2-1)(2-2)(2-3) around the steady-state operating point, it is possible to find a small-signal model as follows. D and I_{in} represent the duty cycle and current at a steady state point.

$$L_1 \frac{d\tilde{i}_{in1}}{dt} = \tilde{v}_{g1} - (1-D_1)\tilde{v}_{out} + \tilde{d}_1 V_{out} - \tilde{i}_{in1}R_{L1} \tag{2-4}$$

$$L_2 \frac{d\tilde{i}_{ini2}}{dt} = \tilde{v}_{g2} - (1-D_2)\tilde{v}_{out} + \tilde{d}_2 V_{out} - \tilde{i}_{in2}R_{L2} \tag{2-5}$$

$$C \frac{d\tilde{v}_{out}}{dt} = (1-D_1)\tilde{i}_{in1} + (1-D_2)\tilde{i}_{in2} - I_{in1}\tilde{d}_1 - I_{in2}\tilde{d}_2 - \tilde{i}_{Load} \tag{2-6}$$

Eqs. (2-4), (2-5) and (2-6) can be expressed in the matrix form. The state-space equation of the two parallel-connected converters system can be written as follows.

$$\dot{\tilde{x}}_o = A\tilde{x}_o + B\tilde{u} + F\tilde{v} \tag{2-7}$$

$$\tilde{y} = C\tilde{x}_o \tag{2-8}$$

where: $\tilde{x}_o = \begin{bmatrix} \tilde{i}_{in1} & \tilde{i}_{in2} & \tilde{v}_{out} \end{bmatrix}^T$, $\tilde{u} = \begin{bmatrix} \tilde{d}_1 & \tilde{d}_2 \end{bmatrix}^T$,

$\tilde{v} = \begin{bmatrix} \tilde{v}_{g1} & \tilde{v}_{g2} & \tilde{i}_{Load} \end{bmatrix}^T$, $\tilde{y} = \begin{bmatrix} \tilde{i}_{in1} & \tilde{i}_{in2} & \tilde{v}_{out} \end{bmatrix}^T$,

$$A = \begin{bmatrix} -\frac{R_{L1}}{L_1} & 0 & -\frac{(1-D_1)}{L_1} \\ 0 & -\frac{R_{L2}}{L_2} & -\frac{(1-D_2)}{L_2} \\ \frac{(1-D_1)}{C} & \frac{(1-D_2)}{C} & 0 \end{bmatrix}, \quad B = \begin{bmatrix} \frac{V_{out}}{L_1} & 0 \\ 0 & \frac{V_{out}}{L_2} \\ -\frac{I_{in1}}{C} & -\frac{I_{in2}}{C} \end{bmatrix},$$

$$F = \begin{bmatrix} \frac{1}{L_1} & 0 & 0 \\ 0 & \frac{1}{L_2} & 0 \\ 0 & 0 & -\frac{1}{C} \end{bmatrix}, \quad C = I .$$

The small-signal equivalent circuit of the two parallel-connected converters system including two boost converters is shown in Fig. 2-3. This model takes into account the effects on the currents of a variety of factors, such as the voltage-current characteristics of individual DC sources, power converter and filter parameters, and controller parameters. The proposed model considers the variations in the power source output currents and DC bus voltage as state variables, the variations in the power converter duty cycles as the control input, and the variations in the DC power source voltages and the load current as external disturbances.

Based on the small-signal model shown in Eqs. (2-7) and (2-8), a frequency-domain model can be derived. By setting disturbances to zero, the open-loop transfer function from the control input $\tilde{d}_1(s)$ to one output $\tilde{v}_{out}(s)$:

$$\tilde{v}_{out}(s)/\tilde{d}_1(s) = (L_2 s + R_{L2}) \frac{(1-D_1)V_{out} - (L_1 s + R_{L1} I_{in1}}{Cs(L_1 s + R_{L1})(L_2 s + R_{L2}) + (L_2 s + R_{L2})(1-D_1)^2 + (L_1 s + R_{L1})(1-D_2)^2} \quad (2\text{-}9)$$

The transfer functions from inputs to other outputs may also be obtained in the same way.

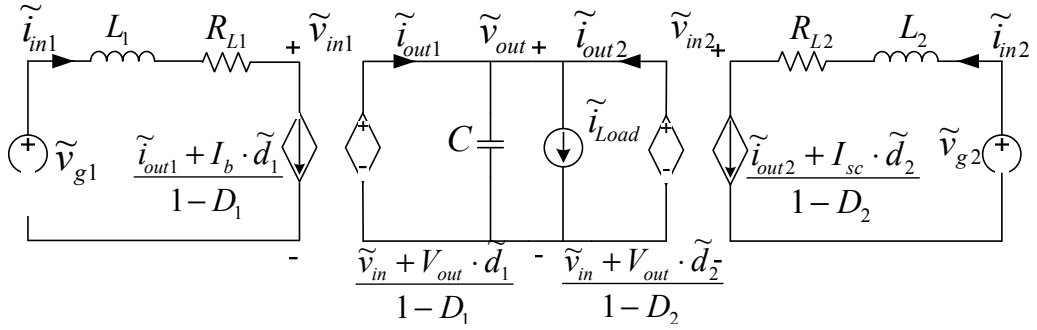

Fig. 2-3. Equivalent circuit of the small-signal model of the two parallel-connected converters system.

2.2 Control Loops Design for Parallel-Connected Converters System

Taking the control system into account, the entire system can be modeled as a multiple-input, multiple-output system, as shown in Fig. 2-4. Block K represents the dynamics of the current measurement circuit. Blocks H1 and H2 represent the control loops of the power sources.

Here block H1 represents the voltage control loop to regulate the bus voltage v_{out} and block H2 is the control loop to regulate the output current of one DC power source. Block K produces the output current reference based on another DC power source.

This model is useful in capturing the small-signal dynamics of the two parallel-connected converters system and can be easily extended to other hybrid energy systems with multiple energy sources.

With the master-slave current sharing strategy, the duty cycles of the power converters can be obtained as follows.

$$\tilde{d}_1 = (\tilde{v}_{out\_ref} - \tilde{v}_{out})H_1 \tag{2-10}$$

$$\tilde{d}_2 = (K\tilde{i}_{in1} - \tilde{i}_{in2})H_2 \tag{2-11}$$

In this study, proportional-integral (PI) control schemes are used for these two controllers H1 and H2 shown in Eq. (2-12) and (2-13). K is selected as a proportional coefficient.

$$H_1 = k_{p1} + \frac{k_{i1}}{s} \tag{2-12}$$

$$H_2 = k_{p2} + \frac{k_{i2}}{s} \tag{2-13}$$

Then, the following are obtained:

$$\tilde{d}_1 = k_{p1}(\tilde{v}_{out\_ref} - \tilde{v}_{out}) + k_{i1}\int(\tilde{v}_{out\_ref} - \tilde{v}_{out})dt \tag{2-14}$$

$$\tilde{d}_2 = k_{p2}(K\tilde{i}_{in1} - \tilde{i}_{in2}) + k_{i2}\int(K\tilde{i}_{in1} - \tilde{i}_{in2})dt \tag{2-15}$$

We define two variables:

$$\tilde{\phi} = \int \left(\tilde{v}_{out\_ref} - \tilde{v}_{out} \right) dt \tag{2-16}$$

$$\tilde{\lambda} = \int \left(K\tilde{i}_b - \tilde{i}_{sc} \right) dt \tag{2-17}$$

Eq. (2-18) represents the linearized small-signal state-space form of the voltage and current controllers.

$$\tilde{u} = B_D \tilde{x} + F_R \tilde{r} \tag{2-18}$$

where: $\tilde{u} = \begin{bmatrix} \tilde{d}_1 & \tilde{d}_2 \end{bmatrix}^T$, $\tilde{x} = \begin{bmatrix} \tilde{i}_{in1} & \tilde{i}_{in2} & \tilde{v}_{out} & \tilde{\phi} & \tilde{\lambda} \end{bmatrix}^T$, $\tilde{r} = \begin{bmatrix} \tilde{v}_{out\_ref} \end{bmatrix}^T$

$$B_D = \begin{bmatrix} 0 & 0 & -k_{p1} & k_{i1} & 0 \\ k_{p2}K & -k_{p2} & 0 & 0 & k_{i2} \end{bmatrix}, \; F_R = \begin{bmatrix} k_{p1} \\ 0 \end{bmatrix}$$

A complete state-space small-signal model of the system can be obtained by combining the state-space models of the open-loop system with the voltage controller and the current controller, given by Eqs. (2-7) and (2-18). There are 5 state variables in total.

$$\dot{\tilde{x}} = \left(A_1 + B_1 B_D \right) \tilde{x} + \left(B_1 F_R + F_2 \right) \tilde{r} + F_1 \tilde{v} \tag{2-19}$$

where:

$$A_1 = \begin{bmatrix} & & & . & 0 & 0 \\ & A & & . & 0 & 0 \\ & & & . & 0 & 0 \\ . & . & . & . & . & . \\ 0 & 0 & -1 & . & 0 & 0 \\ K & -1 & 0 & . & 0 & 0 \end{bmatrix} \quad B_1 = \begin{bmatrix} & B & \\ & ..... & \\ 0 & 0 & \\ 0 & 0 & \end{bmatrix} \quad F_1 = \begin{bmatrix} & F & \\ & ..... & \\ 0 & 0 & 0 \\ 0 & 0 & 0 \end{bmatrix} \quad F_2 = \begin{bmatrix} 0 \\ 0 \\ 0 \\ 1 \\ 0 \end{bmatrix}$$

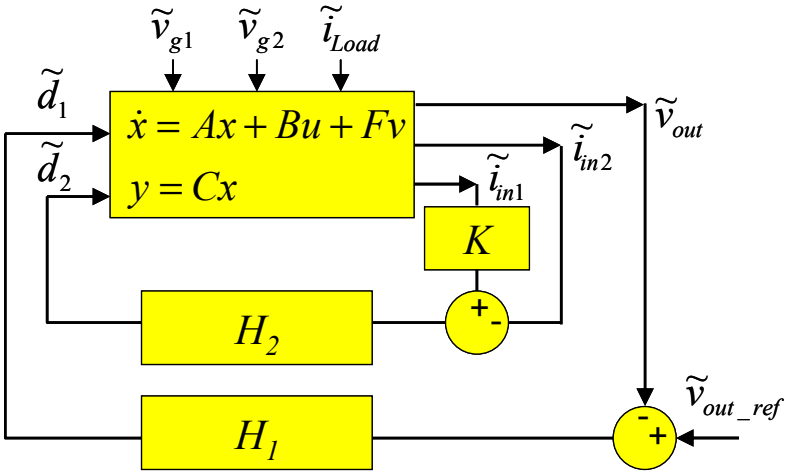

Fig. 2-4. Block diagram of the model representing the dynamics of the two parallel-connected converters system.

A linearized small-signal model of the system is derived in the last part. Then it is used to investigate small-signal dynamic behavior of the parallel DC-DC power converter system, design system and controller parameters for optimum performance. The closed-loop transfer function from $\tilde{v}_{out\_ref}(s)$ to $\tilde{v}_{out}(s)$:

$$\tilde{v}_{out}(s)/\tilde{v}_{out\_ref}(s) = \frac{\left(\frac{(1-D_1)V_{out}}{(L_1 s + R_{L1})} - I_{in1}\right)H_1 + \left(\frac{(1-D_2)V_{out}}{(L_2 s + R_{L2})} - I_{in2}\right)\frac{L_2 s + R_{L2}}{L_2 s + R_{L2} + H_2 V_{out}}\frac{KH_1 H_2 V_{out}}{(L_1 s + R_{L1})}}{\left\{\left(Cs + \frac{(1-D_1)^2}{(L_1 s + R_{L1})} + \frac{(1-D_2)^2}{(L_2 s + R_{L2})}\right) + \left(\frac{(1-D_1)V_{out}}{(L_1 s + R_{L1})} - I_{in1}\right)H_1 \right.} \\ \left. - \left(\frac{(1-D_2)V_{out}}{(L_2 s + R_{L2})} - I_{in2}\right)\frac{L_2 s + R_{L2}}{L_2 s + R_{L2} + H_2 V_{out}}\left(\frac{-KH_2(1-D_1)}{(L_1 s + R_{L1})} - \frac{KH_1 H_2 V_{out}}{(L_1 s + R_{L1})} + \frac{H_2(1-D_2)}{(L_2 s + R_{L2})}\right)\right\} \quad (2\text{-}20)$$

The transfer functions from input to other outputs may also be obtained in the same way.

2.3 Case Study: Battery/Supercapacitor Hybrid Energy Storage Systems

In the next section, parallel-connected DC converters are studied in a hybrid energy storage system. The system proposed in the last section is applied in a hybrid energy storage system comprising a battery and a supercapacitor as well as appropriate bidirectional DC-DC power converters. As shown in Fig. 2-5, the active hybrid energy storage system provides a temporary energy reservoir between the main source and the load. Because power may flow through the battery and supercapacitor in both directions, a bi-directional DC-DC power converter is placed between each energy storage device and the DC voltage bus. In this hybrid energy storage system, several control strategies for power sharing between the two energy storage devices are proposed. In the next part, is the presentation of a frequency-domain analysis based on the proposed small-signal model. In addition, control strategies with different conditions are verified and compared against each other through simulation studies. Frequency-domain analysis is validated through time-domain simulation based on the time-average model. The effects of the controller and system parameter variations on the system performance are also studied.

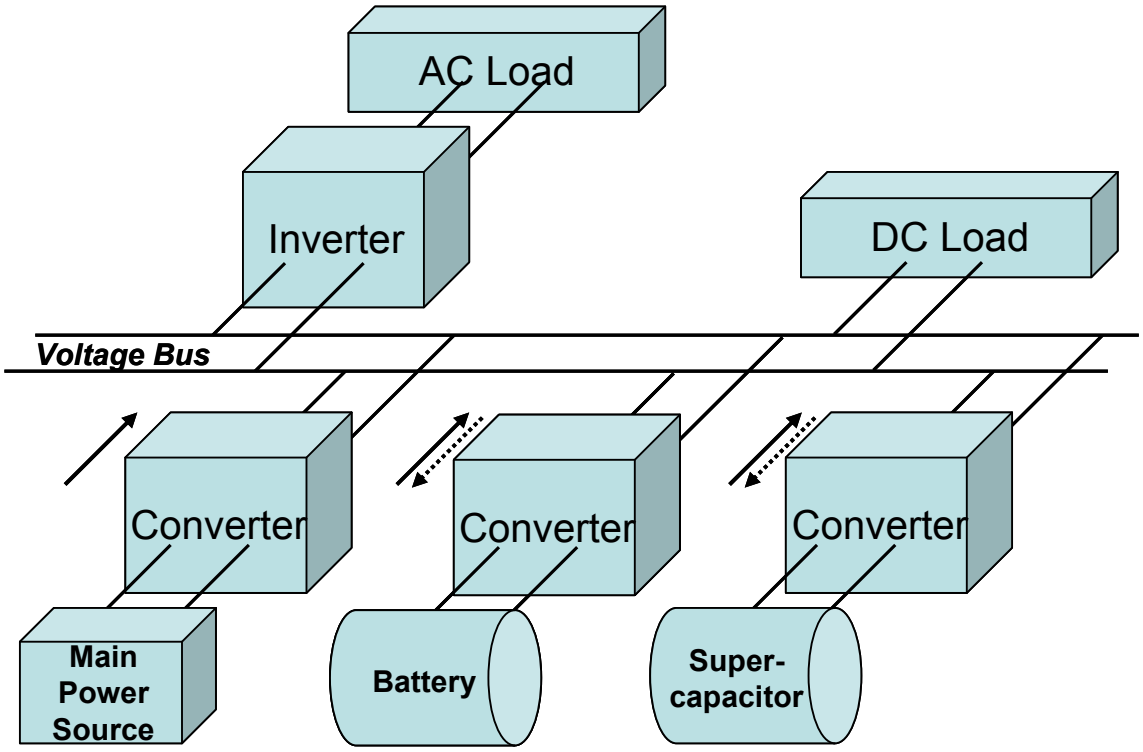

Fig. 2-5. Architecture of an active hybrid energy storage system.

2.3.1 Control Strategies

The objective of the hybrid system is to fulfill the varying load requirements through the regulation of the power sharing between the battery and the supercapacitor. By governing the power converters located between the energy storage devices and the voltage bus, energy management between them can be achieved. The control system for the DC-DC converters is shown in Fig. 2-6. The control for the battery is to keep the bus voltage at the reference point. The control for the supercapacitor is to regulate the charging or discharging current at a reference value which can be determined according to a current sharing strategy and the measured battery current [100].

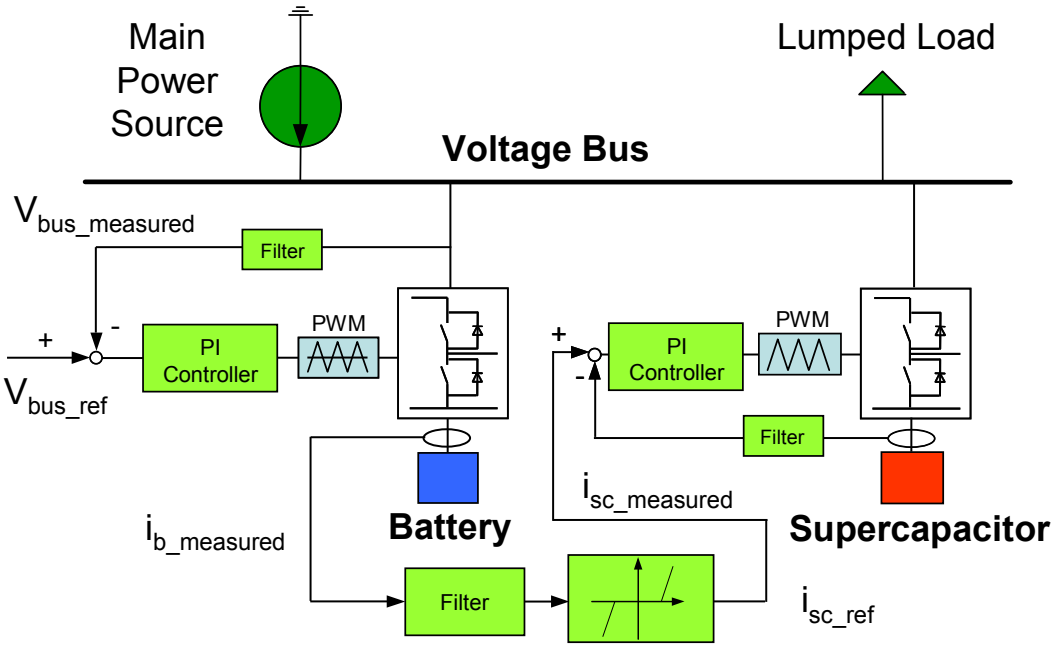

Fig. 2-6. Control loops for the power converters.

The current determination strategy using the master-slave strategy is shown in Fig. 2-7, where i_b and i_{sc} are output currents of the battery and the supercapacitor and i_{b1} and i_{b2} are the battery current threshold values. In Fig. 2-8, there are typically three control strategies for choosing different current sharing ratios that are dependent on the load. These are explained as follows.

Strategy A: When the load demand power exceeds that provided by the main source, the battery is discharged first. After the battery output current reaches a threshold, i_{b1}, the supercapacitor starts to be discharged. On the other hand, when the load demand is relatively low, the power from the main source is more than enough to supply the load, and the remaining power is used to charge the battery and the supercapacitor

simultaneously. The charging current to the supercapacitor will be linearly determined according to the charging current to the battery.

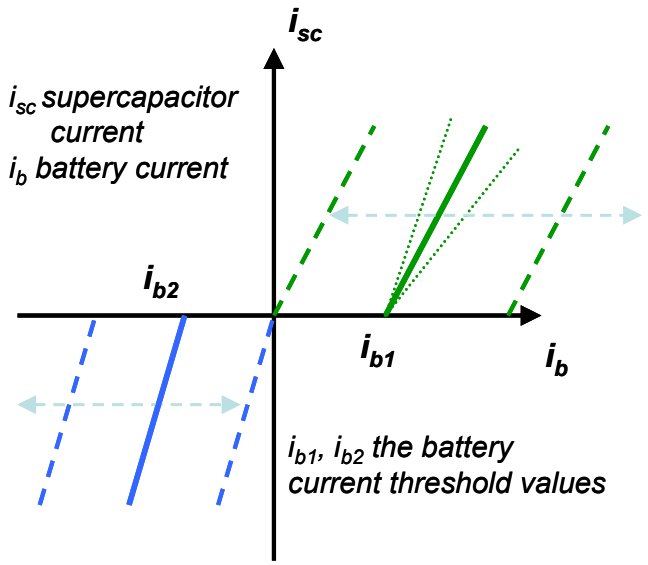

Fig. 2-7. Illustration of current sharing strategies.

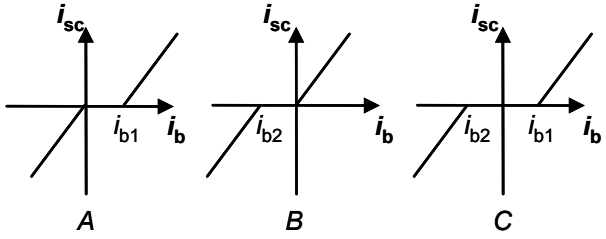

i_{sc} is the output current of the supercapacitor
i_b is the output current of the battery
i_{b1}, i_{b2} are the battery current threshold values

Fig. 2-8. Three control strategies for power sharing between the battery and supercapacitor.

Strategy B: The battery and the supercapacitor are discharged at the same time when the main power source is not enough for the high load demand. When the load demand is relatively low, the excess power from the main source charges the battery first. After the

battery charging current reaches another threshold, i_{b2}, the supercapacitor is triggered to be charged. The charging and discharging currents of the supercapacitor are also regulated through the current of the battery.

Strategy C: When battery discharging current is lower than i_{b1} or charging current is lower than i_{b2}, the supercapacitor is deactivated. When battery discharging current exceeds i_{b1} or charging current exceeds i_{b2}, then the supercapacitor is activated to be discharged or charged correspondingly.

In the strategies shown in Fig. 2-8, the two thresholds, i_{b1} and i_{b2}, are the important parameters that can affect the operation of the hybrid energy systems. In addition, for a particular strategy, the slopes of the two lines may also influence the performance of the hybrid energy storage system. Fig. 2-9 shows the different situations as the slopes vary. The effects of these parameters on energy storage will be discussed later.

Dynamic Power Sharing Strategy

The supercapacitor output current reference is determined by the measured battery output current according to a current sharing strategy (current determination strategy). The current determination strategy is shown in Fig. 2-10. This is a piecewise function. In Fig. 2-10, the X-axis represents the battery output current and the Y-axis represents the supercapacitor output current. The slope of the lines represents the ratio of the varying

currents of these two energy storage devices. Thus, the waveform represents the relationship between the supercapacitor output current and the battery output current. According to this relationship, the supercapacitor charging and discharging current is determined by the battery charging and discharging current dynamically. Because the battery output current is dependent on the load, the supercapacitor current is dependent on the load as well. Therefore, various power sharing ratios can be dynamically chosen under different load demands. The dynamic current sharing strategy in Fig. 2-10 is explained as follows.

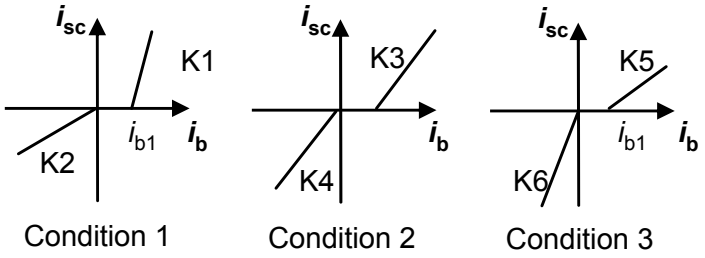

Fig. 2-9. Different situations as the slopes change under Strategy A.

When *x* is smaller than a A, the slope is k1; when *x* is between a A and b A, the slope is k2; when *x* is between b A and c A, the slope is k3; when *x* is between c A and d A, the slope is k4; when *x* is between d A and e A, the slope is k5; when *x* rises larger than e A, the slope increases to k6. Note: for Fig. 2-10, charging current increasing equals the current decreasing. The discharging current increasing equals the current increasing.

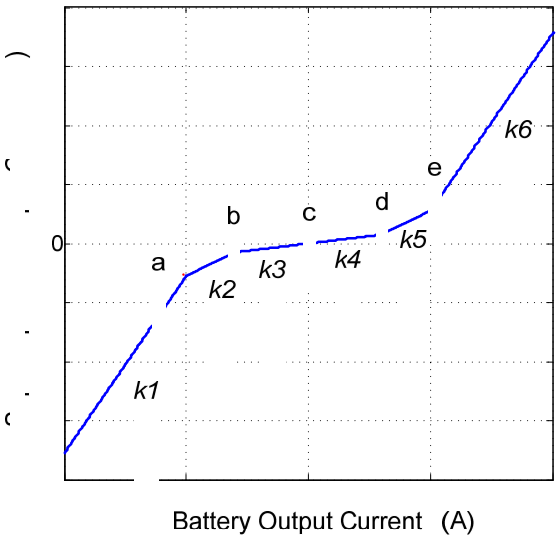

Fig. 2-10. Dynamic power sharing strategy.

In the case of the battery discharging, when the discharging current of the battery is positive and smaller than d A, the power flowing from the battery is enough to satisfy the load demand, so the output current of the supercapacitor can be very small. According to the current determination strategy, the output current reference of the supercapacitor is chosen as k4 times the battery discharging current. When the load requirement is increasing, the output current of the battery is increasing and the power sharing ratio of the supercapacitor is increasing as well. So when the battery discharging current is increasing, the slope of the waveform is piecewise increasing to k5 and k6.

When the battery is charging, the situation is similar to when it is discharging. As the charging current is increasing, the slope is increasing, so the sharing ratio of the supercapacitor is increasing from k3 to k2 and k1 piecewise.

2.3.2 Frequency-Domain Analysis

Based on section 2.1, the frequency characteristic of the battery/supercapacitor hybrid storage system may be obtained. The system is non-minimum phase with a right half plane zero. Since (2-19) is a closed-loop system, the eigenvalues of the system (2-19) are also the poles of the transfer function (2-20).

To obtain the system frequency response, first of all the steady-state operating point is calculated. The steady-state solution determines the matrix coefficients of the system. The initial conditions of the system are given in Table 2-1. In addition, system parameters and controller parameters are listed in Table 2-2. Fig. 2-11 shows the Bode plots from $\tilde{d}_1$, $\tilde{d}_2$ to $\tilde{i}_b$, $\tilde{i}_{sc}$ and $\tilde{v}_{out}$.

TABLE 2-1. STEADY-STATE OPERATING POINTS

I_b	I_{sc}	I_{Load}	V_b	V_{sc}	D_1	D_2
26 A	33 A	37.27 A	22.916	29.433	0.455	0.3

TABLE 2-2. TEST SYSTEM PARAMETERS

Parameter	Value	Parameter	Value
L_1	10 μH	k_{p1}	0.001
L_2	10 μH	k_{i1}	5
C	10 mF	k_{p2}	0.001
K	1.28	k_{i2}	1

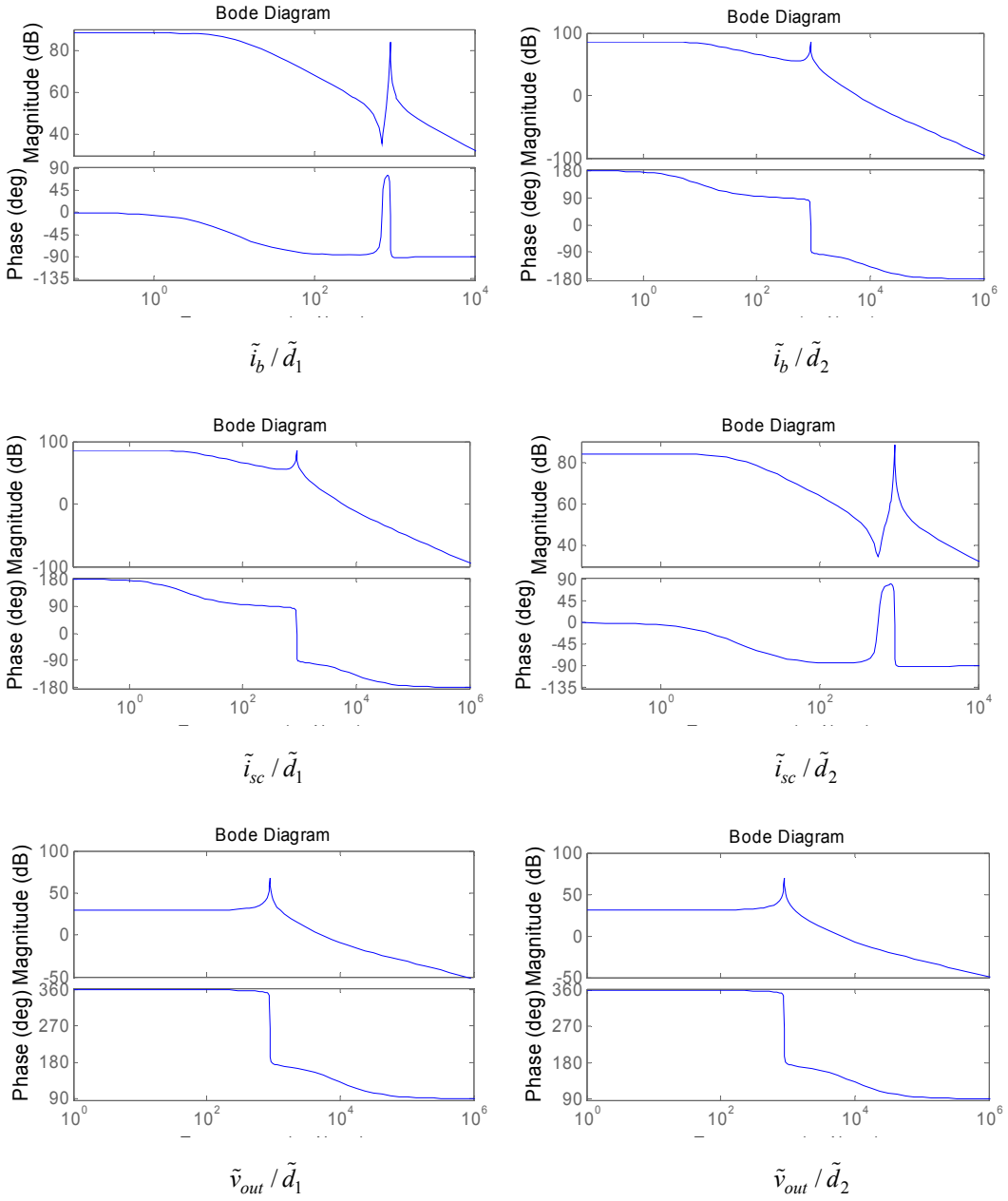

Fig. 2-11. Bode plots for the open-loop transfer functions from $\tilde{d}_1$, $\tilde{d}_2$ to $\tilde{i}_b$, $\tilde{i}_{sc}$ and $\tilde{v}_{out}$.

There are five eigenvalues including one pair of complex conjugate eigenvalues shown in Fig. 2-12. The figure shows that a large range of frequency components exist and these fall into three different clusters. The variations in these controller and output filter parameters have great influence on the eigenvalue locations on the complex plane.

This analysis shows that the stability of the system is not sensitive to the mode in cluster 3. In addition, the oscillation modes in cluster 2 are sensitive to the state variables of output *LC* filter and the proportional and integral k_{p1} and k_{i1} of the DC bus voltage controller H1. Furthermore, the mode in cluster 1 is largely sensitive to the gains k_{p2} and k_{i2} of the supercapacitor current controller H2 and filter inductance *L*.

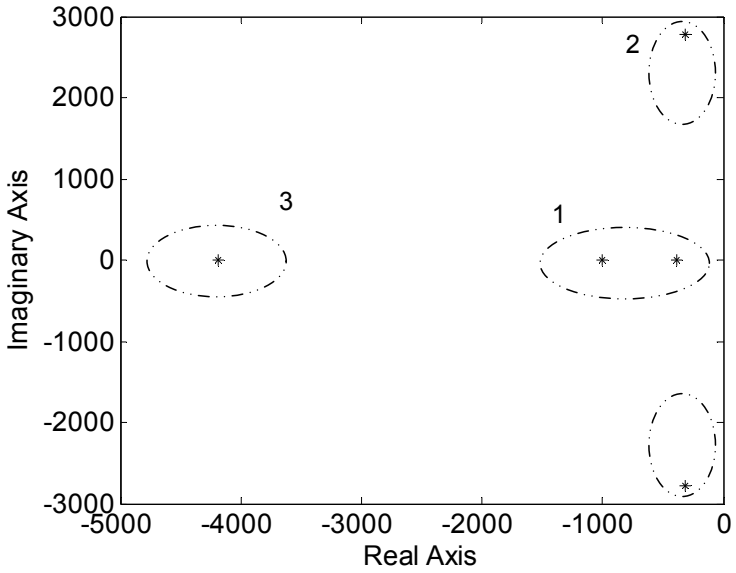

Fig. 2-12. Loci of the eigenvalues of the system.

On a complex plane, the loci of roots are graduated with these parameters. Here the study of the trajectory of eigenvalues is chosen in clusters 1 and 2 with variations of proportional and integral gains k_{p1} and k_{i1} of the voltage controller, output filter inductance and capacitance. The s-domain analysis with variations of the parameters of the current controller, which is not presented here, was also obtained in the same way.

Fig. 2-13 and Fig. 2-14 show the loci of the eigenvalues of the system with two control parameters varying. Fig. 2-13, when k_{p1} is changed from 0.0001 to 0.02, suggests that an increase in k_{p1} results in the departure of the pair of complex conjugate eigenvalues from the left half plane (LHP) to the right half plane (RHP). Therefore, the system may transit from a stable state to an unstable state with a decreasing damping ratio. Considering a trade off between stability and control performance, k_{p1} is selected as 0.001. When k_{i1} is changed from 0.001 to 20, shown in Fig. 2-14, a pair of complex conjugate eigenvalues moves towards RHP. A real eigenvalue, which is nearest to the origin, moves along the real axis to the left. Therefore, k_{i1} cannot be too small or too large, or system stability will decrease. As a consequence, k_{i1} is chosen as 5.

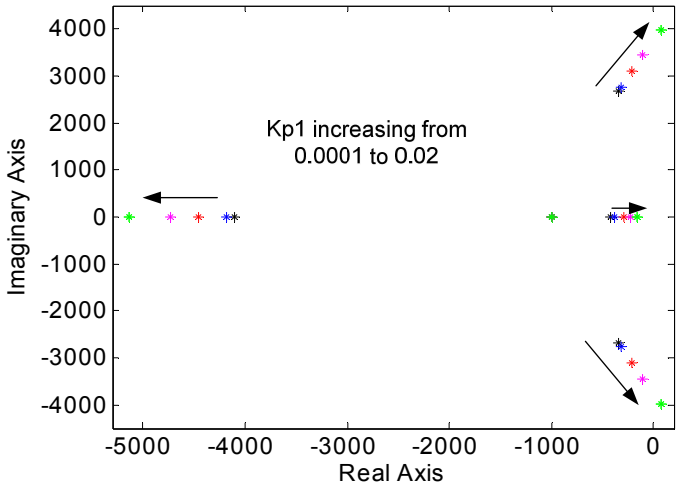

Fig. 2-13. Root locus plots from $\tilde{v}_{out\_ref}$ to $\tilde{v}_{out}$ closed-loop gain as k_{p1} varies from 0.0001 to 0.02.

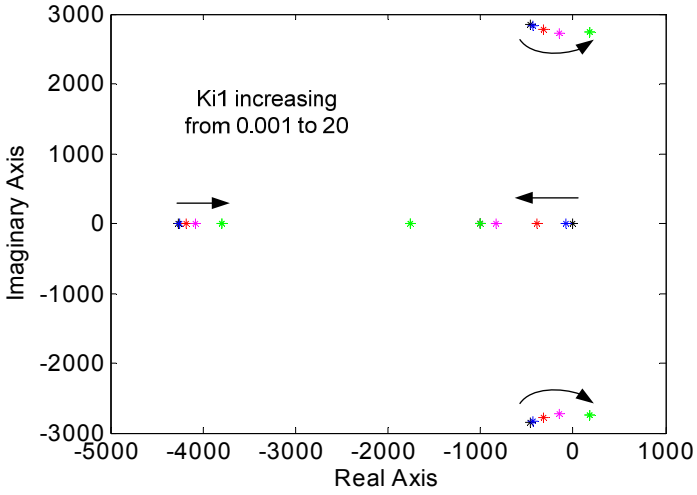

Fig. 2-14. Root locus plots from $\tilde{v}_{out\_ref}$ to $\tilde{v}_{out}$ closed-loop gain as k_{i1} varies from 0.001 to 20.

As shown in Fig. 2-15, while L_1 and L_2 are increasing together from 10 μH to 10 mH, the complex conjugate eigenvalues move towards the real axis from the LHP to the RHP, decreasing the damping ratio, deteriorating the stability of the system, and eventually causing system instability. However, as shown in Fig. 2-16, the complex conjugate eigenvalues move towards the real axis from the RHP to the LHP while C is increasing from 5 μF to 10 mF. In this case, the system changes from an unstable state to a stable state.

Therefore, when the system is in a stable state, an increase in k_{p1} or an increase or decrease in k_{i1} will result in a decrease in system stability. Moreover, the values of the filter inductance and capacitance also affect the damping ratio and system stability. A

relatively large inductance and a relatively small capacitance may cause system instability. The frequency-domain analysis will be verified later through time-domain simulation.

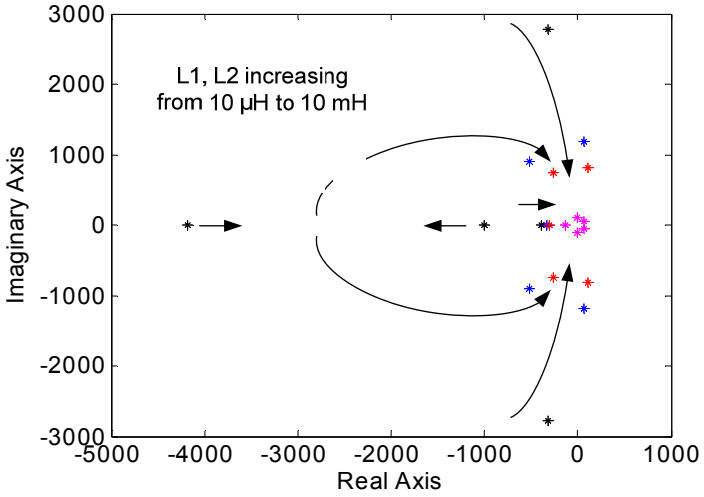

Fig. 2-15. Root locus plots of from $\tilde{v}_{out\_ref}$ to $\tilde{v}_{out}$ closed-loop gain as L varies from 10 µH to 10 mH.

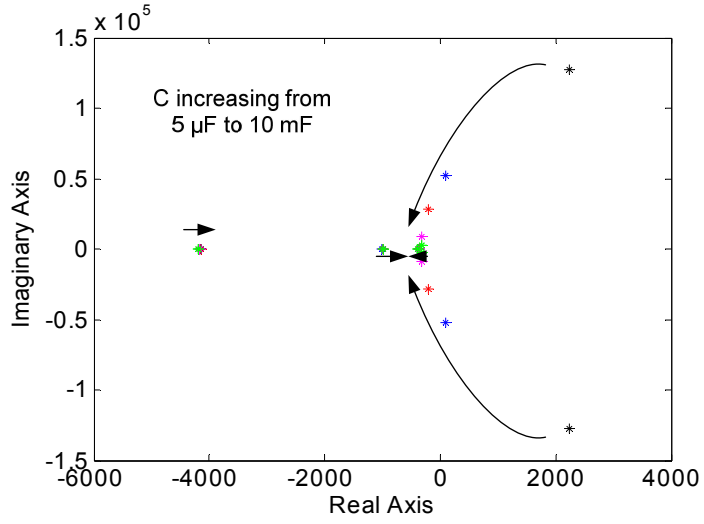

Fig. 2-16. Root locus plots of from $\tilde{v}_{out\_ref}$ to $\tilde{v}_{out}$ closed-loop gain as C varies from 5 µF to 10 mF.

2.3.3 Time-domain Simulation Results

To verify and compare the performances of the variety of control strategies, the hybrid energy storage system is modeled and simulated in the context of a hybrid power supply. A DC voltage source is used to represent a main power source. The battery and supercapacitor parameters are listed in Table 2-3.

TABLE 2-3. PARAMETERS OF BATTERY AND SUPERCAPACITOR IN VTB

Battery		Supercapacitor	
Capacity per cell	1.4 Ah	Nominal Voltage	20 V
Configuration	Parallel:10 Series:6	Total Capacitance	800 F

2.3.3.1 Comparison of Different Power Sharing Strategies

To verify and compare the performances of a variety of control strategies, the hybrid energy storage system is modeled and simulated in the context of a hybrid power supply based on a VTB (virtual test bed) platform. The models of the battery in VTB are validated models of the Sony US18650 lithium ion battery [101]. The equivalent battery model includes three components: an equilibrium potential, an internal resistance, and an effective capacitance. The discharge history is sensitized to rate the discharge and temperature through rate factor α(t) and temperature factor β(t). The state of charge [101]:

$$SOC = [i(t), T(t), t] = 1 - \frac{1}{Q}\int_0^t \alpha[i(t)] \cdot \beta[i(t)] \cdot i(t)dt \tag{2-21}$$

The models of the supercapacitor in VTB are validated models of the Maxwell PC100 ultracapacitor [33]. The ladder model physically mimics the distributed nature of the charge stored in a porous electrode and can be easily combined with various loads.

2.3.3.2 Comparison of Different Power Sharing Strategies.

The battery and supercapacitor parameters in VTB are listed in Table 2-3 using the control strategies described at the beginning of Chapter 2. A DC 20 V voltage source is used to represent a main power source. A power converter is placed between the voltage source and the terminal bus to maintain an output current reference of 30 A. Then the main power source provides a 600 W output power. The reference for the bus voltage is set as 42 V. The load demand is chosen to be repetitive with a period of 600 seconds. The power demand exhibits stepwise progression in each period, which is changing from 50, 300, 560, 704, 900 to 1460 (W) with the same duty cycles respectively.

A. With Different Charging and Discharging Thresholds

The threshold parameters i_{b1} and i_{b2}, shown earlier in Fig. 2-8, are chosen as 5 A and -5 A for the three strategies under test. The simulation runs for 1 hour. The simulation results under three power sharing strategies with different charging and discharging thresholds are shown in Fig. 2-17. Fig. 2-17-a shows the voltages of the DC bus, the battery, and the supercapacitor. The voltage of the DC bus is maintained at 42 V by

controlling the duty cycle of the bi-directional power converter of the battery. The figure of the voltages of the supercapacitor indicates that the supercapacitor loses charge fastest under the same load in Strategy B but slowest in strategy A. After 1 hour of operation the supercapacitor is completely depleted under Strategy B. This is because the supercapacitor has discharged more current but charged less under Strategy B.

Fig. 2-17-b shows the battery and supercapacitor output currents under the three control strategies. Initially under a light load of about 50 W, the battery and the supercapacitor start to be charged simultaneously under all the strategies with higher charging current of the supercapacitor but lower charging current of the battery. However, under a 300 W load, the charging current of the battery surpasses that of the supercapacitor in Strategies B and C. When the load demand increases to 560W, the battery and the supercapacitor are still charged together under Strategy A, but the supercapacitor is deactivated under Strategies B and C. Under a 704 W load demand, the battery is triggered to be discharged and the supercapacitor is deactivated under Strategies A and C; while both are discharged simultaneously under Strategy B. After the load is raised to 900 W, the battery and the supercapacitor are discharged together under all three strategies. The current of the battery is still higher than that of the supercapacitor under Strategies A and C but lower than under Strategy B. As the load reaches the 1460

W peak value, the current of the supercapacitor under Strategies A and C exceeds that of the battery.

Fig. 2-17-c shows different states of charge of the battery under three strategies. Simulation results show that the battery charge decreases after 1 hour of operation under all three strategies. Therefore, the battery would be eventually depleted. The battery loses charge fastest under the same load under Strategy A but slowest under strategy B. This is because the battery has discharged more current under Strategy A.

The selection of i_{b1} and i_{b2} depends on the different system load and the specific requirement. On one hand, when the load variance is relatively large, the supercapacitor is discharged and charged as a priority in order to cover load fluctuation. In such a case, i_{b1} and i_{b2} are set relatively low. On the other hand, when the average load is high but it has relatively small variance, the priority is to discharge and charge the battery. In this case, i_{b1} and i_{b2} should be set relatively high. If the supercapacitor is required to be highly charged in the steady state over time, then a relatively larger i_{b1} and a relatively smaller i_{b2} are chosen. Instead, if the battery is required to be highly charged over time, a relatively smaller i_{b1} and a relatively larger ib2 are set.

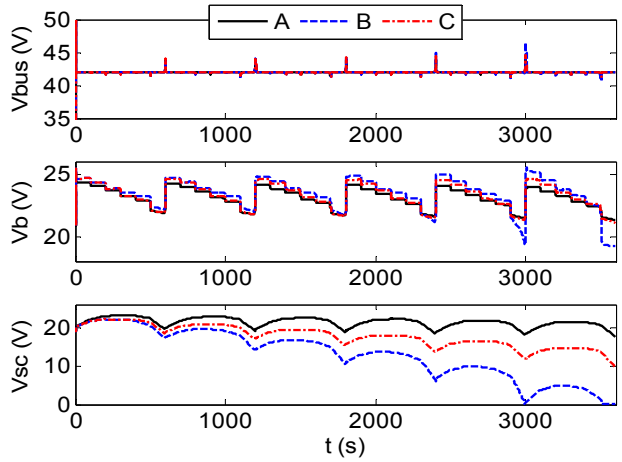

(a) Voltages of the DC bus, the battery and the supercapacitor

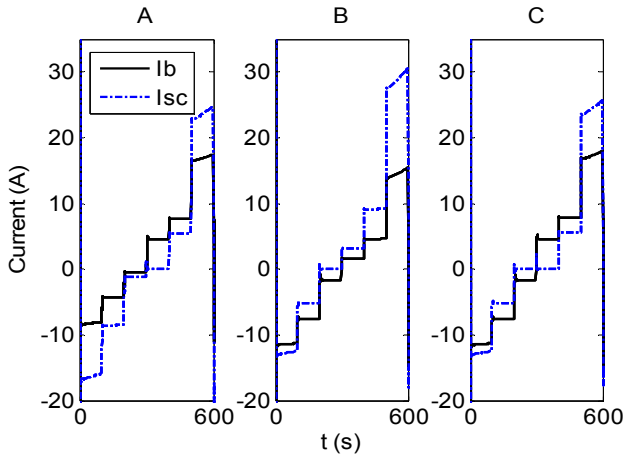

(b) Currents of the battery and supercapacitor

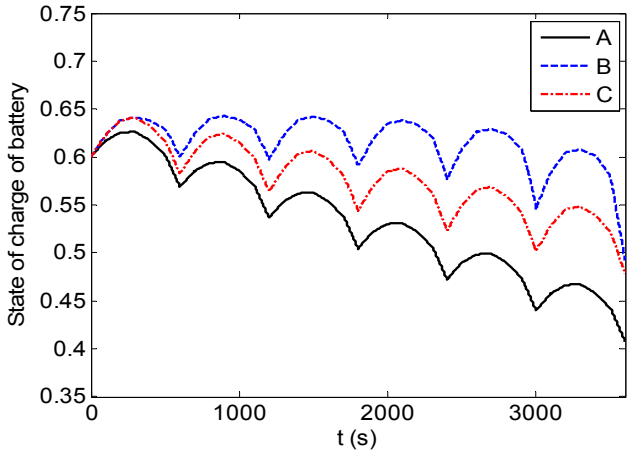

(c) Calculated state-of-charge of the battery

Fig. 2-17. Simulation results for the hybrid energy storage system under control strategies.

B. With Different Current Sharing Ratios

As mentioned before, the current sharing ratio between the two energy storage devices is determined by the slopes of the piecewise lines in Fig. 2-8. The effect of the power sharing ratio on the system performance as set by the controller is also studied. As shown in the block diagram of Fig. 2-9, Strategy A is taken for example and the control strategy is evaluated under Conditions 1, 2 and 3 with different parameters, as shown in Table 2-4, below.

TABLE 2-4. PARAMETER VALUES

Condition	Parameter	Value	Parameter	Value
1	K1	5	K2	1
2	K3	3	K4	3
3	K5	1	K6	5

The simulation for this hybrid energy storage system runs for 1 hour. Simulation results are shown in Fig. 2-18. Fig. 2-18-a shows the voltages of the DC bus, the battery and the supercapacitor under Conditions 1, 2 and 3. The supercapacitor output voltage figure indicates that the supercapacitor charge increases after 1 hour of operation under Condition 3 but decreases under Conditions 1 and 2. The supercapacitor is completely depleted under Condition 1, which loses charge much faster than under Condition 2

Fig. 2-18-b shows the currents of the battery and the supercapacitor under three power sharing conditions. Fig. 2-18-c demonstrates that the battery loses the least charge after 1 hour of operation under Condition 1 compared with other two conditions. This is because the battery gets the most charging current and discharges the least current in Condition 1. In addition, under Condition 3, the battery loses the most charge and is close to depletion.

The selection of the slope depends on the specific system load and the requirement. Slop will also affect system stability. The slope is the sharing ratio of the supercapacitor current and the battery current when they are all activated. It determines which one discharges and charges faster. Note that the slope selection should also consider the maximum allowable current of the battery and the supercapacitor.

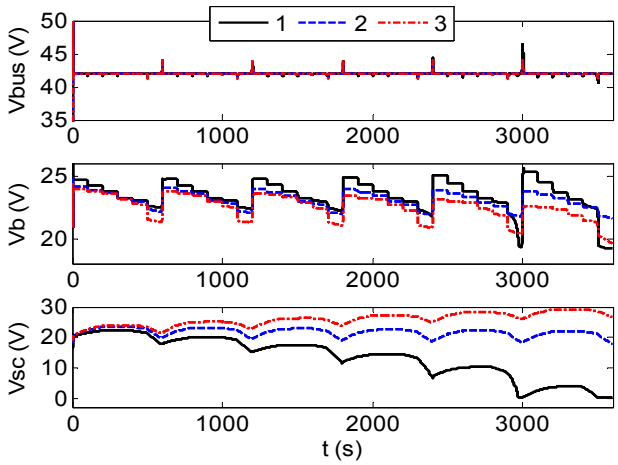

(a) Voltages of the DC bus, the battery and the supercapacitor

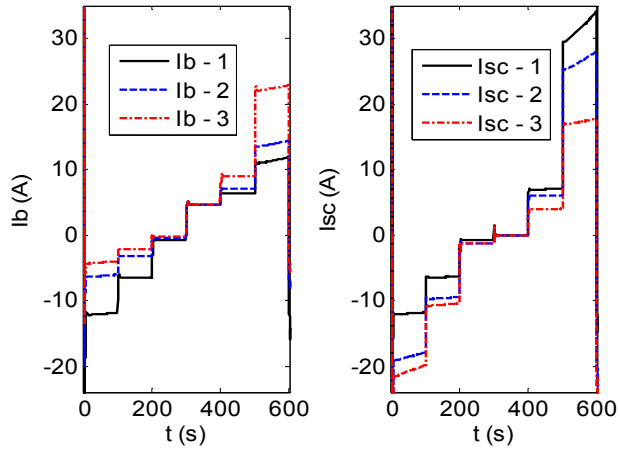

(b) Current of the battery and the supercapacitor

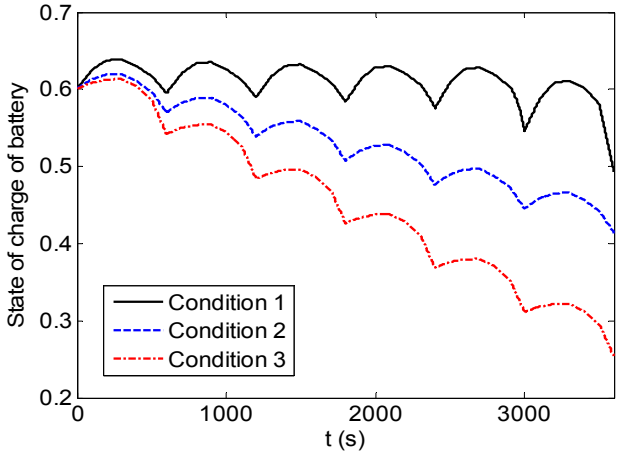

(c) Calculated state-of-charge of the battery

Fig. 2-18. Simulation results for a hybrid energy storage system under Control Strategy A as the power sharing ratio changes.

C. Comparison with an Existing Method

Fig. 2-19 shows the comparison of system behaviours based on an existing method (also termed as M2) and the method proposed in this thesis (also termed as M1). In M2, in a battery/ supercapacitor hybrid storage system, the supercapacitor and the battery both control the bus voltage, which is applied by Yoo (Yoo et al., 2008). Fig. 2-19-a shows the voltages of the supercapacitor under M1 and M2. Fig. 2-19-b shows the states of charge

of the battery under M1 and M2. M1 is implemented using parameters in condition 2 and condition 3 of Table 2-4, which are represented by a solid line and a dotted line respectively. As shown in Fig. 2-19, since different strategies can be applied in M1, the state of charge of each storage device can be adjusted. However, the charge condition of the supercapacitor in M2 is fixed. The simulation shows that proposed method M1 is more flexible than M2 for the following two reasons. First, different strategies can be used in M1 in order to change the state of charge of each storage device according to different scenarios. Second, the power sharing ratio between the battery and the supercapacitor in the proposed method can be adjusted automatically as load conditions change. Although the bus voltage may be regulated more steadily in M2 since both of the storage devices are used to control the bus voltage, the advantage is not remarkable compared with the proposed method. In summary, the method developed for this dissertation M1 can provide more flexibility for applications with comparable performance of voltage regulation.

2.3.3.3 Effects of Variations in Controller and System Parameters

To study the effects of parameter variations and validate the frequency-domain analysis, the average model is tested based on Matlab/Simulink, where the controller parameters (e.g., the proportional and integral gain in the voltage compensation loop) and

circuit parameters (i.e., inductance and capacitance in the power converter) experience variations. The simulation results are presented below. This average model neglects the switching transients and the dynamics of the battery and the supercapacitor voltage. Vb and Vsc are given in Table 2-1 and system parameters are given in Table 2-2. The simulation runs for 0.2s. At a time of 0.1 s, a load change occurs: i_{load} is changed from 10 A to 37.27 A.

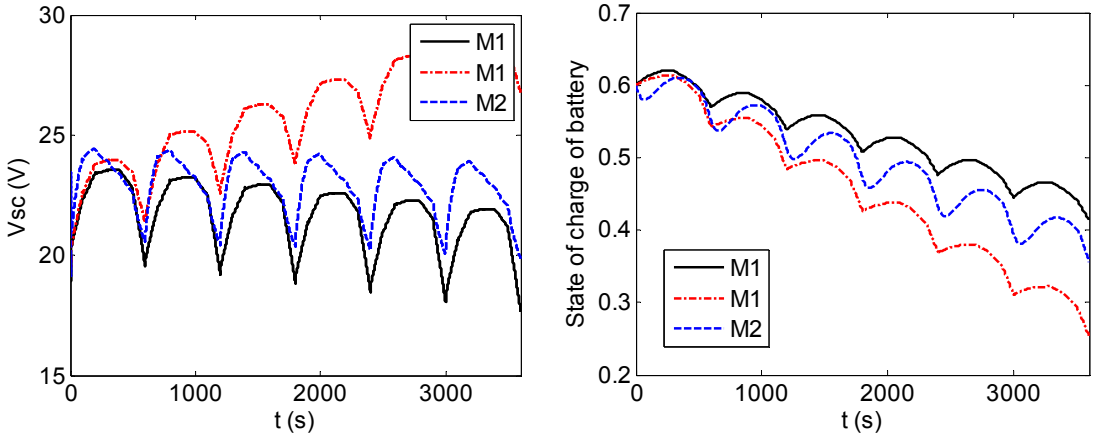

(a) Voltages of the supercapacitor (b) States of charge of the battery

(Note: M1is the method proposed in this dissertation; M2 is an existing method)

Fig. 2-19. Simulation results of the voltages of the supercapacitor and states of charge of the battery under two methods.

In this scenario, system performance under three different proportional and integral gains is compared, as shown in Fig. 2-20. In Fig. 2-20-(a), when k_{p1} is chosen as 0.01, the bus voltage experiences large overshoots and oscillations and converges to a stable state. When this parameter is reduced to 0.001 and 0.0001, the oscillations in the bus voltage are heavily reduced. The overshoot is lower and the convergence time is shorter. From

these simulation results, it can be concluded that the system response is worse when k_{p1} is selected as 0.01 rather than 0.001 or 0.0001. This is consistent with the frequency-domain analysis that as a higher k_{p1} is chosen, the damping ratio becomes smaller. In Fig. 2-20-(b), when k_{i1} is decreased from 5 to 1, the control response is slower and the time to reach the stable state is longer. Meanwhile, when k_{i1} is increased to 10, the bus voltage experiences much larger oscillations than when k_{i1} equals 5. This is also consistent with the frequency-domain analysis.

Simulation results under different output LC filter parameters are shown in Fig. 2-21 and Fig. 2-22.

Fig. 2-21 compares voltage response under three different inductances. It is shown in Fig. 2-21 that the DC bus voltage is regulated very well around 42 V. There are slight oscillations when the changes occur and the bus voltage returns to a new equilibrium value faster with lower overshoots when the inductance equals 10 μH. As L increases to 15 μH and 20 μH, the overshoot and oscillations get larger and larger. Fig. 2-22 presents the voltage response under three different capacitances. The bus voltage is controlled very well with slight oscillations after the change occurs when capacitance equals 10 mF. The oscillations get a little larger when C decreases to 1 mF. When C is chosen as 5 μF, there is a slight divergence before the change occurs. This is not apparent in the figure,

but the change makes the divergence become much faster and larger. These results are also consistent with the frequency-domain analysis.

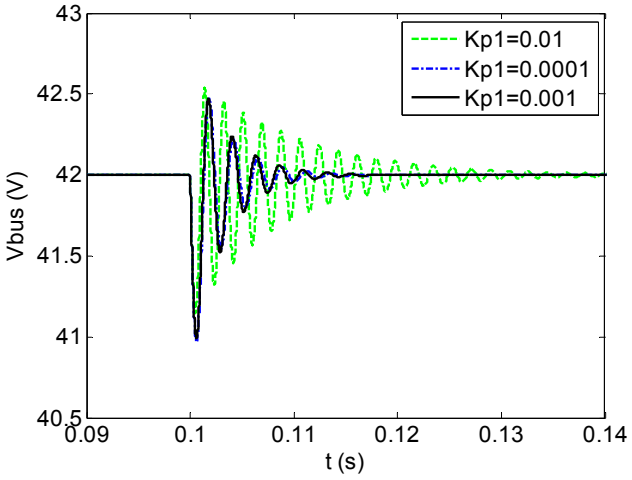

(a) k_{p1} equals 0.01, 0.001 and 0.0001, respectively.

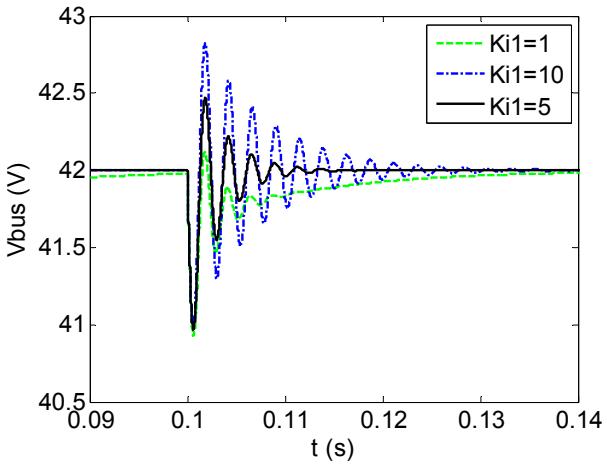

(b) k_{i1} equals 1, 5 and 10, respectively.

Fig. 2-20. Bus voltages.

In the master-slave current sharing control, the reference current of the supercapacitor is determined by the measured battery current. Fig. 2-21 and Fig. 2-22 indicate that under the condition where L equals 10 μH and C equals 10 mF, the supercapacitor

discharge/charge current follows the reference faster with lower overshoots than in the other cases.

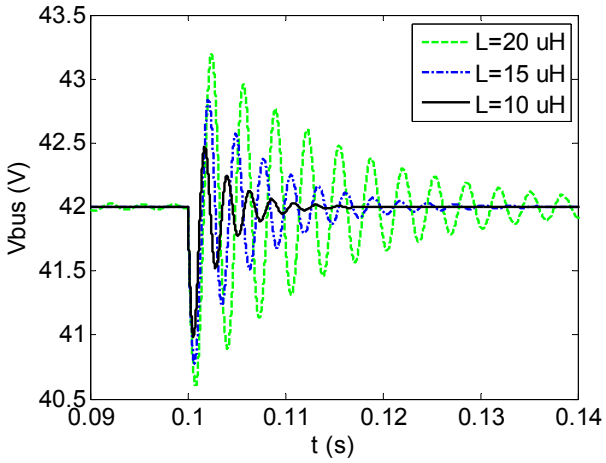

Fig. 2-21. Bus voltages when *L* equals 10 μH, 15 μH and 20 μH.

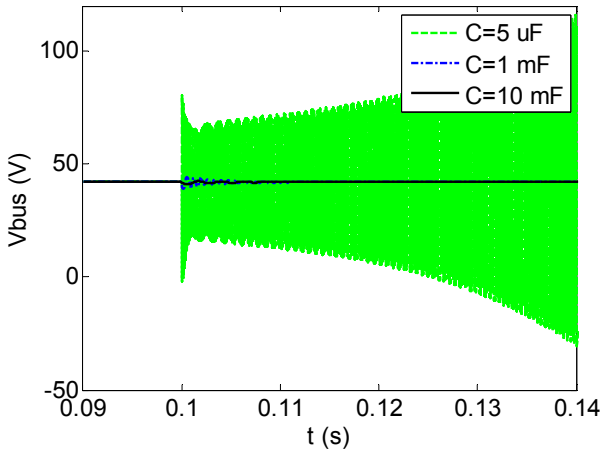

Fig. 2-22. Bus voltages when *C* equals 5 μF, 1 mF and 10 mF.

The simulation results validate the frequency analysis that system damping ratios are larger with a smaller inductor and a larger capacitor respectively. It can be seen that the transient response is largely affected by the variations in the power converter parameters, but they have little effect on the steady-state current sharing.

2.3.3.4 Test of the Dynamic Power Sharing Strategy

To study the dynamic power sharing strategy and investigate system performance, the batteries and supercapacitors hybrid energy storage system is modeled and simulated in the context of a hybrid power supply, which was implemented in VTB platform. The battery is configured as 6 cells in series and 10 cells in parallel. The supercapacitor represents a 200F Maxwell supercapacitor bank with a 32V rated voltage. The DC bus voltage is regulated at 42V. The main power source is represented by a constant current source. The other system parameters are the same as shown Table 2-3.

The test of the dynamic power sharing strategy under repetitive pulsed load condition

The strategy in Fig. 2-10 was verified by the results under a repetitive pulsed load condition. All the parameters are listed in Table 2-5. Load peak power is around 700 W. The main power source is around 200 W. The simulation runs for 1 hour.

TABLE 2-5. PARAMETERS OF CURRENT SHARING STRATEGY

Parameter	k1	k2	k3	k4	k5	k6
Value	3	1	1/4	1/4	1	3
Parameter	a	b	c	d	e	
Value	-5	-3	0	3	5	

The corresponding functions are:

$$y=3x+12.25 \qquad x \in (-\infty, -5) \tag{2-22}$$

$$y=x+2.25 \qquad x \in (3, 5) \tag{2-23}$$

$$y=x/4 \qquad x \in (-3, 3) \tag{2-24}$$

$$y=x-2.25 \qquad x \in (3, 5) \tag{2-25}$$

$$y=3x-12.25 \qquad x \in (5, +\infty) \tag{2-26}$$

Fig. 2-23 shows the output discharging and charging current of the battery and supercapacitor. The pulse lasts 20 second in a 100 second period. In this time period, the supercapacitor discharges more current. The discharging current of the battery is around 8 A. The discharging current of the supercapacitor is around 11.75 A. After the 20 second pulse, both devices are in the charging mode. The battery charging current is about 4 A. The supercapacitor charging current is about 1.75 A. The results match their correlative functions.

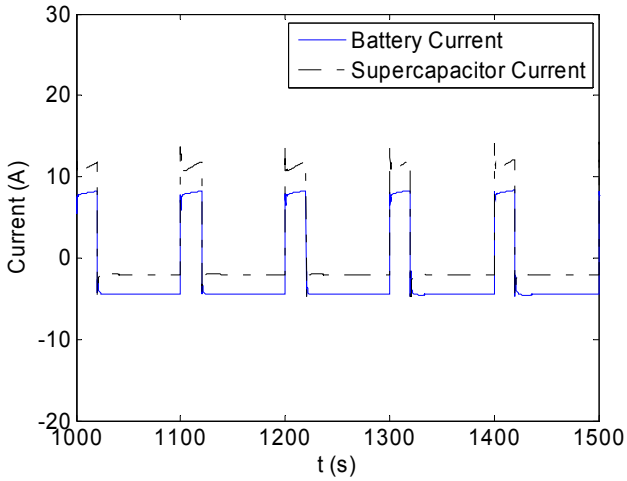

Fig. 2-23. Output current of the battery and supercapacitor.

Fig. 2-24 shows the waveform of the power of the main power source, load, battery, and supercapacitor. The peak load is around 700 W, while the main power is around 200

W. When the battery is in discharging mode, its output power is about 200W and the supercapacitor output power is around 300 W. The load is provided by the battery, the supercapacitor, and the main power source.

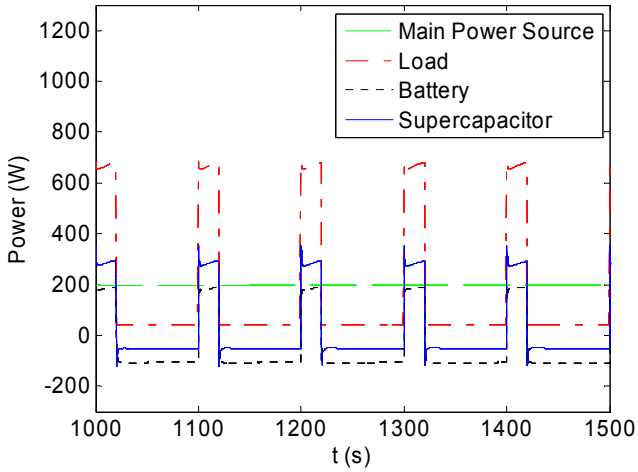

Fig. 2-24. Behavior of power of main power source, load, battery and supercapacitor.

Fig. 2-25 shows that load power demand is effectively shared by the battery, the supercapacitor, and the main power source, using strategy 1 under six certain load states. The load demand is chosen to be a repetitive load with a period of 100 second, as shown in Fig. 2-25. The power demand exhibits six different states in each period, changing from about 880 W to 35 W, 590 W, 350 W, 460 W and 440 W with proportions of 20%, 20%, 15%, 15%, 15%, and 15% respectively. The simulation runs for 1 hour. Power sharing from the main power source, the battery, and the supercapacitor effectively satisfies the load requirement.

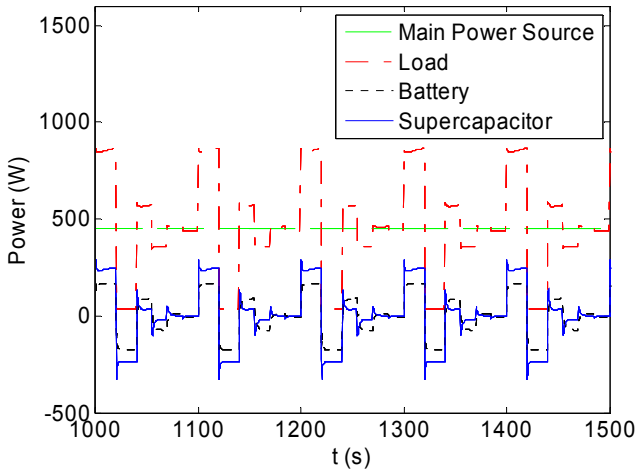

Fig. 2-25. Behavior of power of main power source, load, battery and supercapacitor under strategy 1.

Under Different Repetitive Pulsed Load Conditions

In order to further study the dynamic power sharing strategy, simulations are implemented under different repetitive pulsed load conditions. Three load conditions are shown in Fig. 2-26: within a 100 second period, in load condition 1, the peak load pulse lasts for 10 seconds; in load condition 2, the peak load pulse lasts for 20 seconds; and in load condition 3, the peak load pulse lasts for 30 seconds in a 100 second period. Fig. 2-27 shows the calculated state-of-charge of the battery in three load conditions. The results found in Fig. 2-27 suggest that the battery charge increases after 1 hour of operation under load condition 2, and is greater than under load condition 1. But the battery loses charge under load condition 3. Under load 1 or 2, obviously, the battery is getting more charge than it is releasing. In load condition 3, more charge is released.

On the other hand, Fig. 2-28 shows that under load condition 2, the supercapacitor is fully charged; under condition 1, its charge is reduced; and under condition 3, it is fully depleted. Interestingly, the supercapacitor's charge is reduced but the battery's is increased under condition 1.

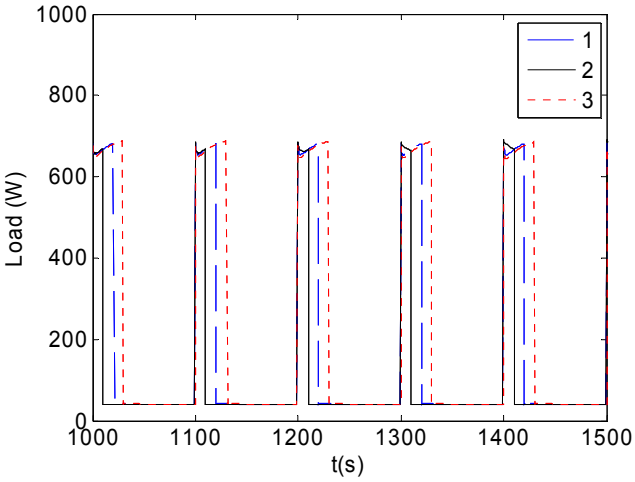

Fig. 2-26. Different Repetitive Pulsed Load Conditions.

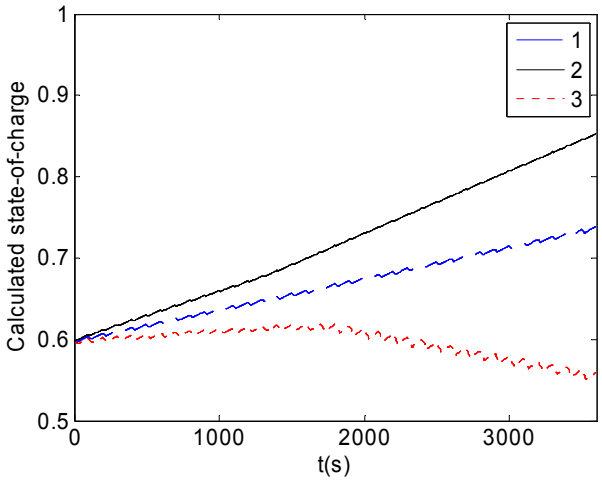

Fig. 2-27. Calculated state-of-charge of the battery under load conditions 1, 2, and 3.

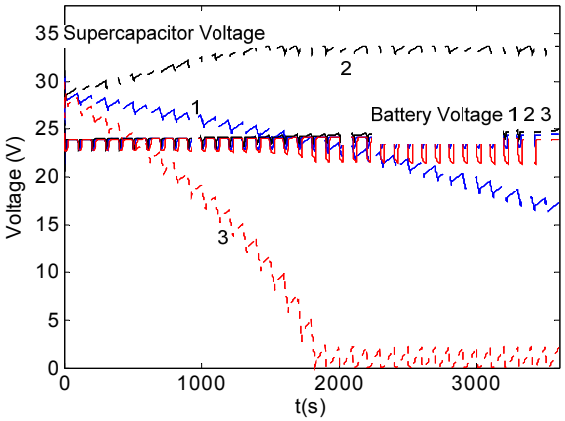

Fig. 2-28. Behavior of battery and supercapacitor voltages under load conditions 1, 2 and 3.

Therefore, in a long term operation, under condition 2, both of them will be fully charged; under condition 3, both of them will be depleted; and under condition 1, the battery will be fully charged but the supercapacitor will be fully depleted.

Strategies with Different Power Sharing Ratios under Various Repetitive Pulsed Load Conditions

Strategies with different slopes are shown in Fig. 2-29. The slopes are the important parameters that can affect the operation of the hybrid energy storage system. All the slope parameters are listed in Table 2-6.

- Strategy 1: the slopes of the piecewise function are the same as those in the simulation part A.
- Strategy 2: the values of the slopes of the piecewise function are also the same as those in the simulation part A, except when x is larger than 5 A or smaller

than -5. When x is larger than 5 A or smaller than -5, the slope decreases to 2.

- Strategy 3: when x is larger than 5 A, the slope is 2. The slopes of the piecewise function are the same as those in the Strategy 1 when x is between -5 A and 5 A.

TABLE 2-6. PARAMETERS OF CURRENT SHARING STRATEGIES

Parameter	k1	k2	k3	k4	k5	k6
Strategy 1	3	1	1/4	1/4	1	3
Strategy 2	3	1	1/4	1/4	1	2
Strategy 3	4	1	1/4	1/4	1	2
Parameter	a	b	c	d	e	
Value	-5	-3	0	3	5	

Slopes in the waveform of Fig. 2-29 represent the changing power sharing ratios of the battery and the supercapacitor. Six values of load in one period were designed, the same as that in Fig. 2-25, to test the strategies. Under three strategies, the results as shown in Fig. 2-30 suggest that battery charge decreases after 1 hour of operation. The order of the amounts of the remaining charge in the battery is 1, 2, and 3. Fig. 2-31 shows that although under all the strategies the charge of the battery is reduced, the charge of the supercapacitor is increased in strategies 2 and 3, and decreased in 1. Therefore, in the long run, the supercapacitor in strategies 2 and 3 would be fully charged, whereas in strategy 1 it would be fully depleted. However, the battery would be depleted under all the strategies in the long run.

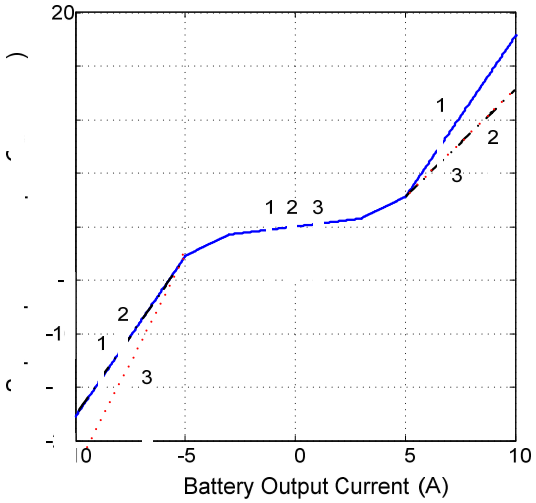

Fig. 2-29. Different dynamic power sharing strategies.

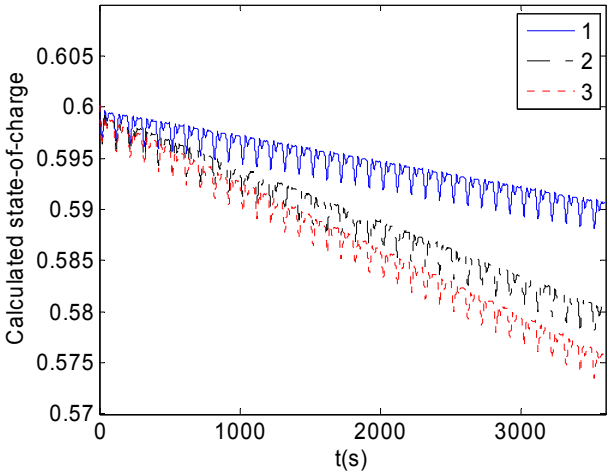

Fig. 2-30. Calculated state-of-charge of the battery.

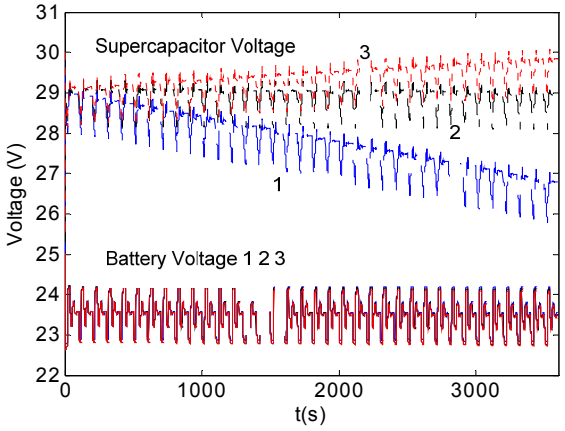

Fig. 2-31. Behavior of battery and supercapacitor voltages under strategies 1, 2, and 3.

2.3.4 Conclusion

In this section, three control strategies with different thresholds and three operating states with different combinations of power sharing ratios are proposed. On one hand, in a specific control strategy, the sharing ratios are dependent on the load. On the other hand, under certain load situations, the strategies proposed can determine the currents of the supercapacitor and the battery according to different current thresholds and sharing ratios. With different control strategies and different current sharing ratio conditions, both the battery and the supercapacitor end up with different states of charge. The dynamic power sharing strategy under various repetitive pulsed load conditions for battery and supercapacitor hybrid energy storage systems were designed and tested. Under the proposed dynamic power sharing strategy, the supercapacitor charging and discharging current is determined by the battery charging and discharging current activity. Different power sharing relationships between the battery and supercapacitor can be dynamically chosen under different load conditions.

We have also presented a small-signal model and frequency-domain analysis for the hybrid energy storage system. This model takes into account the effects of many factors on the currents, such as the voltage-current characteristics of individual energy storage devices, power converter and filter parameters, and controller parameters. In addition,

frequency-domain analysis of the small-signal model is verified by the simulation results based on the average model. Simulation results indicate that an increase in proportional gains k_{p1}, a large change in integral gain k_{i1} of the voltage controller, an increase in inductance, or a decrease in capacitance may each deteriorate the stability of the system. The effects of the controller and system parameter variations were studied in order to help designers to define control parameters, filter inductance, and capacitance to improve performance of the system.

In practical applications, as an energy buffer, the hybrid energy storage system, comprising a battery and a supercapacitor bank, can provide transient power and meet peak load requirements. It is necessary to smooth out the intermittent power generation from power sources and to cover some large power fluctuations. The hybrid energy storage system using the proposed power sharing method can be flexibly adapted to various applications, such as hybrid electric vehicles, renewable energy systems, and microgrids, to save transient power or to provide peak power.

Chapter 3. Small-Signal Modeling and Analysis of Parallel-Connected DC-AC Voltage Source Inverters

This section discusses the small-signal stability analysis of the combined droop control and various control strategies of multiple distributed generation (DG) systems in a grid-connected mode and a stand-alone mode. The small-signal models of the closed-loop inverter systems are developed and their accuracy is verified by simulation results, based on the original time average signal model. It is shown that the small-signal model accurately predicts the stability of the parallel systems.

3.1 Small-Signal Modeling and Control Strategies of an Inverter

3.1.1 Average-Signal Modeling of Single DC-AC Inverters

3.1.1.1 In the Stationary *abc* Coordinates

A voltage source power converter is commonly used to interface distributed generators to the network. The average large-signal model of the three-phase inverter is developed. Conventionally, switching averaging is performed on a phase-leg basis. Assuming ideal switches, the averaged model of each of the inverter branches may be

obtained by neglecting the high frequency components of both the DC voltage and the AC phase currents. d is the duty cycle of the upper switch of one inverter leg in a switching period, whereas v and i denote the average value in a switching period of the voltage across the lower switch, and of the AC current, respectively. i_o denotes the output current. Then, the whole averaged model of the inverter in the stationary three-phase frame may be obtained. The equations in the three-phase stationary frame are derived as shown in Fig. 3-1.

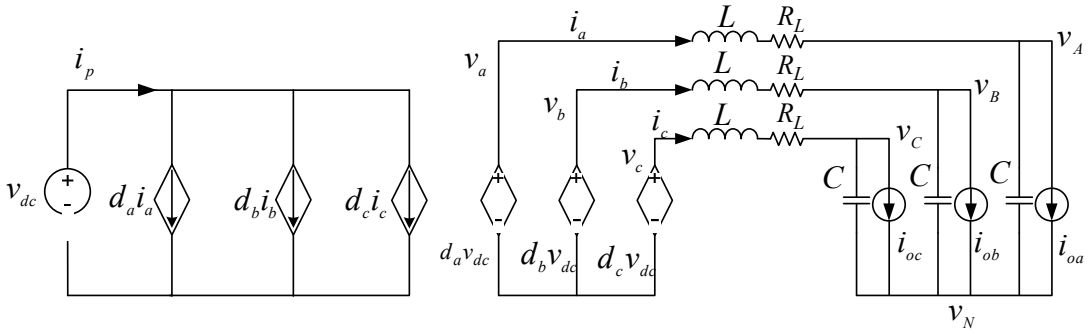

Fig. 3-1. Averaged equivalent circuit in the three-phase stationary frame of a voltage inverter.

The state-space equations of the voltage source inverter are:

$$\frac{d}{dt}\begin{bmatrix} i_a \\ i_b \\ i_c \end{bmatrix} = \frac{1}{L}\begin{bmatrix} d_a \\ d_b \\ d_c \end{bmatrix} v_{dc} - \frac{R_L}{L}\begin{bmatrix} i_a \\ i_b \\ i_c \end{bmatrix} - \frac{1}{L}\begin{bmatrix} v_{AN} \\ v_{BN} \\ v_{CN} \end{bmatrix} - \frac{1}{L}\begin{bmatrix} v_N \\ v_N \\ v_N \end{bmatrix} \tag{3-1}$$

$$\frac{d}{dt}\left(\begin{bmatrix} v_{AN} \\ v_{BN} \\ v_{CN} \end{bmatrix}\right) = \frac{1}{C}\begin{bmatrix} i_a \\ i_b \\ i_c \end{bmatrix} - \frac{1}{C}\begin{bmatrix} i_{oa} \\ i_{ob} \\ i_{oc} \end{bmatrix} \tag{3-2}$$

3.1.1.2 In the Rotating *d-q* Coordinates

The *d-q* frame is rotating at angular speed ω. The *d-q* axis components become constants after the stationary frame transforms to a *d-q* frame. Application of the *d-q* transformation reduces the three AC quantities to two DC quantities in a balanced three-phase circuit. The variable in the stationary coordinates can be transformed into the rotating coordinates by:

$$X_{dqz} = TX_{abc} \tag{3-3}$$

where the transformation function T is expressed as:

$$T = \sqrt{\frac{2}{3}}\begin{bmatrix} \cos\omega t & \cos(\omega t - \frac{2\pi}{3}) & \cos(\omega t + \frac{2\pi}{3}) \\ -\sin\omega t & -\sin(\omega t - \frac{2\pi}{3}) & -\sin(\omega t + \frac{2\pi}{3}) \\ \frac{1}{\sqrt{2}} & \frac{1}{\sqrt{2}} & \frac{1}{\sqrt{2}} \end{bmatrix} \tag{3-4}$$

Assuming the load is balanced, the following is derived:

$$\frac{d}{dt}\begin{bmatrix} i_d \\ i_q \end{bmatrix} = \begin{bmatrix} -\frac{R_L}{L} & \omega \\ -\omega & -\frac{R_L}{L} \end{bmatrix}\begin{bmatrix} i_d \\ i_q \end{bmatrix} - \frac{1}{L}\begin{bmatrix} v_d \\ v_q \end{bmatrix} + \frac{v_{dc}}{L}\begin{bmatrix} d_d \\ d_q \end{bmatrix} \tag{3-5}$$

$$\frac{d}{dt}(\begin{bmatrix} v_d \\ v_q \end{bmatrix}) = \frac{1}{C}\begin{bmatrix} i_d \\ i_q \end{bmatrix} - \frac{1}{C}\begin{bmatrix} i_{od} \\ i_{oq} \end{bmatrix} + \begin{bmatrix} 0 & \omega \\ -\omega & 0 \end{bmatrix}\begin{bmatrix} v_d \\ v_q \end{bmatrix} \tag{3-6}$$

A resistance and inductance *R-L* load is considered for this study, so following equation is derived.

$$\frac{d}{dt}\begin{bmatrix} i_{od} \\ i_{oq} \end{bmatrix} = \begin{bmatrix} \frac{1}{L_o} & 0 \\ 0 & \frac{1}{L_o} \end{bmatrix} \begin{bmatrix} v_d \\ v_q \end{bmatrix} + \begin{bmatrix} \frac{-R_o}{L_o} & \omega \\ -\omega & \frac{-R_o}{L_o} \end{bmatrix} \begin{bmatrix} i_{od} \\ i_{oq} \end{bmatrix} \tag{3-7}$$

Thus, the average model of a voltage source inverter in d-q rotating coordinates is shown in Fig. 3-2.

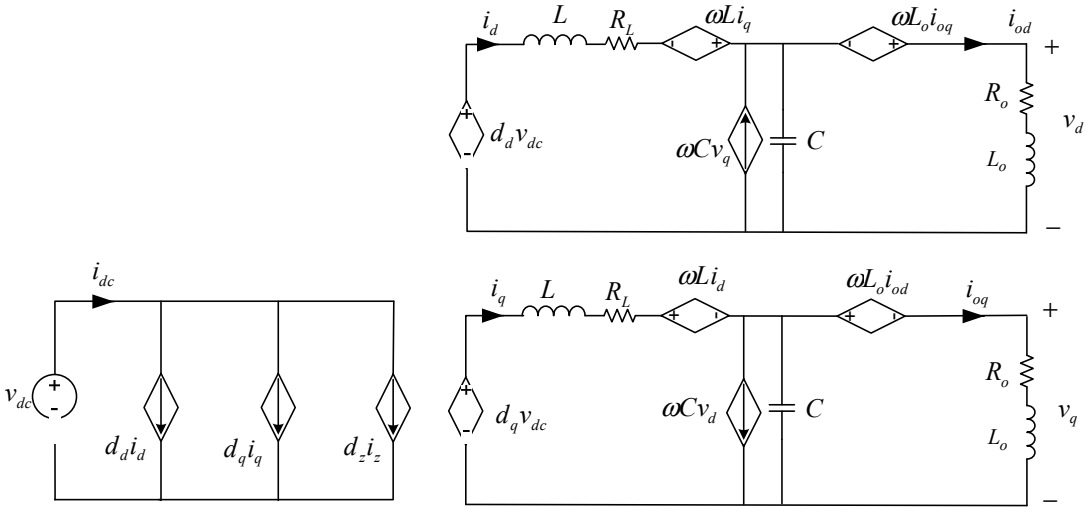

Fig. 3-2. Voltage-source inverter's average model in d-q rotating coordinates.

3.1.2 Control Strategies

A novel active power and voltage control with phase locked loop (PLL) and droop control is presented, as well as voltage control and active power - reactive power (PQ) control scheme.

3.1.2.1 Active Power and Voltage Control

When an *R-L* load is considered, the complex power consumed by the load may be expressed as:

$$\vec{S} = P + jQ = V_{rms} \cdot \vec{I}^{*} \tag{3-8}$$

$$\vec{I} = \frac{V_{rms}}{R_o + j\omega L_o} \tag{3-9}$$

$$\vec{S} = \frac{V_{rms}^{\ 2}}{R_o^2 + (\omega L_o)^2}(R_o + j\omega L_o) \tag{3-10}$$

So, the active power and reactive power of the three-phase load are:

$$P = \frac{3}{2}\frac{V^2 R_o}{R_o^2 + (\omega L_o)^2} \tag{3-11}$$

$$Q = \frac{3}{2}\frac{V^2 \omega L_o}{R_o^2 + (\omega L_o)^2} \tag{3-12}$$

V_{rms} is the phase voltage RMS value. V is the voltage peak value. Eqs.(3-11) and (3-12) suggest that the four variables (P, Q, V, and ω) are governed by these two equations as the load is changing. As two variables, such as P and Q or V and ω are regulated, the other two variables will be dependent on the load (R_o and L_o).

The control scheme of the inverter consists of two cascaded control loops. The inner current control loops independently regulate the inverter output current, id and iq, in the rotating reference frame. The outer control loops produce the references for the inner loops to regulate the active power and the output terminal voltage magnitude.

3.1.2.1.1 Inner Current Control Loops:

From Eq. (3-5):

$$d_d v_{dc} = R_L i_d + L\frac{d}{dt} i_d - L\omega i_q + v_d \tag{3-13}$$

$$d_q v_{dc} = R_L i_q + L\frac{d}{dt} i_q + L\omega i_d + v_q \tag{3-14}$$

Since v_d equals V and v_q equal zero, a proportional-integral (PI) control scheme is adopted. The output of this inner current controllers are inputs of the PWM module to generate the gate control signals to drive the switches.

$$d_d v_{dc} = \left(k_{idp} + \frac{k_{idi}}{s} \right)(i_{d\_ref} - i_d) - L\omega i_q + V \tag{3-15}$$

$$d_q v_{dc} = \left(k_{iqp} + \frac{k_{iqi}}{s} \right)(i_{q\_ref} - i_q) + L\omega i_d \tag{3-16}$$

3.1.2.1.2 Outer Active Power Control Loop:

Since v_d equals V and v_q equal zero, then the active power supplied from the inverter is proportional to i_d.

$$P = \frac{3}{2}\left(v_d i_d + v_q i_q\right) = \frac{3}{2} V i_d \tag{3-17}$$

$$Q = \frac{3}{2}\left(v_q i_d - v_d i_q\right) = -\frac{3}{2} V i_q \tag{3-18}$$

A PI control scheme is adopted.

$$i_{d\_ref} = \left(k_{Pp} + \frac{k_{Pi}}{s} \right)(P_{\_ref} - P) \tag{3-19}$$

3.1.2.1.3 Outer Voltage Control Loop

According to Eqs.(3-12) (3-18):

$$Q = \frac{3}{2} \frac{V^2 \omega L_o}{R_o^2 + (\omega L_o)^2} = -\frac{3}{2} V i_q \tag{3-20}$$

$$i_{q\_ref} = -(k_{Vp} + \frac{k_{Vi}}{s})(V_{\_ref} - V) \tag{3-21}$$

Based on Eqs.(3-15), (3-16), (3-19) and (3-21), the vector control diagram of the PV control of the voltage source inverter is obtained, as shown in Fig. 3-3 [102].

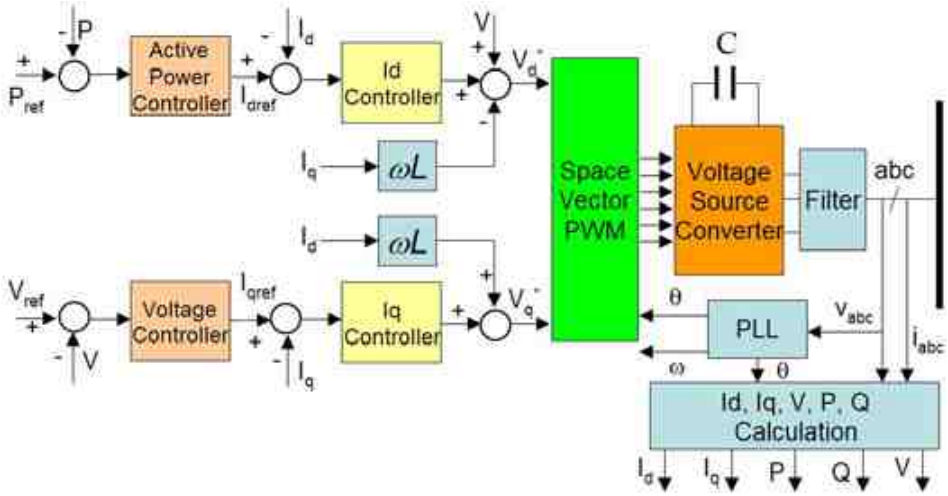

Fig. 3-3. Vector control diagram of the PV control scheme.

3.1.2.2 Voltage Control

The output voltages are controlled by the instantaneous values of converter output current components i_{d_ref} and i_{q_ref}.

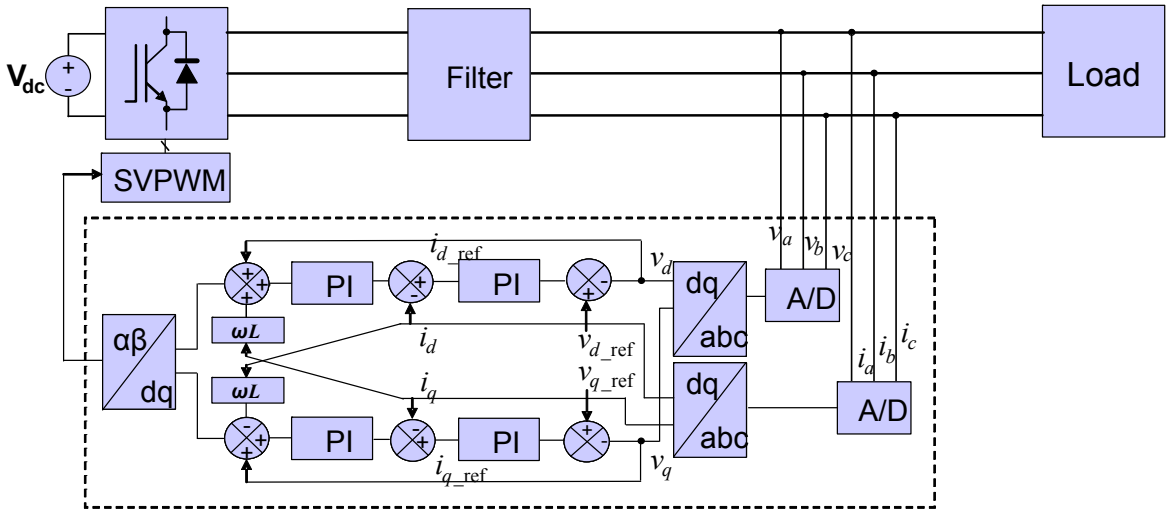

Fig. 3-4. Inverter with voltage control scheme.

3.1.2.2.1 Inner Current Control Loops:

From Eqs. (3-13) and (3-14), a PI control scheme is adopted.

$$d_d v_{dc} = \left(k_{idp} + \frac{k_{idi}}{s} \right)(i_{d\_ref} - i_d) - L\omega i_q + v_d \tag{3-22}$$

$$d_q v_{dc} = \left(k_{iqp} + \frac{k_{iqi}}{s} \right)(i_{q\_ref} - i_q) + L\omega i_d + v_q \tag{3-23}$$

3.1.2.2.2 Outer Voltage Control Loops:

$$i_{d\_ref} = \left(k_{vdp} + \frac{k_{vdi}}{s} \right)(v_{d\_ref} - v_d) \tag{3-24}$$

$$i_{q\_ref} = \left(k_{vdp} + \frac{k_{vdi}}{s} \right)(v_{q\_ref} - v_q) \tag{3-25}$$

3.1.2.3 Active Power and Reactive Power Control

The output active power and reactive power are controlled by the instantaneous values of converter output current components i_{d_ref} and i_{q_ref} respectively.

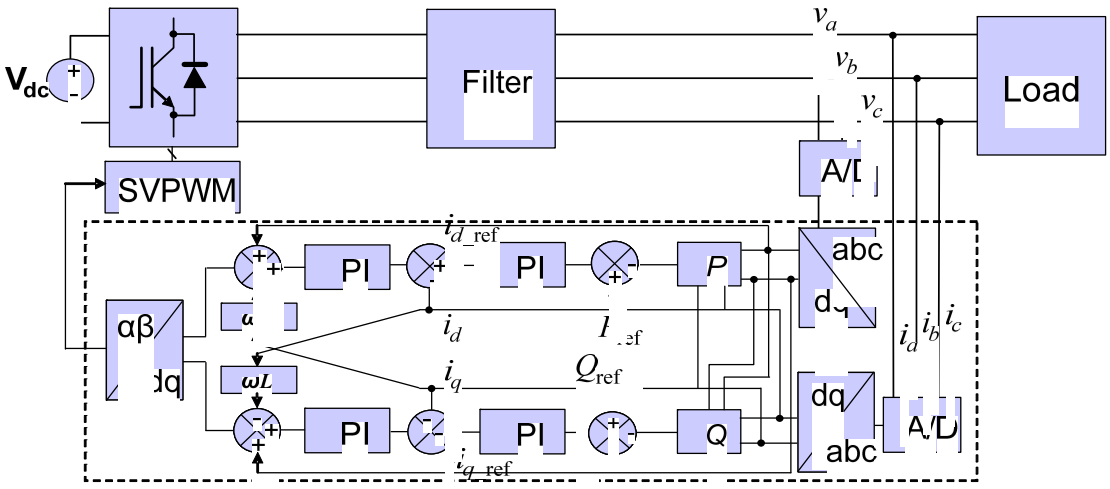

Fig. 3-5. Inverter with active-reactive power control scheme.

3.1.2.3.1 Inner Current Control Loops:

From Eqs. (3-13) and (3-14), since v_d equals the voltage magnitude and v_d equal zero, a PI control scheme is adopted.

$$d_d v_{dc} = \left(k_{idp} + \frac{k_{idi}}{s} \right)(i_{d\_ref} - i_d) - L\omega i_q + v_d \tag{3-26}$$

$$d_q v_{dc} = \left(k_{iqp} + \frac{k_{iqi}}{s} \right)(i_{q\_ref} - i_q) + L\omega i_d + v_q \tag{3-27}$$

3.1.2.3.2 Outer Power Control Loops:

Since v_d equals the voltage magnitude and v_q equal zero, then the active power supplied from the inverter is proportional to i_d.

$$P = \frac{3}{2}\left(v_d i_d + v_q i_q\right) = \frac{3}{2} v_d i_d \tag{3-28}$$

$$Q = \frac{3}{2}\left(v_q i_d - v_d i_q\right) = -\frac{3}{2} v_d i_q \tag{3-29}$$

A PI control scheme is adopted.

$$i_{d\_ref} = \left(k_{Pp} + \frac{k_{Pi}}{s} \right)(P_{\_ref} - P) \tag{3-30}$$

$$i_{q\_ref} = -\left(k_{Qp} + \frac{k_{Qi}}{s} \right)(Q_{\_ref} - Q) \tag{3-31}$$

3.1.2.4 Phase-Locked Loop

PLL is used to estimate phase angle to identify the reference frame for the instantaneous real/reactive power calculator. When the inverter is connected to the power

grid, the voltage is maintained by the grid, and a power control will apply to the inverter. In the power control mode, the inverter output voltage should be synchronized with the grid, which is also achieved by using the phase-locked loop. The principle of the PLL is depicted in following Figure.

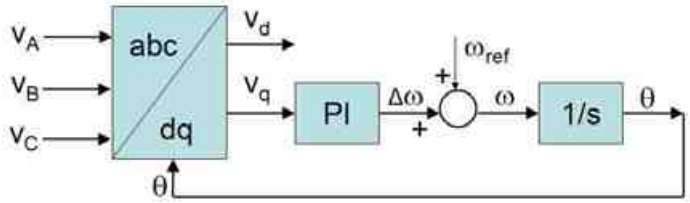

Fig. 3-6. Structure of the phase-locked loop.

First, measured three-phase voltages are transferred to the d-axis and q-axis voltages in the rotational reference frame, v_d and v_q. The q-axis component of the voltage is sent to a PI controller to generate the angular frequency correction $\Delta\omega$. This angular frequency correction $\Delta\omega$ is added to the reference angular frequency ω_0 as follows.

$$\omega = \omega_0 + k_p \cdot v_q + k_i \int v_q dt \tag{3-32}$$

3.1.2.5 Droop Control Loop:

The real power sharing between inverters is obtained by introducing an artificial droop in the inverter frequency as in (3-33). The reactive power sharing between inverters is obtained by introducing an artificial droop in the inverter voltage as in (3-34). The active power is set according to the droop gain. This mimics the governor and inertia characteristics of conventional generators and provides a degree of negative feedback.

For instance, if the power drawn from a generator increases, then the rotation of its voltage slows and its angle retards. In the following Equation (3-33), ω_0 represents the nominal frequency set-point and P_{ref} is accordingly a reactive power reference.

The power angle depends predominantly on P, while the voltage difference depends predominantly on Q. In other words, the angle δ can be controlled through P, while the inverter voltage V is controllable through Q. Control of frequency dynamically controls the power angle and thus the real power flow. Therefore, frequency and amplitude of the grid are determined by regulating P and Q independently, as shown in Fig. 3-7. These conclusions form the basis for the well-known frequency and voltage droop regulation through active and reactive power respectively.

$$P_{\_ref} = P_0 + k_1(\omega_0 - \omega) \tag{3-33}$$

$$Q_{\_ref} = Q_o + k_2(V_0 - V) \tag{3-34}$$

3.1.3 Small-Signal Modeling and Analysis of Inverter with Several Control Strategies

3.1.3.1 Small-Signal Modeling of Three-Phase DC-AC Inverters

To investigate the dynamic behavior of an inverter, including its controllers, a linearized small-signal model of the inverter in the general form is developed by perturbing the time-averaged variables around a steady-state operating point.

$$\dot{\tilde{x}} = A\tilde{x} + B\tilde{u} \tag{3-35}$$

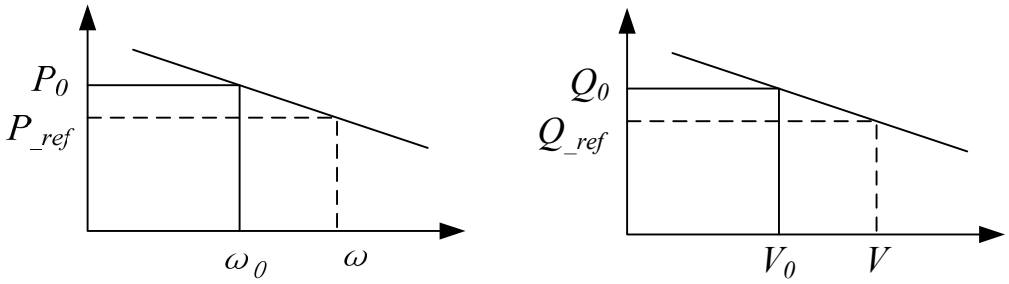

Fig. 3-7. Frequency and voltage droop control characteristics.

In this section, the small-signal model is presented for all of the subsystems: inverter, filter, load and control loops. The differential equations representing the small-signal model of the inverter are developed.

$$\frac{d}{dt}\begin{bmatrix}\tilde{i}_d\\ \tilde{i}_q\end{bmatrix} = \begin{bmatrix}-\frac{R_L}{L} & \omega\\ -\omega & -\frac{R_L}{L}\end{bmatrix}\begin{bmatrix}\tilde{i}_d\\ \tilde{i}_q\end{bmatrix} + \frac{V_{dc}}{L}\begin{bmatrix}\tilde{d}_d\\ \tilde{d}_q\end{bmatrix} - \frac{1}{L}\begin{bmatrix}\tilde{v}_d\\ \tilde{v}_q\end{bmatrix} + \frac{1}{L}\begin{bmatrix}D_d\\ D_q\end{bmatrix}\tilde{v}_{dc} + \begin{bmatrix}I_q\\ I_d\end{bmatrix}\tilde{\omega} \tag{3-36}$$

$$\frac{d}{dt}\left(\begin{bmatrix}\tilde{v}_d\\ \tilde{v}_q\end{bmatrix}\right) = \frac{1}{C}\begin{bmatrix}\tilde{i}_d\\ \tilde{i}_q\end{bmatrix} - \frac{1}{C}\begin{bmatrix}\tilde{i}_{od}\\ \tilde{i}_{oq}\end{bmatrix} + \begin{bmatrix}0 & \omega\\ -\omega & 0\end{bmatrix}\begin{bmatrix}\tilde{v}_d\\ \tilde{v}_q\end{bmatrix} + \tilde{\omega}\begin{bmatrix}V_q\\ V_d\end{bmatrix} \tag{3-37}$$

For the *L*-*R* load:

$$\frac{d}{dt}\begin{bmatrix}\tilde{i}_{od}\\ \tilde{i}_{oq}\end{bmatrix} = \begin{bmatrix}\frac{1}{L_o} & 0\\ 0 & \frac{1}{L_o}\end{bmatrix}\begin{bmatrix}\tilde{v}_d\\ \tilde{v}_q\end{bmatrix} + \begin{bmatrix}\frac{-R}{L_o} & \omega\\ -\omega & \frac{-R}{L_o}\end{bmatrix}\begin{bmatrix}\tilde{i}_{od}\\ \tilde{i}_{oq}\end{bmatrix} + \begin{bmatrix}I_{oq}\\ I_{od}\end{bmatrix}\tilde{\omega} \tag{3-38}$$

3.1.3.2 Small-Signal Modeling of the PV Controller

Outer active power control loop:

The active power may be expressed as:

$$\widetilde{P} = \frac{3}{2}\left(\widetilde{v}_d I_d + V_d \widetilde{i}_d + \widetilde{v}_q I_q + V_q \widetilde{i}_q\right) \tag{3-39}$$

Output active power control is achieved with a standard PI controller. The corresponding small-signal model:

$$\frac{d\widetilde{\phi}_d}{dt} = \widetilde{P}_{\_ref} - \widetilde{P} \tag{3-40}$$

$$\frac{d\widetilde{\phi}_d}{dt} = \widetilde{P}_{\_ref} - \frac{3}{2}\left(\widetilde{v}_d I_d + V_d \widetilde{i}_d + \widetilde{v}_q I_q + V_q \widetilde{i}_q\right) \tag{3-41}$$

Outer voltage control loop:

Peak voltage magnitude is expressed as follows:

$$V = \sqrt{v_d^2 + v_q^2} \tag{3-42}$$

The corresponding small-signal expression is:

$$\begin{aligned} \widetilde{V} &= \left(\left(V_d^2 + V_q^2\right)^{-1/2} \widetilde{v}_d + \left(V_d^2 + V_q^2\right)^{-1/2} \widetilde{v}_q\right) \\ &= \left(\frac{V_d}{V}\widetilde{v}_d + \frac{V_q}{V}\widetilde{v}_q\right) \end{aligned} \tag{3-43}$$

Output voltage control is also obtained with a standard PI controller. The corresponding small-signal model:

$$\frac{d\widetilde{\phi}_q}{dt} = \widetilde{V}_{\_ref} - \widetilde{V} \tag{3-44}$$

$$\frac{d\widetilde{\phi}_q}{dt} = \widetilde{V}_{\_ref} - \left(\frac{V_d}{V}\widetilde{v}_d + \frac{V_q}{V}\widetilde{v}_q\right) \tag{3-45}$$

Thus,

$$\begin{cases} \dfrac{d\widetilde{\phi}_d}{dt} = \widetilde{P}_{\_ref} - \dfrac{3}{2}\left(\widetilde{v}_d I_d + V_d \widetilde{i}_d + \widetilde{v}_q I_q + V_q \widetilde{i}_q\right) \\ \dfrac{d\widetilde{\phi}_q}{dt} = \widetilde{V}_{\_ref} - \left(\dfrac{V_d}{V}\widetilde{v}_d + \dfrac{V_q}{V}\widetilde{v}_q\right) \end{cases} \tag{3-46}$$

According to Eqs.(3-19) (3-21), outer active power controller and voltage controller is derived:

$$\begin{cases} \widetilde{i}_{d\_ref} = k_{Pp}\left(\widetilde{P}_{\_ref} - \dfrac{3}{2}\left(\widetilde{v}_d I_d + V_d \widetilde{i}_d + \widetilde{v}_q I_q + V_q \widetilde{i}_q\right)\right) + k_{Pi}\widetilde{\phi}_d \\ \widetilde{i}_{q\_ref} = -k_{Vp}\left(\widetilde{V}_{\_ref} - \left(\dfrac{V_d}{V}\widetilde{v}_d + \dfrac{V_q}{V}\widetilde{v}_q\right)\right) - k_{Vi}\widetilde{\phi}_q \end{cases} \tag{3-47}$$

Thus, this result :

$$\frac{d}{dt}\left[\widetilde{\phi}_{dq}\right] = E_\phi\left[\widetilde{P}\widetilde{V}_{\_ref}\right] + E_V\left[\widetilde{i}\,\widetilde{v}_{dq}\right] \tag{3-48}$$

$$\left[\widetilde{i}_{dq\_ref}\right] = A_V\left[\widetilde{\phi}_{dq}\right] + J_V\left[\widetilde{P}\widetilde{v}_{q\_ref}\right] + F_V\left[\widetilde{i}\,\widetilde{v}_{dq}\right] \tag{3-49}$$

where:

$$E_\phi = \begin{bmatrix} 1 & 0 \\ 0 & 1 \end{bmatrix},\ E_V = \begin{bmatrix} -\dfrac{3}{2}V_d & -\dfrac{3}{2}V_q & -\dfrac{3}{2}I_d & -\dfrac{3}{2}I_q \\ 0 & 0 & -\dfrac{V_d}{V} & -\dfrac{V_q}{V} \end{bmatrix},\ A_V = \begin{bmatrix} k_{Pi} & 0 \\ 0 & -k_{Vi} \end{bmatrix},$$

$$J_V = \begin{bmatrix} k_{Pp} & 0 \\ 0 & -k_{Vp} \end{bmatrix},\ F_V = \begin{bmatrix} k_{Pp} & 0 \\ 0 & -k_{Vp} \end{bmatrix}\begin{bmatrix} -\dfrac{3}{2}V_d & -\dfrac{3}{2}V_q & -\dfrac{3}{2}I_d & -\dfrac{3}{2}I_q \\ 0 & 0 & -\dfrac{V_d}{V} & -\dfrac{V_q}{V} \end{bmatrix}.$$

Inner control loops:

$$\frac{d}{dt}\left[\widetilde{\gamma}_{dq}\right] = E_\gamma\left[\widetilde{i}_{\_ref}\right] + E_C\left[\widetilde{i}\right] \tag{3-50}$$

where:

$$E_\gamma = \begin{bmatrix} 1 & 0 \\ 0 & 1 \end{bmatrix},\ E_C = \begin{bmatrix} -1 & 0 \\ 0 & -1 \end{bmatrix},\ E_{CC} = \begin{bmatrix} E_C & 0 & 0 \\ 0 & 0 \end{bmatrix} = \begin{bmatrix} -1 & 0 & 0 & 0 \\ 0 & -1 & 0 & 0 \end{bmatrix}$$

$$\frac{d}{dt}\left[\tilde{\gamma}_{dq}\right] = A_V\left[\tilde{\phi}_{dq}\right] + J_V\left[\tilde{P}\tilde{V}_{\_ref}\right] + E_S\left[\tilde{i}\,\tilde{v}_{dq}\right] \tag{3-51}$$

$$E_S = \begin{bmatrix} -\frac{3}{2}V_d k_{Pp} - 1 & -\frac{3}{2}V_q k_{Pp} & -\frac{3}{2}I_d k_{Pp} & -\frac{3}{2}I_q k_{Pp} \\ 0 & -1 & k_{Vp}\frac{V_d}{V} & k_{Vp}\frac{V_q}{V} \end{bmatrix} \tag{3-52}$$

Thus, these equations of duty cycles of the inverter are derived:

$$\tilde{d}_d = \frac{\left(k_{idp} + \frac{k_{idi}}{s}\right)(\tilde{i}_{d\_ref} - \tilde{i}_d) - \omega L\tilde{i}_q - I_q L\tilde{\omega} + \tilde{v}_d}{V_{dc}}$$

$$= \frac{K_{idp}(\tilde{i}_{d\_ref} - \tilde{i}_d) + K_{idi}\tilde{\gamma}_d - \omega L\tilde{i}_q - I_q L\tilde{\omega} + \tilde{v}_d}{V_{dc}} \tag{3-53}$$

$$\tilde{d}_q = \frac{\left(k_{iqp} + \frac{k_{iqi}}{s}\right)(\tilde{i}_{q\_ref} - \tilde{i}_q) + \omega L\tilde{i}_d + I_d L\tilde{\omega} + \tilde{v}_q}{V_{dc}}$$

$$= \frac{k_{iqp}(\tilde{i}_{q\_ref} - \tilde{i}_q) + k_{iqi}\tilde{\gamma}_q + \omega L\tilde{i}_d + I_d L\tilde{\omega} + \tilde{v}_q}{V_{dc}} \tag{3-54}$$

So, Eqs.(3-53) (3-54) may be expressed as:

$$\left[\tilde{d}_{dq}\right] = (A_D + J_C F_V)\begin{bmatrix} \tilde{i}_d \\ \tilde{i}_q \\ \tilde{v}_d \\ \tilde{v}_q \end{bmatrix} + J_C A_V\left[\tilde{\phi}_{dq}\right] + A_C\left[\tilde{\gamma}_{dq}\right] + J_C J_V(:,1)\left[\tilde{P}_{\_ref}\right] \tag{3-55}$$
$$+ J_C J_V(:,2)\left[\tilde{V}_{\_ref}\right] + F_C[\tilde{\omega}]$$

3.1.3.2.1 Phase Locked Loop:

$$\frac{d\mu}{dt} = v_q \tag{3-56}$$

$$\omega = \omega_{ref} + k_p \cdot v_q + k_i\mu \tag{3-57}$$

Small-signal form:

$$\begin{cases} \dfrac{d\tilde{\mu}}{dt} = \tilde{v}_q \\ \tilde{\omega} = k_p \cdot \tilde{v}_q + k_i \tilde{\mu} \end{cases} \tag{3-58}$$

$$\tilde{\omega} = k_p \cdot \tilde{v}_q + k_i \tilde{\mu} = \begin{bmatrix} k_p & k_i \end{bmatrix} \begin{bmatrix} \tilde{v}_q \\ \tilde{\mu} \end{bmatrix} \tag{3-59}$$

3.1.3.2.2 Droop Control Loop:

Based on Eqs (3-33) (3-34), the small-signal form can be obtained:

$$\tilde{P}_{\_ref} = -k\tilde{\omega} = -k\begin{bmatrix} k_p & k_i \end{bmatrix} \begin{bmatrix} \tilde{v}_q \\ \tilde{\mu} \end{bmatrix} \tag{3-60}$$

Frequency droop control is shown earlier in Fig. 3-7. Once load changes, the power outputs of both DG systems must be realized power in accordance with their droop characteristic to supply power to all critical loads.

3.1.3.2.3 Small-Signal Modeling of the Closed Loop Inverter System

Eqs.(3-36)(3-37)(3-38) may be expressed as:

$$\frac{d}{dt}[x_o] = A_o[x_o] + B_o \begin{bmatrix} \tilde{d}_d \\ \tilde{d}_q \end{bmatrix} + F_{o1}\tilde{v}_{dc} + F_{o2}\tilde{\omega} \tag{3-61}$$

where: $\tilde{x}_o = \begin{bmatrix} \tilde{i}_d & \tilde{i}_q & \tilde{v}_d & \tilde{v}_q & \tilde{i}_{od} & \tilde{i}_{oq} \end{bmatrix}$,

$$A_o = \begin{bmatrix} -\frac{R_L}{L} & \omega & -\frac{1}{L} & 0 & 0 & 0 \\ -\omega & -\frac{R_L}{L} & 0 & -\frac{1}{L} & 0 & 0 \\ \frac{1}{C} & 0 & 0 & \omega & -\frac{1}{C} & 0 \\ 0 & \frac{1}{C} & -\omega & 0 & 0 & -\frac{1}{C} \\ 0 & 0 & \frac{1}{L_o} & 0 & \frac{-R}{L_o} & \omega \\ 0 & 0 & 0 & \frac{1}{L_o} & -\omega & \frac{-R}{L_o} \end{bmatrix} B_o = \begin{bmatrix} \frac{V_{dc}}{L} & 0 \\ 0 & \frac{V_{dc}}{L} \\ 0 & 0 \\ 0 & 0 \\ 0 & 0 \\ 0 & 0 \end{bmatrix} F_{o1} = \begin{bmatrix} \frac{D_d}{L} \\ \frac{D_q}{L} \\ 0 \\ 0 \\ 0 \\ 0 \end{bmatrix} F_{o2=} \begin{bmatrix} I_q \\ I_d \\ V_q \\ V_d \\ I_{oq} \\ I_{od} \end{bmatrix}$$

Also, this is derived:

$$\left[\tilde{d}_{dq}\right] = D_D[\tilde{x}] + D_P\left[\tilde{P}_{\_ref}\right] + D_V\left[\tilde{V}_{\_ref}\right] + F_C[\tilde{\omega}] \tag{3-62}$$

where:

$$D_D = \begin{bmatrix} A_D + J_C F_V & 0 & J_C A_V & A_C & 0 \end{bmatrix},$$

$$D_P = J_C J_V(:,1),\ D_V = J_C J_V(:,2),\ E_\mu = \begin{bmatrix} 0 & 0 & 0 & 1 & 0 & 0 \end{bmatrix}.$$

The PV controlled voltage source inverter may be expressed as:

$$\frac{d}{dt}[x] = A[x] + B\begin{bmatrix} \tilde{d}_d \\ \tilde{d}_q \end{bmatrix} + B_{r1}\left[\tilde{P}_{\_ref}\right] + B_{r2}\left[\tilde{V}_{\_ref}\right] + F_1\tilde{v}_{dc} + F_2\tilde{\omega} \tag{3-63}$$

where:

$$A = \begin{bmatrix} A_{o6\times6} & & 0 & 0 & 0 \\ E_{V2\times4} & 0_{2\times2} & 0 & 0 & 0 \\ E_{S2\times4} & 0_{2\times2} & A_{V2\times2} & 0 & 0 \\ E_\mu & & 0 & 0 & 0 \end{bmatrix};\ B = \begin{bmatrix} B_o \\ 0 \end{bmatrix}_{11\times2} B_{r1} = \begin{bmatrix} 0 \\ E_\phi(:,1) \\ J_V(:,1) \\ 0 \end{bmatrix} B_{r2} = \begin{bmatrix} 0 \\ E_\phi(:,2) \\ J_V(:,2) \\ 0 \end{bmatrix}$$

$$F_1 = \begin{bmatrix} F_{o1} \\ 0 \end{bmatrix}; F_2 = \begin{bmatrix} F_{o2} \\ 0 \end{bmatrix}.$$

Considering the PLL and droop control loop, this is derived:

$$\tilde{\omega} = k_p \cdot \tilde{v}_q + k_i \tilde{\mu} = \begin{bmatrix} 0 & 0 & 0 & k_p & 0 & 0 & 0 & 0 & 0 & 0 & k_i \end{bmatrix} [x] = A_\omega [x] \tag{3-64}$$

$$\begin{aligned} \tilde{P}_{\_ref} &= -k\tilde{\omega} = -k \begin{bmatrix} k_p & k_i \end{bmatrix} \begin{bmatrix} \tilde{v}_q \\ \tilde{\mu} \end{bmatrix} \\ &= -k \begin{bmatrix} 0 & 0 & 0 & k_p & 0 & 0 & 0 & 0 & 0 & 0 & k_i \end{bmatrix} [x] = -kA_\omega [x] \end{aligned} \tag{3-65}$$

And then the complete model can be expressed as:

$$\begin{aligned} \frac{d}{dt}[x] &= \left(A + BD_D + \left(F_2 + BF_C - k\left(BD_P + B_{r1}\right)\right)A_\omega\right)[x] \\ &+ \left(BD_V + B_{r2}\right)\left[\tilde{V}_{\_ref}\right] + F_1[\tilde{v}_{dc}] \end{aligned} \tag{3-66}$$

where:

$$A = \begin{bmatrix} A_{o6\times6} & 0 & 0 & 0 \\ E_{V2\times4} & 0_{2\times2} & 0 & 0 & 0 \\ E_{S2\times4} & 0_{2\times2} & A_{V2\times2} & 0 & 0 \\ E_\mu & & 0 & 0 & 0 \end{bmatrix}$$

$$B = \begin{bmatrix} B_o \\ 0 \end{bmatrix}_{11\times2} \quad B_{r1} = \begin{bmatrix} 0 \\ E_\phi(:,1) \\ J_V(:,1) \\ 0 \end{bmatrix} \quad B_{r2} = \begin{bmatrix} 0 \\ E_\phi(:,2) \\ J_V(:,2) \\ 0 \end{bmatrix} \quad F_1 = \begin{bmatrix} F_{o1} \\ 0 \end{bmatrix} \quad F_2 = \begin{bmatrix} F_{o2} \\ 0 \end{bmatrix}$$

$$A_o = \begin{bmatrix} -\frac{R_L}{L} & \omega & -\frac{1}{L} & 0 & 0 & 0 \\ -\omega & -\frac{R_L}{L} & 0 & -\frac{1}{L} & 0 & 0 \\ \frac{1}{C} & 0 & 0 & \omega & -\frac{1}{C} & 0 \\ 0 & \frac{1}{C} & -\omega & 0 & 0 & -\frac{1}{C} \\ 0 & 0 & \frac{1}{L_o} & 0 & \frac{-R}{L_o} & \omega \\ 0 & 0 & 0 & \frac{1}{L_o} & -\omega & \frac{-R}{L_o} \end{bmatrix} \quad B_o = \begin{bmatrix} \frac{V_{dc}}{L} & 0 \\ 0 & \frac{V_{dc}}{L} \\ 0 & 0 \\ 0 & 0 \\ 0 & 0 \\ 0 & 0 \end{bmatrix} \quad F_{o1} = \begin{bmatrix} \frac{D_d}{L} \\ \frac{D_q}{L} \\ 0 \\ 0 \\ 0 \\ 0 \end{bmatrix} \quad F_{o2=} \begin{bmatrix} I_q \\ I_d \\ V_q \\ V_d \\ I_{oq} \\ I_{od} \end{bmatrix}$$

$$A_\omega = \begin{bmatrix} 0 & 0 & 0 & k_p & 0 & 0 & 0 & 0 & 0 & 0 & k_i \end{bmatrix}$$

$$E_\mu = \begin{bmatrix} 0 & 0 & 0 & 1 & 0 & 0 \end{bmatrix}$$

$$D_D = \begin{bmatrix} A_D + J_C F_V & 0 & J_C A_V & A_C & 0 \end{bmatrix} \quad D_P = J_C J_V(:,1) \quad D_V = J_C J_V(:,2)$$

$$E_\phi = \begin{bmatrix} 1 & 0 \\ 0 & 1 \end{bmatrix} \quad E_V = \begin{bmatrix} -\frac{3}{2}V_d & -\frac{3}{2}V_q & -\frac{3}{2}I_d & -\frac{3}{2}I_q \\ 0 & 0 & -\frac{V_d}{V} & -\frac{V_q}{V} \end{bmatrix}$$

$$A_V = \begin{bmatrix} k_{Pi} & 0 \\ 0 & -k_{Vi} \end{bmatrix} \quad J_V = \begin{bmatrix} k_{Pp} & 0 \\ 0 & -k_{Vp} \end{bmatrix} \quad E_\gamma = \begin{bmatrix} 1 & 0 \\ 0 & 1 \end{bmatrix} \quad E_C = \begin{bmatrix} -1 & 0 \\ 0 & -1 \end{bmatrix}$$

$$F_V = \begin{bmatrix} k_{Pp} & 0 \\ 0 & -k_{Vp} \end{bmatrix} \begin{bmatrix} -\frac{3}{2}V_d & -\frac{3}{2}V_q & -\frac{3}{2}I_d & -\frac{3}{2}I_q \\ 0 & 0 & -\frac{V_d}{V} & -\frac{V_q}{V} \end{bmatrix}$$

$$E_S = \begin{bmatrix} -\frac{3}{2}V_d k_{Pp} - 1 & -\frac{3}{2}V_q k_{Pp} & -\frac{3}{2}I_d k_{Pp} & -\frac{3}{2}I_q k_{Pp} \\ 0 & -1 & k_{Vp}\frac{V_d}{V} & k_{Vp}\frac{V_q}{V} \end{bmatrix} \quad F_C = \frac{L}{V_{dc}} \begin{bmatrix} -I_q \\ I_d \end{bmatrix}$$

$$A_D = \frac{1}{V_{dc}} \begin{bmatrix} -k_{idp} & -\omega L & 1 & 0 \\ \omega L & -k_{iqp} & 0 & 1 \end{bmatrix} \quad A_C = \frac{1}{V_{dc}} \begin{bmatrix} k_{idi} & 0 \\ 0 & k_{iqi} \end{bmatrix} \quad J_C = \frac{1}{V_{dc}} \begin{bmatrix} k_{idp} & 0 \\ 0 & k_{iqp} \end{bmatrix}.$$

3.1.3.3 Small-Signal Modeling and Analysis of Inverter with Voltage Control

Outer voltage control loop:

$$\frac{d\tilde{\phi}_d}{dt} = \tilde{v}_{d\_ref} - \tilde{v}_d \tag{3-67}$$

$$\frac{d\tilde{\phi}_q}{dt} = \tilde{v}_{q\_ref} - \tilde{v}_q \tag{3-68}$$

The complete model can be expressed as:

$$\frac{d}{dt}[x] = (A + BD_D)[x] + (BD_P + B_{r1})[\tilde{v}_{d\_ref}] + +(BD_V + B_{r2})[\tilde{v}_{q\_ref}] + F_1[\tilde{v}_{dc}] + (F_2 + BF_C)[\tilde{\omega}] \tag{3-69}$$

where:

$$A=\begin{bmatrix} A_{o6\times 6} & & 0 & 0 \\ E_{V2\times 4} & 0_{2\times 2} & 0 & 0 \\ E_{S2\times 4} & 0_{2\times 2} & 0 & 0 \end{bmatrix} B=\begin{bmatrix} B_o \\ 0 \end{bmatrix} B_{r1}=\begin{bmatrix} 0 \\ E_\phi(:,1) \\ J_V(:,1) \end{bmatrix} B_{r2}=\begin{bmatrix} 0 \\ E_\phi(:,2) \\ J_V(:,2) \end{bmatrix} F_1=\begin{bmatrix} F_{o1} \\ 0 \end{bmatrix} F_2=\begin{bmatrix} F_{o2} \\ 0 \end{bmatrix}$$

$$A_o=\begin{bmatrix} -\frac{R_L}{L} & \omega & -\frac{1}{L} & 0 & 0 & 0 \\ -\omega & -\frac{R_L}{L} & 0 & -\frac{1}{L} & 0 & 0 \\ \frac{1}{C} & 0 & 0 & \omega & -\frac{1}{C} & 0 \\ 0 & \frac{1}{C} & -\omega & 0 & 0 & -\frac{1}{C} \\ 0 & 0 & \frac{1}{L_o} & 0 & \frac{-R}{L_o} & \omega \\ 0 & 0 & 0 & \frac{1}{L_o} & -\omega & \frac{-R}{L_o} \end{bmatrix} B_o=\begin{bmatrix} \frac{V_{dc}}{L} & 0 \\ 0 & \frac{V_{dc}}{L} \\ 0 & 0 \\ 0 & 0 \\ 0 & 0 \\ 0 & 0 \end{bmatrix} F_{o1}=\begin{bmatrix} \frac{D_d}{L} \\ \frac{D_q}{L} \\ 0 \\ 0 \\ 0 \\ 0 \end{bmatrix} F_{o2=}\begin{bmatrix} I_q \\ I_d \\ V_q \\ V_d \\ I_{oq} \\ I_{od} \end{bmatrix}$$

$$A_\omega=\begin{bmatrix} 0 & 0 & 0 & k_p & 0 & 0 & 0 & 0 & 0 & 0 & k_i \end{bmatrix}$$

$$E_\mu=\begin{bmatrix} 0 & 0 & 0 & 1 & 0 & 0 \end{bmatrix}$$

$$D_D=\begin{bmatrix} A_D+J_C F_V & J_C A_V & A_C & 0 \end{bmatrix}$$

$$D_P=J_C J_V(:,1)$$

$$D_V=J_C J_V(:,2)$$

$$E_\phi=\begin{bmatrix} 1 & 0 \\ 0 & 1 \end{bmatrix};\ E_V=\begin{bmatrix} 0 & 0 & -1 & 0 \\ 0 & 0 & 0 & -1 \end{bmatrix};\ A_V=\begin{bmatrix} k_{di} & 0 \\ 0 & k_{qi} \end{bmatrix};\ J_V=\begin{bmatrix} k_{dp} & 0 \\ 0 & k_{qp} \end{bmatrix};$$

$$E_\gamma=\begin{bmatrix} 1 & 0 \\ 0 & 1 \end{bmatrix}\ ;\ E_C=\begin{bmatrix} -1 & 0 \\ 0 & -1 \end{bmatrix};\ E_S=\begin{bmatrix} -1 & 0 & -k_{dp} & 0 \\ 0 & -1 & 0 & -k_{qp} \end{bmatrix};$$

$$F_C=\frac{L}{V_{dc}}\begin{bmatrix} -I_q \\ I_d \end{bmatrix};\ A_D=\frac{1}{V_{dc}}\begin{bmatrix} -k_{idp} & -\omega L & 1 & 0 \\ \omega L & -k_{iqp} & 0 & 1 \end{bmatrix};$$

$$A_C = \frac{1}{V_{dc}}\begin{bmatrix} k_{idi} & 0 \\ 0 & k_{iqi} \end{bmatrix};\ J_C = \frac{1}{V_{dc}}\begin{bmatrix} k_{idp} & 0 \\ 0 & k_{iqp} \end{bmatrix}.$$

3.1.3.4 Small-Signal Modeling and Analysis of Inverter with Active Power and Reactive Power (PQ) Control

The small-signal model of inverter with PQ control can be achieved in the same way as with PV.

$$\frac{d}{dt}[x] = (A + BD_D)[x] + (BD_P + B_{r1})[\tilde{P}_{\_ref}] + +(BD_V + B_{r2})[\tilde{Q}_{\_ref}] + F_1[\tilde{v}_{dc}] + (F_2 + BF_C)[\tilde{\omega}] \tag{3-70}$$

The expression of the small-signal model of inverter with PQ and frequency droop control is the same as it is with PV and frequency droop control.

$$\frac{d}{dt}[x] = (A + BD_D + (F_2 + BF_C - k(BD_P + B_{r1}))A_\omega)[x] + (BD_V + B_{r2})[\tilde{Q}_{\_ref}] + F_1[\tilde{v}_{dc}] \tag{3-71}$$

However, the differences are in matrix of E_v and E_s :

PQ: $E_V = \frac{3}{2}\begin{bmatrix} -V_d & -V_q & -I_d & -I_q \\ V_q & -V_d & -I_q & I_d \end{bmatrix};$

$$E_S = \frac{3}{2}\begin{bmatrix} -V_d k_{Pp} - \frac{2}{3} & -V_q k_{Pp} & -I_d k_{Pp} & -I_q k_{Pp} \\ -V_q k_{Qp} & V_d k_{Qp} - \frac{2}{3} & I_q k_{Qp} & -I_d k_{Qp} \end{bmatrix}$$

PV: $E_V = \begin{bmatrix} -\frac{3}{2}V_d & -\frac{3}{2}V_q & -\frac{3}{2}I_d & -\frac{3}{2}I_q \\ 0 & 0 & -\frac{V_d}{V} & -\frac{V_q}{V} \end{bmatrix}$

$$E_S = \begin{bmatrix} -\frac{3}{2}V_d k_{Pp} - 1 & -\frac{3}{2}V_q k_{Pp} & -\frac{3}{2}I_d k_{Pp} & -\frac{3}{2}I_q k_{Pp} \\ 0 & -1 & k_{Vp}\frac{V_d}{V} & k_{Vp}\frac{V_q}{V} \end{bmatrix}$$

The small-signal model of an inverter with PQ and combined frequency and voltage droop control can be obtained:

$$\frac{d}{dt}[x] = \left(A + BD_D + \left(F_2 + BF_C - k_1\left(BD_P + B_{r1}\right)\right)A_\omega - k_2\left(BD_V + B_{r2}\right)A_Q\right)[x] + F_1[\tilde{v}_{dc}] \tag{3-72}$$

3.1.3.5 In Summary

An inverter system with various control strategies is derived:

- With voltage control scheme:

$$\frac{d}{dt}[x] = (A + BD_D)[x] + (BD_P + B_{r1})[\tilde{v}_{d\_ref}] + +(BD_V + B_{r2})[\tilde{v}_{q\_ref}] + F_1[\tilde{v}_{dc}] + (F_2 + BF_C)[\tilde{\omega}]$$

- With PQ control scheme:

$$\frac{d}{dt}[x] = (A + BD_D + (F_2 + BF_C)A_\omega)[x] + (BD_P + B_{r1})[\tilde{P}_{\_ref}] + +(BD_V + B_{r2})[\tilde{Q}_{\_ref}] + F_1[\tilde{v}_{dc}]$$

- PQ with frequency droop control:

$$\frac{d}{dt}[x] = \left(A + BD_D + \left(F_2 + BF_C - k\left(BD_P + B_{r1}\right)\right)A_\omega\right)[x] + \left(BD_V + B_{r2}\right)[\tilde{Q}_{\_ref}] + F_1[\tilde{v}_{dc}]$$

- PV with frequency droop control:

$$\frac{d}{dt}[x] = \left(A + BD_D + \left(F_2 + BF_C - k\left(BD_P + B_{r1}\right)\right)A_\omega\right)[x] + \left(BD_V + B_{r2}\right)[\tilde{V}_{\_ref}] + F_1[\tilde{v}_{dc}]$$

- PQ with frequency and voltage droop control:

$$\frac{d}{dt}[x] = \left(A + BD_D + \left(F_2 + BF_C - k_1\left(BD_P + B_{r1}\right)\right)A_\omega - k_2\left(BD_V + B_{r2}\right)A_Q\right)[x] + F_1[\tilde{v}_{dc}]$$

3.1.4 Frequency-Domain Analysis

The eigenvalues of the system determine completely the natural response (unforced response). The pole (or eigenvalue) locations in the s-domain move with controller parameters, system parameters and operating points. These movements would result in unsatisfactory oscillatory and even system instability. Therefore, a crucial design factor is the location of the eigenvalues, or closed-loop poles.

3.1.4.1 Controller Parameters

We study the controller parameter variations on the change of locations of eigenvalues. All the controller parameters are listed in Table 3-1. Based on all the parameters and operating points the system is stable. All 11 eigenvalues are listed in Table 3-2, which indicate the frequency and damping of oscillatory components in the transient response. It shows that the system has high natural frequencies and/or high damping. Thus, the system rapidly decays to zero subsequent to a disturbance. On a complex plane, the loci of roots are graduated with these parameters when increasing one parameter but maintaining the other ones constant. The closed loop system changes as the corresponding values of system and controller parameters change. Here the trajectory of the eigenvalues is studied with variations of all the parameters of the controllers, output filter inductance and capacitance, and load resistance and inductance.

The locations of the eigenvalues are shown in Fig. 3-8. Sensitivity of the system eigenvalues to variations in the parameters of the controllers is presented in Fig. 3-9-Fig. 3-22. It will help show how the variations in parameters influence the system characteristics.

TABLE 3-1. PARAMETERS OF REACTIVE POWER AND VOLTAGE CONTROL

External reactive power controller	External voltage controller	Inner d-axis current controller	Inner q-axis current controller	Phase loop controller	Droop gain
Kpp=0.01, Kpi=1.5	Kvp=0.5, Kvi=400	Kidp=1, Kidi=100	Kiqp=0.4, Kiqi=60	Kp=0.1, Ki=200	K=500

TABLE 3-2. EIGENVALUES OF THE REACTIVE POWER AND VOLTAGE CONTROLLED SYSTEM

Eigen Values	Real (1/s)	Im. (rad/s)
1, 2	-1780.4	5141.2
3, 4	-580	1850.5
5, 6	-165.7	282
7	-896.8	0
8	-279.1	0
9	-159.9	0
10	-92.8	0
11	-90.5	0

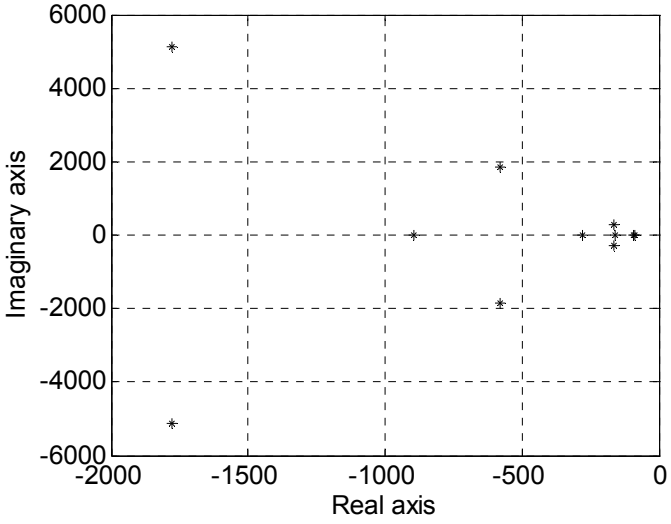

Fig. 3-8. The locations of the eigenvalues.

Active power controller

In the frequency domain, Kpp is increasing from 0 to 0.1 while all other parameters are set constant. Fig. 3-9 shows the loci of the eigenvalues of the system with an increasing Kpp. A pair of complex eigenvalues moves away from the imaginary axis in departure from RHP. The two real eigenvalues near the origin move towards each other, and become a pair of complex eigenvalues moving to the right. They then return to the real axis and move away from each other. When Kpp is 0.01, it's the furthest among all the eigenvalues nearest to the origin when Kpp is selected to be any other value from 0 to 0.1. In the s-domain, the loci of the eigenvalues with an increasing Kpi from 0.5 to 150 are shown in Fig. 3-10. The shifting of eigenvalues towards the RHP results in a decrease in system stability and can even cause instability.

The loci of the eigenvalues with Kvp increasing from 0 to 2.5 are shown in Fig. 3-11. The nearest eigenvalue to the origin, when Kvp is 0.5, is the furthest among all the nearest eigenvalues to the origin when Kvp is selected to be any other values from 0 to 2.5. With Kvp increasing, the shifting of a pair of conjugate complex poles moving to the RHP results in a decreasing damping ratio and even causes system instability. This parameter can be varied over a wider range than Kpp can. Thus, it is a less sensitive parameter in comparison to Kpp. When Kvi is increasing from 0 to 1200, one pole moves from the origin to the left half plane (LHP). The result is that system transitions to a stable state, as shown in Fig. 3-12. It also indicates that an increase in Kvi results in the departure of a pair of complex conjugate poles from the LHP with a decreasing damping ratio. Therefore, the system transitions from a stable state to an unstable one.

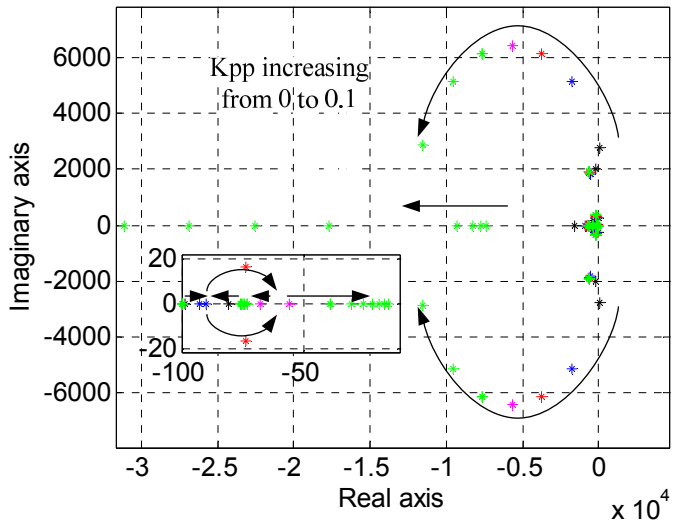

Fig. 3-9. The eigenvalues' location with an increasing Kpp.

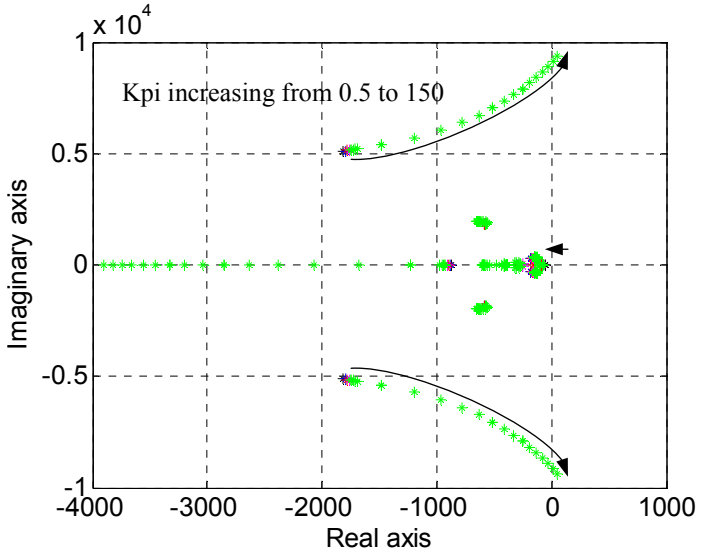

Fig. 3-10. The eigenvalues' location with an increasing Kpi.

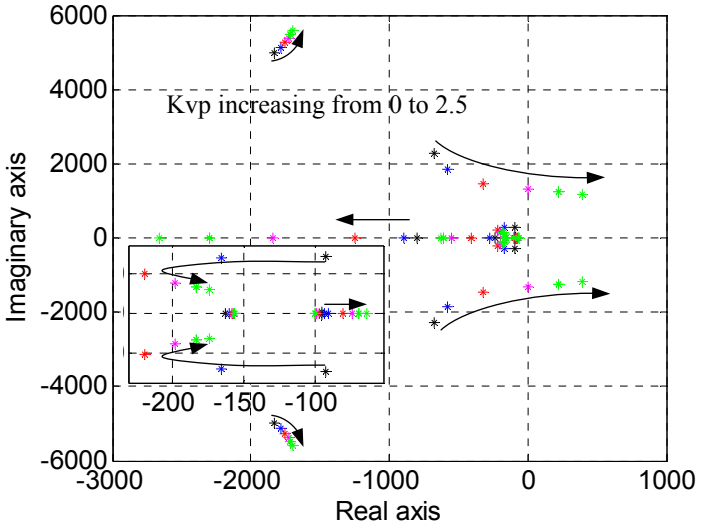

Fig. 3-11. The eigenvalues' location with an increasing Kvp.

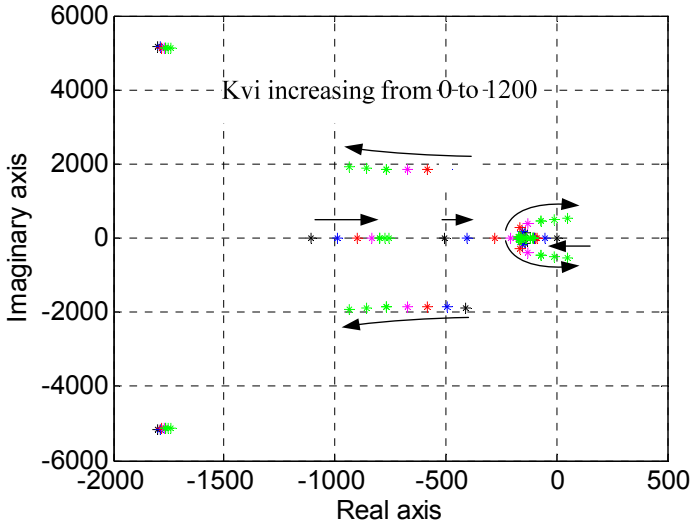

Fig. 3-12. The eigenvalues' location with an increasing Kvi.

Current controller

The loci of the eigenvalues with current controller parameters changing are shown in Fig. 3-13 and Fig. 3-14. In Fig. 3-13, the loci of the eigenvalues with Kidp increasing from 0.001 to 1, 2 and 3 are shown. When Kidp equals 0.001 the system is unstable. When it becomes much larger, almost all the eigenvalues move from the right half plane (RHP) to the LHP and away from the origin. An exception is that only one eigenvalue on the real axis comes near the origin quickly . So Kidp is set to be 1. Kidi increasing from 0 to 200 is shown in Fig. 3-14. There is one real eigenvalue in Fig. 3-14 which is largely influenced by Kidi. With Kidi increasing, the real eigenvalue moves away from the origin to the LHP. This parameter can be varied in a wider range in comparison to other parameters. This shows the stability of the system is less sensitive to this parameter.

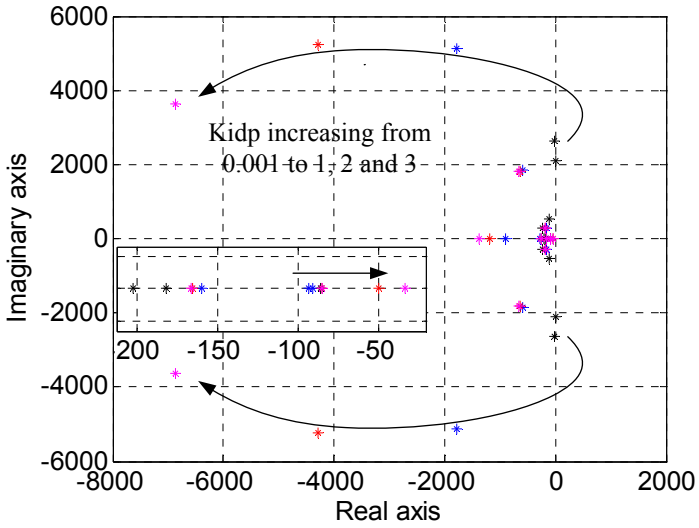

Fig. 3-13. The eigenvalues' location with an increasing Kidp.

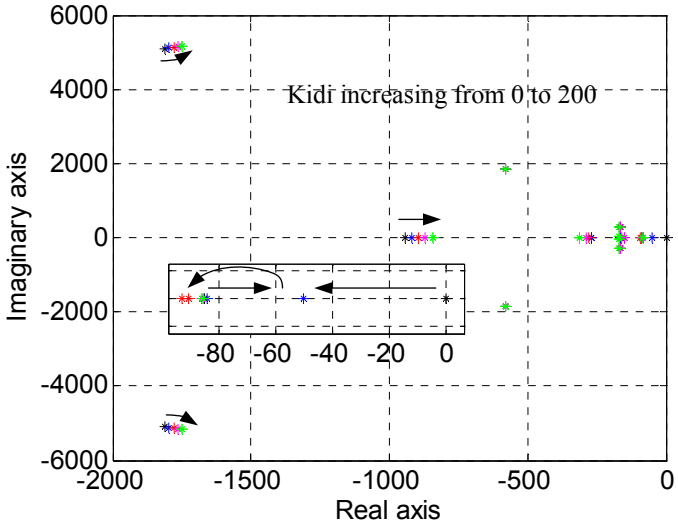

Fig. 3-14. The eigenvalues' location with an increasing Kidi.

As Kiqp increases from 0 to 1.4 shown in Fig. 3-15, a pair of complex conjugate eigenvalues moves from the RHP to the LHP. After Kiqp increases to 1.4, another pair moves from the LHP to the RHP. In this case, the system changes from an unstable state to a stable state and to an unstable state again. So Kiqp is set to be 0.4. when Kiqi is

increasing from 60 to 760, as shown in Fig. 3-16. A pair of complex conjugate eigenvalues nearest to the origin is moving slowly to the origin. The shifting of another pair of eigenvalues from the LHP towards to the RHP causes the system to change to an unstable state.

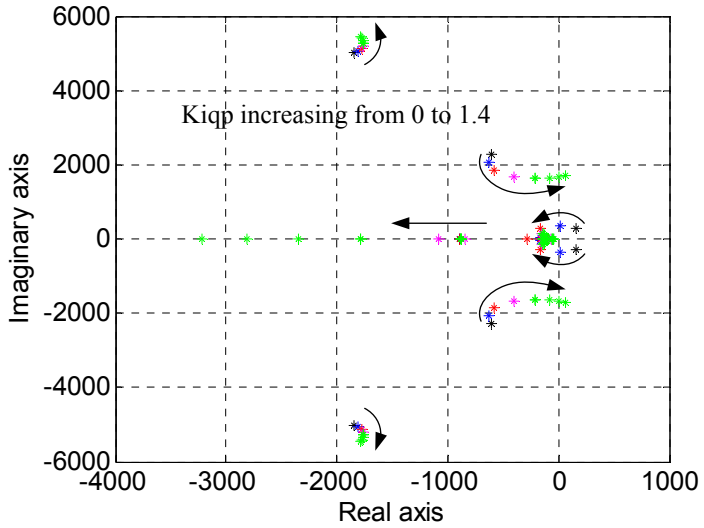

Fig. 3-15. The eigenvalues' location with an increasing Kiqp.

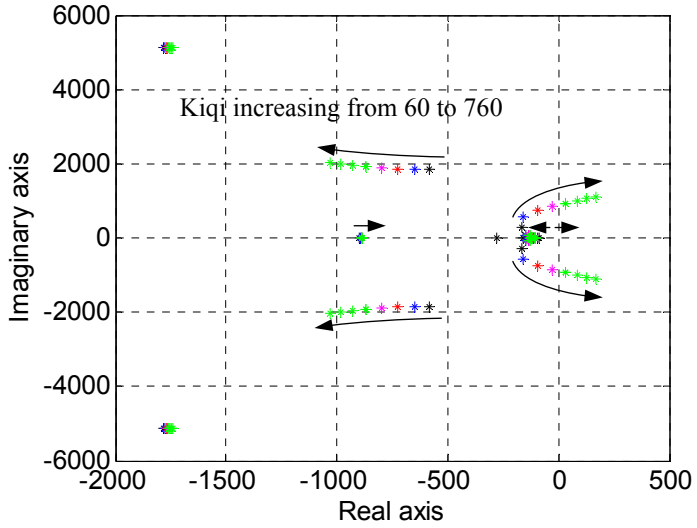

Fig. 3-16. The eigenvalues' location with an increasing Kiqi.

Phase locked controller

With Kp increasing from 0 to 1.2 in Fig. 3-17, a pair of complex conjugate eigenvalues moves from LHP with a decreasing damping ratio to the RHP, thereby the system moves to an unstable state. The loci of the eigenvalues with Ki increasing from 0 to 1200 are shown in Fig. 3-18. When Ki equals 200, the nearest eigenvalue to the origin is the furthest compared with Ki equal to other values. With Ki increasing, one pair of conjugate complex poles moves to the RHP thereby causing system instability.

Frequency droop controller

As K increases from 100 to 2000, the trajectory of all the eigenvalues are shown in Fig. 3-19. One pair of conjugate complex poles moves towards to the left and another pair moves to the RHP. Thus, K cannot be selected too large in order to maintain system stability. K is set to be 500.

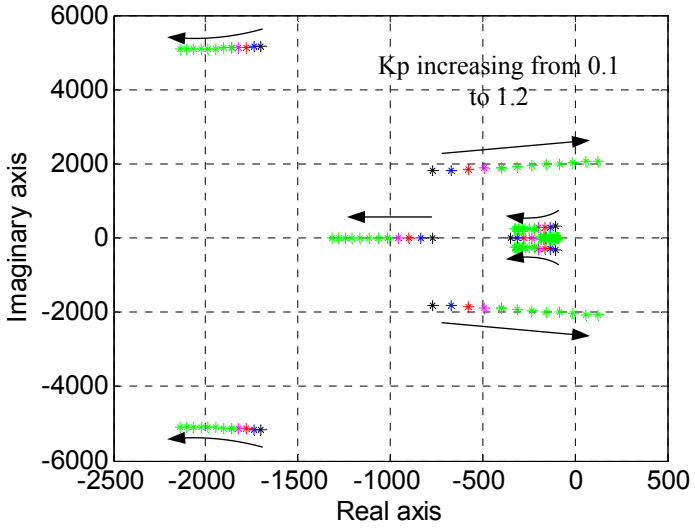

Fig. 3-17. The eigenvalues' location with an increasing Kp.

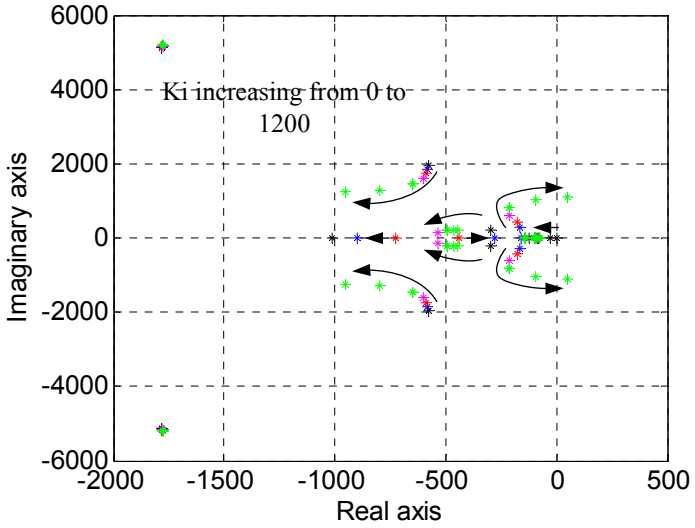

Fig. 3-18. The eigenvalues' location with an increasing Ki.

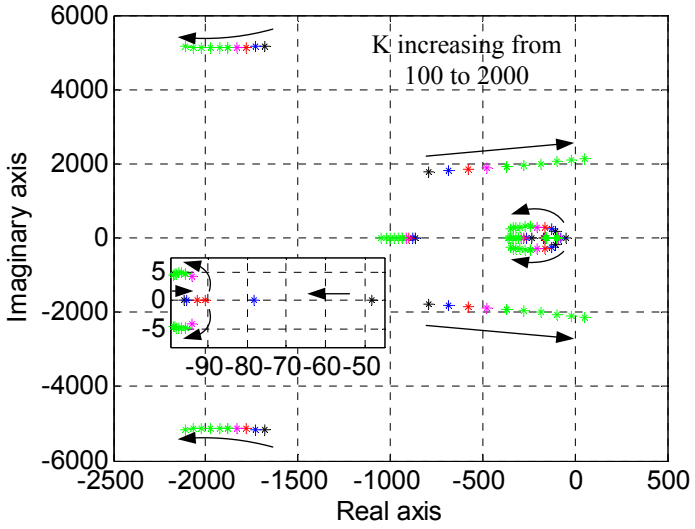

Fig. 3-19. The eigenvalues' location with an increasing K.

3.1.4.2 Filter Parameters

Fig. 3-20 and Fig. 3-21 show the loci of the eigenvalues of the system with two filter parameters varying. When L is increasing from 0.066 mH to 4.6 mH, Fig. 3-20 suggests that a large increase or decrease in L results in the departure of complex conjugate eigenvalues from the LHP to the RHP.

As shown in Fig. 3-21, the complex conjugate eigenvalues move from the LHP to the RHP when C is increasing from 110 μF to 1.54 mF. In this case, the system changes from an unstable state to a stable state.

3.1.4.3 Load Parameters

When load resistant R_o is increasing from 0.024 Ω to 0.83 Ω in Fig. 3-22-a, the shifting of one pair of conjugate complex poles from the RHP to the LHP changes the

system into a stable state. When L_o is increasing from 0.08 mH to 1.8 mH in Fig. 3-22-b, the shifting of one pair of conjugate complex poles from the RHP to the LHP results in the system moving to an unstable state.

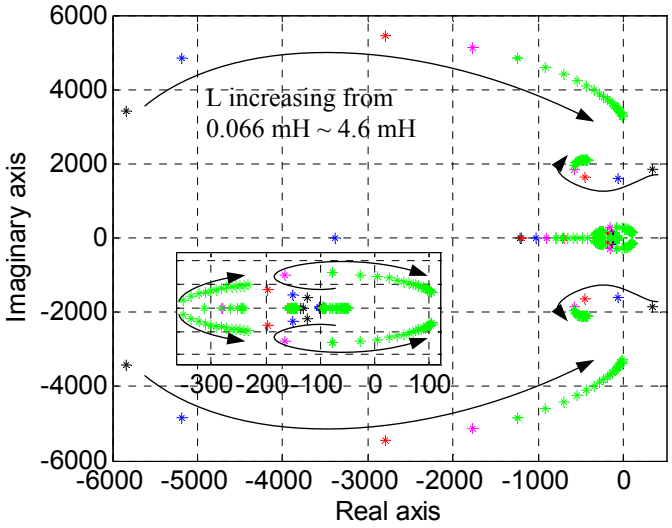

Fig. 3-20. The eigenvalues' location with an increasing L.

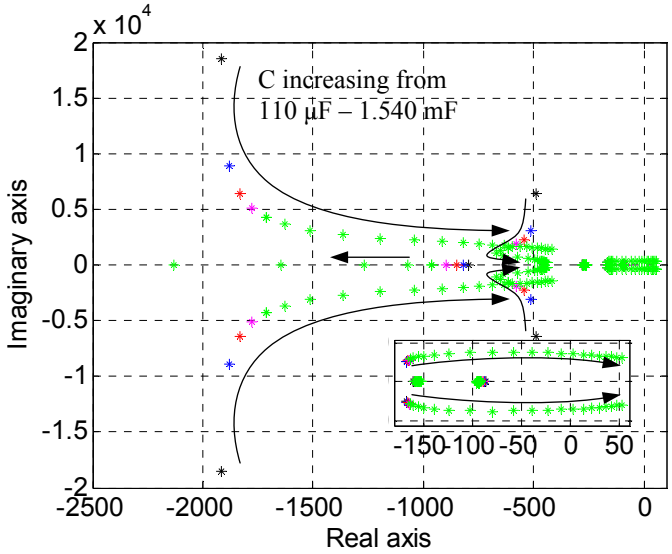

Fig. 3-21. The eigenvalues' location with an increasing C.

3.1.5 Time-Domain Simulation

To verify and compare the performances of different control strategies, one inverter with the reactive power and voltage control mode is modeled based on the averaged model of the inverter and simulated in MATLAB/Simulink. The inductance and capacitance of filters are respectively 0.66 mH and 0.22 mF. The load resistance and inductance are 0.2435 Ω and 8.0236e-4 H and decrease to 95% after 0.5 s. The Vrms magnitude reference is maintained at 120 V. The active power reference is set to be 20 kW. The frequency reference is set to be 60 Hz.

The simulation runs for 1 second. The simulation is under PV control strategy, shown in Fig. 3-3. The simulation results show the voltage is regulated very well around 120 V with slight oscillations when the load increases and the angular frequency drops about 15 rad/s. These simulations demonstrate the droop control scheme works well.

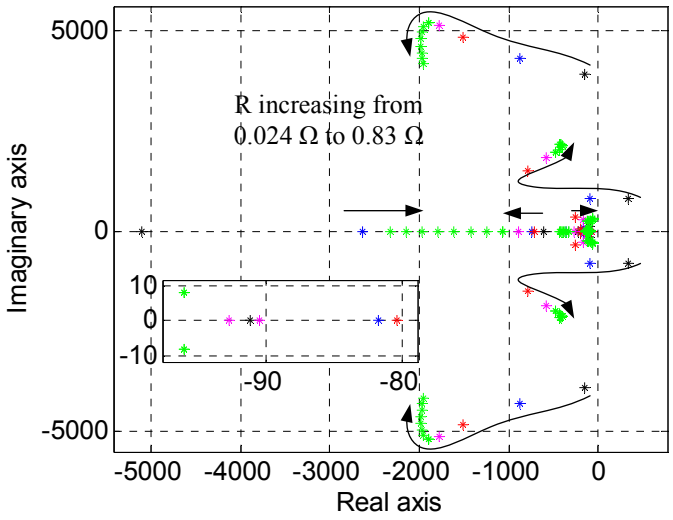

(a)

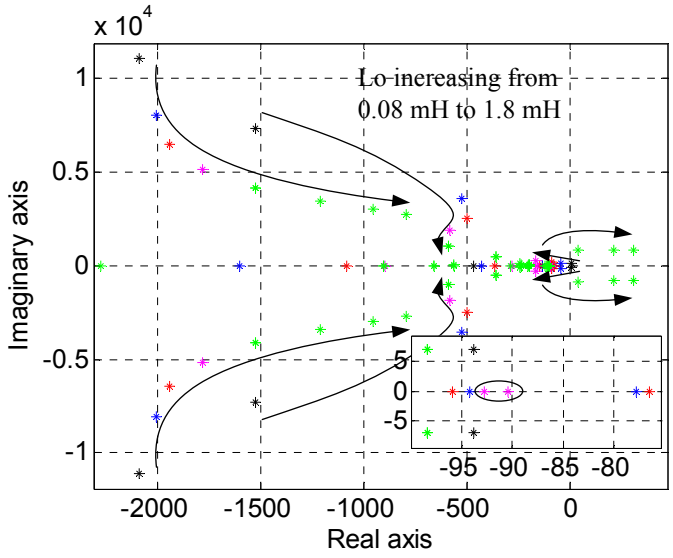

(b)

Fig. 3-22. The eigenvalues' location with an increasing (a) R_o, (b) L_o .

Fig. 3-23 shows inverter output rms voltage, angular frequency, active and reactive power when Kpp equals 0.001, 0.01 and 0.1. Compared with the other two values, when Kpp equals 0.01 the system gets to a stable state faster and its overshoot is lower. When Kpp is 0.1, the oscillation is larger and the oscillatory time is longer than when it is 0.001.

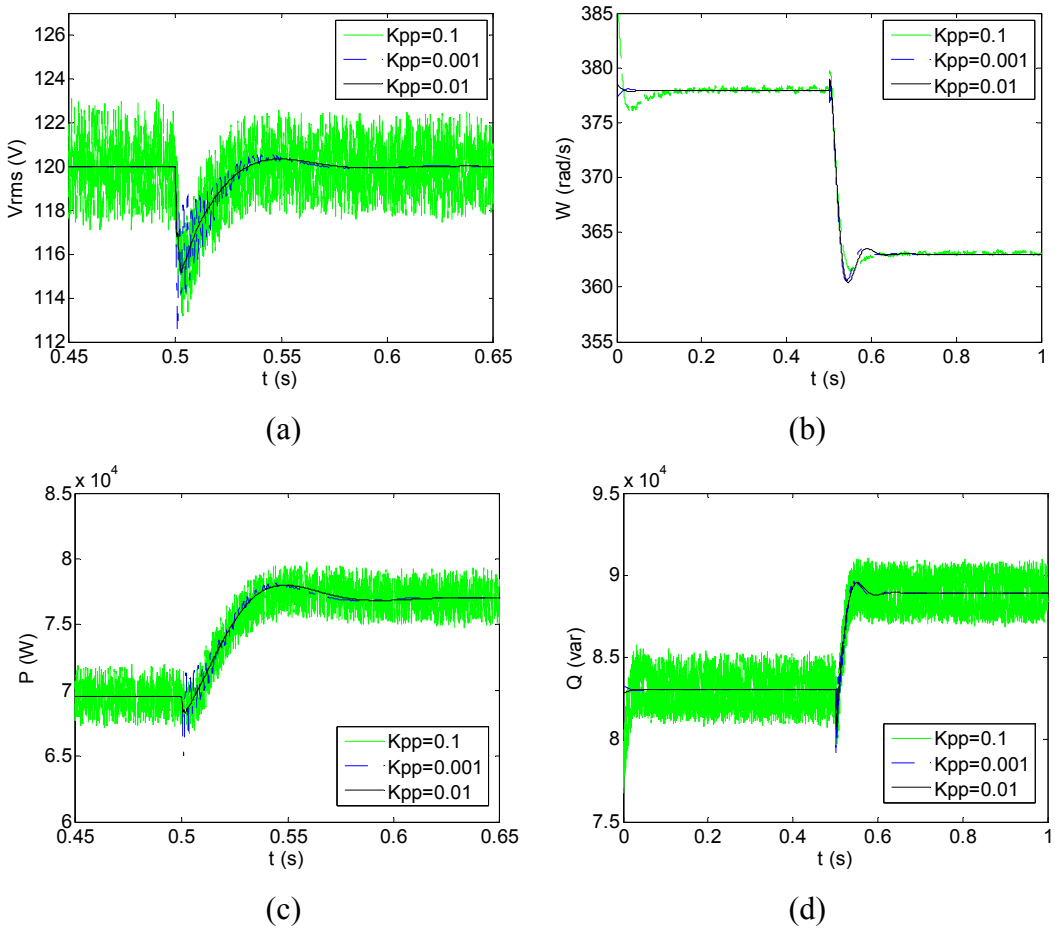

Fig. 3-23. Inverter output when Kpp equals 0.001, 0.01 and 0.1 (a) rms voltage, (b) angular frequency, (c) active power, (d) reactive power.

Inverter output rms voltage, angular frequency, active and reactive power when Kpi equals 0.5, 1.5 and 23.4 are shown in Fig. 3-24. When Kpi equals 1.5, the system gets to a stable state faster than when it equals 0.5, and it is more stable than when Kpi equals 23.4.

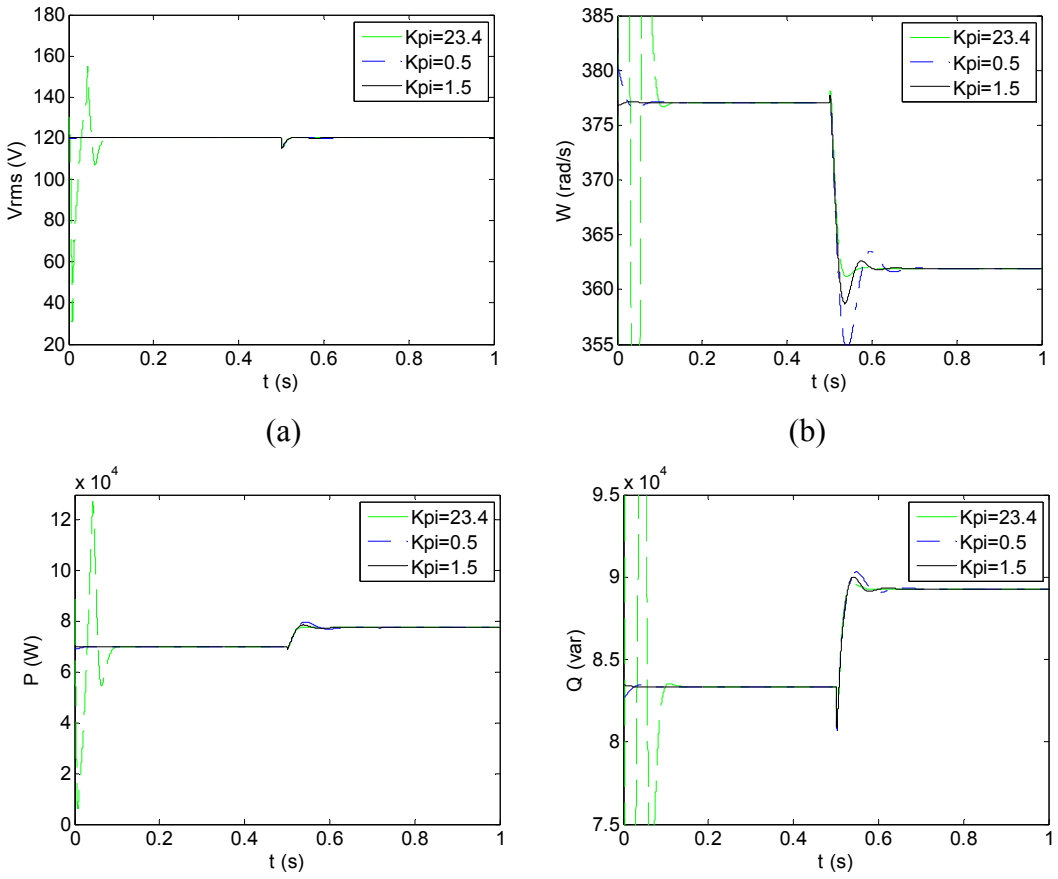

Fig. 3-24. Inverter output when Kpi equals 0.5, 1.5 and 23.4 (a) rms voltage, (b) angular frequency, (c) active power, (d) reactive power.

In the Fig. 3-25, inverter system behavior is shown when Kvp equals 0.001, 0.5 and 2.085. Although the system is stable with these three Kvp values, when Kvp equals 2.085 the system needs a longer time to get to its initial stable state. It has much larger oscillations and the system is less stable; while when it equals 0.001, the system has larger overshoots and slower response when changes occur. The system response is best when Kvp is 0.5.

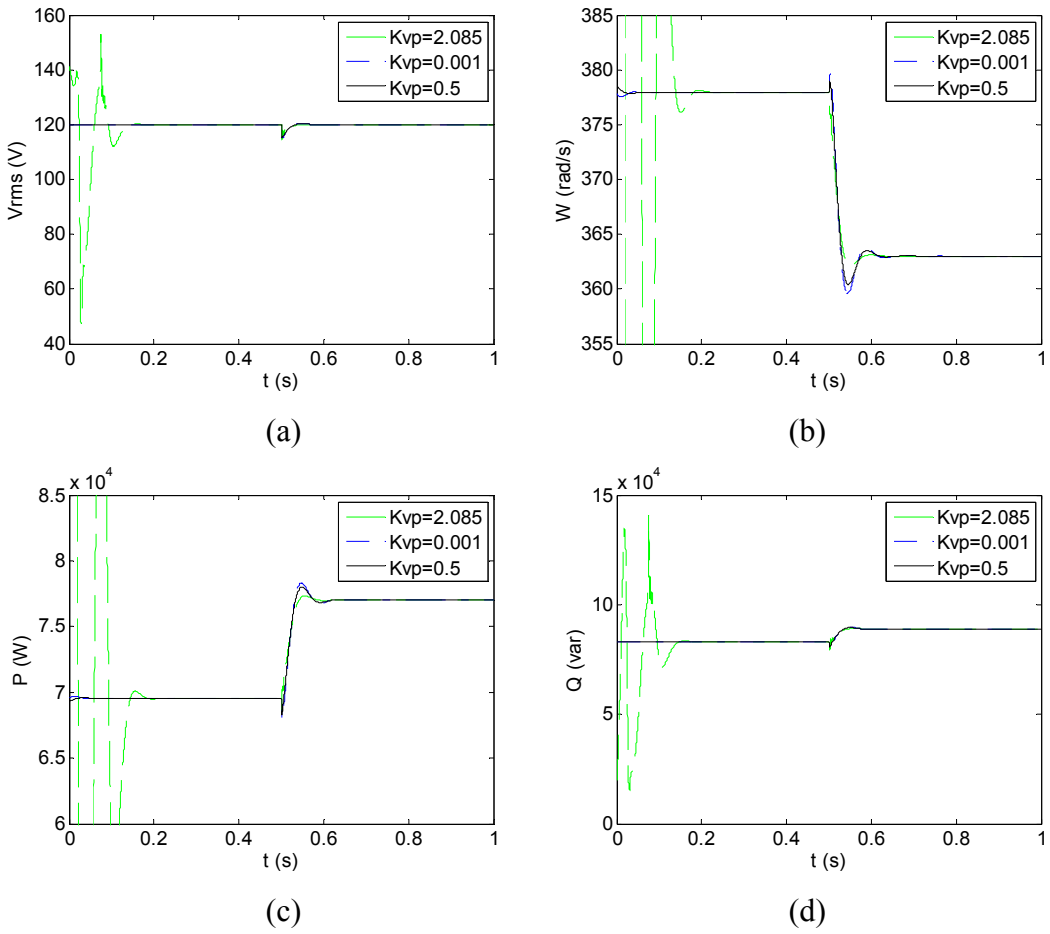

Fig. 3-25. Inverter output when Kvp equals 0.001, 0.5 and 2.085 (a) rms voltage, (b) angular frequency, (c) active power, (d) reactive power.

Fig. 3-26 shows inverter output rms voltage, angular frequency, active and reactive power when Kvi equals 100, 400 and 1020. The system gets to steady state faster and the overshoot is smaller with Kvi equals 400 than when it equals 100. When Kvi is selected as 1020, the system experiences larger oscillations to get to an initial stable state.

In the current loops, the inverter output rms voltage and active power behaviors are shown in Fig. 3-27. Clearly, when Kidp equals 0.1, as shown by the frequency-domain analysis, the system is unstable. The change in the load at 0.5 second makes the

divergence much larger and faster. The oscillations of the system when Kidp equals 10 are larger than when it equals 1. Kidi is increasing from 0 to 100 and 500 in the time-domain simulation shown in Fig. 3-28. From these analyses, it is seen that system stability is not very sensitive to control parameters of Kidi compared with other control parameters.

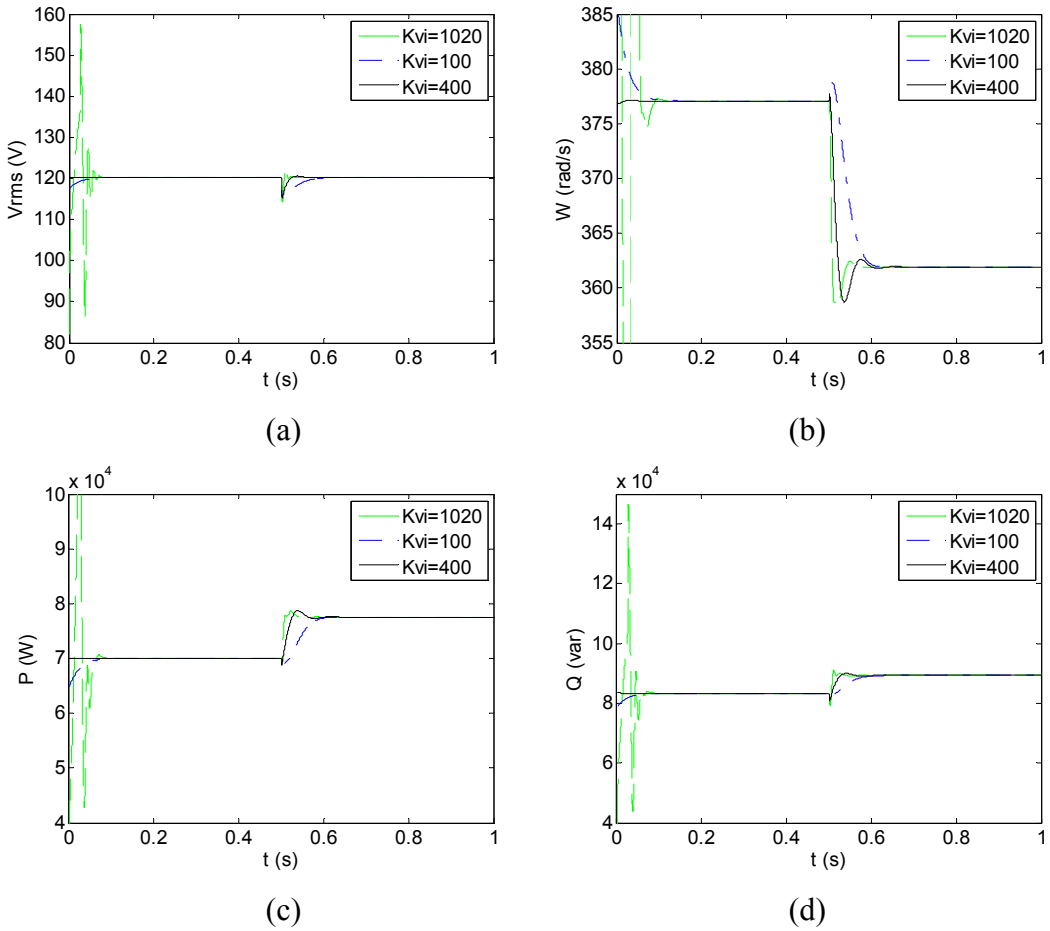

Fig. 3-26. Inverter output when Kvi equals 100, 400 and 1020 (a) rms voltage, (b) angular frequency, (c) active power, (d) reactive power.

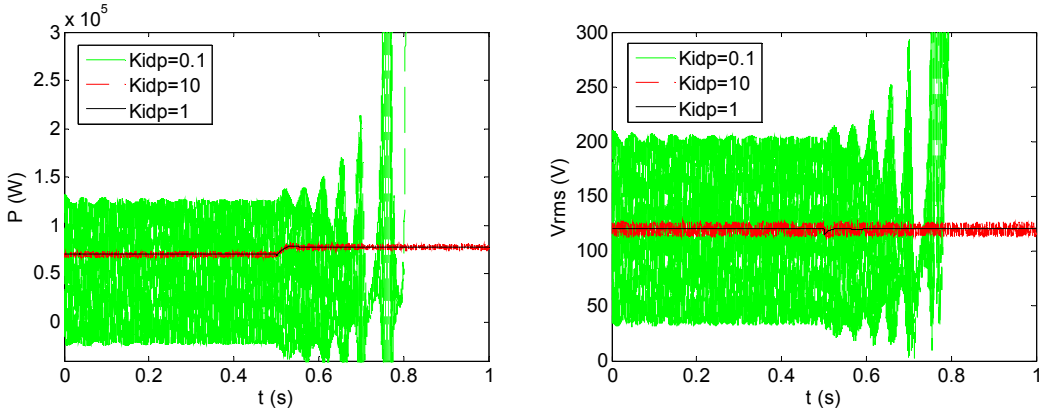

(a) (b)

Fig. 3-27. Inverter output (a) rms voltage and (b) active power when Kidp equals 0.1, 1, and 10.

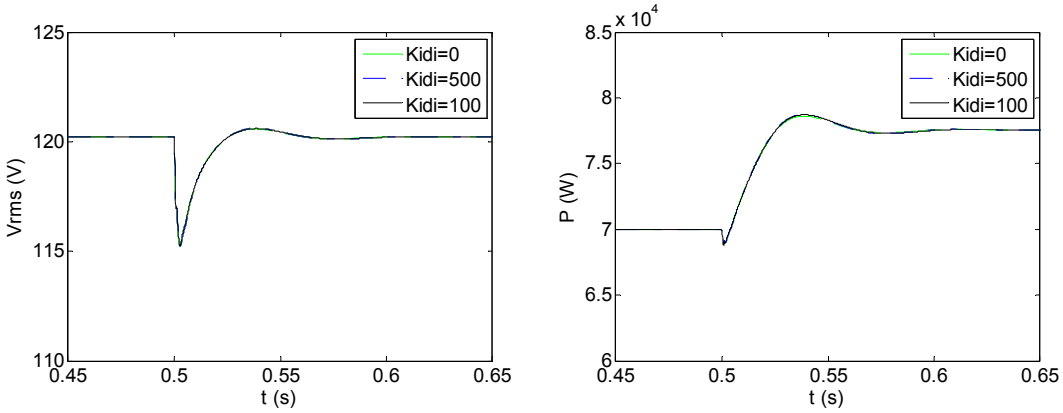

(a) (b)

Fig. 3-28. Inverter output (a) rms voltage and (b) active power when Kidi equals 0, 100, and 500.

Inverter output rms voltage and active power are shown in Fig. 3-29 with Kiqp equaling 0, 0.4 and 1.2. Clearly, when Kiqp equals 0 or 1.2, the system diverges by oscillation. This is consistent with the frequency-domain analysis that the system is unstable.

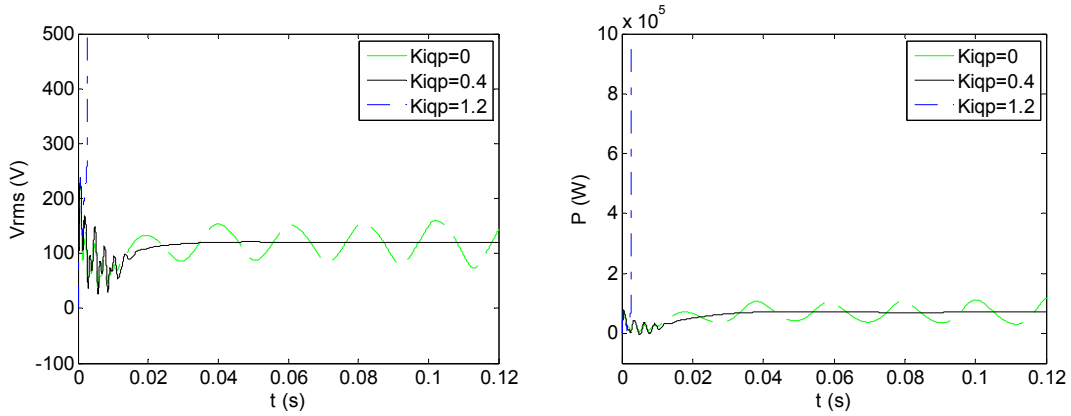

(a) (b)

Fig. 3-29. Inverter output (a) rms voltage and (b) active power when Kiqp equals 0, 0.4 and 1.4.

Inverter output rms voltage and reactive power when Kiqi equals 0, 60 and 600 are shown in Fig. 3-30. Clearly, when Kiqi equals 600, the system is unstable. When Kiqi equals 60, the system has relative smaller steady state error than when Kiqi equals 0. It also shows Kiqi is not a sensitive parameter.

In the phase locked loop, Kp is selected as 0.3 and 1.2 in the time-domain simulations shown in Fig. 3-31. The system is unstable when Kp equals 1.2. In Fig. 3-32, Ki is selected as 0, 200 and 800. When Ki is set to be 200, the system has a much smaller steady state error and a faster response than when it is 0. When Ki equals 800, the system is unstable and, after a saturation block is added to the controller, the system is uncontrollable as shown.

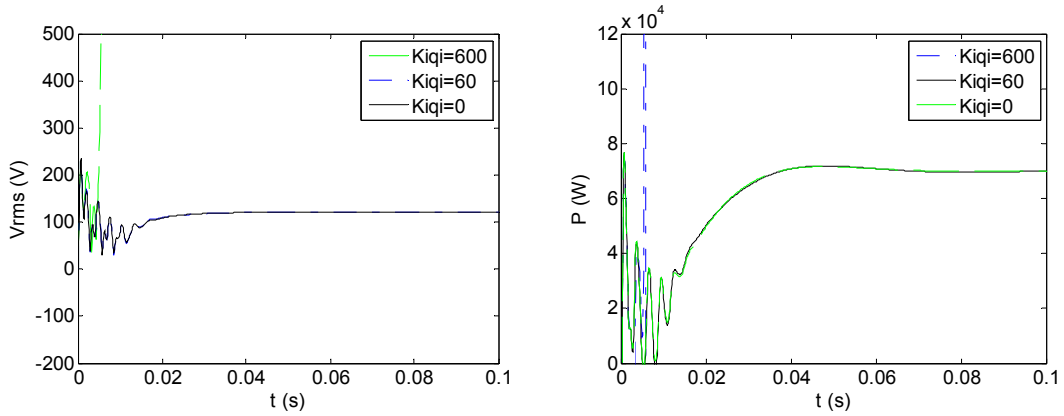

(a) (b)

Fig. 3-30. Inverter output (a) rms voltage and (b) active power when Kiqi equals 600, 60 and 0.

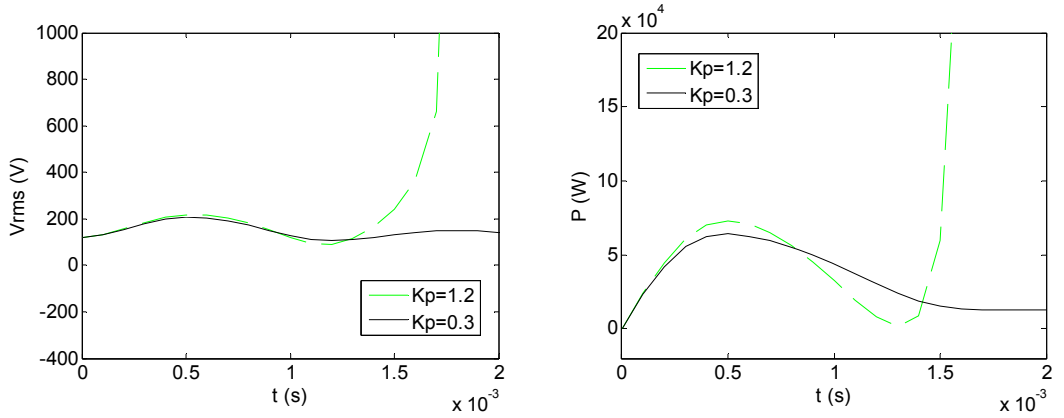

(a) (b)

Fig. 3-31. Inverter output (a) rms voltage and (b) active power when Kp equals 0.3 and 1.2.

The time-domain simulation with K variation is shown in Fig. 3-33. When K is set as 350, the voltage experiences oscillations and converges to a stable state. Meanwhile, there are large overshoots in the inverter active power. When this parameter is increased to 500, the oscillations in the inverter voltage and output reactive power are heavily reduced. When K increases to 2000, the system is unstable and after saturation blocks are

added to the controller, the system is uncontrollable. The results are consistent with the frequency-domain analysis.

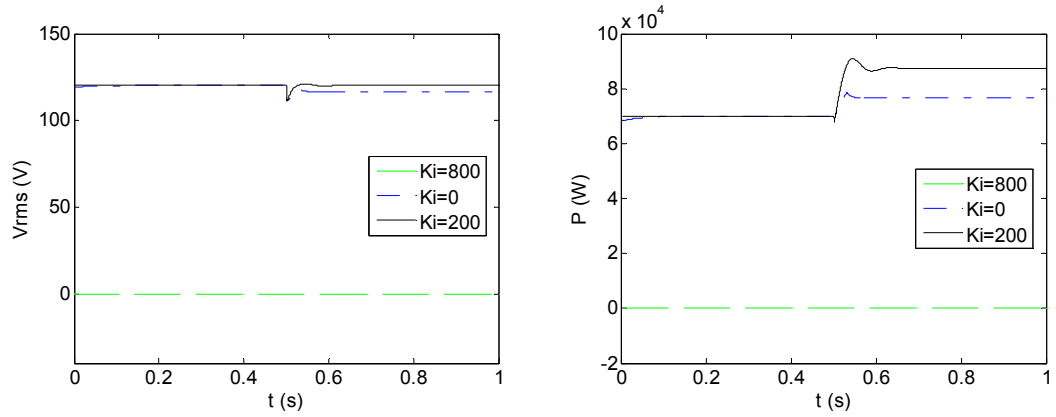

(a) (b)

Fig. 3-32. Inverter output (a) rms voltage and (b) active power when Ki equals 0, 200 and 800.

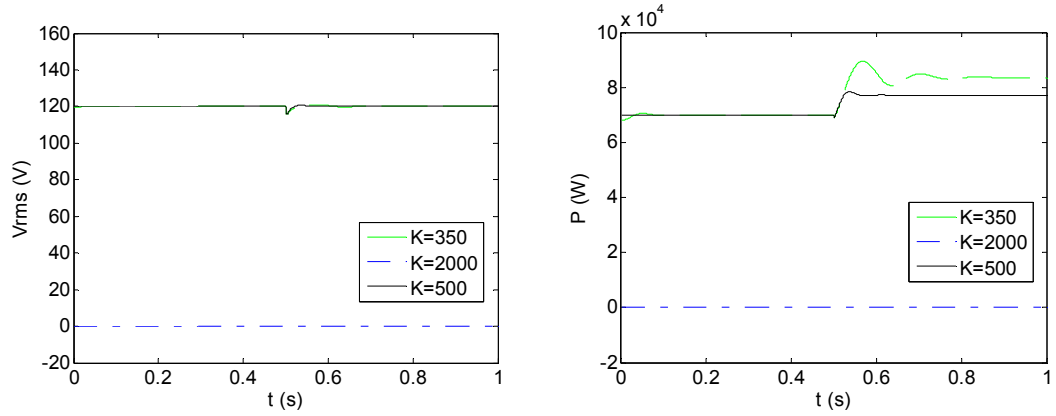

(a) (b)

Fig. 3-33. Inverter output (a) rms voltage and (b) active power when K equals 350, 2000 and 500.

The time-domain simulation with L variation is shown in Fig. 3-34. When L is set as 0.66 mH, the voltage and active power converge to a stable state. From these simulation results, the system is shown to be unstable as this parameter is increased to 4.6 mH or reduced to 66 μH. These are consistent with the frequency-domain analysis. The time-

domain simulation with *C* variation is shown in Fig. 3-35. When *C* is chosen as 220 μF or 110 μF, the voltage and active power converge to a stable state. From these simulation results, it is seen that the system is unstable as this parameter is increased to 1.54 mF. These results are consistent with the frequency-domain analysis.

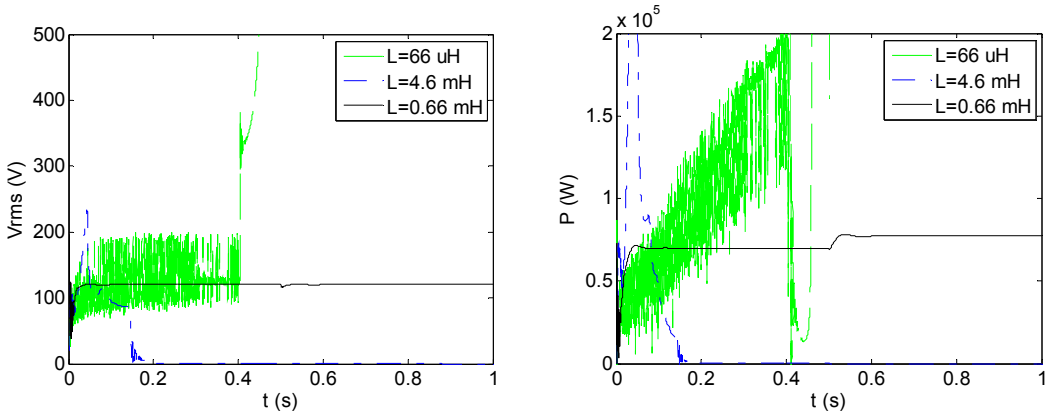

(a) (b)

Fig. 3-34. Inverter output (a) rms voltage and (b) active power when *L* equals 66 μH, 0.66 mH and 4.6 mH.

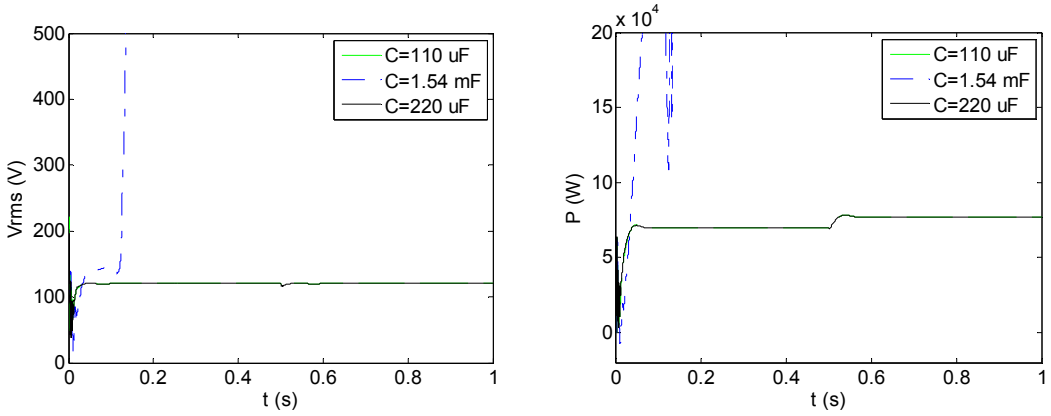

(a) (b)

Fig. 3-35. Inverter output (a) rms voltage and (b) active power when *C* equals 110 μF, 220 μF and 1.54 mF.

The time-domain simulation with Load variation is shown in Fig. 3-36. As the load resistance and inductance decrease from 0.2435 Ω to 0.2313 Ω and from 802.36 μH to

762.24 μH, 95% of the rated values, the inverter has to produce 105% of the rated active power and the angular frequency of the output voltage drops by around 14 rad/s, which is a consequence of the droop control scheme. Interestingly, as the load resistance decrease to 0.24 Ω, 95% of the rated load resistance, while the inductance doesn't change, the output active power decreases and the angular frequency increases (Fig. 3-36-b, c). When R_o is 0.01 Ω or L_o is 1.8 mH, the system is unstable.

3.1.6 Conclusion

This part presents small-signal modeling and analysis of an inverter system with control loops in a rotating *d-q* frame. The active power and voltage control are proposed. The mathematical process and structure for the development of the inverter model are presented in a general form and can be expanded to include additional units, loads and controllers as desired. The time-domain result is almost consistent with the frequency-domain analysis and proves most of the analysis. The frequency-domain analysis is extremely important for control design and parameter selection. It suggests how the parameters affect the eigenvalues' location and thus influence system stability. In the analysis, it is apparent that some eigenvalues are affected by certain parameters. The system stability is relatively sensitive to some parameters compared with other parameters.

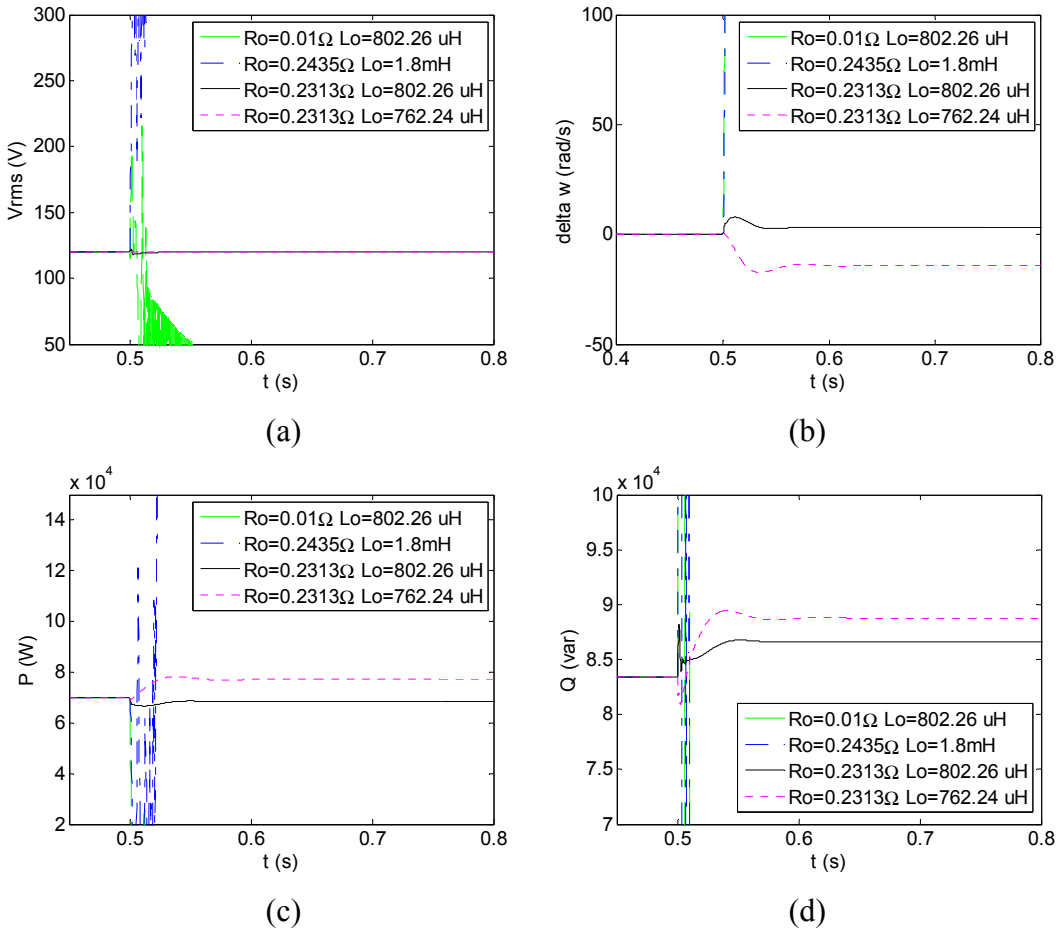

Fig. 3-36. Inverter output (a) rms voltage, (b) angular frequency, (c) active power and (d) reactive power with load variation.

3.2 Parallel-Connected DC-AC Three Phase Power Converter System with Individual DC Power Supplies

There are two structures for parallel three-phase power converters. One is where each power inverter has its individual DC power source and another one is where they share a single DC power source. When parallel three-phase power inverters are in the grid connected mode, inverters are under PQ control, which connect to the point of common coupling (PCC). The load dynamics at PCC can be ignored, because they are handled by the grid. Thus, the focus is on the parallel three-phase power converters in stand-alone mode, which are necessary components in a microgrid. The block of the parallel three-phase power converters in the stand-alone mode is shown in Fig. 3-37.

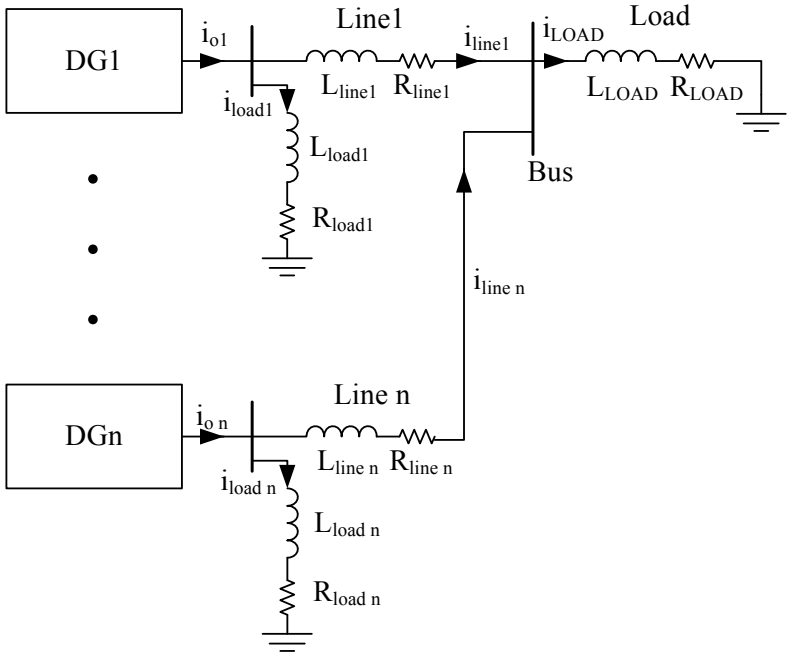

Fig. 3-37. Parallel three-phase power converters in the stand-alone mode.

3.2.1 Small-Signal Modeling and Analysis

To study the dynamic behavior of the power sharing mechanism in a microgrid, the small-signal dynamic model of the microgrid is constructed. The model considers individual small-signal models of different inverters, network impedances and load dynamics. In a microgrid, inverters are in the stand-alone mode and the grid size is limited. It is worthwhile to study the system dynamics caused by disturbances of the voltage, the network, and the load.

For the system under study, the state vector of the microgrid includes the states of the two inverter based distributed generation (DG) units under voltage and PQ control and the line and load states. The overall average model of a microgrid system can be given as follows.

DG1 inverter:

$$\frac{d}{dt}\begin{bmatrix} i_{d1} \\ i_{q1} \end{bmatrix} = \begin{bmatrix} -\frac{R_{L1}}{L_1} & \omega \\ -\omega & -\frac{R_{L1}}{L_1} \end{bmatrix}\begin{bmatrix} i_{d1} \\ i_{q1} \end{bmatrix} - \frac{1}{L_1}\begin{bmatrix} v_{d1} \\ v_{q1} \end{bmatrix} + \frac{v_{dc1}}{L_1}\begin{bmatrix} d_{d1} \\ d_{q1} \end{bmatrix} \tag{3-73}$$

$$\frac{d}{dt}\left(\begin{bmatrix} v_{d1} \\ v_{q1} \end{bmatrix}\right) = \frac{1}{C_1}\begin{bmatrix} i_{d1} \\ i_{q1} \end{bmatrix} - \frac{1}{C_1}\begin{bmatrix} i_{od1} \\ i_{oq1} \end{bmatrix} + \begin{bmatrix} 0 & \omega \\ -\omega & 0 \end{bmatrix}\begin{bmatrix} v_{d1} \\ v_{q1} \end{bmatrix} \tag{3-74}$$

DG1 local load:

$$\frac{d}{dt}\begin{bmatrix} i_{load\_d1} \\ i_{load\_q1} \end{bmatrix} = \begin{bmatrix} \frac{1}{L_{load1}} & 0 \\ 0 & \frac{1}{L_{load1}} \end{bmatrix} \begin{bmatrix} v_d \\ v_q \end{bmatrix} + \begin{bmatrix} \frac{-R_{load1}}{L_{load1}} & \omega \\ -\omega & \frac{-R_{load1}}{L_{load1}} \end{bmatrix} \begin{bmatrix} i_{load\_d1} \\ i_{load\_q1} \end{bmatrix} \tag{3-75}$$

DG1 line:

$$\frac{d}{dt}\begin{bmatrix} i_{line\_d1} \\ i_{line\_q1} \end{bmatrix} = \begin{bmatrix} \frac{1}{L_{line1}} & 0 \\ 0 & \frac{1}{L_{line1}} \end{bmatrix} \begin{bmatrix} v_{d1} \\ v_{q1} \end{bmatrix} - \begin{bmatrix} \frac{1}{L_{line1}} & 0 \\ 0 & \frac{1}{L_{line1}} \end{bmatrix} \begin{bmatrix} v_d^{PCC} \\ v_q^{PCC} \end{bmatrix} + \begin{bmatrix} \frac{-R_{line1}}{L_{line1}} & \omega \\ -\omega & \frac{-R_{line1}}{L_{line1}} \end{bmatrix} \begin{bmatrix} i_{line\_d1} \\ i_{line\_q1} \end{bmatrix} \tag{3-76}$$

Load at PCC:

$$\frac{d}{dt}\begin{bmatrix} i_{LOAD\_d} \\ i_{LOAD\_q} \end{bmatrix} = \begin{bmatrix} \frac{1}{L_{LOAD}} & 0 \\ 0 & \frac{1}{L_{LOAD}} \end{bmatrix} \begin{bmatrix} v_d^{PCC} \\ v_q^{PCC} \end{bmatrix} + \begin{bmatrix} \frac{-R_{LOAD}}{L_{LOAD}} & \omega \\ -\omega & \frac{-R_{LOAD}}{L_{LOAD}} \end{bmatrix} \begin{bmatrix} i_{LOAD\_d} \\ i_{LOAD\_q} \end{bmatrix} \tag{3-77}$$

$$i_{LOAD\_d} = i_{line\_d1} + i_{line\_d2} + \cdots \tag{3-78}$$

$$i_{LOAD\_q} = i_{line\_q1} + i_{line\_q2} + \cdots \tag{3-79}$$

The small-signal mode for voltage controlled power converter can be derived as:

$$\begin{aligned} \frac{d}{dt}\left[\tilde{x}^{DG1}\right] &= \left(A_1 + B_{a1}D_{D1}\right)\left[\tilde{x}^{DG1}\right] + \left(B_{a1}D_{P1} + B_{ra1}\right)\left[\tilde{v}_{d\_ref1}\right] + \left(B_{a1}D_{V1} + B_{rb1}\right)\left[\tilde{v}_{q\_ref1}\right] \\ &+ F_{a1}\left[\tilde{v}_{dc1}\right] + \left(F_{b1} + B_{a1}F_{C1}\right)\left[\tilde{\omega}_1\right] + B_{b1}\left[v_{d,q}^{PCC}\right] \end{aligned} \tag{3-80}$$

where:

$$A_1 = \begin{bmatrix} A_{o1,8\times8} & 0 & 0 & 0 \\ E_{V1,2\times4} & 0_{2\times2} & 0 & 0 & 0 \\ E_{S1,2\times4} & 0_{2\times2} & A_{V1,2\times2} & 0 & 0 \end{bmatrix}_{12\times2} \quad B_{a1} = \begin{bmatrix} B_{oa1,8\times2} \\ 0_{4\times2} \end{bmatrix}_{12\times2} \quad B_{b1} = \begin{bmatrix} B_{ob1,8\times2} \\ 0_{4\times2} \end{bmatrix}$$

$$B_{ra1}=\begin{bmatrix}0\\E_{\phi 1}(:,1)\\J_{V1}(:,1)\end{bmatrix}B_{rb1}=\begin{bmatrix}0\\E_{\phi 1}(:,2)\\J_{V1}(:,2)\end{bmatrix}F_{a1}=\begin{bmatrix}F_{oa1}\\0\end{bmatrix}F_{b1}=\begin{bmatrix}F_{ob1}\\0\end{bmatrix}$$

$$B_{oa1}=\begin{bmatrix}\frac{V_{dc1}}{L_1}&0\\0&\frac{V_{dc1}}{L_1}\\0&0\\0&0\\0&0\\0&0\\0&0\\0&0\end{bmatrix}B_{ob1}=\begin{bmatrix}0&0\\0&0\\0&0\\0&0\\0&0\\0&0\\-\frac{1}{L_{line1}}&0\\0&-\frac{1}{L_{line1}}\end{bmatrix}F_{oa1}=\begin{bmatrix}\frac{D_{d1}}{L_1}\\\frac{D_{q1}}{L_1}\\0\\0\\0\\0\\0\\0\end{bmatrix}F_{ob1}=\begin{bmatrix}I_{q1}\\I_{d1}\\V_{q1}\\V_{d1}\\I_{load\_q1}\\I_{load\_d1}\\I_{line\_q1}\\I_{line\_d1}\end{bmatrix}$$

$$A_{o1}=\begin{bmatrix}-\frac{R_{L1}}{L_1}&\omega&-\frac{1}{L_1}&0&0&0&0&0\\-\omega&-\frac{R_{L1}}{L_1}&0&-\frac{1}{L_1}&0&0&0&0\\\frac{1}{C_1}&0&0&\omega&\frac{-1}{C_1}&0&\frac{-1}{C_1}&0\\0&\frac{1}{C_1}&-\omega&0&0&\frac{-1}{C_1}&0&\frac{-1}{C_1}\\0&0&\frac{1}{L_{load1}}&0&\frac{-R_{load1}}{L_{load1}}&\omega&0&0\\0&0&0&\frac{1}{L_{load1}}&-\omega&\frac{-R_{load1}}{L_{load1}}&0&0\\0&0&\frac{1}{L_{line1}}&0&0&0&\frac{-R_{line1}}{L_{line1}}&\omega\\0&0&0&\frac{1}{L_{line1}}&0&0&-\omega&\frac{-R_{line1}}{L_{line1}}\end{bmatrix}$$

$$D_{D1}=\begin{bmatrix}A_{D1}+J_{C1}F_{V1}&0_{4\times4}&J_{C1}A_{V1}&A_{C1}\end{bmatrix}\quad D_{P1}=J_{C1}J_{V1}(:,1)\quad D_{V1}=J_{C1}J_{V1}(:,2)$$

$$E_{\phi 1}=\begin{bmatrix}1&0\\0&1\end{bmatrix}\qquad E_{V1}=\begin{bmatrix}0&0&-1&0\\0&0&0&-1\end{bmatrix}\quad A_{V1}=\begin{bmatrix}k_{di}&0\\0&k_{qi}\end{bmatrix}\quad J_{V1}=\begin{bmatrix}k_{dp}&0\\0&k_{qp}\end{bmatrix}$$

$$F_{V1}=\begin{bmatrix}k_{dp}&0\\0&k_{qp}\end{bmatrix}\begin{bmatrix}0&0&-1&0\\0&0&0&-1\end{bmatrix}=\begin{bmatrix}0&0&-k_{dp}&0\\0&0&0&-k_{qp}\end{bmatrix}$$

$$E_{\gamma 1}=\begin{bmatrix}1 & 0\\ 0 & 1\end{bmatrix}\quad E_{C1}=\begin{bmatrix}-1 & 0\\ 0 & -1\end{bmatrix}\quad E_{S1}==\begin{bmatrix}-1 & 0 & -k_{dp} & 0\\ 0 & -1 & 0 & -k_{qp}\end{bmatrix}\quad F_{C1}=\frac{L}{V_{dc1}}\begin{bmatrix}-I_q\\ I_d\end{bmatrix}$$

$$A_{D1}=\frac{1}{V_{dc}}\begin{bmatrix}-k_{idp} & -\omega L & 1 & 0\\ \omega L & -k_{iqp} & 0 & 1\end{bmatrix}\quad A_{C1}=\frac{1}{V_{dc}}\begin{bmatrix}k_{idi} & 0\\ 0 & k_{iqi}\end{bmatrix}\quad J_{C1}=\frac{1}{V_{dc}}\begin{bmatrix}k_{idp} & 0\\ 0 & k_{iqp}\end{bmatrix}.$$

The complete small-signal model for DG1 with PQ control can be expressed as:

$$\begin{aligned}\frac{d}{dt}\left[\widetilde{x}^{DG2}\right]&=\left(A_2+B_{a2}D_{D2}+\left(F_{b2}+B_2F_{C2}\right)A_{\omega 2}\right)\left[\widetilde{x}^{DG2}\right]+\left(B_{a2}D_{P2}+B_{ra2}\right)\left[\widetilde{P}_{\_ref2}\right]\\&+\left(B_{a2}D_{V2}+B_{rb2}\right)\left[\widetilde{Q}_{\_ref2}\right]+F_{a2}\left[\widetilde{v}_{dc2}\right]+B_{b2}\left[v_{d,q}^{PCC}\right]\end{aligned}\tag{3-81}$$

where:

$$A_2=\begin{bmatrix}A_{o2,8\times 8} & 0 & 0 & 0\\ E_{V2,2\times 4} & 0_{2\times 2} & 0 & 0 & 0\\ E_{S2,2\times 4} & 0_{2\times 2} & A_{V2,2\times 2} & 0 & 0\\ E_{\mu 2} & & 0 & 0 & 0\end{bmatrix}\quad B_{a2}=\begin{bmatrix}B_{oa2,8\times 2}\\ 0_{5\times 2}\end{bmatrix}_{13\times 2}\quad B_{b2}=\begin{bmatrix}B_{ob2,8\times 2}\\ 0_{5\times 2}\end{bmatrix}_{13\times 2}$$

$$B_{ra2}=\begin{bmatrix}0_{8\times 1}\\ E_{\phi 2}(:,1)\\ J_{V2}(:,1)\\ 0\end{bmatrix}\quad B_{rb2}=\begin{bmatrix}0_{8\times 1}\\ E_{\phi 2}(:,2)\\ J_{V2}(:,2)\\ 0\end{bmatrix}\quad F_{a2}=\begin{bmatrix}F_{oa2}\\ 0_{5\times 1}\end{bmatrix}\quad F_{b2}=\begin{bmatrix}F_{ob2}\\ 0_{5\times 1}\end{bmatrix}$$

$$\widetilde{x}_o^{DG2}=\begin{bmatrix}\widetilde{i}_{d2} & \widetilde{i}_{q2} & \widetilde{v}_{d2} & \widetilde{v}_{q2} & \widetilde{i}_{load\_d2} & \widetilde{i}_{load\_q2} & \widetilde{i}_{line\_d2} & \widetilde{i}_{line\_q2}\end{bmatrix}^{-1}$$

$$B_{oa2}=\begin{bmatrix}\frac{V_{dc2}}{L_2} & 0\\ 0 & \frac{V_{dc2}}{L_2}\\ 0 & 0\\ 0 & 0\\ 0 & 0\\ 0 & 0\\ 0 & 0\\ 0 & 0\end{bmatrix}\quad B_{ob2}=\begin{bmatrix}0 & 0\\ 0 & 0\\ 0 & 0\\ 0 & 0\\ 0 & 0\\ 0 & 0\\ -\frac{1}{L_{line2}} & 0\\ 0 & -\frac{1}{L_{line2}}\end{bmatrix}\quad F_{oa2}=\begin{bmatrix}\frac{D_{d2}}{L_2}\\ \frac{D_{q2}}{L_2}\\ 0\\ 0\\ 0\\ 0\\ 0\\ 0\end{bmatrix}\quad F_{ob2}=\begin{bmatrix}I_{q2}\\ I_{d2}\\ V_{q2}\\ V_{d2}\\ I_{load\_q2}\\ I_{load\_d2}\\ I_{line\_q2}\\ I_{line\_d2}\end{bmatrix}$$

$$A_{o2}=\begin{bmatrix} -\frac{R_{L2}}{L_2} & \omega_2 & -\frac{1}{L_2} & 0 & 0 & 0 & 0 & 0 \\ -\omega_2 & -\frac{R_{L1}}{L_2} & 0 & -\frac{1}{L_2} & 0 & 0 & 0 & 0 \\ \frac{1}{C_2} & 0 & 0 & \omega & \frac{-1}{C_2} & 0 & \frac{-1}{C_2} & 0 \\ 0 & \frac{1}{C_2} & -\omega_2 & 0 & 0 & \frac{-1}{C_2} & 0 & \frac{-1}{C_2} \\ 0 & 0 & \frac{1}{L_{load2}} & 0 & \frac{-R_{load2}}{L_{load2}} & \omega_2 & 0 & 0 \\ 0 & 0 & 0 & \frac{1}{L_{load2}} & -\omega_2 & \frac{-R_{load2}}{L_{load2}} & 0 & 0 \\ 0 & 0 & \frac{1}{L_{line2}} & 0 & 0 & 0 & \frac{-R_{line2}}{L_{line2}} & \omega_2 \\ 0 & 0 & 0 & \frac{1}{L_{line2}} & 0 & 0 & -\omega_2 & \frac{-R_{line2}}{L_{line2}} \end{bmatrix}$$

$$A_{\omega 2}=\begin{bmatrix}0 & 0 & 0 & k_p & 0 & 0 & 0 & 0 & 0 & 0 & 0 & 0 & k_i\end{bmatrix}$$

$$D_{D2}=\begin{bmatrix}A_{D2}+J_{C2}F_{V2} & 0_{4\times 4} & J_{C2}A_{V2} & A_{C2} & 0_1\end{bmatrix} \quad D_{P2}=J_{C2}J_{V2}(:,1)$$

$$D_{V2}=J_{C2}J_{V2}(:,2) \quad E_{\mu 2}=\begin{bmatrix}0 & 0 & 0 & 1 & 0 & 0 & 0 & 0\end{bmatrix}$$

$$E_{\phi 2}=\begin{bmatrix}1 & 0\\ 0 & 1\end{bmatrix} \quad E_{V2}=\frac{3}{2}\begin{bmatrix}-V_{d2} & -V_{q2} & -I_{d2} & -I_{q2}\\ -V_{q2} & +V_{d2} & +I_{q2} & -I_{d2}\end{bmatrix}$$

$$A_{V2}=\begin{bmatrix}k_{Pi2} & 0\\ 0 & -k_{Qi2}\end{bmatrix} \quad J_{V2}=\begin{bmatrix}k_{Pp2} & 0\\ 0 & -k_{Qp2}\end{bmatrix}$$

$$F_{V2}=\frac{3}{2}\begin{bmatrix}k_{Pp2} & 0\\ 0 & -k_{Qp2}\end{bmatrix}\begin{bmatrix}-V_{d2} & -V_{q2} & -I_{d2} & -I_{q2}\\ -V_{q2} & +V_{d2} & +I_{q2} & -I_{d2}\end{bmatrix} \quad E_{\gamma 2}=\begin{bmatrix}1 & 0\\ 0 & 1\end{bmatrix} \quad E_{C2}=\begin{bmatrix}-1 & 0\\ 0 & -1\end{bmatrix}$$

$$E_{S2}=\frac{3}{2}\begin{bmatrix}-V_{d2}k_{Pp2}-\frac{2}{3} & -V_{q2}k_{Pp2} & -I_{d2}k_{Pp2} & -I_{q2}k_{Pp2}\\ V_{q2}k_{Qp2} & -V_{d2}k_{Qp2}-\frac{2}{3} & -I_{q2}k_{Qp2} & I_{d2}k_{Qp2}\end{bmatrix} \quad F_{C2}=\frac{L_2}{V_{dc2}}\begin{bmatrix}-I_{q2}\\ I_{d2}\end{bmatrix}$$

$$A_{D2}=\frac{1}{V_{dc2}}\begin{bmatrix}-k_{idp2} & -\omega_2 L_2 & 1 & 0\\ \omega_2 L_2 & -k_{iqp2} & 0 & 1\end{bmatrix} \quad A_{C2}=\frac{1}{V_{dc2}}\begin{bmatrix}k_{idi2} & 0\\ 0 & k_{iqi2}\end{bmatrix} \quad J_{C2}=\frac{1}{V_{dc2}}\begin{bmatrix}k_{idp2} & 0\\ 0 & k_{iqp2}\end{bmatrix}$$

Load at PCC:

$$\frac{d}{dt}\begin{bmatrix}\tilde{i}_{LOAD\_d}\\ \tilde{i}_{LOAD\_q}\end{bmatrix}=\begin{bmatrix}\frac{1}{L_{LOAD}} & 0\\ 0 & \frac{1}{L_{LOAD}}\end{bmatrix}\begin{bmatrix}\tilde{v}_d^{PCC}\\ \tilde{v}_q^{PCC}\end{bmatrix}+\begin{bmatrix}\frac{-R_{LOAD}}{L_{LOAD}} & \omega\\ -\omega & \frac{-R_{LOAD}}{L_{LOAD}}\end{bmatrix}\begin{bmatrix}\tilde{i}_{LOAD\_d}\\ \tilde{i}_{LOAD\_q}\end{bmatrix} \quad (3\text{-}82)$$
$$+\begin{bmatrix}I_{LOAD\_q}\\ I_{LOAD\_d}\end{bmatrix}\tilde{\omega}$$

Then, *d-q* axis voltages at PCC are derived, for a network with *i* inverters:

$$\begin{bmatrix}\tilde{v}_d^{PCC}\\ \tilde{v}_q^{PCC}\end{bmatrix}=A_{PCC,2\times 25}[\tilde{x}] \quad (3\text{-}83)$$

where:

$$A_{PCC,2\times 25}[\tilde{x}]=\begin{bmatrix}A_{PCC1} & A_{PCC2}\end{bmatrix}[\tilde{x}]$$

$$A_{PCC1}=J_{PCC}^{-1}\begin{bmatrix}0_{2\times 2} & A_{PCCV1} & 0_{2\times 2} & A_{PCCI1} & 0_{2\times 4}\end{bmatrix}$$
$$A_{PCC2}=J_{PCC}^{-1}\begin{bmatrix}0_{2\times 2} & A_{PCCV2} & 0_{2\times 2} & A_{PCCI2} & 0_{2\times 5}\end{bmatrix}$$

$$J_{PPC}=\begin{bmatrix}\frac{1}{L_{LOAD}}+\frac{1}{L_{line,i}}+\cdots+\frac{1}{L_{line,i}} & 0\\ 0 & \frac{1}{L_{LOAD}}+\frac{1}{L_{line,i}}+\cdots+\frac{1}{L_{line,i}}\end{bmatrix} \quad A_{PCC,Vi}=\begin{bmatrix}\frac{1}{L_{line,i}} & 0\\ 0 & \frac{1}{L_{line,i}}\end{bmatrix}$$

$$A_{PCC,Ii}=\begin{bmatrix}\frac{-R_{line,i}}{L_{line,i}}+\frac{R_{LOAD}}{L_{LOAD}} & 0\\ 0 & \frac{-R_{line,i}}{L_{line,i}}+\frac{R_{LOAD}}{L_{LOAD}}\end{bmatrix} \quad A_{LOAD}=-\begin{bmatrix}\frac{-R_{LOAD}}{L_{LOAD}} & \omega\\ -\omega & \frac{-R_{LOAD}}{L_{LOAD}}\end{bmatrix}$$

Based on those equations, the result is the complete system:

$$\frac{d}{dt}[\tilde{x}]=$$
$$\begin{bmatrix} A_1 + B_{a1}D_{D1} + B_{b1}A_{PCC1} & (F_{b1} + B_{a1}F_{C1})A_{\omega 2} \\ 0 & A_2 + B_{a2}D_{D2} + (F_{b2} + B_{a2}F_{C2} - k_2(B_{a2}D_{P2} + B_{ra2}))A_{\omega 2} + B_{b2}A_{PCC2} \end{bmatrix} \begin{bmatrix} \tilde{x}^{DG1} \\ \tilde{x}^{DG2} \end{bmatrix}$$
$$+ \begin{bmatrix} B_{a1}D_{P1} + B_{ra1} & B_{a1}D_{V1} + B_{rb1} & 0 \\ 0 & 0 & B_{a2}D_{V2} + B_{rb2} \end{bmatrix} \begin{bmatrix} \tilde{v}_{d\_ref1} \\ \tilde{v}_{q\_ref1} \\ \tilde{Q}_{\_ref2} \end{bmatrix} + \begin{bmatrix} F_{a1} & 0 \\ 0 & F_{a2} \end{bmatrix} \begin{bmatrix} \tilde{v}_{dc1} \\ \tilde{v}_{dc2} \end{bmatrix}$$

(3-84)

where:

$$\tilde{x}^{DG1} = \begin{bmatrix} \tilde{i}_{d1} & \tilde{i}_{q1} & \tilde{v}_{d1} & \tilde{v}_{q1} & \tilde{i}_{load\_d1} & \tilde{i}_{load\_q1} & \tilde{i}_{line\_d1} & \tilde{i}_{line\_q1} & \tilde{\phi}_{d1} & \tilde{\phi}_{q1} & \tilde{\gamma}_{d1} & \tilde{\gamma}_{q1} \end{bmatrix},$$

$$\tilde{x}^{DG2} = \begin{bmatrix} \tilde{i}_{d2} & \tilde{i}_{q2} & \tilde{v}_{d2} & \tilde{v}_{q2} & \tilde{i}_{load\_d2} & \tilde{i}_{load\_q2} & \tilde{i}_{line\_d2} & \tilde{i}_{line\_q2} & \tilde{\phi}_{d2} & \tilde{\phi}_{q2} & \tilde{\gamma}_{d2} & \tilde{\gamma}_{q2} & \tilde{\mu}_2 \end{bmatrix}.$$

The system order is 25. This small-signal model of a parallel-connected power inverter system is a general system, which can easily be expanded to larger systems with more than two inverters and with more control strategies. The system parameters and control parameters are given in Table 3-3 and Table 3-4. The steady state operating points are given in Table 3-5. Eigenvalues which are close to the imaginary axis are more relevant.

Thus the selection is of eigenvalues whose real part is larger than -3500, shown in Fig. 3-38. All the eigenvalues are given in Table 3-6.

TABLE 3-3. PARAMETERS OF THE SYSTEM

Parameter	Value	Parameter	Value
L1(H)	0.66e-3	L2 (H)	0.66e-3
RL1(Ω)	0.15	RL2 Ω)	0.15
C1 (F)	120e-6	C2 (F)	120e-6
Lline1 (H)	5.3e-4	Lline2 (H)	5.3e-4
Rline1 (Ω)	0.01	Rline2 (Ω)	0.01
Llload1 (H)	2.65e-4	Llload2 (H)	2.65e-4
Rlload1 (Ω)	10	Rlload2 (Ω)	10
LLOAD (H)	1e-4	RLOAD (Ω)	1

TABLE 3-4. CONTROLLER PARAMETERS

Parameter	Value	Parameter	Value
Kdp1	2	Kpp2	0.01
Kdi1	200	Kpi2	1.5
Kqp1	2	Kqp2	0.01
Kqi1	200	Kqi2	1.3
Kidp1	0.6	Kidp2	1
Kidi1	20	Kidi2	100
Kiqp1	0.3	Kiqp2	1
Kiqi1	80	Kiqi2	100
Kp	0.1	Ki	200
K	500		

TABLE 3-5. STEADY STATE OPERATING POINTS OF THE NETWORK SYSTEM

Parameter	Value	Parameter	Value
Vd1(V)	170	Vd2	172.6
Vq1(V)	0	Vq2	0
Id1(A)	100.33	Id2	101.25
Iq1(A)	9.0256	Iq2	-3.8619
Iline_d1(A)	83.334	Iline_d2	83.99
Iline_q1(A)	-4.903	Iline_q2	-18.005
Ilload_d1(A)	16.998	Ilload_d2	17.261
Ilload_q1(A)	-0.17	Ilload_q2	-0.1726
Dd1	0.3656	Dd2	0.3775
Dq1	0.0526	Dq2	0.0492

TABLE 3-6. THE EIGENVALUES OF THE NETWORK SYSTEM

Eigenvalues $\lambda_{1\sim25}$	
-36899.41020±376.9176878*i	-36892.04165±374.7858957*i
-1006.462340±5510.244046*i	-1729.839992±5000.431513*i
-924.9257529±4530.541897*i	-5788.482238
-1194.647545	-2968.693009
-766.6715074	-253.8944524±2664.003433*i
-286.2483055	-79.86844575±82.85374323*i
-37.74045391	-98.92627989±14.24694595*i
-55.53254049	-76.30226774
-59.73556683	

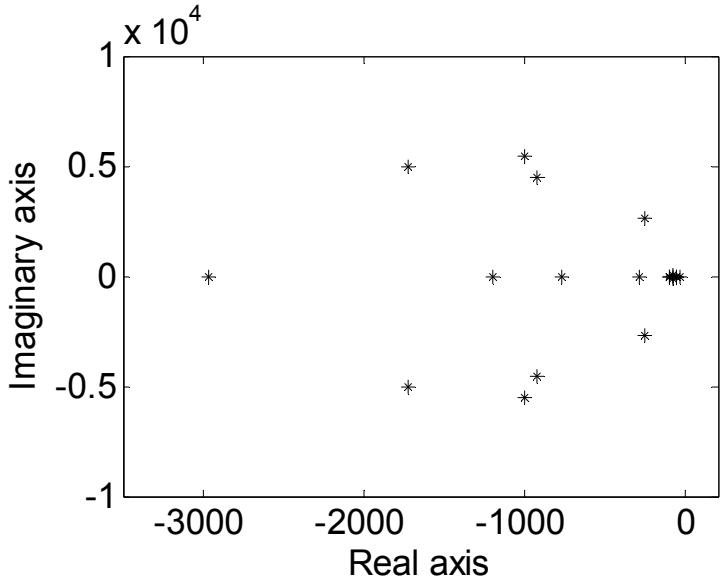

Fig. 3-38. Loci of the eigenvalues of the system.

Fig. 3-39 shows a trace of several eigenvalues of the system which are close to the imaginary axis with K increasing from 0 to 3000. The shifting of a pair of complex conjugate eigenvalues from LHP to RHP indicates that the system changes from a stable

state to an unstable state. Droop control parameter K, is an important parameter in a parallel-connected inverters system with droop control loop. Once load changes, the output power of the DG system must be changed in accordance with their droop characteristic to supply power to all critical loads.

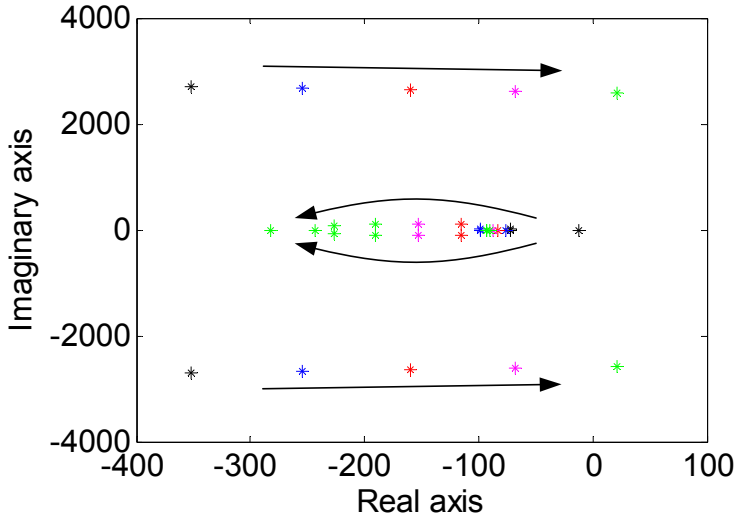

Fig. 3-39. Loci of the eigenvalues of the system with K increasing from 0 to 3000.

Simulation is carried out based on an average model of the two inverter system. One is with voltage control and the other is under PQ control. Droop control loop and PLL are used in the PQ controlled inverter. System and control parameters are listed in Table 3-3 and Table 3-4. Before 0.455s, K is 500 as listed in Table 3-4. Fig. 3-40 and Fig. 3-41 show the simulation results with different droop control parameters K. At a time of 0.455 s, K is changed to 100, 3000 or remains 500 respectively. Obviously, the system is still operating in the steady state. At a time of 0.5 s, the load resistance and inductance

decrease to 80%. When K is 3000, both the output rms voltage of inverter I and the output active power of inverter II experience large divergent oscillations.

The output rms voltage of inverter I decreases slightly and recovers to the nominal value quickly when K equals 500 and 100. When K equals 100, the output active power of inverter II increases less than when K equals 500, because of the droop frequency and active power characteristics.

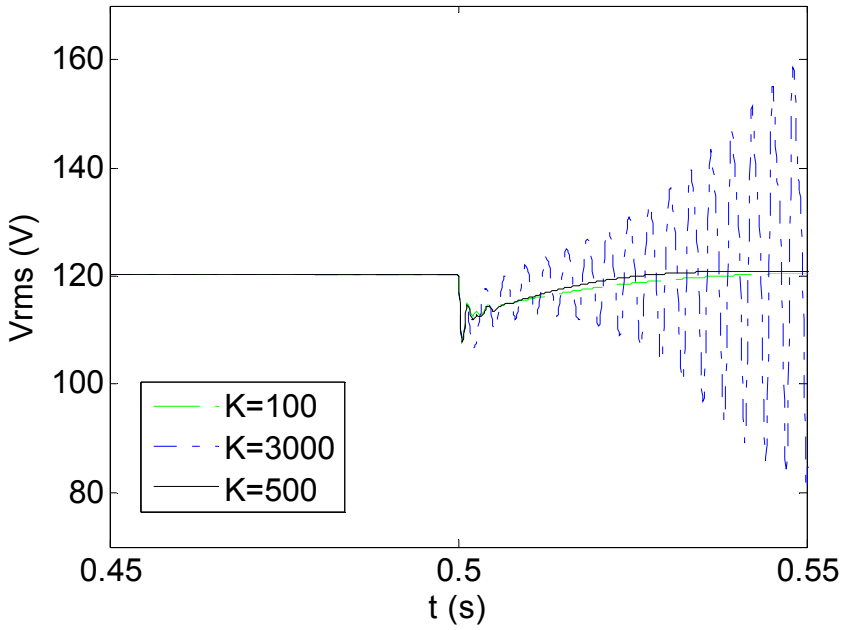

Fig. 3-40. Inverter I output Vrms value when K is selected as 100, 500 and 3000.

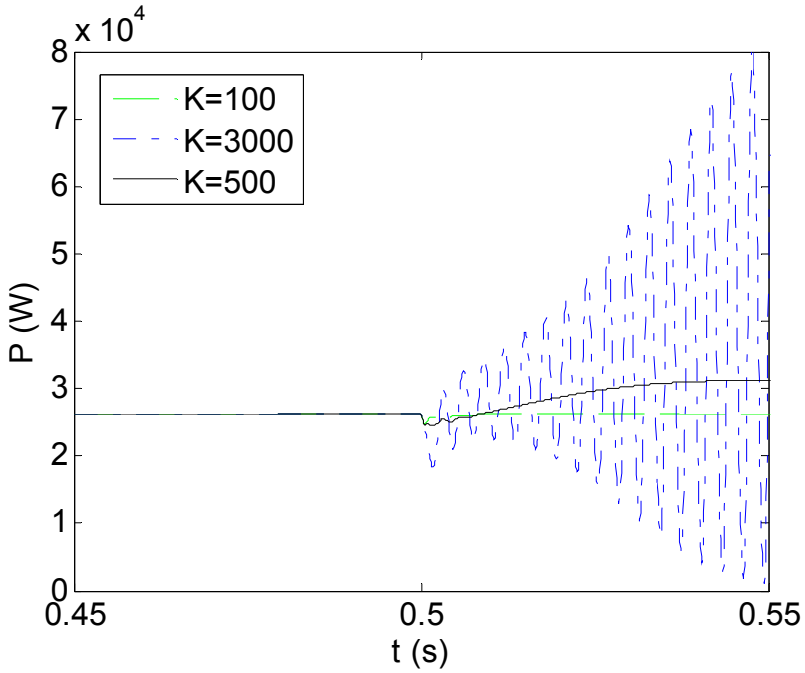

Fig. 3-41. Inverter II output active power when K is selected as 100, 500 and 3000.

3.2.2 Case Studies

A. Three Parallel Inverters in Stand-Alone Mode of Operation

The system under study consists of three local AC loads and three parallel-connected voltage source DC-AC power converters, as shown in Fig. 3-37. It includes three inverters connected to PCC, where the local load, inverters and the network are connected. Simulations are carried out based on the average model of the system. The following two scenarios are considered in this study.

In the first scenario, inverter I is under PV control. The output power reference from the inverter at the rated frequency (60Hz) is set as P_0 equals 18.7 kW. The load impedance at PCC decreases 20% at 0.5 second. The actual active power reference is

P_0+600 * (ω_0 - ω). Inverter II and inverter III are under PQ control. The actual active power reference of inverter II is P_0+300 *(ω_0 - ω). The actual active power reference of inverter III is P_0+200 *(ω_0 - ω). Their reactive power references are regulated at 1000 Var. The output voltage is regulated at 120 Vrms and the reactive power is unregulated. The simulation results are shown in Fig. 3-42-Fig. 3-44.

The three parallel inverters system works well under combined PV, PQ, and frequency droop control. The d-axis and q-axis voltage is regulated at 170 V and 0 V shown in Fig. 3-42. When the load experiences a step change at 0.5s, the output voltage of inverter I decreases slightly and recovers to the nominal value quickly. As the load resistance and inductance decrease to 80% of the rated values, the inverters have to produce the increased active power and the angular frequency of the output voltage drops by around 7 rad/s. This is shown in Fig. 3-43 and Fig. 3-44, and is a consequence of the droop control scheme. In Fig. 3-43, the output power from inverters I, II, and III are increased from around 18.7 kW, 20 kW and 20 kW to around 23.2 kW, 22.3 kW and 21.5 kW to share the increased power demand according to a predefined ratio 6:3:2. Thus, an inverter will share more increased load with a higher droop loop gain K. In addition, the reactive power of inverters II and III are held constant at 1000 Var, while the reactive power from inverter I undergoes a rapid increase to cover the load demand change.

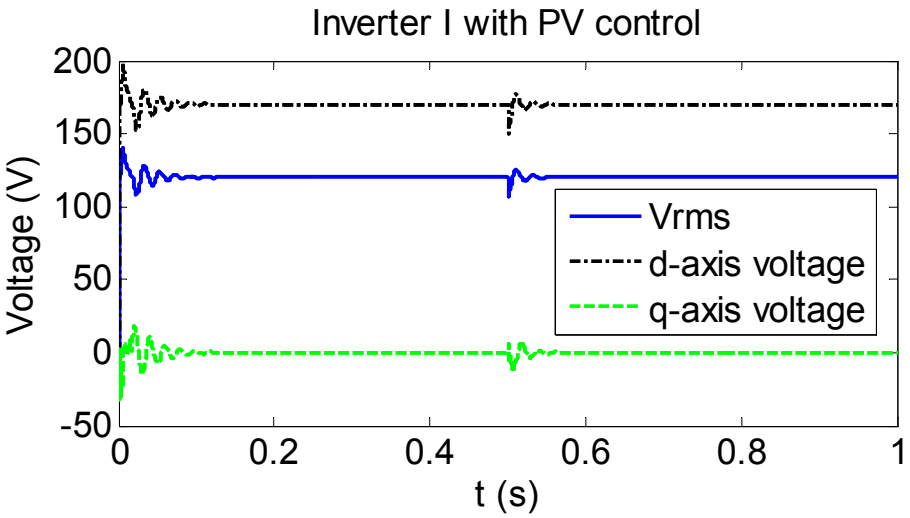

Fig. 3-42. Voltages of inverter I.

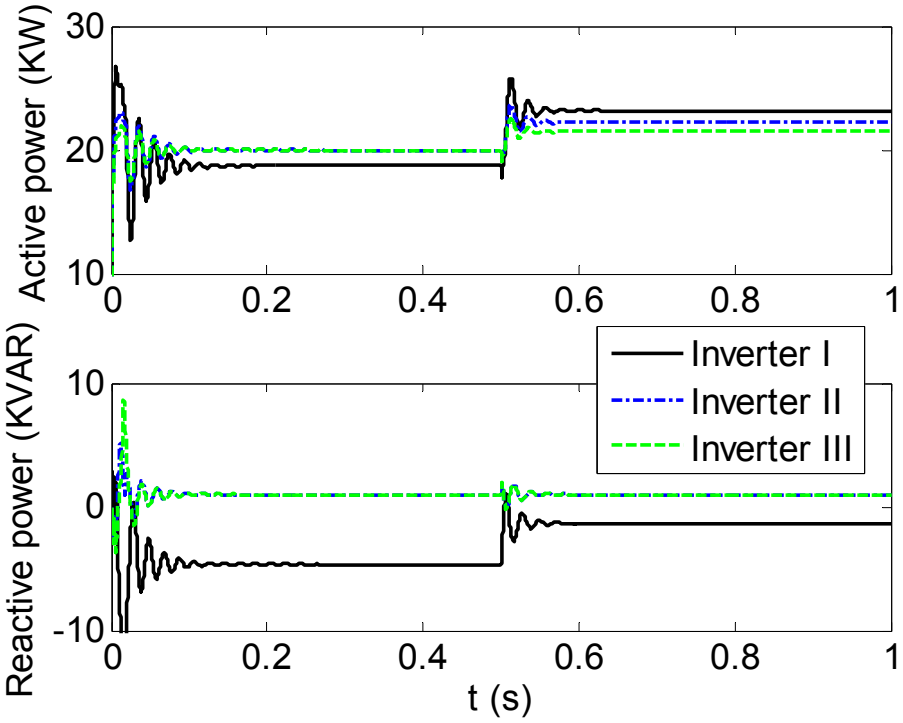

Fig. 3-43. Active and reactive power of three inverters.

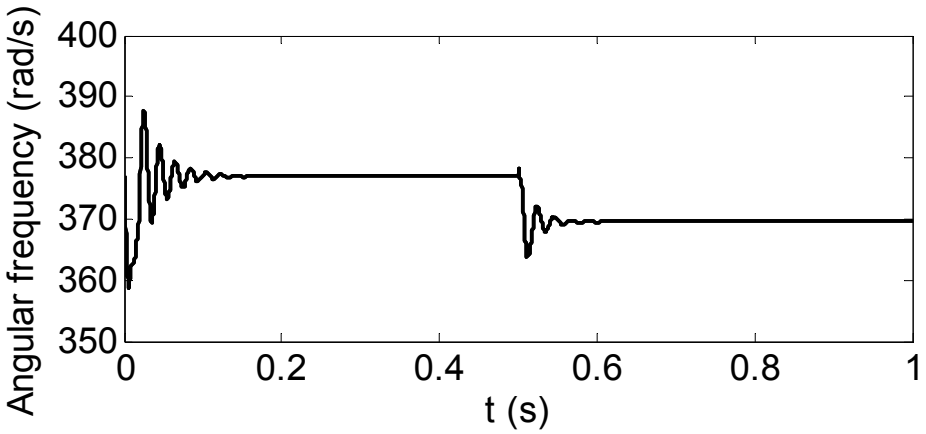

Fig. 3-44. Angular frequency.

In the second scenario, inverter I is under voltage control. The d-axis voltage is regulated at 170 V and q-axis voltage is regulated at 0 V. Inverter II and inverter III are under PQ control. The actual active power references and reactive power references of inverter II and III are P_0+500*(ω_0 - ω) and 1000 Var. The simulation results are shown is Fig. 3-45-Fig. 3-47.

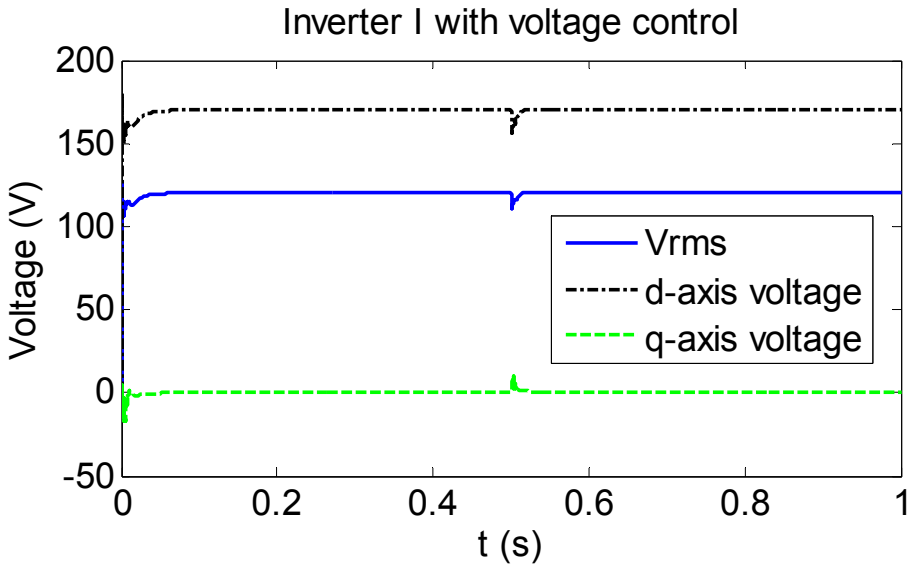

Fig. 3-45. Voltages of inverter I.

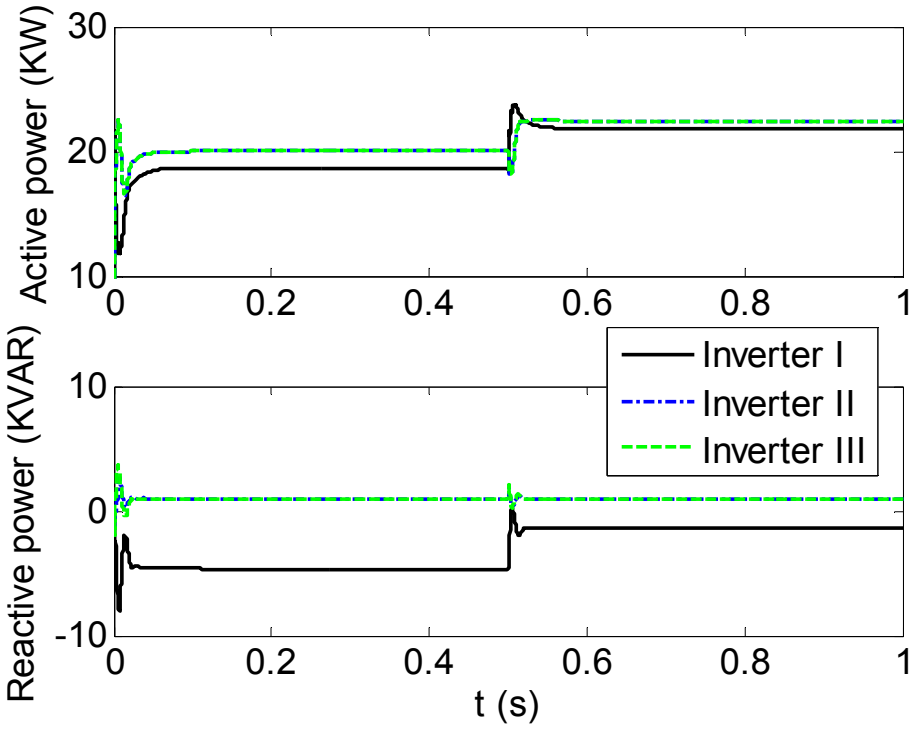

Fig. 3-46. Active and reactive power of three inverters.

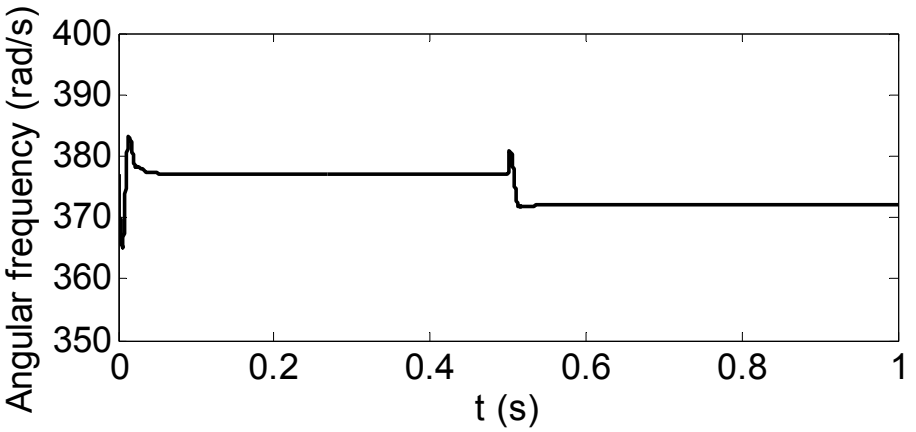

Fig. 3-47. Angular frequency.

The three parallel inverters system works well under combined Voltage, PQ, and frequency droop control. In Fig. 3-45, when the load experiences a step change at 0.5s, the output voltage of inverter I decreases slightly and recovers to the nominal value quickly. In Fig. 3-46, the output powers from inverter I, II and III are increased from

around 18.7 kW, 20 kW and 20 kW to around 21.8 kW, 22.5 kW and 22.5 kW to share the increased power demand. The reactive power from inverters II and III is maintained constant at 1000 Var after a slight disturbance, while the reactive power from inverter I undergoes a rapid increase to compensate for the load change. As the load resistance and inductance decrease to 80% of the rated values, the inverters have to produce the increased active power, and the angular frequency of the output voltage drops by around 5 rad/s shown in Fig. 3-47. Thus, the simulation results show increased output power from inverters will be the same if they use the same value of K.

B. Two Parallel Inverters in Grid-Connected Mode and Stand-Alone Mode

A simulation study of two parallel-connected inverters system[103] is carried out in MATLAB/Simulink/SimPowerSystems platform, as shown in Fig. 3-48. The AC bus voltage rms value is 110 V. At 0.15 s, the grid disconnects from the inverter system and the load decreases from 118 kW to 98 kW. At a time of 0.5 s, the grid reconnects with the inverter system. At 0.6 s the load increases to the beginning level. In the grid-connected mode, two inverters are under PQ control. Once contingency occurs, they are switched to stand-alone (islanded) operation. Once islanded, inverter I is changed to use voltage control while inverter II is still under PQ control.

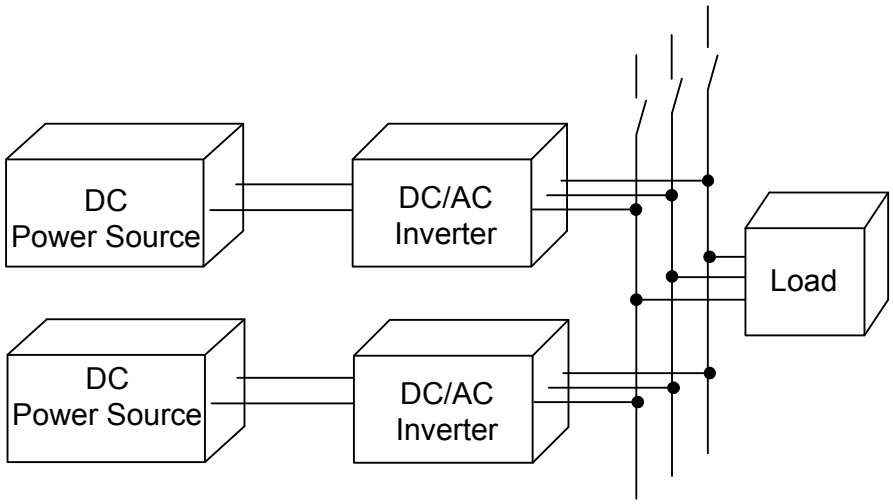

Fig. 3-48. Parallel-connected inverters in grid-connected mode and stand-alone mode.

Fig. 3-49 shows output active and reactive power from the grid. Fig. 3-50 and Fig. 3-51 show output active and reactive power from two parallel-connected power inverters. Initially, the grid provides 58 kW active power and 17 kVar reactive power. Meanwhile, two inverters under PQ control provide 20 kW and 40 kW active power and 3 kVar and 10 kVar reactive power. At 0.15 s, the output active and reactive power from the grid decrease to zero, because the grid disconnects with the inverter system. Inverter I switches to voltage control to maintain bus voltage and provide extra load demand. The active power and reactive power from inverter I increase to 58 kW and 17 kVar. At a time of 0.5 s, the grid active and reactive power increase to 38 kW and 10 kVar when the grid reconnects with the inverter system. Meanwhile, inverter I switches back to PQ controller and provides constant active and reactive power of 20 kW and 3 kVar. At 0.6 s, the output active and reactive power from the grid return to 58 kW and 17 kVar because the load

return to the beginning value. Inverter I still provides constant active and reactive power. Inverter II provides constant active and reactive power of 40 kW and 10 kVar at all times.

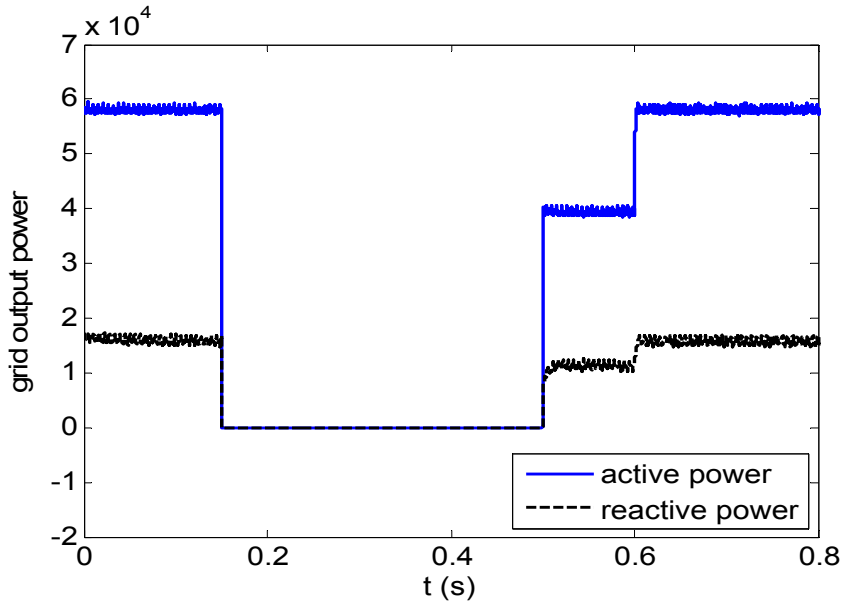

Fig. 3-49. Output active and reactive power from grid.

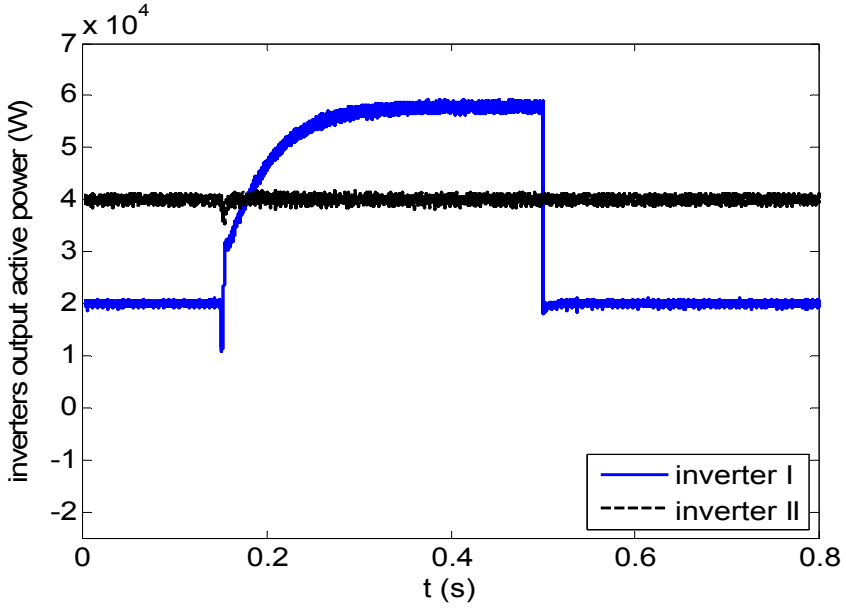

Fig. 3-50. Output active power from inverters I and II.

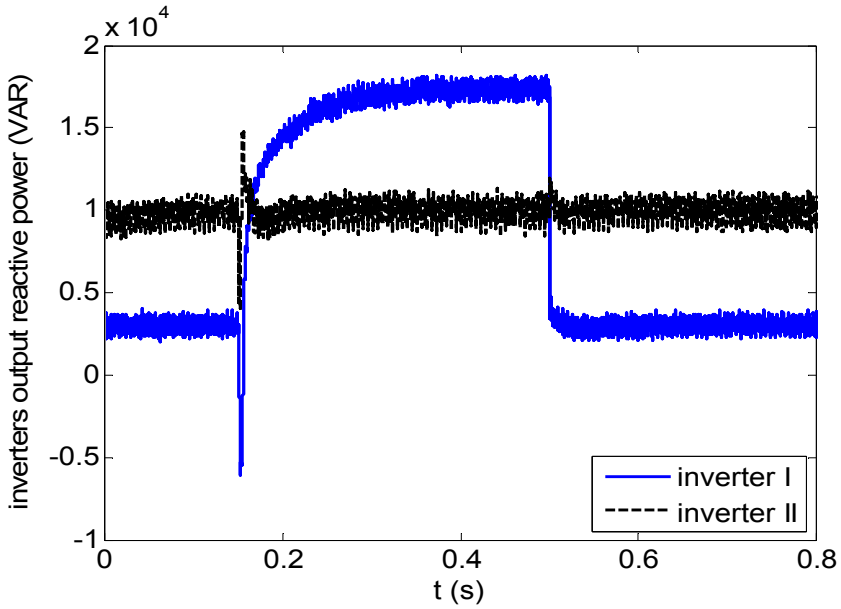

Fig. 3-51. Output reactive power from inverters I and II.

Fig. 3-52 and Fig. 3-53 show d-axis, q-axis and rms voltages. Both rms voltages in Fig. 3-52 and Fig. 3-53 are 110 V before 0.25 s, but the voltages decrease after being islanded and gradually return to 110 V because of the voltage regulation of inverter I. A transient drop in d-axis voltage is caused by a huge drop in output active power when inverter I switches from voltage control to PQ control. Fig. 3-54 shows three-phase line-line voltages of inverter I. Fig. 3-54-a shows the voltages drop at 0.25 and reach references about 270 V after a short time, about 0.15 s. Fig. 3-54-b shows there are only small disturbances at 0.5 s and at 0.6 s there are no disturbances because bus voltage is fixed by the stiff grid. Bus voltage is well maintained in stand-alone mode and in the transient process.

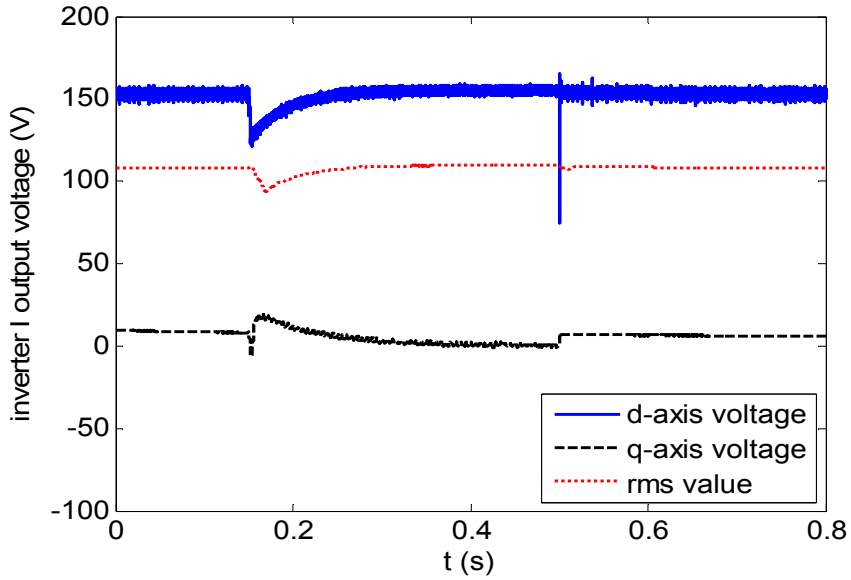

Fig. 3-52. Inverter I output voltages.

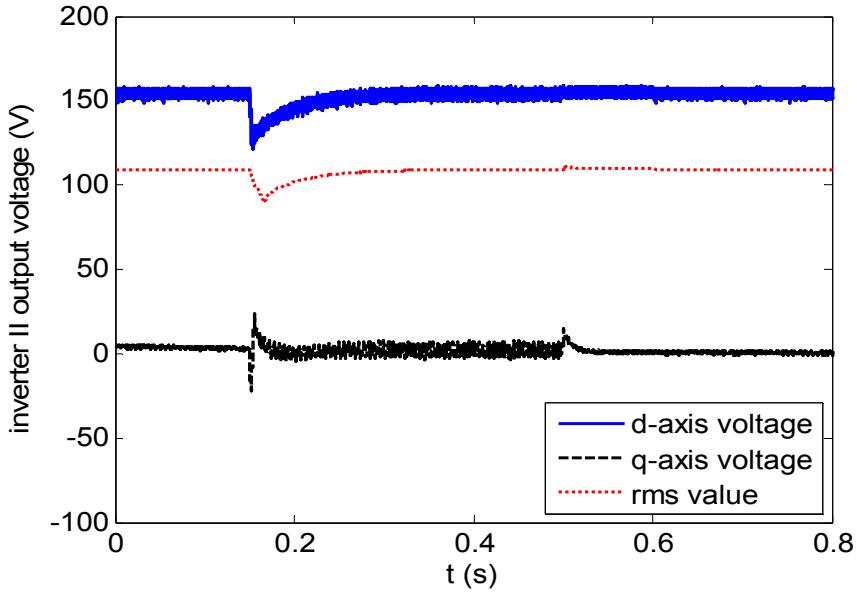

Fig. 3-53. Inverter II output voltages.

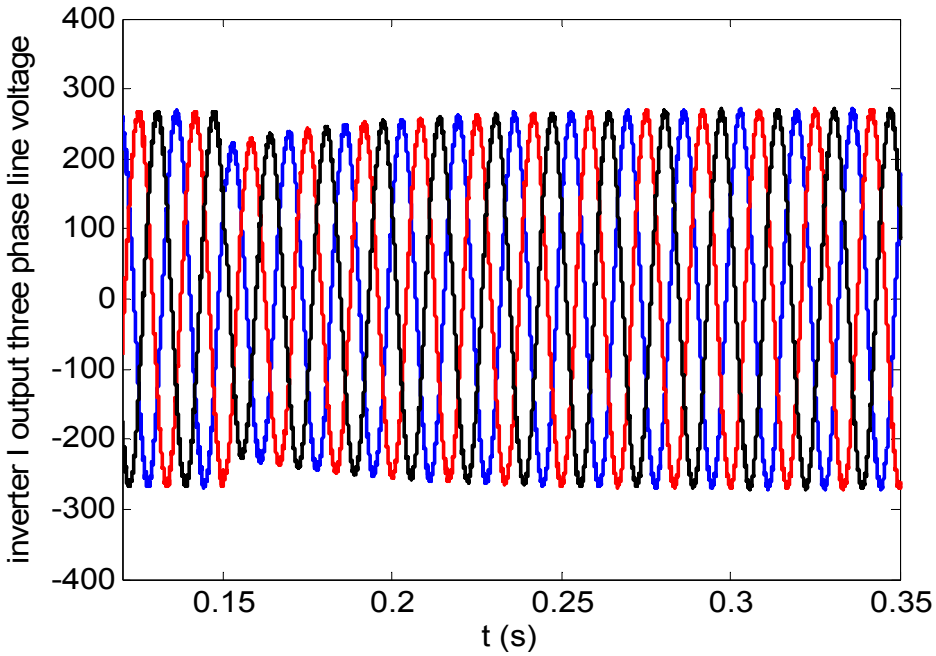

(a) grid-connected switch mode to stand-alone mode

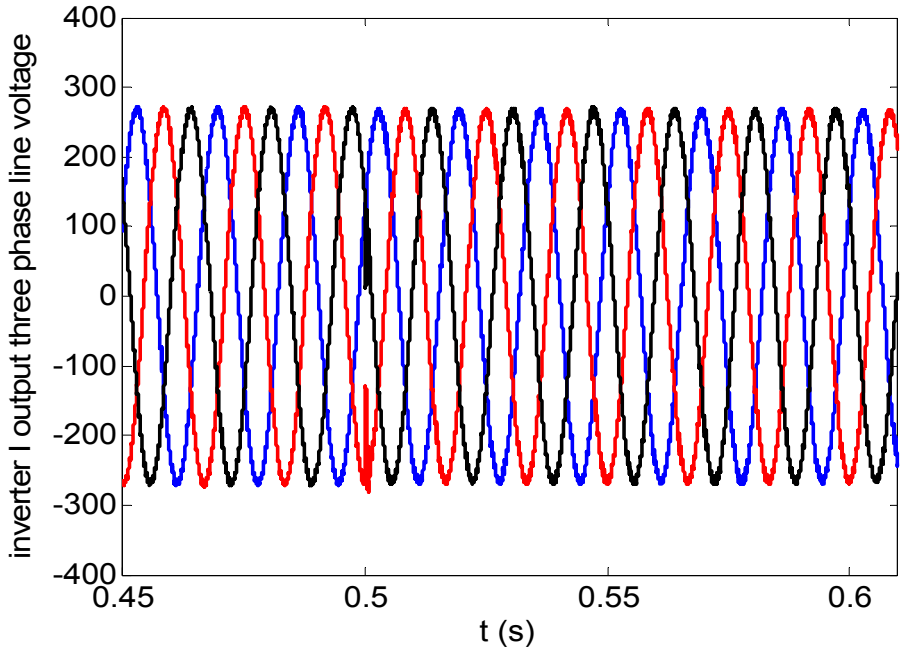

(b) stand-alone mode switch to grid-connected mode

Fig. 3-54. Inverter I output three-phase line-line voltages.

3.3 Parallel Connected DC-AC Space Vector Pulse Width Modulation (SVPWM) Inverters Shared with the Same DC Power Supply

There are several possible structures of three-phase power converter parallel connection. One possibility is to connect the AC sides of power converters together and have different DC-side inputs, which is similar to using separate power supplies. This approach is useful for distributed power systems. Another possibility is to connect both sides of the power converters together, as shown in Fig. 3-55. This approach enables higher power to be shared by a set of power converters and can also achieve different goals such as voltage and power regulation. With this approach, the open-circuit zero-sequence channel of each three-phase power converter is connected together, and a path for the circulating current is then created. Therefore, there are potential zero-sequence currents circulating among the parallel converters.

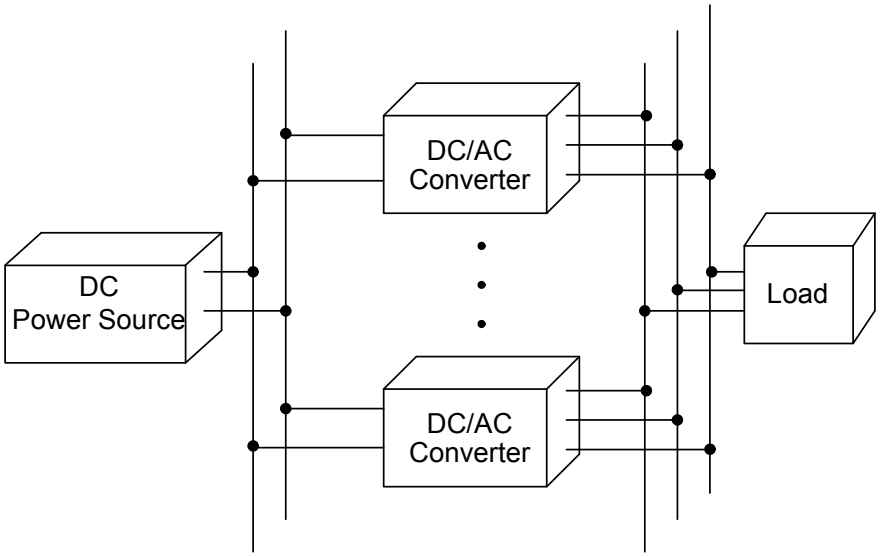

Fig. 3-55. Parallel-connected inverters shared with a DC source.

$$\frac{d}{dt}\begin{bmatrix} i_{d1} \\ i_{q1} \end{bmatrix} = \frac{1}{L_1}\begin{bmatrix} d_{d1} \\ d_{q1} \end{bmatrix} \cdot v_{dc1} - \frac{1}{L_1}\begin{bmatrix} v_d \\ v_q \end{bmatrix} - \begin{bmatrix} 0 & -\omega_1 \\ \omega_1 & 0 \end{bmatrix}\begin{bmatrix} i_{d1} \\ i_{q1} \end{bmatrix} \tag{3-85}$$

$$\frac{d}{dt}\begin{bmatrix} i_{d2} \\ i_{q2} \end{bmatrix} = \frac{1}{L_1}\begin{bmatrix} d_{d2} \\ d_{q2} \end{bmatrix} \cdot v_{dc2} - \frac{1}{L_1}\begin{bmatrix} v_d \\ v_q \end{bmatrix} - \begin{bmatrix} 0 & -\omega_2 \\ \omega_2 & 0 \end{bmatrix}\begin{bmatrix} i_{d2} \\ i_{q2} \end{bmatrix} \tag{3-86}$$

$$\frac{d}{dt} i_z = \frac{v_{dc}}{L_1 + L_2}(d_{z1} - d_{z2}) \tag{3-87}$$

$$\frac{d}{dt}\begin{bmatrix} v_d \\ v_q \\ v_z \end{bmatrix} = \frac{1}{2C}\left(\begin{bmatrix} i_{d1} \\ i_{q1} \\ i_z \end{bmatrix} + \begin{bmatrix} i_{d2} \\ i_{q2} \\ -i_z \end{bmatrix}\right)$$

$$-\frac{1}{2}\begin{bmatrix} \frac{1}{C}\left(\frac{1}{R_1} + \frac{1}{R_2}\right) & -(\omega_1 + \omega_2) & 0 \\ \omega_1 + \omega_2 & \frac{1}{2C}\left(\frac{1}{R_1} + \frac{1}{R_2}\right) & 0 \\ 0 & 0 & \frac{1}{2C}\left(\frac{1}{R_1} + \frac{1}{R_2}\right) \end{bmatrix}\begin{bmatrix} v_d \\ v_q \\ v_z \end{bmatrix} \tag{3-88}$$

Assuming ω is constant, the small-signal model is represented by Eqs. (3-89)- (3-92) and shown in Fig. 3-56.

$$\frac{d}{dt}\begin{bmatrix}\tilde{i}_{d1}\\ \tilde{i}_{q1}\end{bmatrix}=\frac{1}{L_1}\left(\begin{bmatrix}\tilde{d}_{d1}\\ \tilde{d}_{q1}\end{bmatrix}\cdot V_{dc1}+\begin{bmatrix}D_{d1}\\ D_{q1}\end{bmatrix}\cdot\tilde{v}_{dc1}\right)-\frac{1}{L_1}\begin{bmatrix}\tilde{v}_d\\ \tilde{v}_q\end{bmatrix}-\begin{bmatrix}0 & -\omega_1\\ \omega_1 & 0\end{bmatrix}\begin{bmatrix}\tilde{i}_{d1}\\ \tilde{i}_{q1}\end{bmatrix} \tag{3-89}$$

$$\frac{d}{dt}\begin{bmatrix}\tilde{i}_{d2}\\ \tilde{i}_{q2}\end{bmatrix}=\frac{1}{L_2}\left(\begin{bmatrix}\tilde{d}_{d2}\\ \tilde{d}_{q2}\end{bmatrix}\cdot V_{dc2}+\begin{bmatrix}D_{d2}\\ D_{q2}\end{bmatrix}\cdot\tilde{v}_{dc2}\right)-\frac{1}{L_2}\begin{bmatrix}\tilde{v}_d\\ \tilde{v}_q\end{bmatrix}-\begin{bmatrix}0 & -\omega_2\\ \omega_2 & 0\end{bmatrix}\begin{bmatrix}\tilde{i}_{d2}\\ \tilde{i}_{q2}\end{bmatrix} \tag{3-90}$$

$$\frac{d}{dt}\tilde{i}_z=\frac{V_{dc}}{L_1+L_2}(d_{z1}-d_{z2})+\frac{D_{z1}-D_{z2}}{L_1+L_2}\tilde{v}_{dc} \tag{3-91}$$

$$\frac{d}{dt}\begin{bmatrix}\tilde{v}_d\\ \tilde{v}_q\\ \tilde{v}_z\end{bmatrix}=\frac{1}{2C}\left(\begin{bmatrix}\tilde{i}_{d1}\\ \tilde{i}_{q1}\\ \tilde{i}_z\end{bmatrix}+\begin{bmatrix}\tilde{i}_{d2}\\ \tilde{i}_{q2}\\ -\tilde{i}_z\end{bmatrix}\right)$$

$$-\frac{1}{2}\begin{bmatrix}\frac{1}{C}(\frac{1}{R_1}+\frac{1}{R_2}) & -(\omega_1+\omega_2) & 0\\ \omega_1+\omega_2 & \frac{1}{2C}(\frac{1}{R_1}+\frac{1}{R_2}) & 0\\ 0 & 0 & \frac{1}{2C}(\frac{1}{R_1}+\frac{1}{R_2})\end{bmatrix}\begin{bmatrix}\tilde{v}_d\\ \tilde{v}_q\\ \tilde{v}_z\end{bmatrix} \tag{3-92}$$

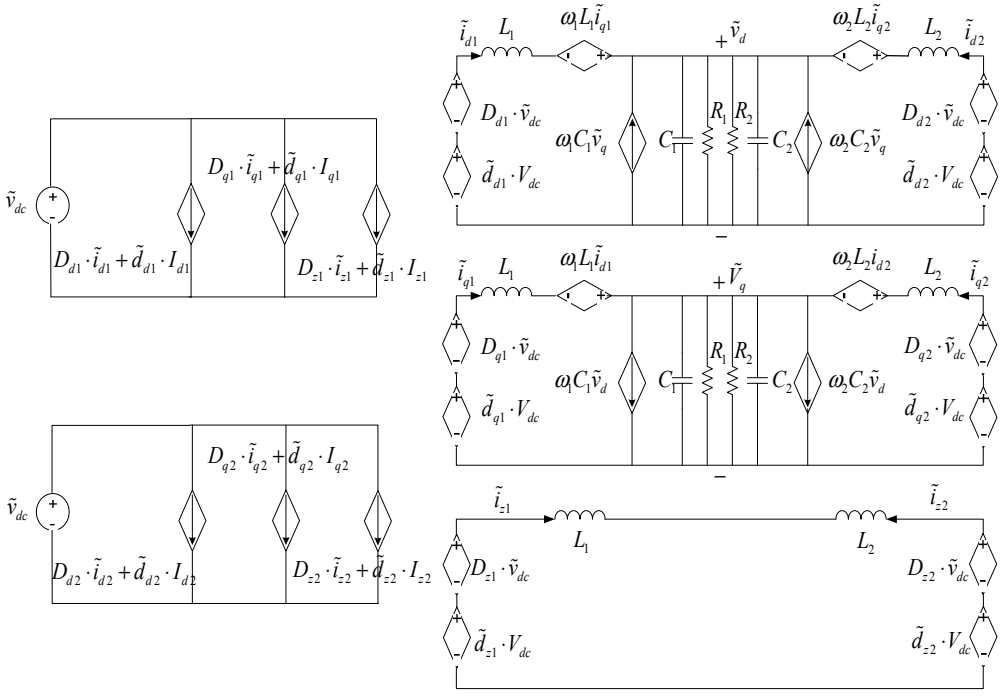

Fig. 3-56. Small-signal model of parallel voltage-source inverters.

It can be seen that a zero-sequence current is present in the z channel. The zero-sequence dynamics model of two parallel three-phase voltage inverters is shown in Fig. 3-57. So, the zero-sequence dynamics are governed by their z channels.

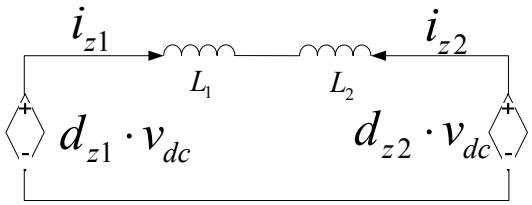

Fig. 3-57. Zero-sequence dynamics model of two parallel inverters.

The model as shown in Eqs. (3-89)-(3-92) considers as state variables the variations in the d-axis, q-axis current components of two paralleled inverters, z-axis current and d-, q-, z-axis voltage components of the AC bus voltage; takes the variations in d-, q-, z-axis duty cycles of the two power converters as the control input; and regards the variations in the DC voltage as an external disturbance. Taking the control system into account, the closed-loop zero-sequence current dynamic system can be modeled as a single-input, single-output system, as shown in Fig. 3-58.

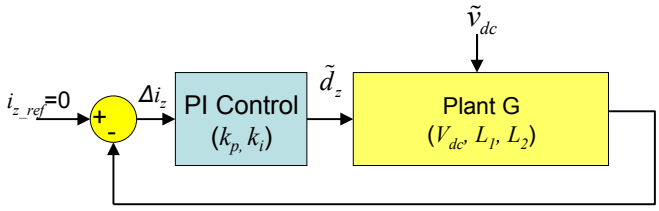

Fig. 3-58. Block diagram of the model representing the closed-loop zero-sequence dynamics of the parallel converter system.

3.3.1 Space Vector Pulse Width Modulation

Space vector (SV) pulse width modulation (PWM) technique has become a popular PWM technique for three-phase voltage-source inverters (VSI) in applications such as control of AC induction and permanent-magnet synchronous motors. This section gives an in-depth discussion of the theory and implementation of the SVPWM technique. It is also well known that the space vector PWM approach (SVPWM) is better than the sinusoidal PWM approach in utilizing the available dc-bus voltage by approximately 15%, a significant difference.

The circuit model of a typical three-phase voltage source PWM inverter is shown in Fig. 3-59.

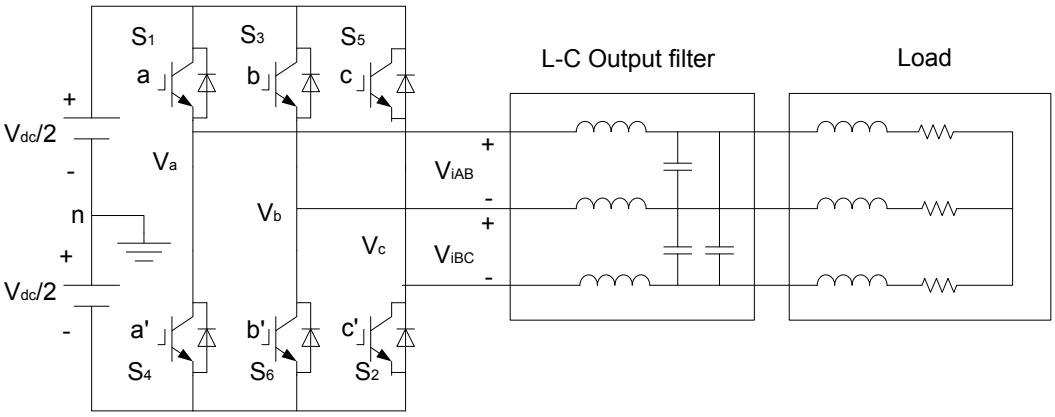

Fig. 3-59. Circuit model of three-phase PWM inverter with a center-taped grounded DC bus.

S1 to S6 are the six power switches that shape the output, which are controlled by the switching variables a, a', b, b', c and c'. When an upper transistor is switched on, i.e.

when a, b or c is 1, the corresponding lower transistor is switched off, i.e., the corresponding a', b' or c' is 0. Therefore, the on and off states of the upper transistors S1, S3 and S5 can be used to determine the output voltage.

Fig. 3-60 shows the circuit model of a single-phase inverter.

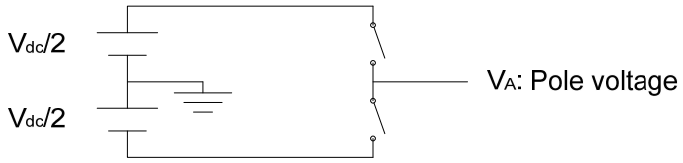

Fig. 3-60. Circuit model of a single-phase inverter.

The relationship between the switching variable vector and the line-to-line voltage vector is given in the following equation.

$$\begin{bmatrix} V_{ab} \\ V_{bc} \\ V_{ca} \end{bmatrix} = V_{dc} \begin{bmatrix} 1 & -1 & 0 \\ 0 & 1 & -1 \\ -1 & 0 & 1 \end{bmatrix} \begin{bmatrix} a \\ b \\ c \end{bmatrix} \tag{3-93}$$

Also, the relationship between the switching variable vector and the phase voltage vector can be expressed below.

$$\begin{bmatrix} V_{an} \\ V_{bn} \\ V_{cn} \end{bmatrix} = \frac{V_{dc}}{3} \begin{bmatrix} 2 & -1 & -1 \\ -1 & 2 & -1 \\ -1 & -1 & 2 \end{bmatrix} \begin{bmatrix} a \\ b \\ c \end{bmatrix} \tag{3-94}$$

There are eight possible combinations of on-off patterns for the three upper power switches. The on and off states of the lower power devices are opposite to the upper one, so are easily determined once the states of the upper power transistors are determined.

According to equations, eight switching vectors, output line to neutral voltage (phase voltage), and out put line-to-line voltages in terms of DC-link V_{dc}, are given in Table 3-7 below. Fig. 3-61 shows the eight inverter voltage vectors (V0-V7).

TABLE 3-7. SWITCHING VECTORS, PHASE VOLTAGES AND OUTPUT LINE TO LINE VOLTAGE

Voltage Vectors	Switching Vectors			Line to neutral voltage			Line to line voltage		
	a	b	c	V_{an}	V_{bn}	V_{cn}	V_{ab}	V_{bc}	V_{ca}
V_0	0	0	0	0	0	0	0	0	0
V_1	1	0	0	2/3	-1/3	-1/3	1	0	-1
V_2	1	1	0	1/3	1/3	-2/3	0	1	-1
V_3	0	1	0	-1/3	2/3	-1/3	-1	1	0
V_4	0	1	1	-2/3	1/3	1/3	-1	0	1
V_5	0	0	1	-1/3	-1/3	2/3	0	-1	1
V_6	1	0	1	1/3	-2/3	1/3	1	-1	0
V_7	1	1	1	0	0	0	0	0	0

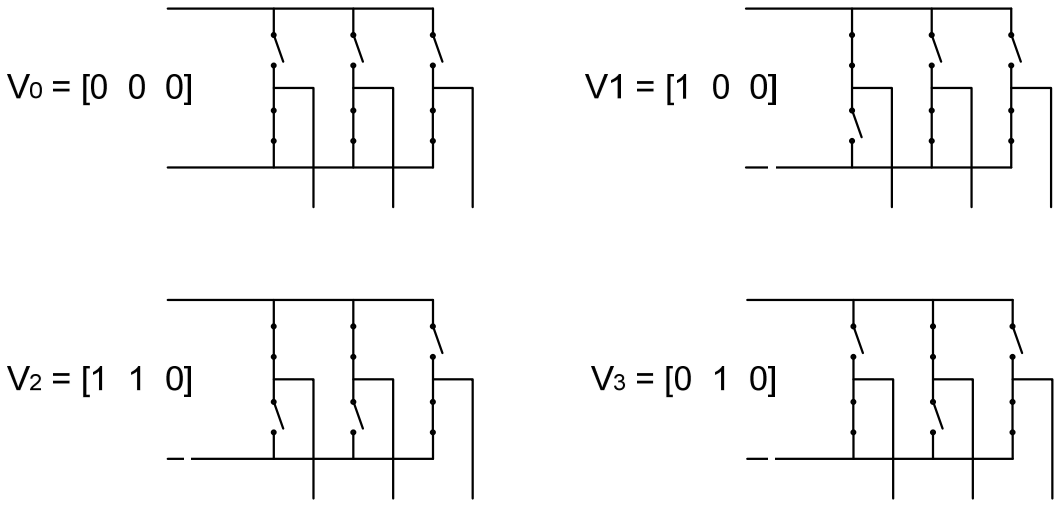

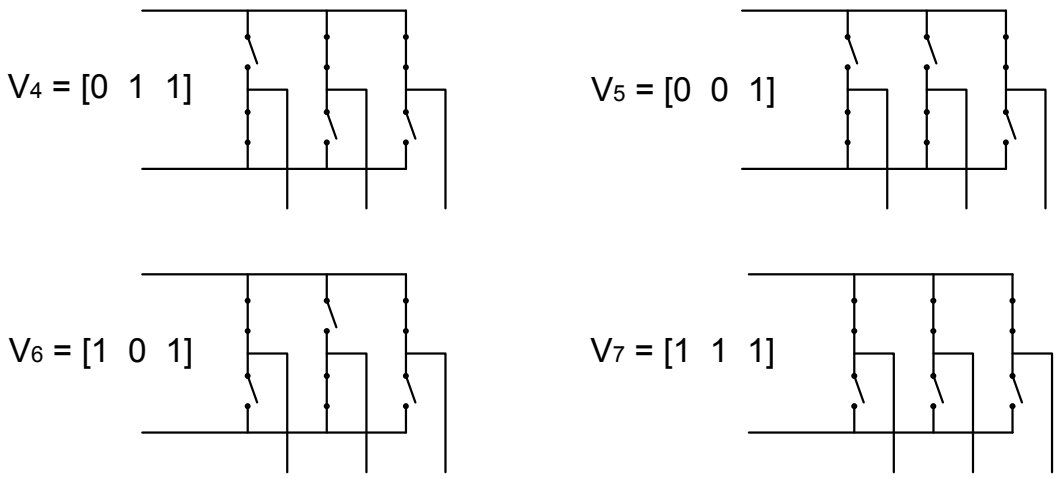

Fig. 3-61. The eight inverter voltage vectors (V0 to V7).

To implement the space vector PWM, the voltage equations in the *abc* reference frame can be transformed into the stationary *d-q* reference frame that consists of the horizontal (*d*) and vertical (*q*) axes as depicted in Fig. 3-62.

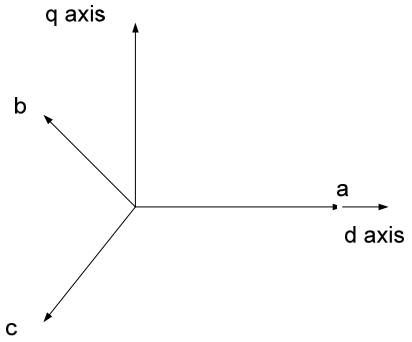

Fig. 3-62. The relationship of *abc* reference frame and stationary *d-q* reference frame.

The vector representations of the phase voltages corresponding to the eight combinations can be obtained by applying the following so-called *d-q* transformation to the phase voltages.

This transformation is equivalent to an orthogonal projection of [a, b, c] onto the two dimensional plane perpendicular to the vector [1, 1, 1] in a three-dimensional coordinate

system, the results of which are six non-zero vectors and two zero vectors. The nonzero vectors form the axes of a hexagonal. The angle between any adjacent two non-zero vectors is 60 degrees. The zero vectors are at the origin and apply zero voltage to a three-phase load. The eight vectors are called the Basic Space Vectors and are denoted here by V0, V1, V2, V3, V4, V5, V6, and V7.

The same *d-q* transformation can be applied to a desired three-phase voltage output to obtain a desired reference voltage vector Vref in the *d-q* plane as shown in Fig. 3-63. Note that the magnitude of Vref is the rms value of the corresponding line-to-line voltage with the defined *d-q* transform.

Therefore, space vector PWM can be implemented by the following steps: Determine Vd, Vq, Vref and the angle; Determine time duration T1, T2, T0; Determine the switching time of each transistor (S1 to S6).

The objective of SVPWM technique is to approximate the reference voltage Vref instantaneously by combination of the switching states corresponding to the basic space vectors. One way to achieve this is to require, for any small period of time T, the average inverter output be the same as the average reference voltage Vref.

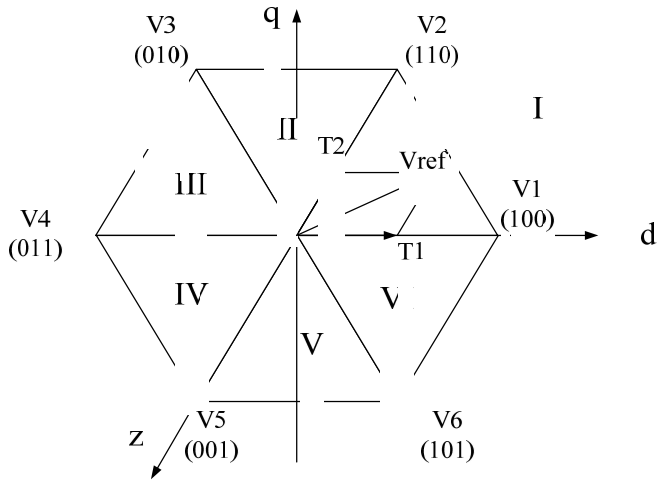

Fig. 3-63. Basic switching vectors and sectors.

The concept of voltage vectors and the methods of space vector pulse width modulation have been studied for many years. The well-defined voltage sectors are shown in Fig. 3-61. In the SVPWM scheme, the time durations for 3 adjacent voltage vectors are given in (3-95).

$$\begin{aligned} T_1 &= T_z M \frac{\sqrt{3}}{2} \sin(\frac{n\pi}{3} - \alpha) \\ T_2 &= T_z M \frac{\sqrt{3}}{2} \sin(\alpha - \frac{n-1}{3}\pi) \\ T_0 &= T_z - T_1 - T_2 \end{aligned} \tag{3-95}$$

where n= 1 through 6, for Sectors 1 to 6.

Therefore, the duty cycles of the non-zero and zero vectors may be written as:

$$\begin{aligned} d_1 &= M \frac{\sqrt{3}}{2} \sin(\frac{n\pi}{3} - \alpha) \\ d_2 &= M \frac{\sqrt{3}}{2} \sin(\alpha - \frac{n-1}{3}\pi) \\ d_0 &= 1 - d_1 - d_2 \end{aligned} \tag{3-96}$$

VTB schematic view of the SVPWM inverter is shown in Fig. 3-64.

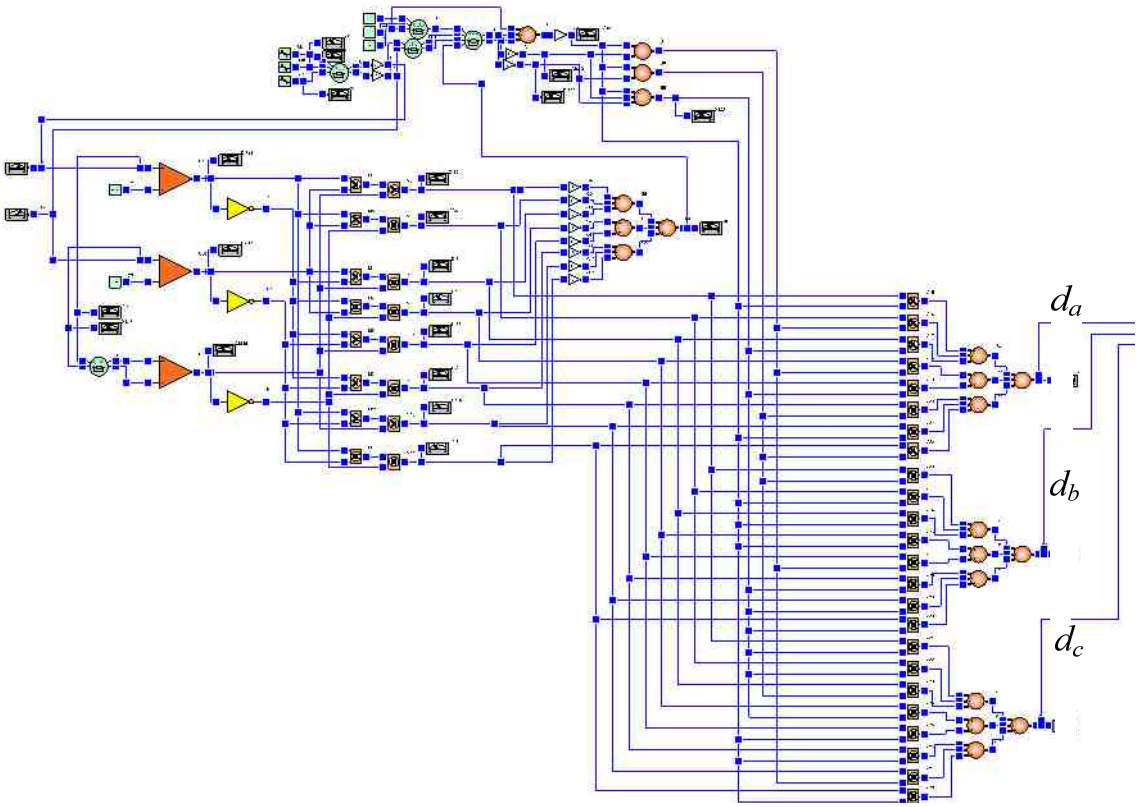

(a) Generation of three-phase duty cycles

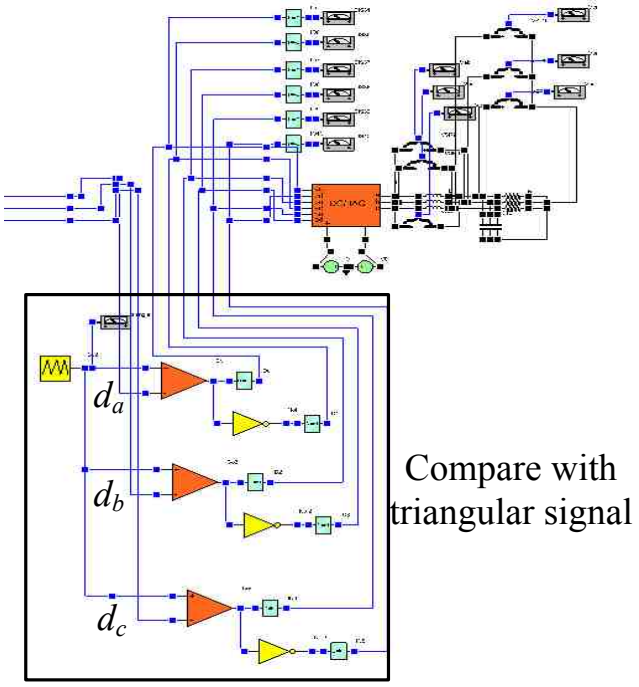

(b) Duty cycles compared with a triangular signal to control switches of the inverter

Fig. 3-64. VTB schematic view of the SVPWM inverter.

Simulation results are shown in Fig. 3-65-Fig. 3-70.

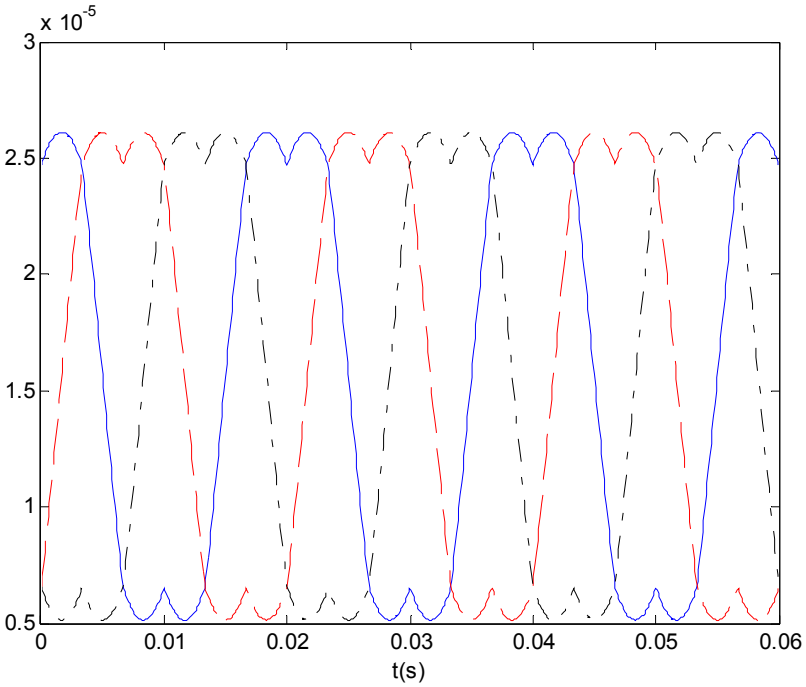

Fig. 3-65. VTB simulation results of three-phase carrier waves.

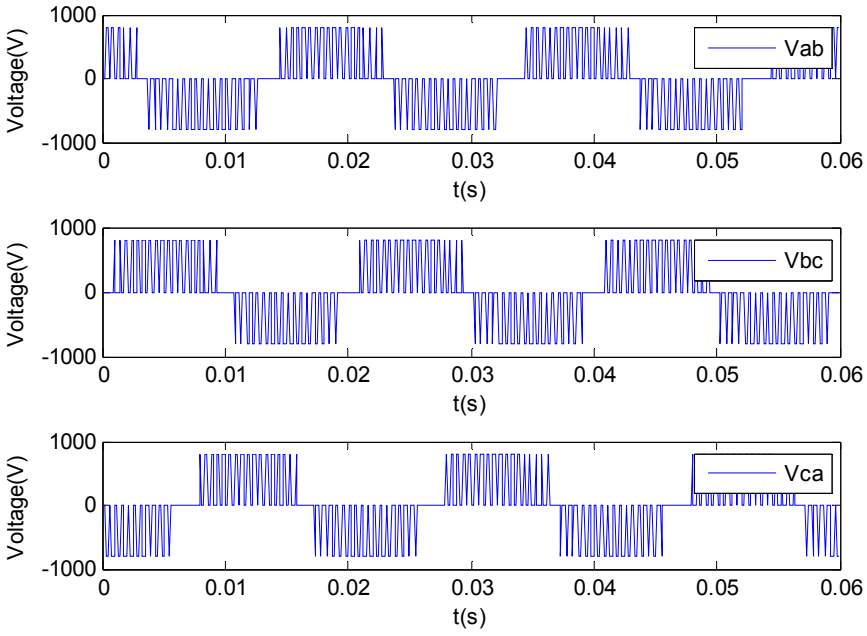

Fig. 3-66. VTB simulation results of inverter output line to line voltages.

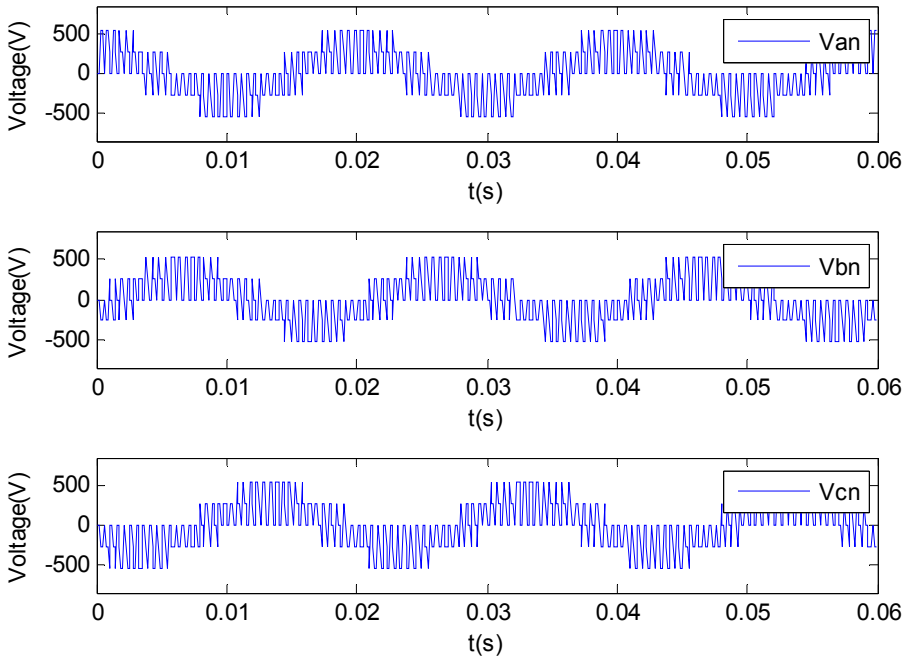

Fig. 3-67. VTB simulation results of inverter output phase voltages.

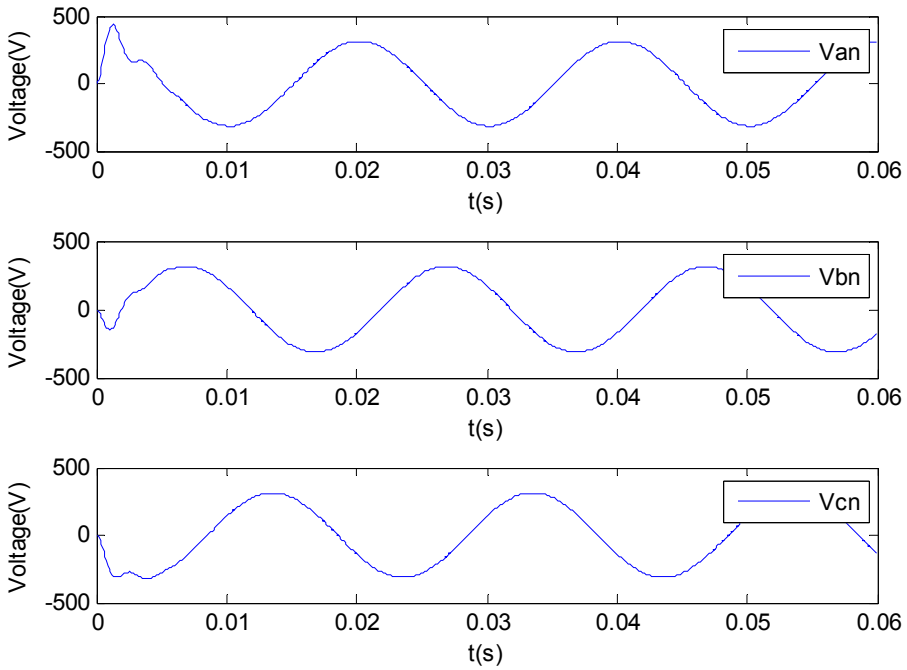

Fig. 3-68. VTB simulation results of load line to line voltages.

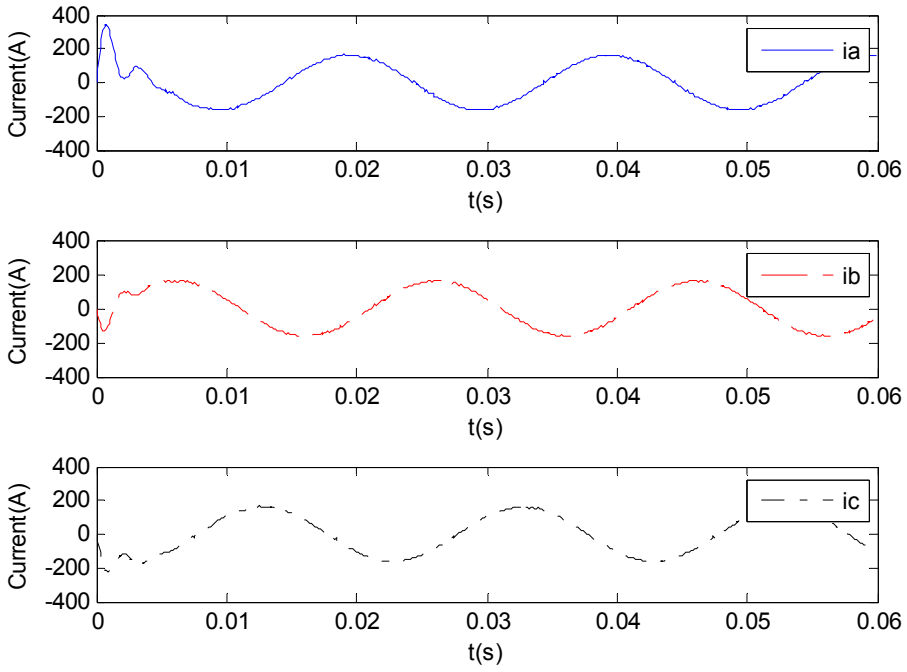

Fig. 3-69. VTB simulation results of load line to line currents.

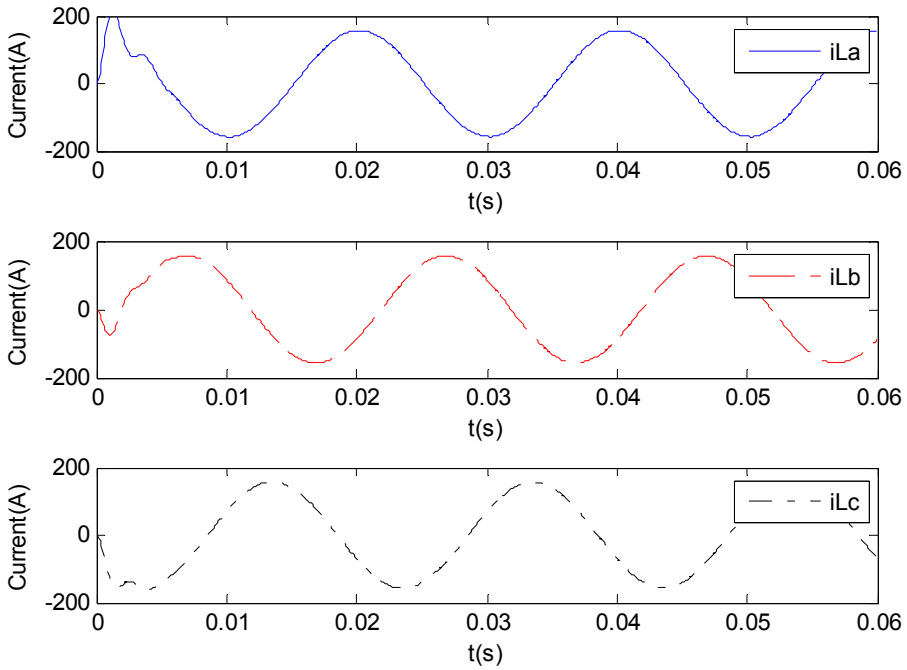

Fig. 3-70. VTB simulation results of load phase currents.

3.3.2 Zero-Sequence Current Control Using SVPWM

3.3.2.1 The Z-Axis Component

Through appropriate control of the time durations for the zero vectors, i.e., state (000) and (111), the zero-sequence current may be minimized. It is possible to choose the time duration for the (111) vector as

$$d_0^{'} = k(1 - d_1 - d_2) \tag{3-97}$$

Taking Sector 1 as an example, an alternating zero-vector Space Vector PWM switching pattern is shown in Fig. 3-71, and the duty cycles for the three-phases can then be expressed as:

$$\begin{aligned} d_a &= d_1 + d_2 + d_0^{'} = k + (1-k)d_1 + (1-k)d_2 \\ d_b &= d_2 + d_0^{'} = k - kd_1 + (1-k)d_2 \\ d_c &= d_0^{'} = k(1 - d_1 - d_2) \end{aligned} \tag{3-98}$$

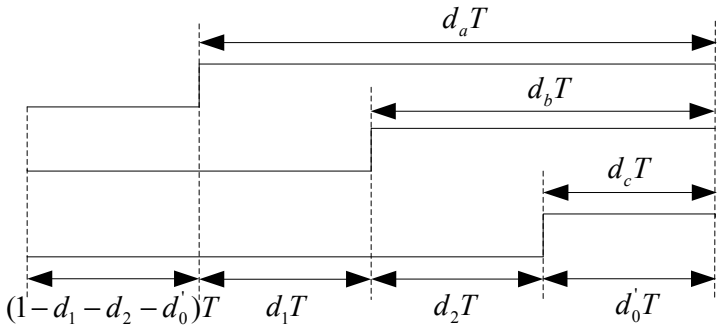

Fig. 3-71. Alternating zero-vector scheme of SVM.

We can get:

$$
\begin{aligned}
d_a &= k + (1-k)M\frac{\sqrt{3}}{2}\left(\sin(\frac{\pi}{3}-\alpha)+\sin(\alpha)\right) \\
d_b &= k - kM\frac{\sqrt{3}}{2}\sin(\frac{n\pi}{3}-\alpha) - (1-k)M\frac{\sqrt{3}}{2}\sin(\alpha-\frac{n-1}{3}\pi) \\
d_c &= k - kM\frac{\sqrt{3}}{2}\left(\sin(\frac{\pi}{3}-\alpha)+\sin(\alpha)\right)
\end{aligned}
\tag{3-99}
$$

These are the duty cycles that are determined for three-phases and change with time. The variables in the stationary frame can be transformed into those in the rotating frame by using the transformation.

The z-axis component of the duty cycle is

$$
d_z = \sqrt{3}k + M\frac{1-3k}{2}\sin(\frac{\pi}{3}-\alpha) + M\frac{2-3k}{2}\sin(\alpha) \tag{3-100}
$$

where: $\alpha=\omega t=2\pi ft$. It is seen that d_z is time-varying with a triple line frequency.

3.3.2.2 Frequency-Domain Analysis and Simulations

Based on the small-signal model in Eqs. (3-89)-(3-92), a frequency-domain model can be derived. To regulate the zero-sequence current, a z-channel model is needed. Assuming that z-axis current can be decoupled from the d- and q-channels, the space state equation of zero-sequence current can be achieved.

$$
\frac{d}{dt}\tilde{i}_z = \frac{V_{dc}}{L_1+L_2}\begin{bmatrix}1 & -1\end{bmatrix}\begin{bmatrix}\tilde{d}_{z1}\\ \tilde{d}_{z2}\end{bmatrix} + \frac{D_{z1}-D_{z2}}{L_1+L_2}\tilde{v}_{dc} \tag{3-101}
$$

Converting Eq. (3-101) into the frequency domain yields:

$$\tilde{i}_z(s) = \frac{V_{dc}}{L_1 + L_2}\frac{1}{s}\tilde{d}_{z1}(s) - \frac{V_{dc}}{L_1 + L_2}\frac{1}{s}\tilde{d}_{z2}(s) + \frac{D_{z1} - D_{z2}}{L_1 + L_2}\frac{1}{s}\tilde{v}_{dc}(s) \tag{3-102}$$

The Bode plots of the open-loop transfer functions from the control inputs $\tilde{d}_{z1}$, $\tilde{d}_{z2}$ to output $\tilde{i}_z$, respectively, are shown in Fig. 3-72. Assuming $\tilde{d}_{z2}(s) = 0$ and $\tilde{v}_{dc}(s) = 0$, with the zero-sequence current control, the z-channel duty cycles of the power converters can be obtained as follows:

$$\tilde{d}_{z1}(s) = (\tilde{i}_{z\_ref}(s) - \tilde{i}_z(s))H(s) \tag{3-103}$$

Since the zero-sequence current should be minimized, the reference current should be zero and thus $\tilde{i}_{z\_ref}(s) = 0$. If a PI controller is used, i.e., $H(s) = K_p + \frac{K_i}{s}$, this is obtained:

$$\frac{\tilde{i}_z(s)}{\tilde{i}_{ref}(s)} = \frac{V_{dc}(K_p s + K_i)}{s^2 + \frac{V_{dc}K_p}{L_1 + L_2}s + \frac{V_{dc}K_i}{L_1 + L_2}} \tag{3-104}$$

Then, the closed loop gain's poles:

$$\lambda_{1,2} = \frac{-\frac{V_{dc}K_p}{(L_1 + L_2)} \pm \sqrt{\left(\frac{V_{dc}K_p}{L_1 + L_2}\right)^2 - 4\frac{V_{dc}K_i}{L_1 + L_2}}}{2} \tag{3-105}$$

Assuming $\tilde{i}_{ref}(s) = 0$,

$$\frac{\tilde{i}_z(s)}{\tilde{v}_{dc}(s)} = \frac{\frac{(D_{z1} - D_{z2})}{L_1 + L_2}s}{s^2 + \frac{V_{dc}K_p}{L_1 + L_2}s + \frac{V_{dc}K_i}{L_1 + L_2}} \tag{3-106}$$

The denominators in Eqs. (3-104) and (3-106) are the same. Therefore, their pole placements are the same.

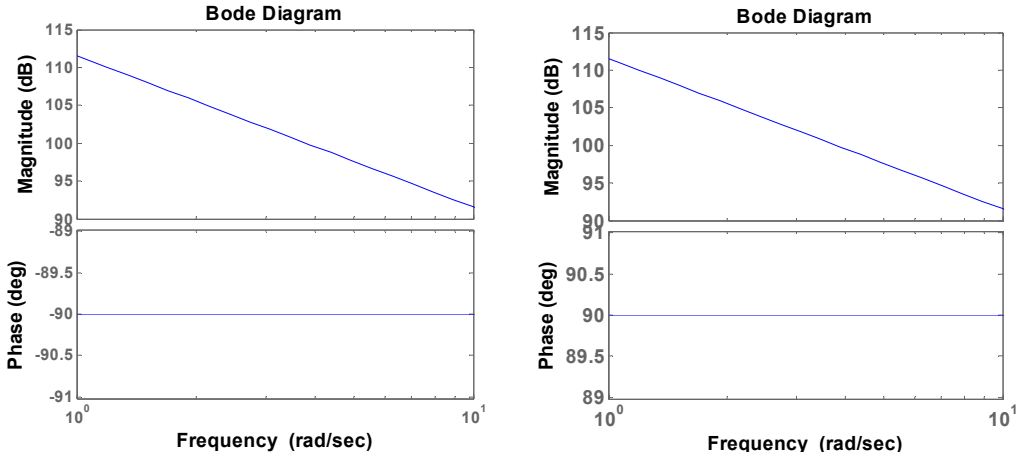

(a) $\widetilde{i}_z / \widetilde{d}_{z1}$ (b) $\widetilde{i}_z / \widetilde{d}_{z2}$

Fig. 3-72. Bode plots for the open-loop transfer functions from control inputs $\widetilde{d}_{z1}$, $\widetilde{d}_{z2}$ to outputs $\widetilde{i}_z$.

In order to further study the level of pole-zero sensitivity, Bode plots and various root loci are presented by changing a particular parameter with the others kept constant at some selected nominal values of V_{dc} =500 V, L=660 μH, C=22 μF, R=5 Ω, Dz1=0.25, and Dz2=0.24.

Influence of variations in control parameters

The Bode plots of the closed loop gain corresponding to control parameters K_p and K_i increasing are shown in Fig. 3-73 (a)-(b). A higher value of the magnitude at frequency ω indicates less capability of the system to reject a disturbance at that frequency.

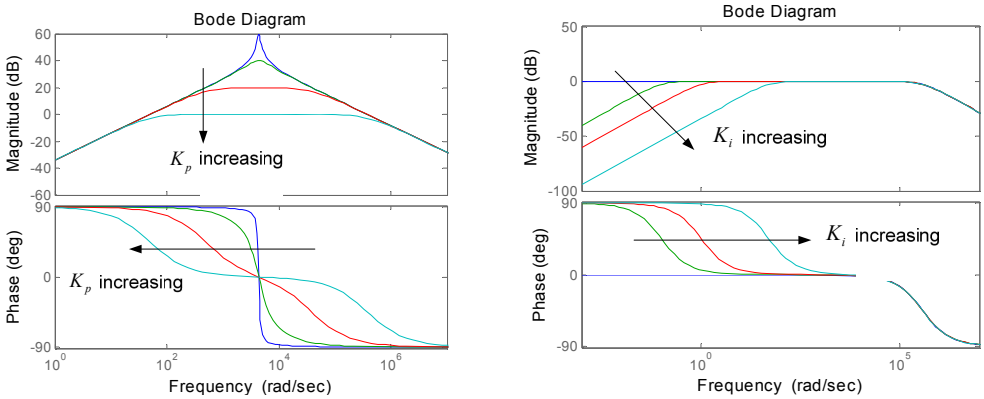

(a) K_p increasing (b) K_i increasing

Fig. 3-73. Bode plot of closed loop gain with variation of K_p and K_i.

The zero and pole locations in the frequency-domain move with system parameters and operating points. These movements would result in unsatisfactorily oscillatory. Pole and zero trajectories of closed loop gain with main parametric variations may be obtained. With K_p increasing, Fig. 3-74(a) shows the shifting of poles away from the imaginary axis and towards the real axis result in an increase in system damping ratio. Then, two poles move away from each other along the real axis once they reach it. The pole which moves fast to the left can be ignored as an insignificant pole when it is far away from the imaginary axis. The other pole, which is a dominant pole, moves slowly towards the imaginary axis, resulting in a decrease in system damping.

Fig. 3-74(b) shows two poles moving toward each other when K_i is increasing. The right one is the dominant pole and its position determines system stability. Therefore,

with K_i increasing, the shifting of the pole away from the imaginary axis along the real axis increases system stability.

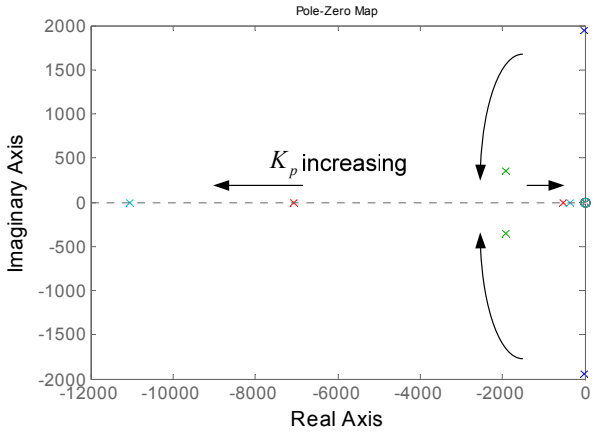

(a) K_p increasing

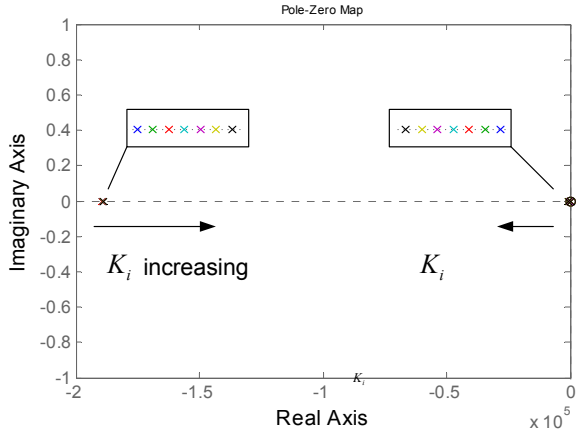

(b) K_i increasing

Fig. 3-74. Root loci of closed loop gain with increasing K_p and K_i.

Influence of variations in system parameters

By varying the filter inductance $L_{1,2}$ (from 0.46 mH to 2.46 mH), Fig. 3-75 shows the shifting of poles of the closed loop gain. The shifting of poles is towards and away from the imaginary axis horizontally on the real axis when L is increasing, as shown in Fig.

3-75. Because the left one is far from the imaginary axis, it can be ignored; the right one is the dominant pole, so the shifting of the right-side pole away from the imaginary axis increases system stability when L is increasing.

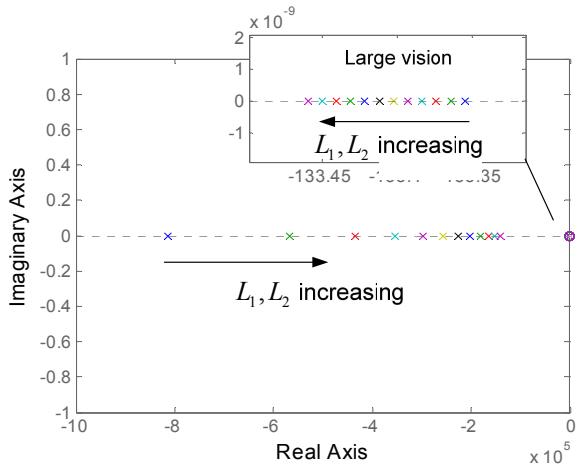

Fig. 3-75. Root loci of closed loop gain with $L_{1,2}$ increasing.

On the other hand, with L increasing, the pole placement of the closed loop transfer function from disturbance $\tilde{v}_{dc}(s)$ to output $\tilde{i}_z(s)$ is the same as that of closed loop gain.

Influence of variations in steady state operating points

Steady state operating conditions are also considered to have an important impact on the pole placements, as shown in Fig. 3-76 and Fig. 3-77. Fig. 3-76 shows that as V_{dc} is increasing, the dominant pole moves towards the imaginary axis along the real axis while the left insignificant pole can be ignored , resulting in a decrease in system stability. Fig. 3-77 shows that the poles of the closed loop gain do not move on the real axis when Dz2 is varied from 0.01 to 0.25 and Dz1 remains 0.25. This means the change in the duty

cycle has no impact on the system response. This is consistent with Equation (2-16) in the previous section, indicating that difference between two z-axis duty cycles doesn't affect the poles placement. Based on the above analysis, it appears that it is crucial to choose appropriate control parameters and system parameters in order to enable the system to perform well.

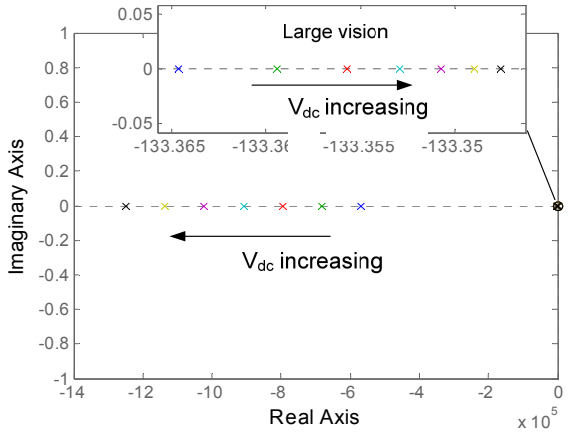

Fig. 3-76. Root loci of closed loop gain with V_{dc} increasing.

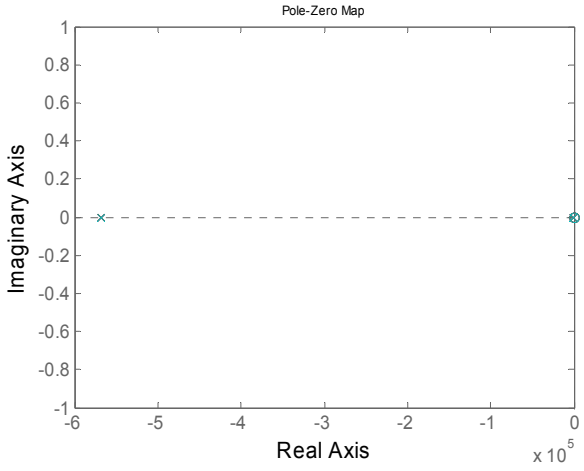

Fig. 3-77. Root loci of closed loop gain with steady state operating points changing.

3.3.2.3 Time-Domain Simulations

A system of parallel-connected three-phase voltage source converters shown in Fig. 3-78 is modeled and simulated in Matlab/Simulink to validate the control approach and small-signal analysis. The DC-side voltage is V_{dc} =500 V. The parameters of the filters are L=660 μH and C=22 μF, and the load is R=5 Ω. A PI control scheme is used to minimize the zero-sequence circulating current between the two inverters, with one inverter under voltage control, and the other under power control.

Fig. 3-79 shows the zero-sequence current responses with and without a zero-sequence current controller. Without a controller, the zero-sequence current is relatively large, up to 10A, with a frequency triple the line frequency. The results demonstrate that the zero-sequence current can be reduced with a mitigation control scheme.

Fig. 3-80 shows that the zero-sequence current is regulated within a lower range when L=1.66 mH than when L=0.66 mH. This suggests that a larger inductor helps reduce zero-sequence current.

System performance with different values of the control parameter K_p is compared in Fig. 3-81. It verifies that when K_p equals 0.5, the system has a superior response to that when K_p equals 1.5 or 0.05, with DC voltage changing from 500 V to 1000 V. It is easily seen that response is not necessarily better with a larger value of K_p. This observation is

consistent with the frequency-domain analysis results, as shown in Fig. 3-74(a). The system damping ratio with K_p=0.5 is larger than that with K_p=0.05 and 1.5.

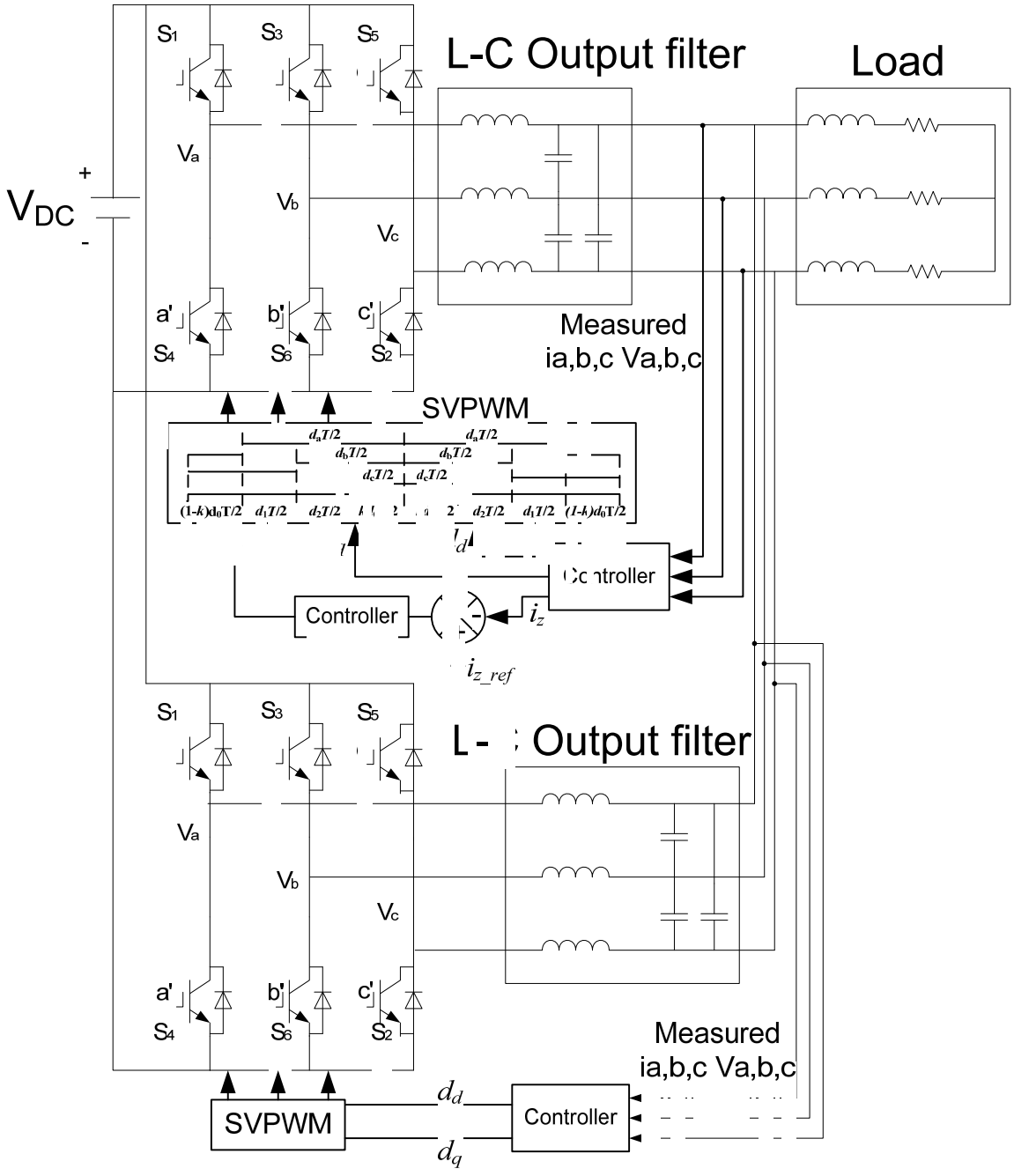

Fig. 3-78. Two parallel-connected inverters with zero-sequence current control.

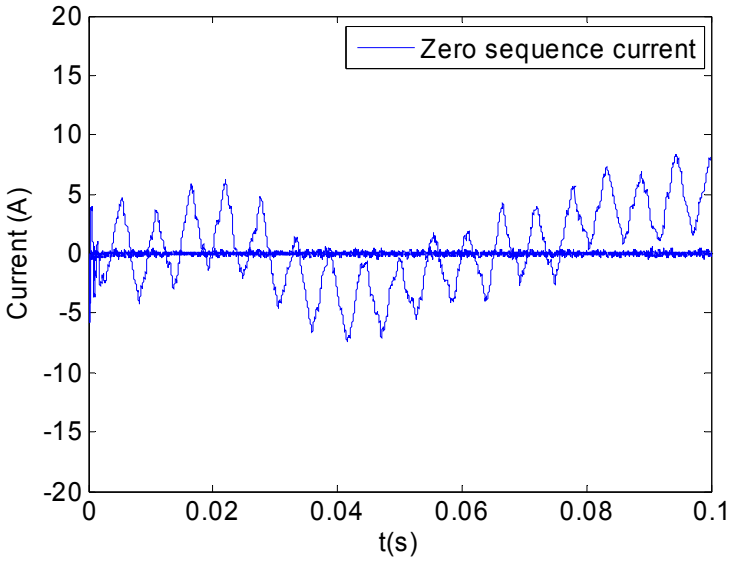

Fig. 3-79. Zero-sequence currents without and with a zero-sequence current controller.

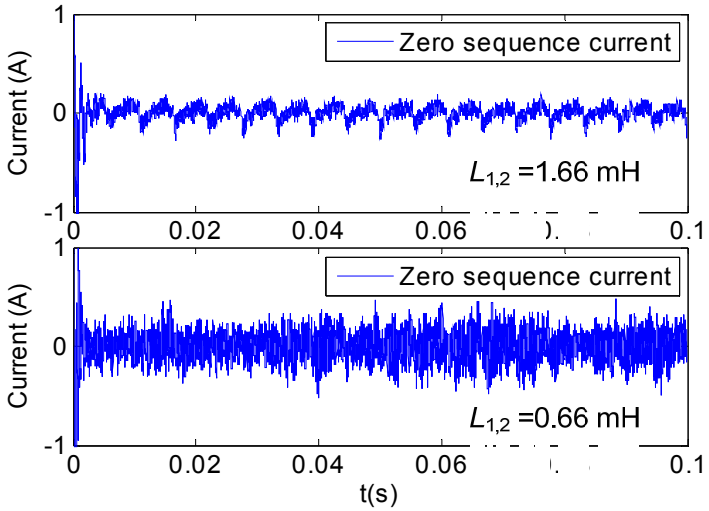

Fig. 3-80. Zero-sequence current with different filter inductances.

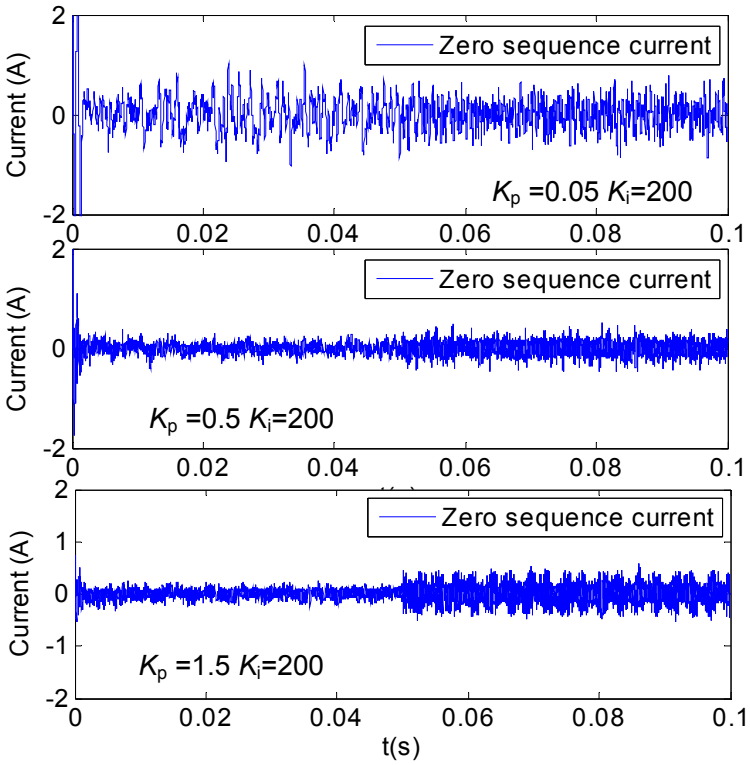

Fig. 3-81. Zero-sequence current with three different K_p (V_{dc} changes from 500 V to 1000 V at 0.05s).

Chapter 4. Parallel-Connected Three–Phase Converters with Nonlinear Load

The objective of an electric utility is to provide its customers with a sinusoidal voltage of fairly constant magnitude and frequency. The generators or inverters generate a very close approximation to a sinusoidal signal. Power systems are designed to operate at a specific frequency, usually 50 or 60 Hz. When a linear electrical load is connected to the system, it draws sinusoidal current at the same frequency as the voltage. However, there are many electric loads on the grid with nonlinear characteristics. They can cause harmonic distortion of both the voltage and current signals. The waveform of voltage and current will become more distorted when more nonlinear loads are introduced.

Electronic loads use diodes, rectifiers, power transistors, other electronic switches, variable speed drives, and even common office equipment such as computers and printers to either chop waveforms to control power, or to convert 50/60 Hz from AC to DC. When a non-linear load is connected to the system, it draws a current that is not necessarily sinusoidal. The current waveform can become quite complex, depending on the type of load and its interaction with other components of the system. Regardless of how complex

the current waveform becomes, as described through Fourier series analysis, it is possible to decompose it into a series of simple sinusoids, which start at the fundamental power system frequency and occur at integer multiples of the fundamental frequency.

Harmonic frequencies in the power grid are a frequent cause of power quality problems. Harmonics can be damped to a low value by artificial control. The harmonic compensation can be achieved by different approaches, such as passive filter, power filter corrector, static var compensator (SVC), and active power filter (APF).

APF is a very useful tool for eliminating harmonic pollution from the power grid. APF injects a current equal in magnitude but opposite in phase to the harmonic current. Compared with traditional passive filters, APF has significant advantages, such as good controllability, fast response, and high control accuracy.

4.1 **Description of Active Power Filter (APF)**

Fig. 4-1 shows the structure of a three-phase shunt APF. This is mainly made up of a voltage source converter with a large capacitor to maintain the voltage constant on the DC side, and three inductors to output the compensation current on the AC side, in connection with the utility.

$$I_{APC} = I_S - I_{load} \tag{4-1}$$

where I_{APC} is the compensation input current, I_S is the source current and I_{load} is the load current.

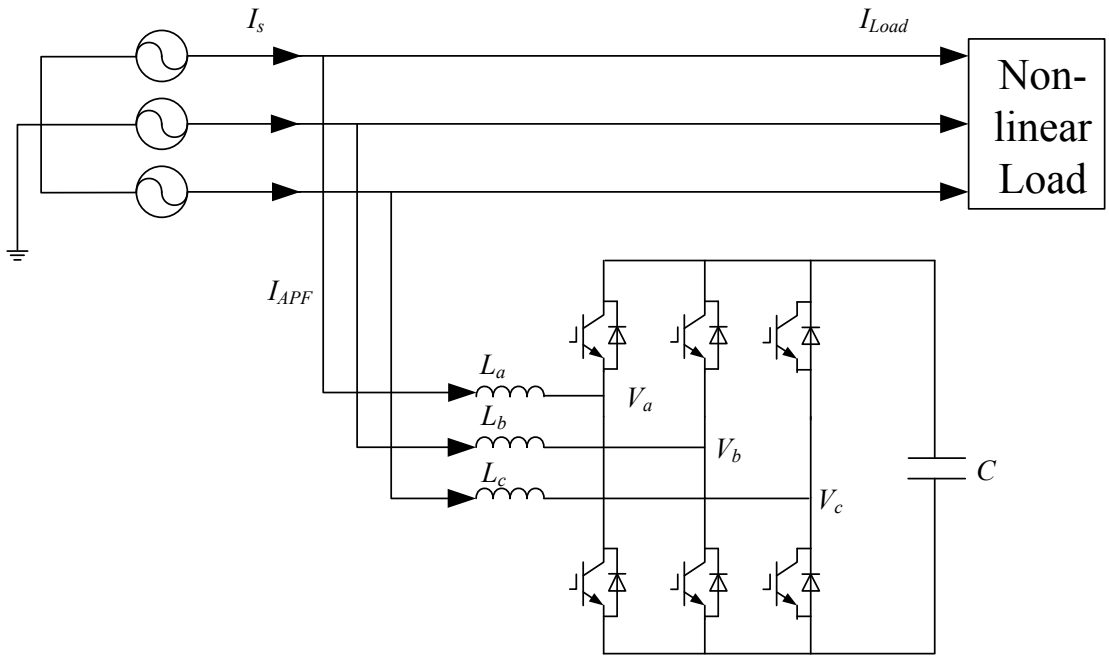

Fig. 4-1. The structure of a three-phase shunt APF system.

The AC voltages of the network deliver power to a harmonic producing, load drawing, fixed current I_{load}. Load current harmonics therefore directly translate into source current harmonics. Source current harmonics, in turn, cause a harmonic voltage drop across the source impedance, resulting in harmonic distortion at the point of common coupling.

This APF structure in nature is a boost converter circuit as the same as the high frequency reversible PWM rectifier. The phase voltage is required to be higher than peak-to-peak value of the bus line-to-line voltage in order to control the output current completely.

The APF mathematical model is shown below:

$$\begin{cases} L_a \dfrac{di_{a\_APF}}{dt} = v_{sa} - Ri_{a\_APF} - v_{ra} \\ L_b \dfrac{di_{b\_APF}}{dt} = v_{sb} - Ri_{b\_APF} - v_{rb} \\ L_c \dfrac{di_{c\_APF}}{dt} = v_{sc} - Ri_{c\_APF} - v_{rc} \end{cases} \tag{4-2}$$

Where V_{sa}, V_{sb} *and* V_{sc} are utility voltage, V_{ra}, V_{rb} and V_{rc} are PWM voltage, and i_a, i_b and i_c are the output current. R is the equivalent resistance of the connection inductor. Fig. 4-2 shows its equivalent average model, where d_{an}, d_{bn}, and d_{cn} are the duty ratios of the upper switches.

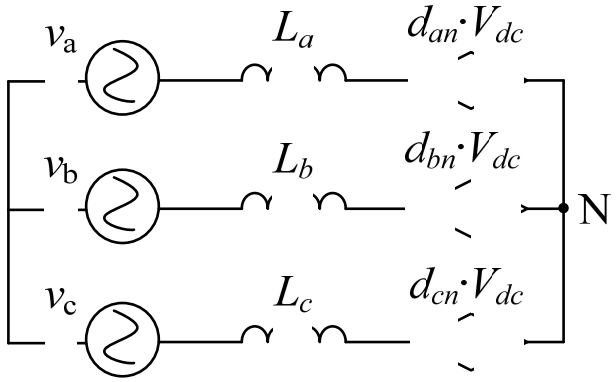

Fig. 4-2. Average model of AFC.

In order to cancel the original current distortion and improve power quality on the grid, current harmonic compensation is achieved by injecting equal but opposite current harmonics at the point of connection. The control block diagram of APF is shown in Fig. 4-3. It includes a current reference generator, a current controller, and a gating signals generator. In this circuit, the fundamental component is extracted by filtering the distorted

load current. The current signal, obtained from the second order band pass filter, is synchronized with the respective phase to neutral source voltage. It uses PLL to force the inverter AC output current to lead the AC inverter output voltage. The active power is controlled by the amplitude of the fundamental current reference waveform, which can be obtained from the reference generator. The current error signal is compared with a triangular reference waveform, which can stabilize the converter switching frequency and force it to equal the triangular reference frequency.

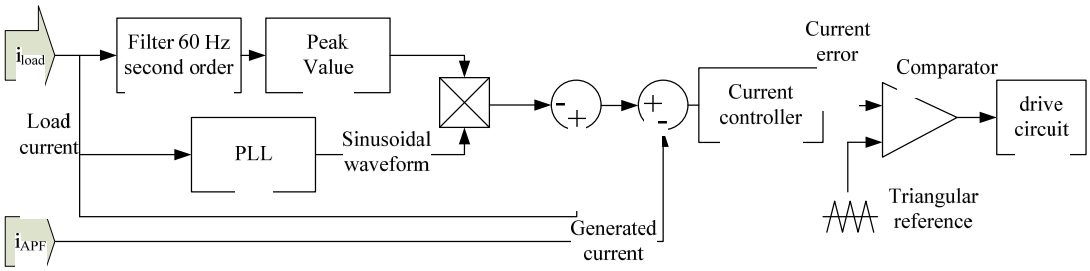

Fig. 4-3. Block diagram of an APF control system.

The block diagram of an APF with a DC voltage controller is shown in Fig. 4-4. The DC-link voltage error is added to the fundamental current reference waveform to produce a sinusoidal waveform. In this way, the current signal allows the inverter to supply the current harmonic components, to supply the reactive power required by the load, to absorb a small amount of active power, to cover the switching losses, and to keep the DC voltage constant. In order to improve APF stability, the maximum amount of active power absorbed by the inverter should be limited. Thus, the DC voltage error signal can

be limited to regulate the amplitude of the fundamental component of the current reference.

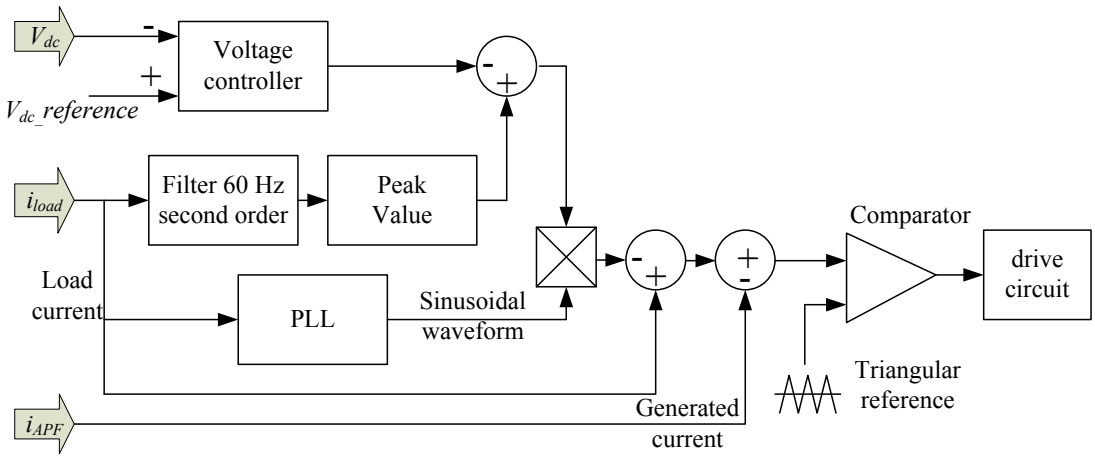

Fig. 4-4. Block diagram of an APF control system with a DC voltage controller.

4.2 A Parallel-Connected Inverter System with Nonlinear Load and APF

Fig. 4-5 shows a parallel-connected inverter system with nonlinear load. Simulations are carried out in MATLAB/Simulink/SimPowerSystems platform. The system consists of two inverters, a linear load and a nonlinear load. For the nonlinear load, a three-phase rectifier with RL (10 Ω, 1 mH) load is used. The two inverters are operating in stand-alone mode. Inverter I uses voltage control to maintain the AC bus voltage at the reference point. *d-axis* voltage reference is set to be 155.5 V. *q-axis* voltage is set to be 0 V. Inverter II uses PQ control to regulate the output active power and reactive power; their references are 10 kW and 2 kVar. A nonlinear load and an APF connect to the PCC.

The DC-link voltage reference value of the APF is set to be 500 V. The switching frequency of the APF is 100 kHz. The capacitance at the DC side of the APF is 0.5 mF.

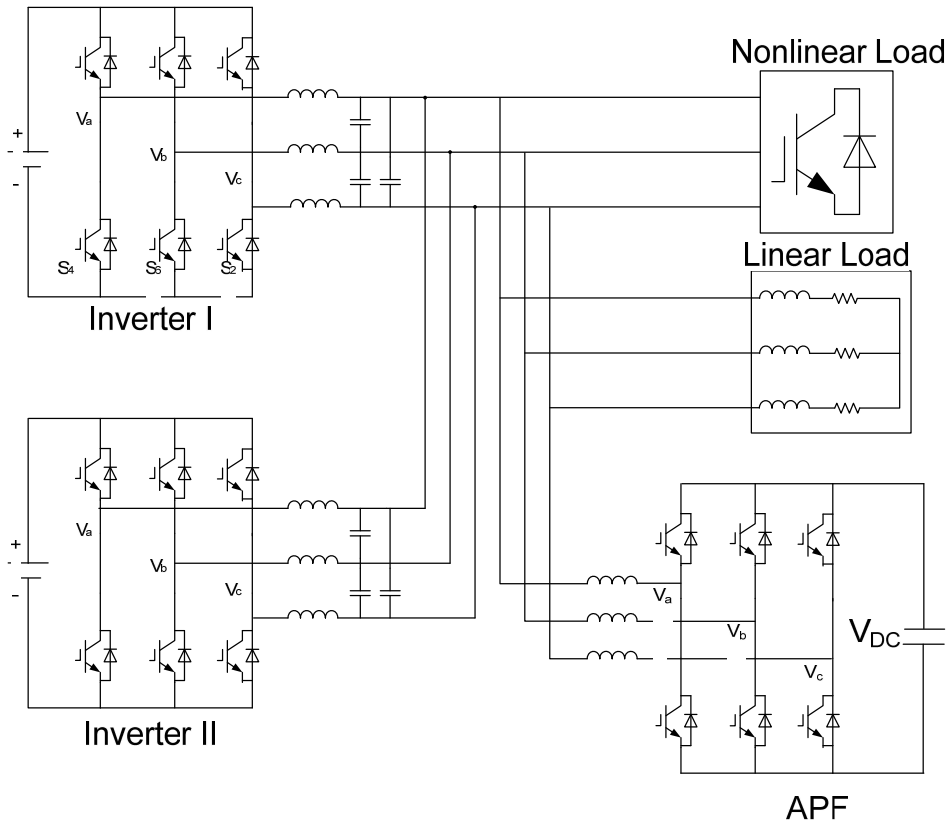

Fig. 4-5. A two parallel-connected inverters system with nonlinear load and APF.

4.3 **Case Studies**

Case I: Steady State Response

Simulations are carried out based on the proposed parallel-connected inverters system without APF, with APF, and with a DC voltage controller in APF.

In the system without an APF, Fig. 4-6 and Fig. 4-7 show the one phase currents of the source and the nonlinear load and the active and reactive power of inverter I. Fig. 4-6

indicates that the source current is equal to the nonlinear current when the system has a nonlinear load but no APF. This source current is heavily distorted. (The source current I_S in this simulation is the current flow to the nonlinear load and the APF). The reactive power spikes in Fig. 4-7 indicate that, without an APF, inverter I has to provide reactive power to the nonlinear load since inverter II has constant output reactive power. In this case, the total harmonic distortion (THD) is 30.15%, shown in Fig. 4-8.

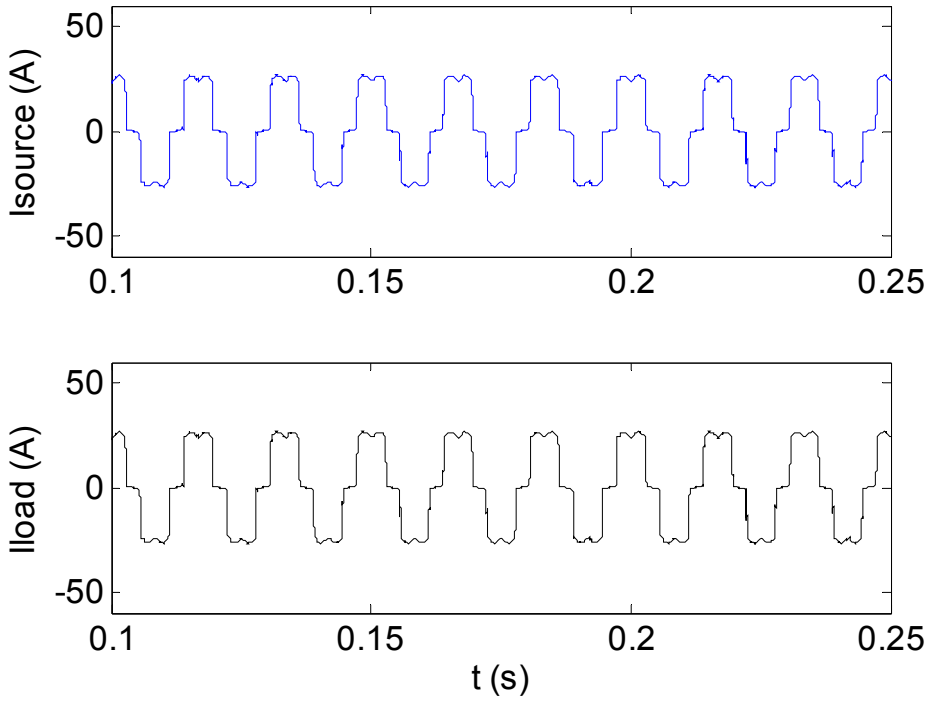

Fig. 4-6. The one phase currents of the source and the nonlinear load in a parallel-connected inverters system without an APF.

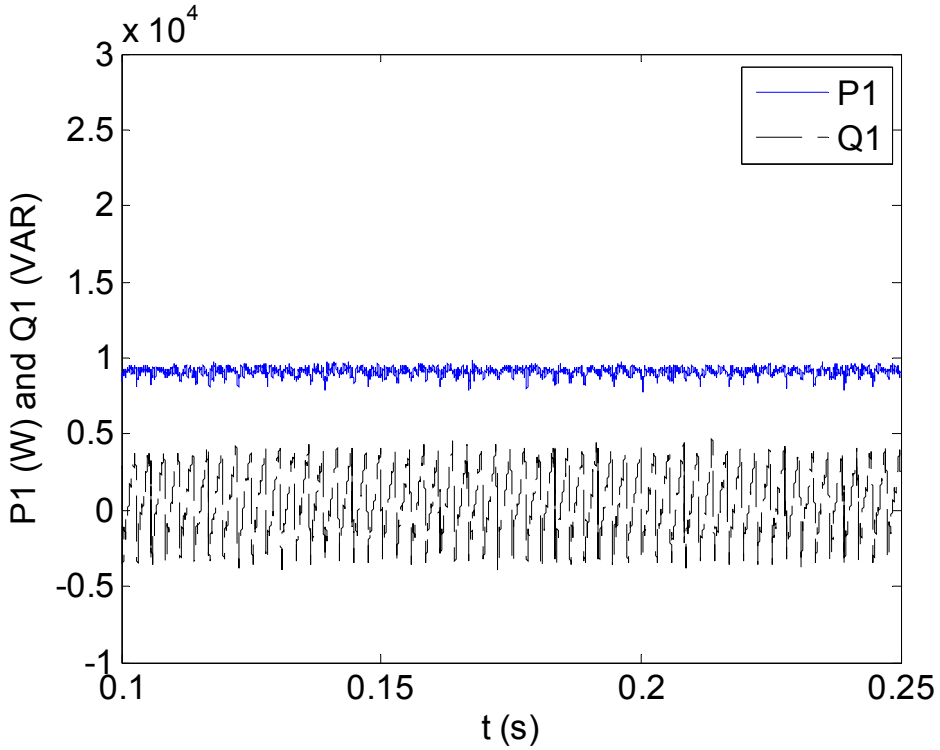

Fig. 4-7. The active and reactive power of inverter I in a parallel-connected inverters system without an APF.

The THD of the source current with an APF, both without and with DC voltage control in the APF, are shown in Fig. 4-9 and Fig. 4-10. When a system uses an APF, the THD of the source current is 5.74% after compensation by the APF, as shown in Fig. 4-9. Current distortion is still obvious in that figure. The THD reduces to 2.2% when the DC voltage controller is applied in the APF, as shown in Fig. 4-10. From these tests, clearly the THD of the source current in the parallel-inverters system is highly reduced when an APF with DC-link control is applied in this parallel-connected inverters system.

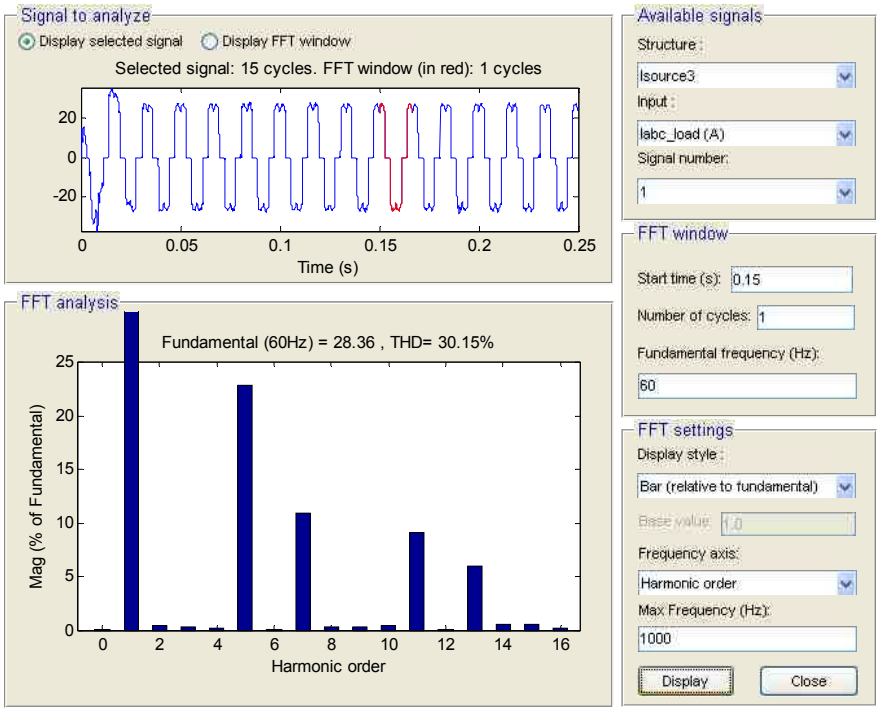

Fig. 4-8. THD of the load current of a two parallel-connected inverters system without an APF.

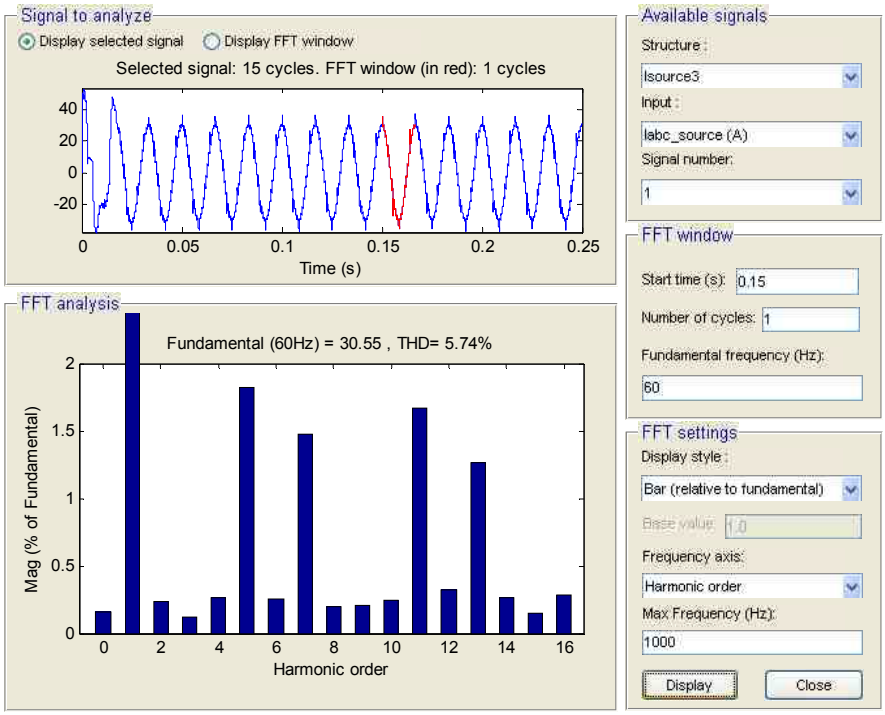

Fig. 4-9. THD of the load current of a two parallel-connected inverters system with APF but without DC-link voltage control.

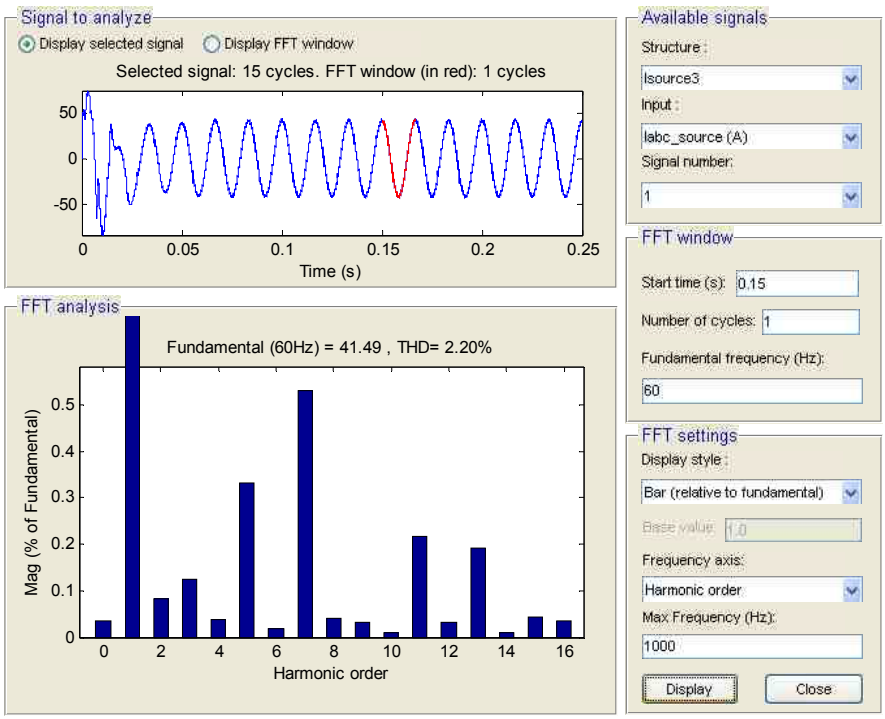

Fig. 4-10. THD of the load current of a two parallel-connected inverters system with APF and DC-link voltage control.

Case II: Transient Responses of Step References

The simulation runs for 0.25 s. At 0.15 s, there is a step change in the PQ references of inverter II. The PQ references change from 10 kW and 2 kVar to 5 kW and 1 kVar.

The APF output three-phase currents are shown in Fig. 4-11. Fig. 4-12 shows output currents of inverters I and II. At 0.15 s, there is a step decrease in the output of active and reactive power of inverter II, following their references. The load remains the same. Thus, inverter II shares less load demand, while inverter I has to supply more power. The currents of inverters I and II are shown in Fig. 4-12. Output currents of source and nonlinear load are the same as before, shown in Fig. 4-13. The currents of the source and

the nonlinear load are shown in Fig. 4-13. Compared with Fig. 4-6, the nonlinear load current is the same as before, but the source current is in a sinusoidal waveform, with little harmonics distortion.

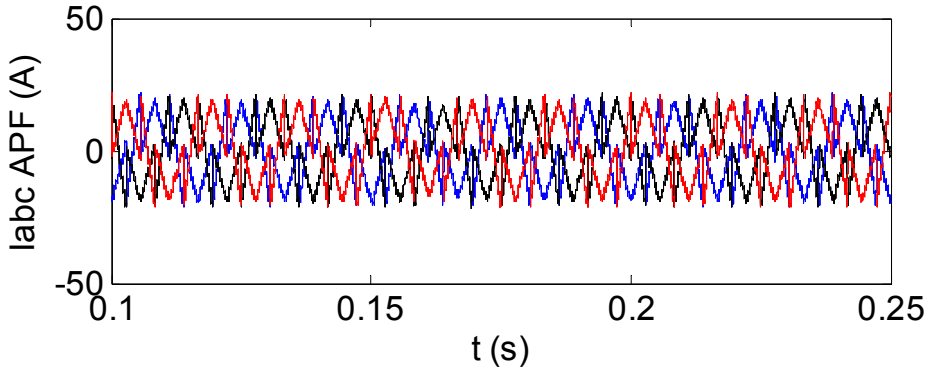

Fig. 4-11. APF output three-phase currents.

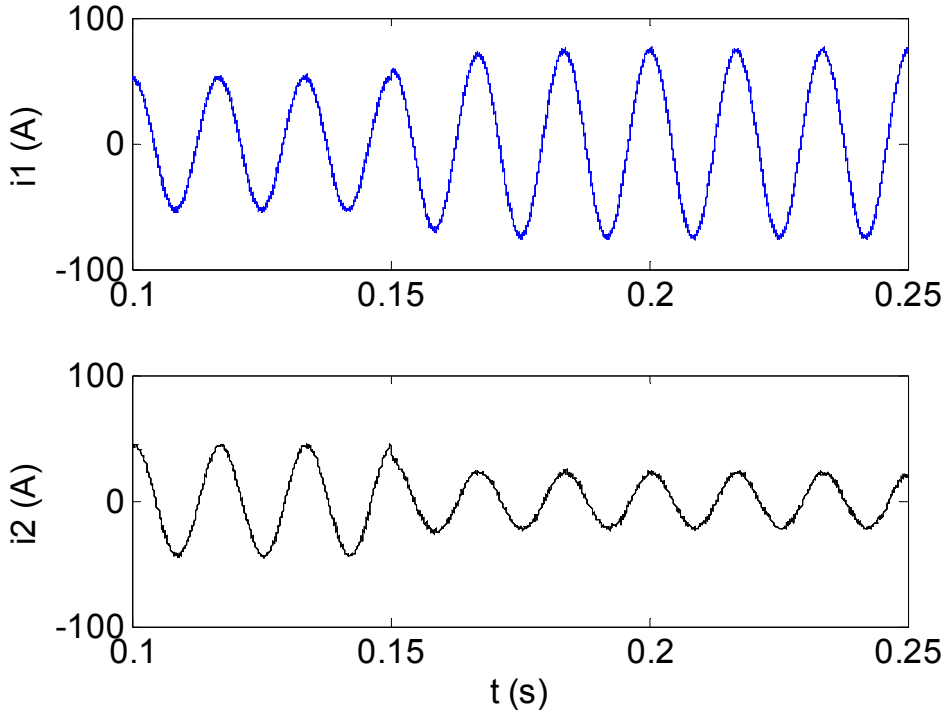

Fig. 4-12. Output currents of inverters I and II when the P and Q reference change.

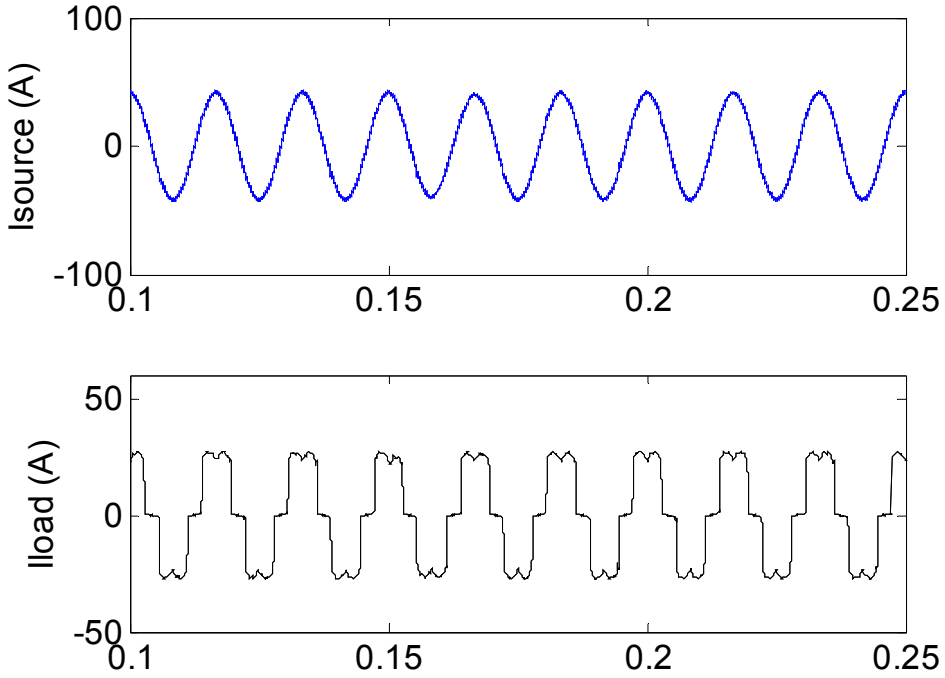

Fig. 4-13. Output currents of the source and nonlinear loads.

Fig. 4-14 and Fig. 4-15 show the output of active and reactive power from inverters I and II. P2 and Q2 decrease, while P1 and Q1 increase accordingly. This is similar to the currents of inverters I and II. AC bus three-phase line-line voltages at PCC are regulated well, as shown in Fig. 4-16. DC-link voltage drops a little at 0.15 s, as shown in Fig. 4-17, but quickly increases to the reference value.

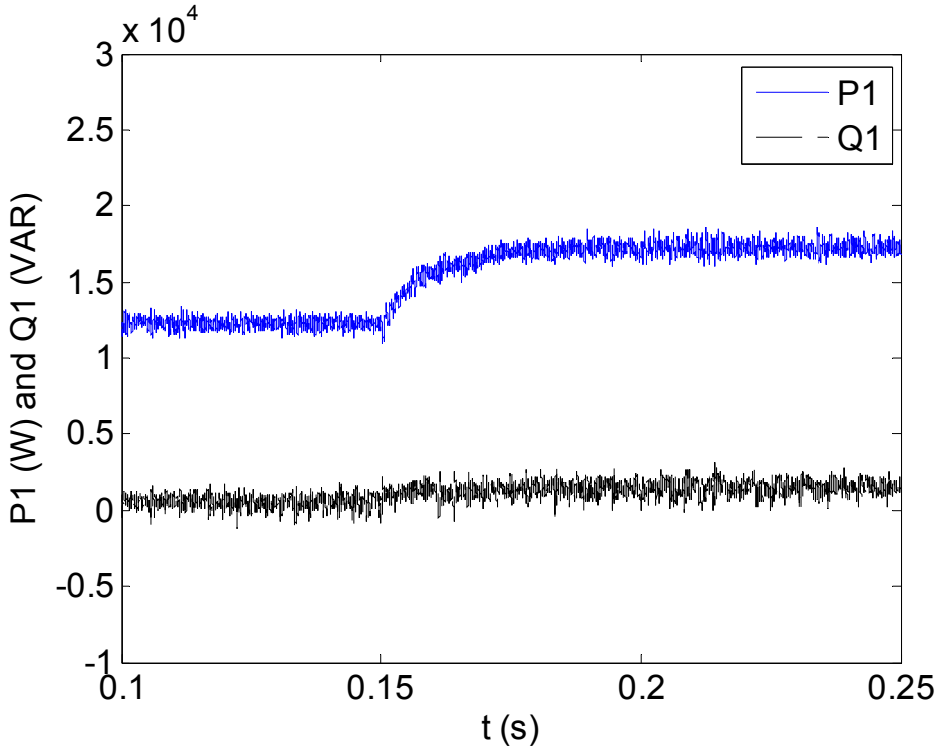

Fig. 4-14. The active and reactive power of inverter I.

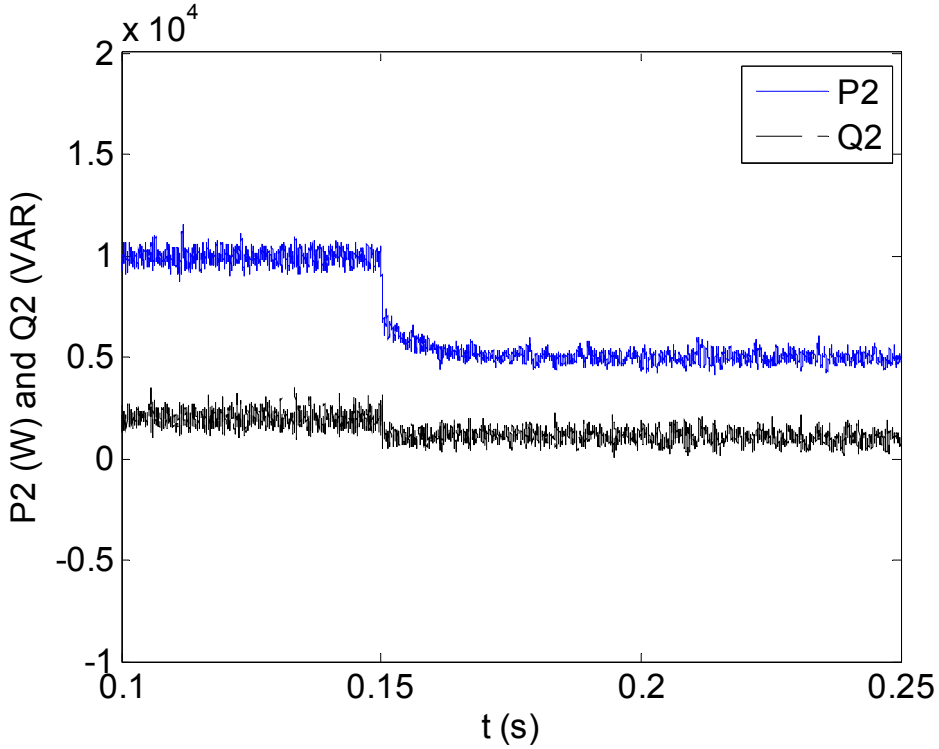

Fig. 4-15. The active and reactive power of inverter II.

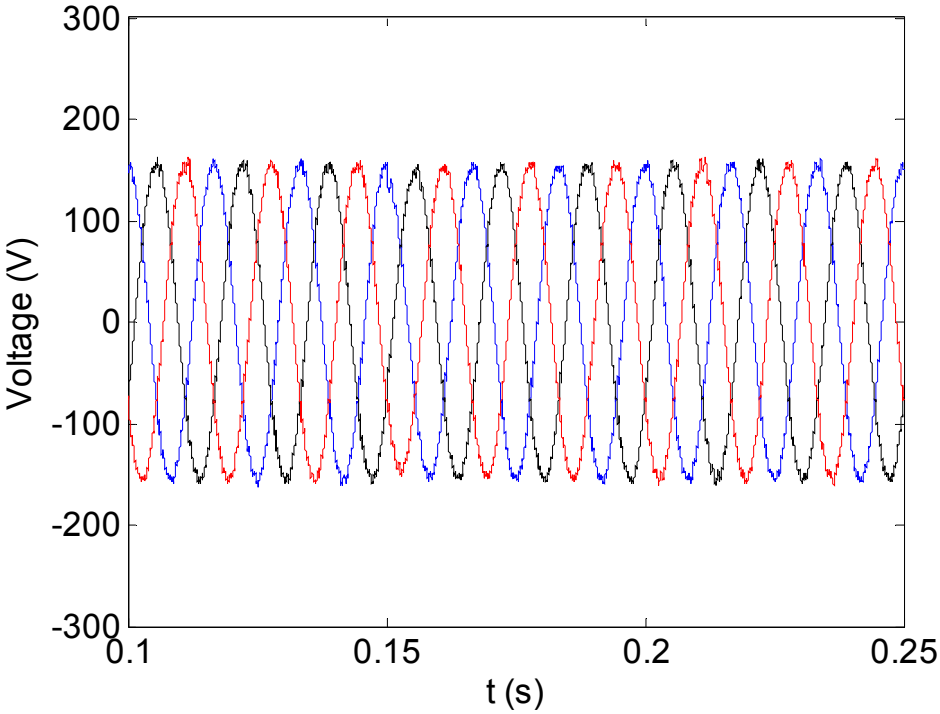

Fig. 4-16. AC bus three-phase line-line voltages.

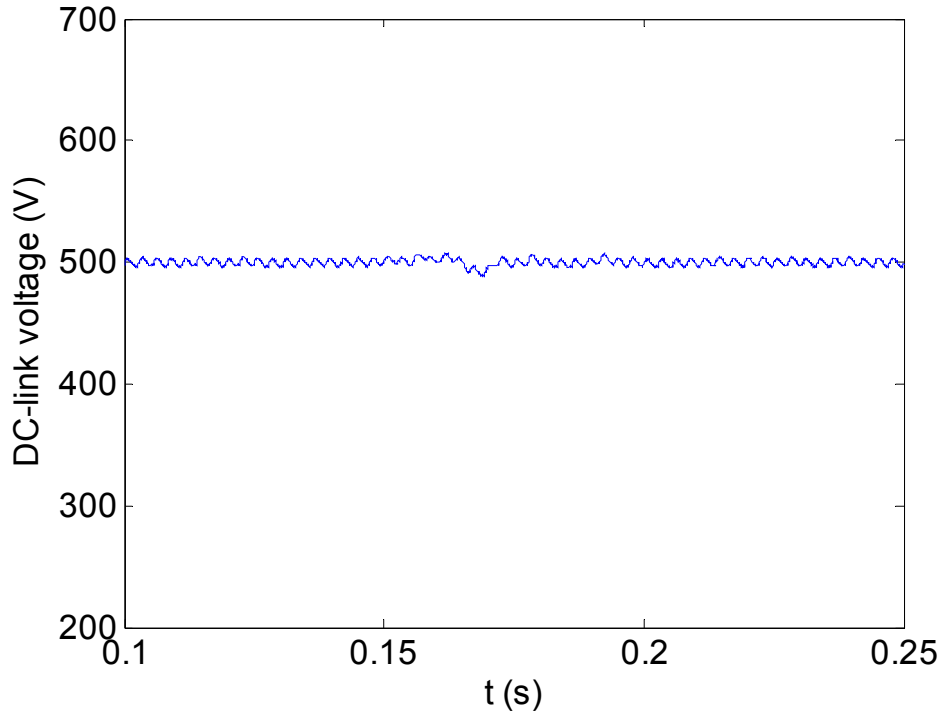

Fig. 4-17. APF DC-link voltage.

Case III: Transient Response of Step Load

The simulation runs for 0.25 s. At 0.15 s, there is a step change in the three-phase nonlinear load. Fig. 4-18 shows output currents of the source and the load. Fig. 4-19 shows three-phase currents of the APF. The output current peak-peak value of the APF increases after the change occurs. It needs the APF to inject more current to smooth the increased harmonics. Fig. 4-20 shows output currents of inverters I and II when the load increases. The current of inverter I increases a little, but the current of inverter II remains the same. This is because inverter II maintains constant PQ output, thus inverter I covers the growing load. Fig. 4-21 shows APF DC-link voltage. When the load increases at 0.15 s, the voltage experiences slight disturbances then becomes stable. Active power and reactive power of two inverters are shown in Fig. 4-22 and Fig. 4-23. When load impedance decreases, the load current increases. The source current increases accordingly to cover the increased load demand. The output active power and reactive power of inverter II remain the same. The output active power and reactive power of inverter I increase to supply the load.

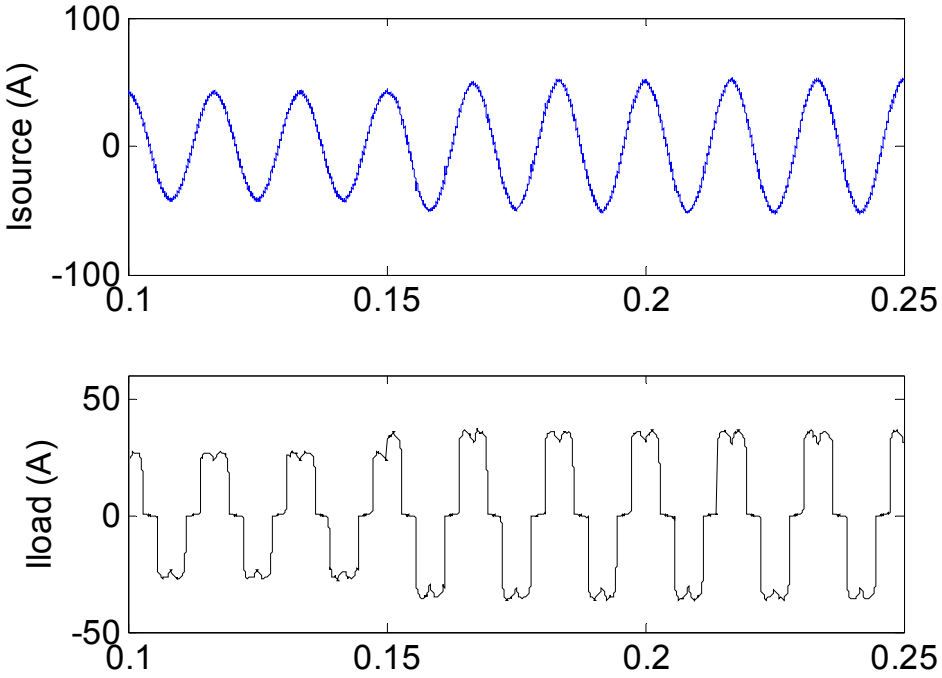

Fig. 4-18. Output currents of the source and the load.

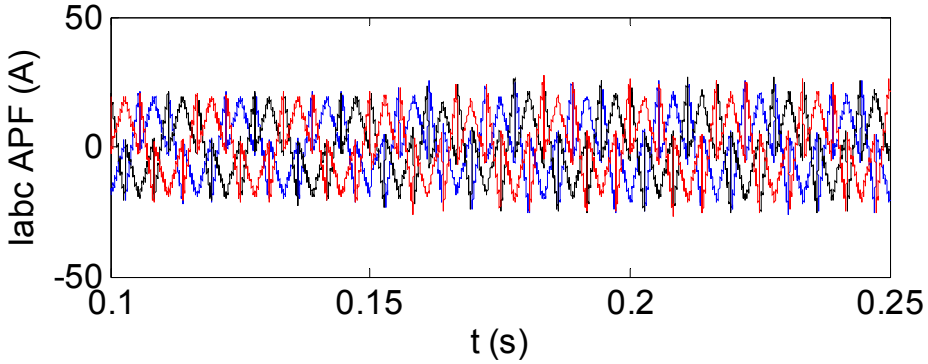

Fig. 4-19. APF three-phase currents.

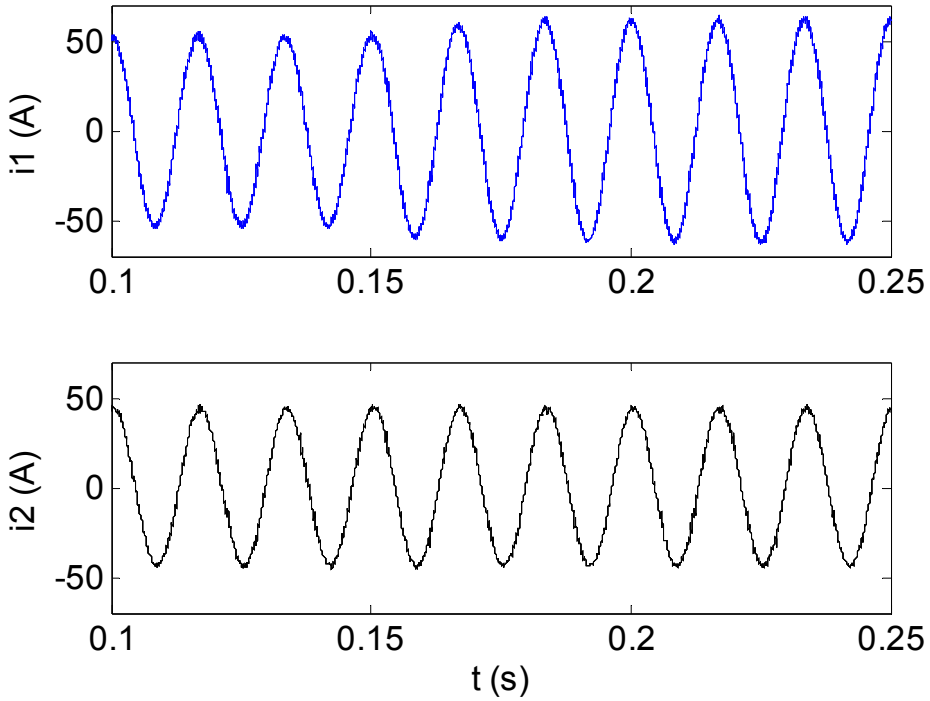

Fig. 4-20. Output currents of inverters I and II when the load increases.

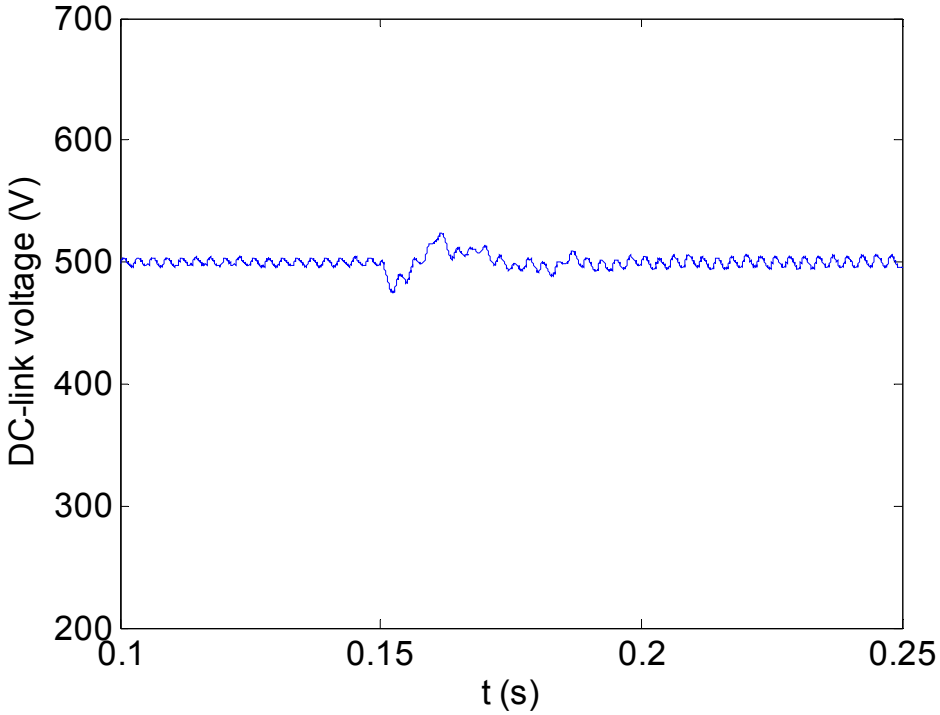

Fig. 4-21. APF DC-link voltage.

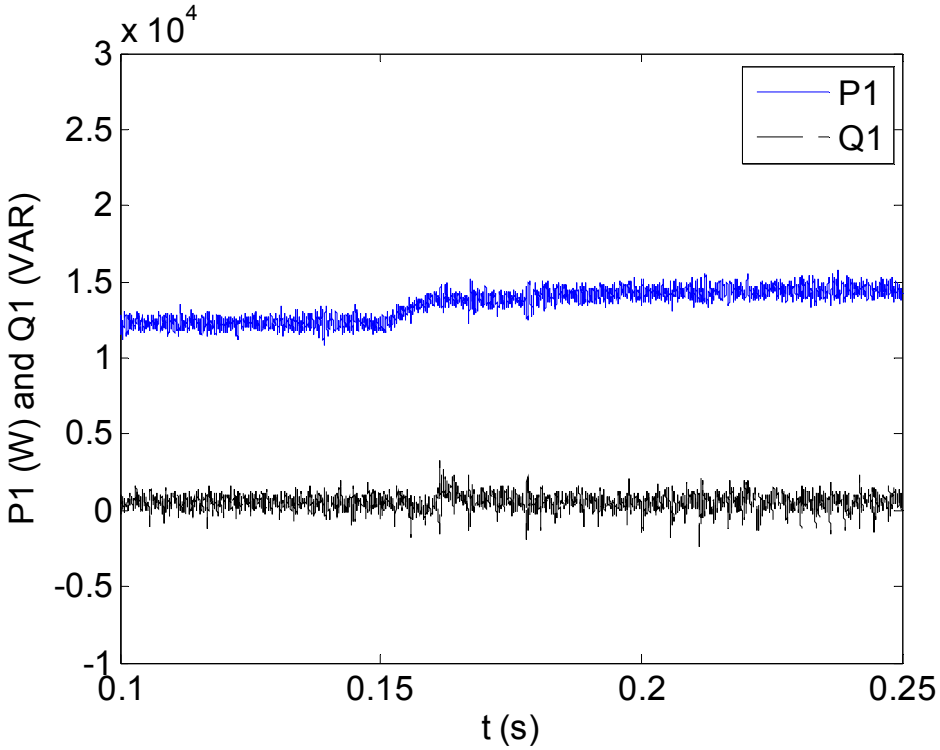

Fig. 4-22. The active and reactive power of inverter I.

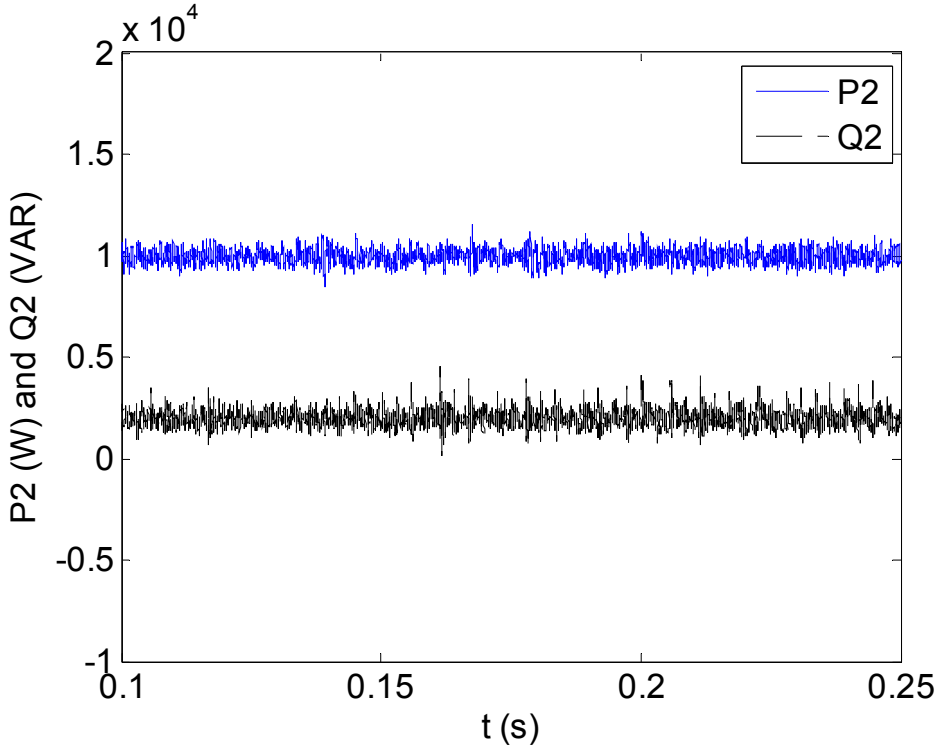

Fig. 4-23. The active and reactive power of inverter II.

Conclusion:

The use of the APF gives very good results in the parallel-connected inverters system with nonlinear load, in three cases: steady state response, transient responses of step references, and step load. The results demonstrate that the implemented APF can suppress harmonic current and supply reactive power in the parallel-connected inverters system. Power quality can be greatly improved.

In case I, after the APF is implemented in the parallel-connected inverters system with nonlinear load, the THD reduces from 30.15% to 5.47%. When a DC-link voltage controller is used, the THD reduces to 2.2%. Without an APF, the source current equals the nonlinear load current. Inverter I output reactive power experiences heavy fluctuation in order to supply the nonlinear load without the APF reactive power compensation, since the reactive power of the inverter II is constant. After the APF is utilized, the source current equals the nonlinear load current and the APF compensating current. The source current is a sinusoidal waveform.

The APF compensating current peak-peak magnitude remains the same in case II but it increases in case III, at 0.15 s of each simulation. This is because the nonlinear load does not change in case II. The power sharing ratio changes between the two inverters. Thus, it indicates that the power sharing ratio does not impact the APF compensating

current. In case III, the active power and reactive power demand of the nonlinear load increases, so does the harmonic current. Thus, the output active power and the current of inverter I increase and the APF compensating current increases.

Chapter 5. Summary and Future Work

5.1 Summary

In this thesis, first addressed is the small-signal modeling and analysis of a parallel-connected power converters system and applied it in a battery/supercapacitor hybrid energy storage system. A novel energy management method is proposed using three control strategies and in three different conditions. The proposed method is more flexible than previous methods. Under certain load situations, the proposed strategies can determine the current sharing ratio of the supercapacitor and the battery. Moreover, in a specific control strategy, the power sharing ratios are dependent on the load. In addition, frequency-domain analysis of the small-signal model was verified by the simulation results based on the average model. Simulation results indicate that an increase in proportional gains k_{p1}, a large change in integral gain k_{i1} of the voltage controller, an increase in inductance, or a decrease in capacitance may deteriorate the stability of the system. The study was of the effects of the controller and system parameter variations in order to help designers to define control parameters, filter inductance and capacitance for improved performance of the system. And last, simulation studies were carried out using

the VTB platform under various load conditions to verify the proposed control strategies and their effect on the final states of the energy storage devices.

We also identified and investigated control strategies for single DC-AC three-phase power converters. These include a novel PV control with frequency droop control loop, PQ control, voltage control, PQ control with frequency droop control, and PQ control with voltage and frequency droop control. Small-signal modeling in *d-q* rotating reference frame of a three-phase power converter system with these control strategies is developed. The impact of parameter variations on the stability of a PV controlled converter is explored.

Moreover, this thesis proposed small-signal modeling of parallel-connected three-phase converters with individual DC power supplies and network. The loci of the eigenvalues show that an increase in droop control parameter K will decrease damping ratio and eventually cause system instability. Several simulations were carried out in stand-alone and grid-connected modes and verified small-signal analysis results and the combined control strategies.

Furthermore, a detailed small-signal mathematical model is shown that can represent the zero-sequence current dynamics in parallel-connected three-phase voltage source converters that share a single DC power source. Also investigated were the effects of a

variety of factors on the zero-sequence current and a control strategy was proposed to minimize the zero-sequence current. Time-domain simulation studies verified the results.

Simulation of a parallel-connected DC-AC power converter system with nonlinear load was carried out. The use of the APF has given very good results in the parallel-connected inverters system with nonlinear load. The THD of the source current reduced from 30.15% to 2.2%. The system study shows three cases: steady state response, transient response of step change in PQ references, and transient response in step load. These results provide evidence that the implemented APF reduces harmonic distortion at the nonlinear load by harmonic compensation and supply reactive power in the parallel-connected inverters system. The power quality was largely improved.

5.2 **Future Work**

Although there is good progress made in the modeling, stability analysis, and control strategies of parallel-connected power converter systems, there are several research topics that are worth further investigation, as follows:

- We could expand the small-signal model of a hybrid energy storage system to include plug-in hybrid electric vehicles considering vehicle engines and load characteristics, and alternative energies, such as wind turbines and photovoltaics, considering their power supply characteristics. The output power of alternative energies depends on the

environment and natural conditions. Thus the output power is not constant and usually has large fluctuations. A choice could be to develop a better system with energy storage and improve the system stability.

- Considering more and more alternative energies used in DERs, development of a larger small-signal model considering parallel three-phase power converters, alternative power supply characteristics and a more complex network with various load characteristics can be considered. Development of droop control and other power management strategies to improve the system efficiency and stability is a possibility. Studying the system in voltage and frequency events and in short circuit tests is another area to pursue.
- Developing optimization methodology to automate the procedure to synthesize parallel-connected power converters based on design specifications may be fruitful.
- In smart grid, more and more loads present nonlinear characteristics with lower power factors. Development of APF and reactive power compensation methods can be explored to further improve power quality.
- In smart grid, development of centralized control and decentralized control might solve peak load problems, and developing modeling and analysis to study the system can be useful.

- An investigation can be undertaken with multi-agent approaches and using communication technology.

References

1. S. Alepuz, et al., Interfacing Renewable Energy Sources to the Utility Grid Using a Three-Level Inverter. *IEEE Transactions on Industrial Electronics*, 2006. 53(5): pp. 1504-1511.
2. C.J. Hatziadoniu, F.E. Chalkiadakis, and V.K. Feiste, A Power Conditioner for a Grid-Connected Photovoltaic Generator Based on the 3-Level Inverter. *IEEE Transactions on Energy Conversion*, 1999. 14(4): pp. 1605-1610.
3. J.W. Plastow, Energy Services for an Electricity Industry Based on Renewable Energy. *Power Engineering Journal*, 2001. 15(5): pp. 239-247.
4. S.C. W. Kramer, B. Kroposki, and H. Thomas, Advanced Power Electronic Interfaces for Distributed Energy Systems Part 1: Systems and Topologies. *National Renewable Energy Laboratory Technical Report, NREL/TP-581-42672*, 2008.
5. J. Arai, et al., Power Electronics and Its Applications to Renewable Energy in Japan. *IEEE Circuits and Systems Magazine*, 2008. 8(3): pp. 52-66.
6. S.R. Bull, Renewable Energy Today and Tomorrow. *Proceedings of the IEEE*, 2001. 89(8): pp. 1216-1226.
7. R. Ramakumar, et al., Design Scenarios for Integrated Renewable Energy Systems. *IEEE Transactions on Energy Conversion*, 1995. 10(4): pp. 736-746.
8. S.J. Chiang, S. Hsin-Jang, and C. Ming-Chieh, Modeling and Control of Pv Charger System with Sepic Converter. *IEEE Transactions on Industrial Electronics*, 2009. 56(11): pp. 4344-4353.
9. S.J. Chiang, K.T. Chang, and C.Y. Yen, Residential Photovoltaic Energy Storage System. *IEEE Transactions on Industrial Electronics*, 1998. 45(3): pp. 385-394.
10. J.M. Carrasco, et al., Power-Electronic Systems for the Grid Integration of Renewable Energy Sources: A Survey. *IEEE Transactions on Industrial Electronics*, 2006. 53(4): pp. 1002-1016.
11. S. Heier, Grid Integration of Wind Energy Conversion Systems. 2006, Hoboken, NJ: Wiley.
12. *World Wind Energy Association*. [cited; Available from: http://www.wwindea.org/home/index.php.

13. G.M. Masters, Renewable and Efficient Electric Power Systems. 2004: John Wiley & Sons.
14. P.F. Ribeiro, et al., Energy Storage Systems for Advanced Power Applications. *Proceedings of the IEEE*, 2001. 89(12): pp. 1744-1756.
15. H. Ertl, J.W. Kolar, and F.C. Zach, A Novel Multicell Dc-Ac Converter for Applications in Renewable Energy Systems. *IEEE Transactions on Industrial Electronics*, 2002. 49(5): pp. 1048-1057.
16. G. Martin, Renewable Energy Gets The "Green" Light in Chicago. *IEEE Power and Energy Magazine*, 2003. 1(6): pp. 34-39.
17. T. Bhattacharya, et al., Multiphase Bidirectional Flyback Converter Topology for Hybrid Electric Vehicles. *IEEE Transactions on Industrial Electronics*, 2009. 56(1): pp. 78-84.
18. M.B. Camara, et al., Design and New Control of Dc/Dc Converters to Share Energy between Supercapacitors and Batteries in Hybrid Vehicles. *IEEE Transactions on Vehicular Technology*, 2008. 57(5): pp. 2721-2735.
19. J. McDowall. Conventional Battery Technologies-Present and Future. *IEEE Power Engineering Society Summer Meeting*. 2000. pp. 1538-1540.
20. K. Yoshimoto, T. Nanahara, and G. Koshimizu. New Control Method for Regulating State-of- Charge of a Battery in Hybrid Wind Power/Battery Energy Storage System. *IEEE Power Systems Conference and Exposition*. 2006. pp. 1244-1251.
21. S. Duryea, S. Islam, and W. Lawrance, A Battery Management System for Stand-Alone Photovoltaic Energy Systems. *IEEE Industry Applications Magazine*, 2001. 7(3): pp. 67-72.
22. R.F. Nelson, Power Requirements for Batteries in Hybrid Electric Vehicles. *Journal of Power Sources*, 2000. 91(1): pp. 2-26.
23. A. Rufer and P. Barrade, A Supercapacitor-Based Energy-Storage System for Elevators with Soft Commutated Interface. *IEEE Transactions on Industry Applications*, 2002. 38(5): pp. 1151-1159.
24. D. Linzen, et al. Analysis and Evaluation of Charge Balancing Circuits on Performance, Reliability and Lifetime of Supercapacitor Systems. *Industry Applications Conference*. 2003. pp. 1589-1595.
25. C. Abbey and G. Joos, Supercapacitor Energy Storage for Wind Energy Applications. *IEEE Transactions on Industry Applications*, 2007. 43(3): pp. 769-776.

26. K. Sang-Min and S. Seung-Ki, Control of Rubber Tyred Gantry Crane with Energy Storage Based on Supercapacitor Bank. *IEEE Transactions on Power Electronics*, 2006. 21(5): pp. 1420-1427.
27. S. Lemofouet and A. Rufer, A Hybrid Energy Storage System Based on Compressed Air and Supercapacitors with Maximum Efficiency Point Tracking (Mept). *IEEE Transactions on Industrial Electronics*, 2006. 53(4): pp. 1105-1115.
28. P. Thounthong, S. Rael, and B. Davat, Analysis of Supercapacitor as Second Source Based on Fuel Cell Power Generation. *IEEE Transactions on Energy Conversion*, 2009. 24(1): pp. 247-255.
29. Z. Jiang, et al., Design and Experimental Tests of Control Strategies for Active Hybrid Fuel Cell/Battery Power Sources. *Journal of Power Sources*, 2004. 130(1-2): pp. 163-171.
30. S.M. Lukic, et al., Energy Storage Systems for Automotive Applications. *IEEE Transactions on Industrial Electronics*, 2008. 55(6): pp. 2258-2267.
31. W. Ying and G. Hongwei, Optimization of Fuel Cell and Supercapacitor for Fuel-Cell Electric Vehicles. *IEEE Transactions on Vehicular Technology*, 2006. 55(6): pp. 1748-1755.
32. S. Pay and Y. Baghzouz. Effectiveness of Battery-Supercapacitor Combination in Electric Vehicles. *IEEE Power Tech Conference Proceedings*. 2003. pp. 6.
33. L. Gao, R.A. Dougal, and S. Liu. Active Power Sharing in Hybrid Battery/Capacitor Power Sources. *IEEE Applied Power Electronics Conference and Exposition*. 2003. pp. 497-503 vol.1.
34. Y. Zhang and Z. Jiang. Dynamic Power Sharing Strategy for Active Hybrid Energy Storage Systems. *IEEE Vehicle Power and Propulsion Conference*. 2009. pp. 558-563.
35. H. Yoo, et al., System Integration and Power-Flow Management for a Series Hybrid Electric Vehicle Using Supercapacitors and Batteries. *IEEE Transactions on Industry Applications*, 2008. 44(1): pp. 108-114.
36. Z. Jiang and R.A. Dougal. A Hybrid Fuel Cell Power Supply with Rapid Dynamic Response and High Peak-Power Capacity. *Applied Power Electronics Conference and Exposition*. 2006. pp. 6.
37. K.K. Hedel, High-Density Avionic Power Supply. *IEEE Transactions on Aerospace and Electronic Systems*, 1980. AES-16(5): pp. 615-619.

38. R.B. Redley, Small-Signal Analysis of Parallel Power Converters. *MS Thesis, Department of Electrical and Computer Engineering, Virginia Polytechic Institute and State University, Blacksburg, Virginia*, 1986.
39. H. Tanaka, et al. Method for Centralized Voltage Control and Current Balancing for Parallel Operation of Power Supply Equipment. *Telecommunications Energy Conference*. 1988. pp. 434-440.
40. B. Choi, et al. Control Strategy for Multi-Module Parallel Converter System. *Power Electronics Specialists Conference*. 1990. pp. 225-234.
41. K. Siri, C.Q. Lee, and T.E. Wu, Current Distribution Control for Parallel Connected Converters. I. *IEEE Transactions on Aerospace and Electronic Systems*, 1992. 28(3): pp. 829-840.
42. T. Kohama, et al. Dynamic Analysis of Parallel-Module Converter System with Current Balance Controllers. *Telecommunications Energy Conference*. 1994. pp. 190-195.
43. J.S. Glaser and A.F. Witulski, Output Plane Analysis of Load-Sharing in Multiple-Module Converter Systems. *IEEE Transactions on Power Electronics*, 1994. 9(1): pp. 43-50.
44. C. Byungcho, Comparative Study on Paralleling Schemes of Converter Modules for Distributed Power Applications. *IEEE Transactions on Industrial Electronics*, 1998. 45(2): pp. 194-199.
45. V.J. Thottuvelil and G.C. Verghese, Analysis and Control Design of Paralleled Dc/Dc Converters with Current Sharing. *IEEE Transactions on Power Electronics*, 1998. 13(4): pp. 635-644.
46. S. Luo, et al. A Classification and Evaluation of Paralleling Methods for Power Supply Modules. *IEEE Power Electronics Specialists Conference*. 1999. pp. 901-908.
47. H.H.C. Iu and C.K. Tse, Bifurcation Behavior in Parallel-Connected Buck Converters. *IEEE Transactions on Circuits and Systems I: Fundamental Theory and Applications*, 2001. 48(2): pp. 233-240.
48. K. Jung-Won, C. Hang-Seok, and C. Bo Hyung, A Novel Droop Method for Converter Parallel Operation. *IEEE Transactions on Power Electronics*, 2002. 17(1): pp. 25-32.
49. Y. Panov and M.M. Jovanovic, Stability and Dynamic Performance of Current-Sharing Control for Paralleled Voltage Regulator Modules. *IEEE Transactions on Power Electronics*, 2002. 17(2): pp. 172-179.

50. M. Lopez, et al., Current Distribution Control Design for Paralleled Dc/Dc Converters Using Sliding-Mode Control. *IEEE Transactions on Industrial Electronics*, 2004. 51(2): pp. 419-428.
51. Y. Huang and C.K. Tse, Circuit Theoretic Classification of Parallel Connected Dc&Ndash;Dc Converters. *IEEE Transactions on Circuits and Systems I: Regular Papers*, 2007. 54(5): pp. 1099-1108.
52. S.K. Mazumder, M. Tahir, and S.L. Kamisetty, Wireless Pwm Control of a Parallel Dc-Dc Buck Converter. *Power Electronics, IEEE Transactions on*, 2005. 20(6): pp. 1280-1286.
53. M. Jordan, Uc3907 Load Share Ic Simplifies Parallel Power Supply Design. *Texas Instruments Application Note U-129, Dallas, TX.*
54. N. Pogaku, M. Prodanovic, and T.C. Green, Modeling, Analysis and Testing of Autonomous Operation of an Inverter-Based Microgrid. *IEEE Transactions on Power Electronics*, 2007. 22(2): pp. 613-625.
55. A. Tabesh and R. Iravani, Small-Signal Model and Dynamic Analysis of Variable Speed Induction Machine Wind Farms. *IET Renewable Power Generation*, 2008. 2(4): pp. 215-227.
56. A. Arulampalam, et al., Control of Power Electronic Interfaces in Distributed Generation Microgrids. *International Journal of Electronics*, 2004. 91(9): pp. 503.
57. N. Hatziargyriou, et al., Microgrids. *IEEE Power and Energy Magazine*, 2007. 5(4): pp. 78-94.
58. R.H. Lasseter. Microgrids. *IEEE Power Engineering Society Winter Meeting*. 2002. pp. 305-308.
59. C. Marnay and G. Venkataramanan. Microgrids in the Evolving Electricity Generation and Delivery Infrastructure. *IEEE Power Engineering Society General Meeting*. 2006.
60. J. Driesen and F. Katiraei, Design for Distributed Energy Resources. *IEEE Power and Energy Magazine*, 2008. 6(3): pp. 30-40.
61. J.A.P. Lopes, C.L. Moreira, and A.G. Madureira, Defining Control Strategies for Microgrids Islanded Operation. *IEEE Transactions on Power Systems*, 2006. 21(2): pp. 916-924.
62. A.G. Tsikalakis and N.D. Hatziargyriou, Centralized Control for Optimizing Microgrids Operation. *IEEE Transactions on Energy Conversion*, 2008. 23(1): pp. 241-248.

63. T. Funabashi, et al. An Autonomous Agent for Reliable Operation of Power Market and Systems Including Microgrids. *Third International Conference on Electric Utility Deregulation and Restructuring and Power Technologies*. 2008. pp. 173-177.
64. A.L. Dimeas and N.D. Hatziargyriou, Operation of a Multiagent System for Microgrid Control. *Power Systems, IEEE Transactions on*, 2005. 20(3): pp. 1447-1455.
65. M.S. Illindala, et al., Hardware Development of a Laboratory-Scale Microgrid Phase 2: Operation and Control of a Two-Inverter Microgrid. 2004.
66. Y. Li, D.M. Vilathgamuwa, and L. Poh Chiang, Design, Analysis, and Real-Time Testing of a Controller for Multibus Microgrid System. *IEEE Transactions on Power Electronics*, 2004. 19(5): pp. 1195-1204.
67. A.L. Dimeas and N.D. Hatziargyriou, Operation of a Multiagent System for Microgrid Control. *IEEE Transactions on Power Systems*, 2005. 20(3): pp. 1447-1455.
68. M.C. Chandorkar, D.M. Divan, and R. Adapa, Control of Parallel Connected Inverters in Standalone Ac Supply Systems. *IEEE Transactions on Industry Applications*, 1993. 29(1): pp. 136-143.
69. F. Katiraei and M.R. Iravani, Power Management Strategies for a Microgrid with Multiple Distributed Generation Units. *IEEE Transactions on Power Systems*, 2006. 21(4): pp. 1821-1831.
70. S.J. Chiang, C.Y. Yen, and K.T. Chang, A Multimodule Parallelable Series-Connected Pwm Voltage Regulator. *IEEE Transactions on Industrial Electronics*, 2001. 48(3): pp. 506-516.
71. J.M. Guerrero, et al., A Wireless Controller to Enhance Dynamic Performance of Parallel Inverters in Distributed Generation Systems. *IEEE Transactions on Power Electronics*, 2004. 19(5): pp. 1205-1213.
72. Z. Ye, D. Boroyevich, and F.C. Lee. Modeling and Control of Zero-Sequence Current in Parallel Multi-Phase Converters. *IEEE Power Electronics Specialists Conference*. 2000. pp. 680-685.
73. Z. Ye, P.K. Jain, and P.C. Sen, Circulating Current Minimization in High-Frequency Ac Power Distribution Architecture with Multiple Inverter Modules Operated in Parallel. *IEEE Transactions on Industrial Electronics*, 2007. 54(5): pp. 2673-2687.

74. Z. Ye, D. Boroyevich, and F.C. Lee, Dynamics Analysis of Parallel Three-Phase Converters. *Journal of Vibration and Control*, 2002. 8: pp. 243-259.
75. C.S. Lee, et al. Parallel Ups with a Instantaneous Current Sharing Control. *IEEE Industrial Electronics Society*. 1998. pp. 568-573.
76. S. Ogasawara, et al., A Novel Control Scheme of a Parallel Current-Controlled Pwm Inverter. *IEEE Transactions on Industry Applications*, 1992. 28(5): pp. 1023-1030.
77. M. Hashii, K. Kousaka, and M. Kaimoto, New Approach to a High-Power Gto Pwm Inverter for Ac Motor Drives. *IEEE Transactions on Industry Applications*, 1987. IA-23(2): pp. 263-269.
78. S. Ogasawara, et al., A Novel Control Scheme of a Parallel Current-Controlled Pwm Inverter. *Industry Applications, IEEE Transactions on*, 1992. 28(5): pp. 1023-1030.
79. A.E. Emanuel, et al., A Survey of Harmonic Voltages and Currents at the Customer's Bus. *IEEE Transactions on Power Delivery*, 1993. 8(1): pp. 411-421.
80. D. Karlsson and D.J. Hill, Modelling and Identification of Nonlinear Dynamic Loads in Power Systems. *IEEE Transactions on Power Systems*, 1994. 9(1): pp. 157-166.
81. J. Nastran, et al., Active Power Filter for Nonlinear Ac Loads. *IEEE Transactions on Power Electronics*, 1994. 9(1): pp. 92-96.
82. R. Arseneau, et al., Practical Definitions for Powers in Systems with Nonsinusoidal Waveforms and Unbalanced Loads: A Discussion. *IEEE Transactions on Power Delivery*, 1996. 11(1): pp. 79-101.
83. B. Singh, K. Al-Haddad, and A. Chandra, A Review of Active Filters for Power Quality Improvement. *IEEE Transactions on Industrial Electronics*, 1999. 46(5): pp. 960-971.
84. U. Borup, F. Blaabjerg, and P.N. Enjeti, Sharing of Nonlinear Load in Parallel-Connected Three-Phase Converters. *IEEE Transactions on Industry Applications*, 2001. 37(6): pp. 1817-1823.
85. H. Akagi, A. Nabae, and S. Atoh, Control Strategy of Active Power Filters Using Multiple Voltage-Source Pwm Converters. *IEEE Transactions on Industry Applications*, 1986. IA-22(3): pp. 460-465.

86. L.A. Moran, J.W. Dixon, and R.R. Wallace, A Three-Phase Active Power Filter Operating with Fixed Switching Frequency for Reactive Power and Current Harmonic Compensation. *IEEE Transactions on Industrial Electronics*, 1995. 42(4): pp. 402-408.
87. K. Sangsun and P.N. Enjeti, A New Hybrid Active Power Filter (Apf) Topology. *IEEE Transactions on Power Electronics*, 2002. 17(1): pp. 48-54.
88. D.A. Torrey and A.M.A.M. Al-Zamel, Single-Phase Active Power Filters for Multiple Nonlinear Loads. *IEEE Transactions on Power Electronics*, 1995. 10(3): pp. 263-272.
89. A. Chandra, et al., An Improved Control Algorithm of Shunt Active Filter for Voltage Regulation, Harmonic Elimination, Power-Factor Correction, and Balancing of Nonlinear Loads. *IEEE Transactions on Power Electronics*, 2000. 15(3): pp. 495-507.
90. S. Saetieo, R. Devaraj, and D.A. Torrey, The Design and Implementation of a Three-Phase Active Power Filter Based on Sliding Mode Control. *IEEE Transactions on Industry Applications*, 1995. 31(5): pp. 993-1000.
91. J. Hu and Y. He, Modeling and Control of Grid-Connected Voltage-Sourced Converters under Generalized Unbalanced Operation Conditions. *IEEE Transactions on Energy Conversion*, 2008. 23(3): pp. 903-913.
92. A.M. Cross, P.D. Evans, and A.J. Forsyth, Dc Link Current in Pwm Inverters with Unbalanced and Nonlinear Loads. *IEE Proceedings-Electric Power Applications*, 1999. 146(6): pp. 620-626.
93. J.S. Linder, Small-Signal Model of the Parallel-Plane Vacuum Diode. *Electronics Letters*, 1965. 1(5): pp. 141-142.
94. F.A. Lindholm and P.R. Gray, Large-Signal and Small-Signal Models for Arbitrarily-Doped Four-Terminal Field-Effect Transistors. *IEEE Transactions on Electron Devices*, 1966. 13(12): pp. 819-829.
95. F.C. Fitchen, Limiting Amplitude for Mosfet Small-Signal Models. *Proceedings of the IEEE*, 1967. 55(12): pp. 2176-2177.
96. F. Lindholm, A. and D.J. hamilton, A Systematic Modeling Theory for Solid State Device. *Solid State Electronics*, 1964(7): pp. 171.
97. A. Tabesh and R. Iravani, Small-Signal Model and Dynamic Analysis of Variable Speed Induction Machine Wind Farms, in *IET Renewable Power Generation*. 2008. p. 215-227.

98. E.A.A. Coelho, P.C. Cortizo, and P.F.D. Garcia, Small-Signal Stability for Parallel-Connected Inverters in Stand-Alone Ac Supply Systems. *IEEE Transactions on Industry Applications*, 2002. 38(2): pp. 533-542.
99. A.L. Shenkman, B. Axelrod, and V. Chudnovsky, A New Simplified Model of the Dynamics of the Current-Fed Parallel Resonant Inverter. *IEEE Transactions on Industrial Electronics*, 2000. 47(2): pp. 282-286.
100. Y. Zhang, Z. Jiang, and X. Yu. Control Strategies for Battery/Supercapacitor Hybrid Energy Storage Systems. *IEEE Energy 2030 Conference*. 2008. pp. 1-6.
101. L. Gao, S. Liu, and R.A. Dougal, Dynamic Lithium-Ion Battery Model for System Simulation. *IEEE Transactions on Components and Packaging Technologies*, 2002. 25(3): pp. 495-505.
102. Z. Jiang and X. Yu. Active Power - Voltage Control Scheme for Islanding Operation of Inverter-Interfaced Microgrids. *IEEE Power & Energy Society General Meeting*. 2009. pp. 1-7.
103. X. Yu, Z. Jiang, and Y. Zhang. Control of Parallel Inverter-Interfaced Distributed Energy Resources. *IEEE Energy 2030 Conference*. 2008. pp. 1-8.